

Structural studies of the mitochondrial ribosome and co-translational insertion of membrane proteins



Nirupa Desai

MRC-Laboratory of Molecular Biology
Cambridge, United Kingdom

Gonville and Caius College
University of Cambridge

This thesis is submitted for the degree of
Doctor of Philosophy
September 2019

Preface

This thesis is the result of my own work and includes nothing which is the outcome of work done in collaboration except as declared in the preface and specified in the text.

It is not substantially the same as any that I have submitted, or, is being concurrently submitted for a degree or diploma or other qualification at the University of Cambridge or any other University or similar institution except as declared in the Preface and specified in the text. I further state that no substantial part of my dissertation has already been submitted, or, is being concurrently submitted for any such degree, diploma or other qualification at the University of Cambridge or any other University or similar institution except as declared in the Preface and specified in the text.

It does not exceed the prescribed word limit as specified by the Degree Committee.

The yeast mitoribosome project was done in collaboration with Dr Alan Brown and Dr Alexey Amunts. The human mitoribosome translocon project is a collaboration with Dr Hanting Yang. The selenocysteine incorporation project is a collaboration with Dr Krishna Chatterjee, Dr Erik Schoenmakers and Dr Yuliya Gordiyenko.

This work was funded by the Wellcome Trust PhD Programme for Clinicians.

Abstract

Structural studies of the mitochondrial ribosome and co-translational insertion of membrane proteins – Nirupa Desai

The mitochondrion, a constituent of eukaryotic cells is important in the synthesis of ATP through a process called oxidative phosphorylation. The enzymes that make up the subunits of oxidative phosphorylation in humans and yeast are encoded by both nuclear DNA and in mitochondrial DNA. As such the mitochondrion has retained its own translational system to include mitochondrial ribosomes (mitoribosome) to translate these proteins along with other proteins which is species dependent. The mitoribosome is also involved in co-translational insertion of proteins destined for the inner mitochondrial membrane through binding of its translocon OXA1.

My study has revealed the structure of the complete 75-component yeast *Saccharomyces cerevisiae* mitochondrial ribosome solved to 3.3 Å by single particle cryo-electron microscopy (cryo-EM). The previously unsolved small subunit of the mitoribosome was built de novo to include 34 proteins, of which 7 are specific to the yeast mitochondrial ribosome and the 15S ribosomal RNA. This mitochondrial ribosome has a distinct architecture compared to other mitochondrial ribosome and its ancestral bacterial ribosome. Elements specific to the yeast mitoribosome give it a distinct shape and architecture to include a putatively active enzyme on the periphery. An expanded messenger RNA exit channel has also been found harbouring a platform suitable for translational activator binding. In general this structure has provided insight into translation specialisation amongst species and its continued evolution.

Multiple states of actively translating human mitoribosome have been elucidated using single particle cryo-EM. The human mitoribosome structures, stalled by different antibiotics, have been seen with A/A and P/P site tRNAs in situ as well as structures with an unidentified factor in the mitoribosomal factor site. In addition the human mitochondrial large subunit and stalled complete mitoribosome has been found at low resolution likely complexed to its translocon OXA1L following detergent solubilisation.

Acknowledgements

Many people have supported and assisted me over the course of my PhD and I am grateful to each of them, including all members of the Ramakrishnan lab and all of my friends at the LMB. However, the following people went above and beyond to help me complete my thesis, whom I would like to acknowledge here to express my gratitude.

Firstly I would like to thank Venki for all his support, advice and for taking a gamble on his first medic lab member. Manu and Edmund have also been invaluable in their guidance as my secondary supervisors, and I am grateful to Michal for his advice and collaboration. In the Venki lab I would especially like to thank Alexey and Alan, who undertook a large part of my initial training and to Vish who subsequently took up this mantle! Also to Song for all his valued guidance and camaraderie. Thanks to Jose, Nathan, Jailson and Yuliya who have all provided much support and technical knowledge and to Jason and Chris for great discussions at breakfast club. A huge thank you to Hanting, for all her hard work on our projects, for making me the best lunches and for the most beautiful art gifts. I am grateful to Christos, Shaoxia, Guiseppe and Joanna who have all been an important part of my cryo-EM training and to Jake and Toby for their computing support. Thanks to Pat for her help, expertise and collaboration with tissue culture. Thanks to Krish and Erik for their collaboration and dedication to our projects. Also to Seb for his patient and meticulous thesis proof reading. I would like to thank my mother and late father for always encouraging me in my educational path, and to Simon and Beatrice for our continued journey together. Finally I would like to thank KJ, whose advice throughout my PhD and career is greatly appreciated.

Publication

Desai N, Brown A, Amunts A, Ramakrishnan V. The structure of the yeast mitochondrial ribosome. *Science*. 2017;355(6324):528–531.

doi:10.1126/science.aal2415

Abbreviations

A-site	aminoacyl site
ADP	adenosine diphosphate
AML	acute myeloid leukaemia
ATP	adenosine 5'- triphosphate
C-terminus	carboxyl terminus
CL	cardiolipin
CMC	critical micelle concentration
Cox	cytochrome oxidase
CP	central protuberance
Cyt	cytochrome
β -DDM	n-Dodecyl β -D-maltoside
DNA	deoxyribonucleic acid
e-	eukaryotic
E-site	exit site
E. coli	Escherichia coli
EEFSEC	Selenocysteine-specific GTPase translation elongation factor
EF-G	elongation factor-G
EF-Tu	elongation factor-Tu
EM	electron microscopy
EMD	Electron Microscopy Data (Bank)
ER	endoplasmic reticulum
FCwSS	focussed classification with signal subtraction
FSC	Fourier-shell-correlation
GDP	guanosine 5'- diphosphate
GDPCP	5'-guanosyl-methylene-triphosphate
GDPNP	5'-Guanylyl imidodiphosphate
GTP	guanosine 5'- triphosphate
IF	initiation factor
LSU	large subunit
mRNA	messenger RNA

mt-	mitochondrial
mt-DNA	mitochondrial DNA
MW	molecular weight
N-terminus	amino terminus
OXA	cytochrome oxidase assembly translocase
OXPHOS	oxidative phosphorylation
P-site	peptidyl site
PDB	Protein Data Bank
PoTC	post termination complex
PTC	peptidyl transferase centre
RF	release factor
RNA	ribonucleic acid
RRF	ribosome recycling factor
rRNA	ribosomal RNA
<i>S. cerevisiae</i>	<i>Saccharomyces cerevisiae</i>
Sec	selenocysteine
SECIS	selenocysteine insertion sequence
SECISBP2	SECIS binding protein 2
SSU	small subunit
TOCL	tetraoleoyl cardiolipin
tRNA	transfer RNA
UTR	untranslated region

Table of Contents

1	Introduction	1
1.1	Background	1
1.1.1	Translation and the Mitochondrion.....	1
1.1.1.1	The mitochondrion.....	1
1.1.1.2	The mitochondrial genome.....	1
1.1.1.3	Protein translation and ribosome structure	4
1.1.1.4	The mitochondrial ribosome	6
1.1.1.5	Expression, maturation and characteristics of mitochondrial RNA	8
1.1.1.6	Translation initiation.....	10
1.1.1.7	Translation elongation.....	13
1.1.1.8	Translation termination and recycling.....	14
1.1.1.9	Mitochondrial translation in human health and disease	15
1.1.1.10	Polypeptide exit tunnel and mitoribosome localisation	17
1.1.1.11	Cooperation between mitochondrial and cytosolic ribosomes.....	20
1.1.2	Single particle cryo-electron microscopy.....	22
1.1.3	The state of the mitoribosomal structural field.....	25
2	Yeast Mitochondrial Ribosome	27
2.1	Scientific aims.....	27
2.2	Strategy	28
2.2.1	Sample preparation	28
2.2.2	Data processing and map generation.....	28
2.3	Results and Discussion	38
2.3.1	Overall Structure.....	38
2.3.2	Mt-SSU protein elements and mt-rRNA expansion segments.....	45
2.3.3	Intersubunit Connections.....	52
2.3.4	Features of the yeast mt-SSU	59
2.3.5	The mt-mRNA channel	62
2.4	Conclusions	67
2.5	Materials and Methods	71
2.5.1	Isolation of mitochondria	71
2.5.2	Purification of mitoribosomes	71
2.5.3	Electron microscopy.....	72
2.5.4	Image Processing	72
2.5.5	Model building	73

2.5.6	Model refinement and validation.....	75
2.5.7	Figures.....	75
3	Co-translational insertion of mitochondrial membrane proteins	76
3.1	Scientific Aims	76
3.2	Strategy.....	80
3.3	Results and Discussion	84
3.3.1	Purification 1 - Actively translating mitoribosome with mt-tRNA	84
3.3.2	Purification 2 - Mitoribosome mt-LSU.....	91
3.3.3	Purification 3 – P-site mt-tRNA and density in factor site	100
3.3.4	Purification 4 – extended factor site density	105
3.3.5	Purification 5 – Density at the polypeptide exit site on the mt-LSU.....	112
3.3.6	Purification 6 – Density at the polypeptide exit site on the monosome	124
3.4	Further work and conclusions.....	135
3.5	Materials and Methods	137
3.5.1	Purification of human mitochondria	137
3.5.2	Preparation of Cardiolipin	138
3.5.3	Purification of human mitoribosome OXA1L complex from HEK293S cells	138
3.5.4	Trial of initiation of translation in mitochondria (Purification 3).....	139
3.5.5	10-50% sucrose gradients.....	139
3.5.6	Western Blotting.....	139
3.5.7	Purification of ribosomes from PDE12 -/- HEK293 cells.....	140
3.5.8	Electron microscopy.....	141
3.5.9	Image processing and figures.....	141
4	Final remarks	142
5	Appendix.....	143
5.1	A specialised case of elongation	143
5.1.1	Background	143
5.1.1.1	Selenium, Selenocysteine and Selenoproteins	143
5.1.1.2	Eukaryotic Translation Termination.....	143
5.1.1.3	Ribosome Sec Incorporation.....	144
5.1.1.3.1	Selenocysteine biogenesis.....	146
5.1.1.3.2	Pathogenesis of selenocysteine incorporation.....	146
5.1.1.3.3	Structural studies of the selenocysteine incorporation pathway	148
5.1.2	Scientific Aims.....	149
5.1.3	Strategy	149

5.1.4	Results and Discussion	151
5.1.4.1	Preparation of materials	151
5.1.4.2	Initial complex formation	155
5.1.5	Conclusions.....	160
5.1.6	Materials and Methods	163
5.1.6.1	Cloning.....	163
5.1.6.2	In vitro transcription	167
5.1.6.3	Protein Purification.....	167
5.1.6.3.1	EEFSEC for complex formation	167
5.1.6.3.2	EEFSEC for Sec-tRNA ^{[Ser]^{Sec}} purification.....	169
5.1.6.4	SECISBP2	169
5.1.6.5	Pig liver tRNA purification	170
5.1.6.6	Sec-tRNA ^{[Ser]^{Sec}} purification from pig Liver	171
5.1.6.7	Sec-tRNA ^{[Ser]^{Sec}} purification from pig testis.....	171
5.1.6.8	Reverse transcription Sec-tRNA ^{[Ser]^{Sec}}	173
5.1.6.9	In Vitro Translation radioactive and 10-50% Sucrose gradient	173
5.1.6.10	Complex formation	173
5.1.6.11	Grid preparation	174
5.1.6.12	Electron microscopy and Image Processing.....	174
6	References.....	175

Table of Figures

FIGURE 1 – TAKEN FROM OTT M, AMUNTS A, BROWN A. ORGANIZATION AND REGULATION OF MITOCHONDRIAL PROTEIN SYNTHESIS. ANNU REV BIOCHEM. 2016 JUN 2;85:77-101 (10). (A) HUMAN MITOCHONDRIAL GENOME. (B) <i>SACCHAROMYCES CEREVISIAE</i> MITOCHONDRIAL GENOME. THE GENES ARE COLOUR CODED ACCORDING TO FUNCTION AS DENOTED BY THE LEGEND.	3
FIGURE 2 – LARGE SUBUNIT OF THE YEAST MITOCHONDRIAL RIBOSOME ADAPTED FROM AMUNTS A, BROWN A, BAI XC, ET AL. STRUCTURE OF THE YEAST MITOCHONDRIAL LARGE RIBOSOMAL SUBUNIT. <i>SCIENCE</i> . 2014;343(6178):1485–1489 (46). THE 54S IS SHOWN IN TWO VIEWS WITH THE MITORIBOSOMAL PROTEINS COLOURED AND LABELLED INDIVIDUALLY. THE 21S rRNA IS COLOURED IN GREY.	7
FIGURE 3 – TAKEN FROM AMUNTS A, BROWN A, TOOTS J, SCHERES SHW, RAMAKRISHNAN V. RIBOSOME. THE STRUCTURE OF THE HUMAN MITOCHONDRIAL RIBOSOME. <i>SCIENCE</i> . 2015;348(6230):95–98 (48). OVERVIEW OF THE HUMAN MITORIBOSOME. THE AREAS WITH BACTERIAL CONSERVATION ARE COLOURED IN BLUE. THE EXTENSIONS OF HOMOLOGOUS BACTERIAL PROTEINS ARE COLOURED IN YELLOW AND THE MITOCHONDRIA-SPECIFIC PROTEINS ARE COLOURED IN RED. MT-rRNA IS COLOURED IN GREY.	8
FIGURE 4 – TAKEN FROM ENGLMEIER, ROBERT ET AL. “STRUCTURE OF THE HUMAN MITOCHONDRIAL RIBOSOME STUDIED IN SITU BY CRYOELECTRON TOMOGRAPHY.” <i>STRUCTURE</i> 25 10 (2017): 1574-1581.e2 (100). TOP LEFT IS A TOMOGRAPHIC SLICE SHOWING A CLUSTER OF MITORIBOSOME. SCALE BAR, 50NM. THE COLOURED IMAGES SHOW TOMOGRAPHIC RECONSTRUCTIONS OF MITORIBOSOME DISTRIBUTION. ORANGE = OUTER MITOCHONDRIAL MEMBRANE. GREY = INNER MITOCHONDRIAL MEMBRANE. BLUE = MT-LSU. YELLOW = MT-SSU.	19
FIGURE 5 – (A) A REPRESENTATIVE ELECTRON MICROGRAPH. (B) REPRESENTATIVE 2D CLASSES. ADAPTED FROM DESAI ET AL (135).	29
FIGURE 6 – RELION DATA PROCESSING SCHEME (135).	30
FIGURE 7 - (A) CLASS B IS RELATED TO CLASS A BY A SMALL 1.5° ROTATION OF THE MT-SSU BODY AND AN 8° ROTATION OF THE MT-SSU HEAD. (B) CLASS C IS RELATED TO CLASS A BY SMALL ROTATIONS OF 2.5° AND 1.5° OF THE MT-SSU BODY AND HEAD RESPECTIVELY. THE BODY ATOMS AND HEAD VECTORS ARE COLOURED BY ROOT-MEAN-SQUARE DISPLACEMENT (RMSD), ACCORDING TO THE FIGURE LEGEND, FROM THEIR POSITION IN CLASS A AND POSITIONED IN THE RIGHT HAND IMAGES (135).	31
FIGURE 8 – (A) FOURIER-SHELL-CORRELATION (FSC) CURVES FOR THE THREE DIFFERENT CONFORMATIONS OF THE YEAST MITORIBOSOME MONOSOMES. (B) FCS CURVES FOR EACH FOR THE MASKED MAPS FOR THE DIFFERENT SEGMENTS OF THE MITORIBOSOME. ADAPTED FROM DESAI ET AL (135).	32
FIGURE 9 – MAPS FOR EACH MAIN YEAST MITORIBOSOME MONOSOME CLASS A-C, AND MAPS FOR EACH MASKED MAP COLOURED BY LOCAL RESOLUTION ACCORDING TO THE FIGURE LEGEND. ADAPTED FROM DESAI ET AL (135).	33
FIGURE 10 – (A) FSC CURVES COMPARING THE OBTAINED MASKED MAP OF THE MT-LSU AND THE PREVIOUSLY PUBLISHED MAP (EMD-2566) (B) POST PROCESSED MAPS (46). ADAPTED FROM DESAI ET AL (135).	34
FIGURE 11 – FSC CURVES REPRESENTING THE FIT OF THE REFINED MODEL TO THE FINAL MAP (BLACK LINE) FOR EACH OF THE THREE YEAST MITORIBOSOME CONFORMATIONS. THE DASHED LINE INDICATES THE RESOLUTION AT	

FSC=0.5. DENOTED BY BLUE AND RED LINES ARE THE SELF- (FSC_{WORK}) AND CROSS-VALIDATED (FSC_{FREE}) CORRELATIONS RESPECTIVELY. ADAPTED FROM DESAI <i>ET AL</i> (135).....	35
FIGURE 12 – EXAMPLES OF REGIONS IMPROVED COMPARING THE OLD MAP (EMD-2566) WITH OUR NEW MAP, WITH NEWLY BUILT AMINO ACIDS (46). ADAPTED FROM DESAI <i>ET AL</i> (135)	36
FIGURE 13 – (A) THE OVERALL STRUCTURE OF THE YEAST MITOCHONDRIAL RIBOSOME. (B) PROTEIN CONSTITUENTS OF THE YEAST MT-SSU (135). THE FIGURES REPRESENT THE PYMOL SURFACE REPRESENTATIONS OF THE MODEL.....	40
FIGURE 14 – E-SITE MT-tRNA (135). (A) E-SITE MT-tRNA BOUND IN THE INTERSUBUNIT SPACE SHOWN AS A SLICE THROUGH THE UNFILTERED MAP OF THE YEAST MITORIBOSOME. THE MT-LSU MAKES CONTACT WITH THE ACCEPTOR STEM AND ELBOW OF THE MT-tRNA AND THE MT-SSU MAKES CONTACT WITH THE ANTICODON STEM-LOOP. (B) MASKED MAPS OF THE SUBUNIT WERE USED TO MODEL THE ACCEPTOR STEM AND ANTICODON STEM-LOOP OF THE MT-tRNA	43
FIGURE 15 – mS38 (Cox24) (135). MODEL OF S38 (Cox24) FITTED TO THE DENSITY. FROM THE DENSITY MS38 WAS IDENTIFIED AS BEING A CONSTITUENT OF THE YEAST MITORIBOSOMES.....	45
FIGURE 16 – PROTEIN ELEMENTS OF THE MT-SSU COLOURED BY CONSERVATION (135). THE BLUE COLOURED REGIONS ARE ELEMENTS CONSERVED WITH THE BACTERIAL RIBOSOME. THE RED COLOURED REGIONS ARE ELEMENTS CONSERVED WITH THE HUMAN MITOCHONDRIAL RIBOSOME BUT NOT THE BACTERIAL RIBOSOME. YEAST SPECIFIC ELEMENTS ARE COLOURED YELLOW. MT-rRNA IS COLOURED IN GREY. THE FIGURE REPRESENTS THE PYMOL SURFACE REPRESENTATION OF THE MODEL.....	47
FIGURE 17 – MITORIBOSOMAL PROTEIN EXPANSIONS (135). (A) EACH MITORIBOSOMAL PROTEIN OF THE YEAST MT-SSU REPRESENTED BY THEIR TERTIARY FOLDS, COLOURED BY CONSERVATION. THE BLUE COLOURED REGIONS ARE ELEMENTS CONSERVED WITH THE BACTERIAL RIBOSOME. THE RED COLOURED REGIONS ARE ELEMENTS CONSERVED WITH THE HUMAN MITOCHONDRIAL RIBOSOME BUT NOT THE BACTERIAL RIBOSOME. YEAST SPECIFIC ELEMENTS ARE COLOURED YELLOW.....	48
FIGURE 18 – INTERACTIONS BETWEEN PROTEINS OF THE YEAST MT-SSU. (A) YEAST MITORIBOSOMAL PROTEINS WITH BACTERIAL RIBOSOME HOMOLOGUES ARE SHOWN IN BLUE. YEAST MITORIBOSOMAL PROTEINS WITH HUMAN MITORIBOSOMAL HOMOLOGUES ARE SHOWN IN RED. YEAST SPECIFIC PROTEINS ARE SHOWN IN YELLOW. THE FIGURE REPRESENTS THE PYMOL SURFACE REPRESENTATIONS OF THE MODEL. (B) THE PROTEIN-PROTEIN NETWORK OF THE MT-SSU. THE SIZE OF THE NODES REPRESENTS THE RELATIVE MOLECULAR MASSES OF THE PROTEINS, AND THE THICKNESS OF THE EDGE REPRESENTS THE EXTENT OF THE INTERFACE BETWEEN THE INTERACTING PROTEINS. INTERACTIONS ALSO OCCURRING IN BACTERIAL AND HUMAN MITORIBOSOMES ARE SHOWN IN BLUE AND RED, RESPECTIVELY. YEAST MITORIBOSOME SPECIFIC INTERACTIONS ARE SHOWN IN GREY. EDGELESS NODES REPRESENT PROTEINS THAT ONLY CONTACT MT-rRNA. ADAPTED FROM DESAI <i>ET AL</i> (135)...	49
FIGURE 19 – SECONDARY STRUCTURE DIAGRAM OF THE YEAST MT-SSU 15S rRNA. (A) THE 15S MT-rRNA COLOURED BY THE DIFFERENT DOMAINS AND LABELLED ACCORDING TO THE <i>E. COLI</i> COUNTERPARTS WHEN APPROPRIATE. THE YEAST MITORIBOSOME SPECIFIC EXPANSIONS ARE HIGHLIGHTED IN RED. THE NUCLEOTIDES THAT COULD NOT BE MODELLED ARE SHOWN WITH NO BACKGROUND COLOURING. UNMODELLED AREAS SPECIFIC TO THE YEAST MITORIBOSOME ARE DENOTED IN RED LETTERING. (B) SECONDARY STRUCTURE DIAGRAM OF THE	

<i>E. COLI</i> 16S rRNA. THE HELICES THAT ARE NOT PRESENT IN THE YEAST MITORIBOSOME ARE COLOURED IN BLUE. ADAPTED FROM DESAI <i>ET AL</i> (135).....	50
FIGURE 20 - COMPARISON BETWEEN THE YEAST MITORIBOSOME, HUMAN MITORIBOSOME AND <i>E. COLI</i> RIBOSOME. MT-rRNA IS COLOURED IN GREY. HOMOLOGOUS PROTEINS ARE ASSIGNED THE SAME COLOUR. ADAPTED FROM DESAI <i>ET AL</i> (135). THE FIGURES REPRESENT PYMOL SURFACE REPRESENTATIONS OF THE MODELS.	51
FIGURE 21 – INTERSUBUNIT BRIDGES (135). (1) THE INTERSUBUNIT INTERFACE OF THE MT-SSU AND MT-LSU ARE SHOWN. RESIDUES INVOLVED IN INTERSUBUNIT CONTACTS ARE COLOURED AND LABELLED WITH THE RESPECTIVE BRIDGE NAMES. RESIDUES COLOURED BLUE REPRESENT BRIDGES ALSO PRESENT IN THE BACTERIAL RIBOSOME. RESIDUES COLOURED RED REPRESENT BRIDGES PRESENT IN THE YEAST AND HUMAN MITORIBOSOME. RESIDUES COLOURED YELLOW REPRESENT YEAST SPECIFIC BRIDGES. YEAST SPECIFIC RESIDUES THAT ARE FOUND ONLY IN CLASS B ARE COLOURED IN TEAL. B = BODY, H = HEAD AND CP = CENTRAL PROTUBERANCE. THE FIGURE REPRESENTS THE PYMOL SURFACE REPRESENTATION OF THE MODEL.	52
FIGURE 22 – CONSERVED BRIDGES (135). MOLECULAR DETAILS OF THE INTERSUBUNIT BRIDGES OF THE YEAST MITORIBOSOME THAT ARE CONSERVED WITH THE BACTERIAL RIBOSOME OR HUMAN MITORIBOSOME. WHEN THE BRIDGE IS ONLY CONSERVED WITH THE HUMAN MITORIBOSOME THE PREFIX ‘M’ IS GIVEN.	54
FIGURE 23 – YEAST MITORIBOSOME SPECIFIC BRIDGES (135). MOLECULAR DETAILS FOR YEAST MITORIBOSOME SPECIFIC INTERSUBUNIT BRIDGES. BRIDGES MB7, MB8, MB9 AND MB10R ARE ONLY PRESENT IN CLASS B. THE 8° ROTATION OF THE MT-SSU CREATES ADDITIONAL CONTACTS WITH THE CENTRAL PROTUBERANCE OF THE MT-LSU. BLUE = MT-LSU. YELLOW = MT-SSU.....	56
FIGURE 24 – FIGURE SHOWING REPRESENTATIVE DENSITY FOR BRIDGES B5 AND B6. (A) BRIDGE B5. (B) B5 REPRESENTATIVE DENSITY IN BOXED AREA. SURROUNDING DENSITY INCLUDED. (C) BRIDGE B6. (D) B6 REPRESENTATIVE DENSITY SHOWN.	58
FIGURE 25 – POSITION OF MS29 IN THE YEAST AND HUMAN MITORIBOSOME. (A) POSITION OF MS29 SHOWN IN PURPLE IN THE YEAST MITORIBOSOME CLASS A. CLOSE UP OF THE BOXED SECTION. (B) MS29 CONTACTS H82-ES4 OF THE MT-LSU MT-rRNA IN CLASS B (BRIDGE MB7) IN THE YEAST MITORIBOSOME DUE TO AN 8° ROTATION OF THE MT-SSU HEAD. (C) THE EQUIVALENT POSITION IN HUMAN MITORIBOSOMES WHERE CONTACT WITH MS29 IS MEDIATED BY MT-LSU PROTEINS ML46 AND ML48. ADAPTED FROM DESAI <i>ET AL</i> (135). THE FIGURES REPRESENT PYMOL SURFACE REPRESENTATIONS OF THE MODELS.....	59
FIGURE 26 – FEATURES OF THE YEAST MT-SSU. (A) STRUCTURE OF THE MT-SSU WITH US3M, MS42, MS43, AND MS47 COLOURED. THIS FIGURE REPRESENTS THE PYMOL SURFACE REPRESENTATION OF THE MODEL. (B) MS42 AND MS43 FORM A HETERODIMER THAT STRUCTURALLY RESEMBLES THE YEAST MITOCHONDRIAL SUPEROXIDE DISMUTASE DIMER (PDB 3LSU). THE IMAGE IS RELATED TO (A) BY A 90° ROTATION AROUND THE Y-AXIS. (C) MS47, CATALYTIC RESIDUES CONSERVED WITH HUMAN β-HYDROXYISOBUTYRYL-CoA HYDROLASE (PDB 3BPT). THE IMAGE IS RELATED TO (A) BY AN APPROXIMATE 180° ROTATION AROUND THE X-AXIS. (D) US3M HAS MULTIPLE ASPARAGINE RESIDUES DISTRIBUTED ON ITS SURFACE. AMINO ACID RESIDUE ABBREVIATIONS: E, GLU; F, PHE. ADAPTED FROM DESAI <i>ET AL</i> (135).....	61
FIGURE 27 – THE EXTENDED MT-mRNA EXIT CHANNEL. VIEW FROM THE MT-LSU. THE PATH OF THE MT-mRNA CHANNEL CURVING AROUND THE NECK OF THE YEAST MT-SSU IS SHOWN BY THE RED ARROWED LINE.	

ADDITIONAL UNIDENTIFIED DENSITY IS LOCATED ABOVE A CANYON AT THE MT-mRNA EXIT CHANNEL. H = HEAD OF SSU, B = BODY OF SSU. ADAPTED FROM DESAI <i>ET AL</i> (135).	64
FIGURE 28 - (A) AND (B) REPRESENT THE BOXED AREA IN FIGURE 27. (B) THE PROTEINS THAT FORM THE MT-mRNA EXIT CANYON. (C) THE CANYON WALLS COLOURED BY CONSERVATION. YELLOW = YEAST MITOCHONDRIAL SPECIFIC. RED = HUMAN AND YEAST MITOCHONDRIAL SPECIFIC. BLUE = PROTEINS HOMOLOGOUS WITH THE BACTERIAL RIBOSOME. ADAPTED FROM DESAI <i>ET AL</i> (135). THESE FIGURES REPRESENT THE PYMOL SURFACE REPRESENTATION OF THE MODEL.	65
FIGURE 29 – RELION CLASSIFICATION SCHEME FOR UNKNOWN DENSITY AT THE MT-mRNA EXIT CHANNEL (135). MULTIPLE ROUNDS OF FOCUSED CLASSIFICATION WITH SIGNAL SUBTRACTION (FCWSS) WAS EMPLOYED WITH THE AIM OF SEPARATING OUT PARTICLES CONTAINING DENSITY AT THE MT-mRNA EXIT SITE. A PARTIAL MASK WAS USED TO ONLY MASK A SECTION OF THE UNKNOWN DENSITY.	66
FIGURE 30 – SCHEMATIC FOR SCIENTIFIC AIMS. ADAPTED BY DR HANTING YANG FROM THE STRUCTURE OF HUMAN MITOCHONDRIAL RIBOSOME (PDB 3J9M) (48). THE MT-SSU AND MT-LSU OF THE MITORIBOSOME ARE COLOURED IN YELLOW AND LIGHT CYAN RESPECTIVELY. THE RIBOSOMAL EXIT TUNNEL IS DEPICTED IN BLUE. MITORIBOSOMES BIND TO THE INNER MEMBRANE VIA MITORIBOSOMAL PROTEIN ML45 (CYAN). THE NASCENT CHAIN IS TRANSFERRED TO OXA1L (LIGHT RED) FOR TRANSPORT OF THE NASCENT PEPTIDE ACROSS FOR INSERTION INTO THE MITOCHONDRIAL INNER MEMBRANE.	77
FIGURE 31 – ADAPTED FROM HIGH-RESOLUTION STRUCTURES OF MITOCHONDRIAL RIBOSOMES AND THEIR FUNCTIONAL IMPLICATION. BIERI P, GREBER BJ, BAN N. CURR OPIN STRUCT BIOL. 2018 APR;49:44-53 (195). PTC = PEPTIDYL TRANSFERASE CENTRE.	79
FIGURE 32 – PURIFICATION 1. 15-30% SUCROSE GRADIENT FRACTIONS. PEAK 1 WAS COMPOSED OF FRACTIONS 16-20 AND PEAK 2 COMPOSED OF FRACTIONS 21-26 AS CIRCLED.	84
FIGURE 33 – PURIFICATION 1 - WESTERN BLOTTING RESULTS. POOLED FRACTIONS 16-20 (PEAK 1) AND 21-26 (PEAK 2) WERE RUN ON A 10-50% SUCROSE GRADIENT AND 11 EQUAL FRACTIONS COLLECTED. RED BANDS REPRESENT ANTI-MS27 SIGNAL. GREEN BANDS REPRESENT ANTI-OXA1L SIGNAL. PREDICTED BAND SIZE OF BOTH ANTIBODIES WAS 48kDa.	87
FIGURE 34 – PURIFICATION 1. (A) REPRESENTATIVE MICROGRAPH. (B) REPRESENTATIVE 2D CLASSES.	87
FIGURE 35 - PURIFICATION 1. RELION PROCESSING CLASSIFICATION SCHEME.	88
FIGURE 36 – PURIFICATION 1 – 5.3 Å UNSHARPENED MAP. 1ST 3D REFINEMENT. LIGHT BLUE = MT-LSU, YELLOW = MT-SSU, GREEN = P-SITE MT-tRNA AND DARK BLUE = A-SITE MT-tRNA	89
FIGURE 37 – PURIFICATION 1 - 5.3 Å UNSHARPENED MAPS. (A) CLASS 4 FROM 1 ST 3D CLASSIFICATION. (B) CLASS 5 FROM 1 ST 3D CLASSIFICATION. LIGHT BLUE = MT-LSU, YELLOW = MT-SSU, GREEN = P-SITE MT-tRNA, DARK BLUE = A-SITE MT-tRNA	90
FIGURE 38 - PURIFICATION 2. 15-30% SUCROSE GRADIENT FRACTIONS. PEAK 1 COMPOSED OF FRACTIONS 17-20 AND PEAK 2 COMPOSED OF FRACTIONS 23-27 HIGHLIGHTED.	92
FIGURE 39 – PURIFICATION 2 WESTERN BLOTTING RESULTS. FRACTIONS 17-30 FROM THE 15-30% SUCROSE GRADIENT WERE RUN ON A PROTEIN GEL AND SUBJECTED TO WESTERN BLOTTING. RED BANDS REPRESENT ANTI-MS27 SIGNAL. GREEN BANDS REPRESENT ANTI-OXA1L SIGNAL. PREDICTED BAND SIZE OF BOTH ANTIBODIES IS 48kDa.	92

FIGURE 40 – PURIFICATION 2. RELION CLASSIFICATION SCHEME.	94
FIGURE 41 – PURIFICATION 2 - 5.3 Å UNSHARPENED MAP. 1 ST 3D REFINE. MT-LSU LATE ASSEMBLY INTERMEDIATE. LIGHT BLUE = MT-LSU. DARK BLUE = MALSU1-LOR8F8-MT-ACP MODULE.	95
FIGURE 42 – PURIFICATION 2. 1 ST 3D REFINEMENT - 5.3 Å UNSHARPENED MAP. MT-LSU LATE ASSEMBLY INTERMEDIATE WITH MT-SSU MODEL DOCKED TO DEMONSTRATE CLASH WITH NEW MODULE. LIGHT BLUE = MT- LSU. DARK BLUE = MALSU1-LOR8F8-MT-ACP MODULE. YELLOW MESH = MT-SSU.....	96
FIGURE 43 – TAKEN FROM (214). (A) SHOWS THE MALSU1-LOR8F-MT-ACP MODULE IN CONTEXT OF THE MT-LSU IN LIGHT BLUE. (B) SHOWS MALSU1 ADJACENT TO UL14M AND BL19M.....	97
FIGURE 44 – PURIFICATION 2. MT-LSU LATE ASSEMBLY INTERMEDIATE 1 ST 3D REFINEMENT. THE ASSEMBLY PROTEINS ARE SHOWN IN COLOUR (PDB 500M) (214). (A) FRONT VIEW. (B) SIDE VIEW.	99
FIGURE 45 – PURIFICATION 3 WESTERN BLOTTING RESULTS. THE SAMPLE WAS RUN ON A 10-50% SUCROSE GRADIENT AND 11 EQUAL FRACTIONS COLLECTED. RED BANDS REPRESENT ANTI-MS27 SIGNAL. GREEN BANDS REPRESENT ANTI-OXA1L SIGNAL. PREDICTED BAND SIZE OF BOTH ANTIBODIES IS 48kDA.	101
FIGURE 46 – PURIFICATION 3. RELION CLASSIFICATION SCHEME.	101
FIGURE 47 – PURIFICATION 3. (A) REPRESENTATIVE MICROGRAPH AND (B) REPRESENTATIVE 2D CLASSES.	102
FIGURE 48 – PURIFICATION 3. 1 ST 3D CLASSIFICATION CLASS 3 - 6.6 Å UNSHARPENED MAP. (A) FRONT VIEW. (B) SIDE VIEW. LIGHT BLUE = MT-LSU. YELLOW = MT-SSU. GREEN = P-SITE MT-TRNA. GREY = UNKNOWN DENSITY IN FACTOR SITE.....	104
FIGURE 49 – PURIFICATION 3. (A) FCWSS CLASS 1 FRONT VIEW. 7.6 Å UNSHARPENED MAP. (B) FCWSS CLASS 1 SIDE VIEW. (C) FCWSS CLASS 5 FRONT VIEW. 10.1 Å UNSHARPENED MAP. (D) FCWSS CLASS5 SIDE VIEW. LIGHT BLUE = MT-LSU. YELLOW = MT-SSU. GREY = UNKNOWN DENSITY IN FACTOR SITE.....	105
FIGURE 50 - PURIFICATION 4. 15-30% SUCROSE GRADIENT FRACTIONS. PEAK 1 IS COMPOSED OF FRACTIONS 15-27 AND PEAK 2 IS COMPOSED OF FRACTIONS 20-24 AS HIGHLIGHTED.	106
FIGURE 51 - PURIFICATION 4 - WESTERN BLOTTING RESULTS. FRACTIONS 13-24 FROM THE 15-30% SUCROSE GRADIENT WERE RUN ON A PROTEIN GEL AND SUBJECTED TO WESTERN BLOTTING. RED BANDS REPRESENT ANTI- MS27 SIGNAL. (A) GREEN BANDS REPRESENT ANTI-OXA1L SIGNAL. PREDICTED BAND SIZE OF BOTH ANTIBODIES IS 48kDA. (B) ALTERNATIVE REPRESENTATION OF THE ANTI-OXA1L SIGNAL.....	107
FIGURE 52 - PURIFICATION 4. (A) REPRESENTATIVE MICROGRAPH. (B) REPRESENTATIVE 2D CLASSES.....	107
FIGURE 53 – PURIFICATION 4- RELION PROCESSING SCHEME.....	108
FIGURE 54 – (A) CLASS 6 FROM FCWSS OF THE RIBOSOMAL FACTOR SITE MASK FROM CLASS 3 OF THE 1 ST 3D CLASSIFICATION. 5.3 Å UNSHARPENED MAP. (B) CLASS 3 FROM FCWSS RIBOSOMAL FACTOR SITE MASK FROM CLASS 7 OF THE 1 ST 3D CLASSIFICATION. 4.3 Å UNSHARPENED MAP. LIGHT BLUE = MT-LSU. YELLOW = MT-SSU. GREY = UNKNOWN DENSITY IN FACTOR SITE.	110
FIGURE 55 – (A) CLASS 5 (6.5 Å UNSHARPENED MAP) AND (B) CLASS 7 (7.2 Å UNSHARPENED MAP) FROM FCWSS OF THE EXIT SITE FROM CLASS 3 OF THE INITIAL 3D REFINEMENT. LIGHT BLUE = MT-LSU. YELLOW = MT-SSU. GREEN = P-SITE MT-TRNA. GREY = UNKNOWN DENSITY IN FACTOR SITE. DARK GREY = UNKNOWN DENSITY IN P-SITE.....	111
FIGURE 56 – LOCAL RESOLUTION MAP OF CLASS 3 FROM FCWSS RIBOSOMAL FACTOR SITE MASK FROM CLASS 7 OF THE 1 ST 3D CLASSIFICATION.....	111

FIGURE 57 – TAKEN FROM PEARCE SF, RORBACH J, VAN HAUTE L, <i>ET AL.</i> MATURATION OF SELECTED HUMAN MITOCHONDRIAL TRNAs REQUIRES DEADENYLATION. <i>ELIFE</i> . 2017;6:e27596 (218).....	112
FIGURE 58 - PURIFICATION 5. 15-30% SUCROSE GRADIENT FRACTIONS. PEAKS 10-14 WERE POOLED TOGETHER.	114
FIGURE 59 – (A) PURIFICATION 5 WESTERN BLOTTING RESULT. FRACTIONS 1-11 FROM THE 10-15% SUCROSE GRADIENT. (B) REPEAT OF PURIFICATION 5. 15-30% SUCROSE GRADIENT FRACTIONS. (C) FRACTIONS FROM (B) SUBJECTED TO WESTERN BLOTTING. RED BANDS REPRESENT ANTI-MS27 SIGNAL. GREEN BANDS REPRESENT ANTI-OXA1L SIGNAL. PREDICTED BAND SIZE OF BOTH ANTIBODIES IS 48kDA.	114
FIGURE 60 - PURIFICATION 5, 1 ST COLLECTION. (A) REPRESENTATIVE MICROGRAPH AND (B) 2D CLASSES.	115
FIGURE 61 – PURIFICATION 5, 1 ST COLLECTION, RELION PROCESSING SCHEME.	116
FIGURE 62 - MT-LSU. RE-EXTRACTED (PIXEL SIZE 1.25 Å) FCWSS CLASS 1 ON THE EXIT SITE OF CLASS 1 FROM THE 1 ST 3D REFINEMENT COLOURED BY LOCAL RESOLUTION.	117
FIGURE 63 – MT-LSU. CLASS 1 FROM FOCUSSED CLASSIFICATION WITH SIGNAL SUBTRACTION ON THE EXIT SITE OF CLASS 1 FROM THE 1 ST 3D REFINEMENT. 5.1 Å POST PROCESSED MAP.	118
FIGURE 64 – PURIFICATION 5, 2 ND COLLECTION RELION CLASSIFICATION SCHEME.	119
FIGURE 65 – PURIFICATION 5, 2 ND COLLECTION (A) MT-LSU CLASS 8 (6.8 Å UNSHARPENED MAP) FROM INITIAL 3D CLASSIFICATION SHOWING A HINT OF DENSITY FOR OXA1L. (B) DIFFERENT VIEW OF SAME CLASS TO SHOW DENSITY FOR THE MALSU1-L0R8F8-MT-ACP MODULE. PDB 5AJ4 DOCKED IN TO INCLUDE POSITION OF P-SITE MT-tRNA (50). (C) ENLARGED IMAGE FROM (B) SHOWING THE POSITION OF THE P-SITE MT-tRNA IN THE MONOSOME AND ADJACENT DENSITY TO THE LEFT IN THIS STRUCTURE FOR A MT-tRNA.	121
FIGURE 66 – PURIFICATION 5, 2 ND COLLECTION. FCWSS AT THE EXIT SITE OF CLASS 8 (5.4 Å UNSHARPENED MAP). (A) MT-LSU. PDB 500M (214). (B) ENLARGED REPRESENTATION OF FIGURE (A). TWO MT-tRNAs HAVE BEEN MODELLED INTO THE DENSITY, PURPLE AND GREEN.	122
FIGURE 67 – PURIFICATION 5, 2 ND COLLECTION. CLASSES FROM FCWSS AT THE EXIT SITE OF CLASS 8. (A) CLASS 2 (18.2 Å UNSHARPENED MAP) (B) CLASS 4 (12.8 Å UNSHARPENED MAP) (C) CLASS 8 (5.4 Å UNSHARPENED MAP).	124
FIGURE 68 - PURIFICATION 6. FIGURE SHOWS THE 15-30% SUCROSE GRADIENT FRACTIONS. FRACTIONS 8-11 (PEAK 1) WERE POOLED AND BUFFER EXCHANGED IN 0.05% β-DDM BUFFER. FRACTIONS 13-15 (PEAK 2) WERE POOLED AND DIVIDED INTO TWO AND BUFFER EXCHANGED WITH EITHER 0.05% β-DDM/0.005% CHS OR 0.05% DIGITONIN. POOLED FRACTIONS FROM THE THREE CONCENTRATED SAMPLES WERE SUBJECTED TO WESTERN BLOTTING. RED BANDS REPRESENT ANTI-MS27 SIGNAL. GREEN BANDS REPRESENT ANTI-OXA1L SIGNAL. PREDICTED BAND SIZE OF BOTH ANTIBODIES IS 48kDA.	125
FIGURE 69 – PURIFICATION 6 – DIGITONIN BUFFER (A) A REPRESENTATIVE MICROGRAPH. (B) REPRESENTATIVE 2D CLASSES.	126
FIGURE 70 – PURIFICATION 6 – DIGITONIN BUFFER. RELION PROCESSING SCHEME.	128
FIGURE 71 – PURIFICATION 6 – DIGITONIN BUFFER. CLASS 2 OF INITIAL 3D CLASSIFICATION. CYTOSOLIC RIBOSOME COLOURED IN TAUPE. SEC61 IS COLOURED IN MAUVE. THE TOP IMAGE FEATURES A ZOOMED IN REPRESENTATION SHOWING THE LSU MEMBRANE FACING SURFACE WITH CLEAR DENSITY FOR SEC61.	129

FIGURE 72 – PURIFICATION 6 – DIGITONIN BUFFER. CLASS 1 FROM FCWSS OF CLASS 4. 9.8 Å UNSHARPENED MAP (A) FRONT VIEW SHOWING THE PSITE MT-tRNA IN GREEN AND THE UNKNOWN FACTOR IN GREY. (B) SIDE VIEW SHOWING DENSITY FOR OXA1L. LIGHT BLUE = MT-LSU. YELLOW = MT-SSU.	129
FIGURE 73 – PURIFICATION 6 – β-DDM BUFFER. (A) A REPRESENTATIVE MICROGRAPH. (B) REPRESENTATIVE 2D CLASSES.	131
FIGURE 74 - PURIFICATION 6 – β-DDM BUFFER. RELION CLASSIFICATION SCHEME.....	132
FIGURE 75 – PURIFICATION 6 – β-DDM BUFFER. FCWSS CLASS 4 OF CLASS 3 OF THE INITIAL 3D CLASSIFICATION. 15.7 Å UNSHARPENED MAP (A) FRONT VIEW SHOWING THE P-SITE tRNA IN GREEN AND THE UNKNOWN FACTOR IN GREY. (B) SIDE VIEW SHOWING OXA1L DENSITY. LIGHT BLUE = MT-LSU. YELLOW = MT-SSU.....	133
FIGURE 76 – PURIFICATION 6 – β-DDM BUFFER. FCWSS CLASS 2 OF CLASS 6 OF THE INITIAL 3D CLASSIFICATION. 18.4 Å UNSHARPENED MAP (A) FRONT VIEW SHOWING THE P-SITE tRNA IN GREEN AND THE UNKNOWN FACTOR IN GREY. (B) SIDE VIEW SHOWING OXA1L DENSITY. LIGHT BLUE = MT-LSU. YELLOW = MT-SSU.....	134
FIGURE 77 – ADAPTED IMAGE COURTESY OF DR KRISHNA CHATTERJEE (IMS-MRL) (239). GRAPHICAL REPRESENTATION OF SELENOCYSTEINE INCORPORATION INTO THE GROWING POLYPEPTIDE BY THE DELIVERY OF SEC-tRNA ^[SER] _{SEC} TO THE A-SITE UGA ON THE mRNA BY EEFSEC (eEFSEC) WITH THE HELP OF SECISBP2 (SBP2) THROUGH ITS BINDING TO THE SECIS ELEMENT.	146
FIGURE 78 – TAKEN FROM SCHMIDT RL, SIMONOVIĆ M. SYNTHESIS AND DECODING OF SELENOCYSTEINE AND HUMAN HEALTH. <i>CROAT Med J.</i> 2012;53(6):535–550 (222). CLINICAL ABNORMALITIES ACCORDING TO THE PERTURBATIONS ALONG THE PATHWAY.....	147
FIGURE 79 – mRNA DESIGNS. 3X FLAG-TAG FOLLOWED BY A β-VHP (VILLIN HEAD PIECE) AND THE PHGPX GENE TO INCLUDE THE SECIS ELEMENT. (A) HUMAN PHGPX. (B) HUMAN PHGPX MODIFIED TO HAVE A VALINE CODON BEFORE THE SELENOCYSTEINE INCORPORATING TGA. (C) RAT PHGPX.	152
FIGURE 80 - COURTESY OF DR ERIK SCHOENMAKERS. LUCIFERASE ASSAY. (A) UGA OR UAA AT POSITION 258 IN LUCIFERASE GENE FOLLOWED BY A SECIS ELEMENT SEQUENCE. (B) RESULTS OF LUCIFERASE ASSAY AFTER ADDING INCREASING AMOUNTS OF SECISBP2 OR EEFSEC. TAA (UAA) REPRESENTS THE CONTROL.	153
THE COMPETENCE OF THE COMPONENTS TO FORM A STALLED COMPLEX WAS EVALUATED WITH AN <i>IN VITRO</i> TRANSLATION EXPERIMENT WAS SET UP USING S ³⁵ METHIONINE WITH AND WITHOUT ERF1(AAQ). THE RESULTS OF THE CRUDE <i>IN VITRO</i> TRANSLATION EXPERIMENT SHOWED THAT WITHOUT ERF1(AAQ) THE POLYPEPTIDE WAS LARGELY DETECTED AT ~17 kDa (AS PREDICTED BY THE MOLECULAR WEIGHT OF THE FULL RELEASED NASCENT CHAIN) AND THAT WITH ADDITION OF ERF1(AAQ) THE RADIOACTIVE BAND WAS LARGELY DETECTED AT ~37 kDa SUGGESTING THE TRAPPED NASCENT CHAIN tRNA COMPLEX (FIGURE 82 (A)). THIS SHOWED, THAT WITHOUT ERF1(AAQ), THERE WAS LIMITED READ THROUGH AND THE TRANSCRIPT TERMINATED AT THE UGA STOP CODON. HOWEVER, TERMINATION AT THIS STOP CODON WOULD ALSO RESULT IN RIBOSOME DISSOCIATION. IN THE PRESENCE OF ERF1(AAQ) THERE WAS THE SAME TERMINATION AT THE STOP CODON BUT IN ADDITION THE POLYPEPTIDE WAS LIKELY STILL ATTACHED TO THE RIBOSOME AS EVIDENCED BY THE POLYPEPTIDE CHAIN BEING DETECTED IN COMPLEX WITH THE tRNA AT ~37 kDa. TO FURTHER TEST THIS, THE CRUDE SAMPLES WERE RUN ON A 10-50% SUCROSE GRADIENT AND 11 EQUAL FRACTIONS TAKEN. ALIQUOTS OF THESE FRACTIONS WERE RUN ON A PROTEIN GEL AND THE S ³⁵ METHIONINE RADIOACTIVITY DETECTED (FIGURE 81 B-D). THE RESULTS SHOWED THAT WITHOUT ERF1(AAQ), FOR ALL THE mRNA	

TRANSCRIPTS, THE MAJORITY OF THE POLYPEPTIDE WAS IN THE FREE FRACTIONS IN LANES 1-4. THERE WAS ALSO SOME EVIDENCE OF STALLING ON THE RIBOSOME TOO AS EVIDENCED BY THE HIGHER ~37 kDa BAND BEING PRESENT IN THE RIBOSOME FRACTIONS, APPROXIMATELY LANES 6-9. WITH eRF1(AAQ), FOR ALL THE TRANSCRIPTS, THERE WAS AN INCREASE IN THE POLYPEPTIDE CHAIN IN FRACTIONS 6-9 REPRESENTING RIBOSOMES WITH tRNA BOUND POLYPEPTIDES.	154
FIGURE 82 - <i>IN VITRO</i> TRANSLATION EXPERIMENTS USING S ³⁵ METHIONINE. (A) USING THE 3 PHGPX TRANSCRIPTS HUMAN, HUMAN (VAL) AND RAT, WITH OR WITHOUT eRF1(AAQ). (B-D) ALIQUOTS FROM THE EXPERIMENTS WERE RUN ON A 10-50% SUCROSE GRADIENTS WITH AND WITHOUT eRF1(AAQ) AND 11 EQUAL ALIQUOTS TAKEN FOR ANALYSIS.....	155
FIGURE 83 – DATA COLLECTION. (A) REPRESENTATIVE MICROGRAPH. (B) REPRESENTATIVE 2D's.....	156
FIGURE 84 – RELION CLASSIFICATION SCHEME OF SELENOCYSTEINE DATA COLLECTION	158
FIGURE 85 – POST 3 ROUNDS OF FOCUSED CLASSIFICATION WITH SIGNAL SUBTRACTION ON RIBOSOMAL FACTOR SITE. (A) CLASS 2 (B) CLASS 3.	159
FIGURE 86 – PCR DNA AND <i>IN VITRO</i> TRANSCRIPTION mRNA OF HUMAN, HUMAN(VAL) AND RAT PHGPX.....	167
FIGURE 87 – PROTEIN GELS COURTESY OF DR YULIYA GORDIYENKO. (A) EEfSEC (B) FLAG-EEfSEC (C) SECISBP2	168

Table of Tables

TABLE 1 – DATA COLLECTION PARAMETERS AND MODEL STATISTICS. ADAPTED FROM DESAI <i>ET AL</i> (135).	37
TABLE 2 – YEAST SMALL SUBUNIT MITORIBOSOMAL PROTEINS. THE SHADING OF THE BACKGROUND IS COLOURED BY PROTEIN CONSERVATION WITH THE BACTERIAL RIBOSOME (BLUE) AND HUMAN MITOCHONDRIAL RIBOSOME (RED), AND YEAST MITORIBOSOME SPECIFIC PROTEINS (YELLOW) (135). MRP – MITOCHONDRIAL RIBOSOMAL PROTEIN. MRR - MATURE RESIDUE RANGE. MW – MOLECULAR WEIGHT.....	42
TABLE 3 – ANALYSIS OF PURIFIED YEAST MITORIBOSOMES BY TANDEM MASS SPECTROMETRY (135).	44
TABLE 4 - INTERSUBUNIT-BRIDGE COMPOSITIONS THAT ARE CONSERVED WITH THE BACTERIAL RIBOSOME (135).....	55
TABLE 5 - INTERSUBUNIT-BRIDGE COMPOSITIONS COLOURED BY CONSERVATION WITH THE HUMAN MITORIBOSOME HAVE A RED BACKGROUND (135). BRIDGES ONLY FOUND IN CLASS B HAVE A TEAL BACKGROUND. BRIDGES ONLY SEEN IN THE YEAST HAVE A YELLOW BACKGROUND.	57
TABLE 6 – TANDEM MASS SPECTROMETRY ANALYSIS. PURIFIED HUMAN MITORIBOSOMES FROM PREPARATION 1, PEAK 2 WERE ANALYSED.....	86
TABLE 7 – CRYO-EM DATA COLLECTION ON THE FEI TITAN KRIOS, FALCON III DETECTOR.....	141
TABLE 8 – THE PRIMERS USED FOR OBTAINING THE LINEAR VECTOR AND INSERTS FOR CLONING AND THE ROUND THE HORN MUTAGENESIS.	163
TABLE 9 – POLYMERASE CHAIN REACTION COMPONENTS AND CONCENTRATIONS.....	164
TABLE 10 – POLYMERASE CHAIN REACTION CYCLING PARAMETERS.....	164
TABLE 11 – SELENOPROTEIN HUMAN AND RAT PHGPX GENEBLOCKS.	166
TABLE 12 – PRIMERS USED FOR REVERSE TRANSCRIPTION OF SEC-tRNA ^[SER] _{SEC} EXPERIMENT.	172

1 Introduction

1.1 Background

1.1.1 Translation and the Mitochondrion

1.1.1.1 The mitochondrion

The mitochondrion is an important organelle in eukaryotic cells and is involved in a variety of cellular processes, including synthesising adenosine triphosphate (ATP), regulating cellular metabolism, apoptosis and aging. Mitochondria have double membranes consisting of an inner and outer membrane, separated by the inter-membrane space. In addition, the inner membrane forms cristae folds, which protrude into the interior matrix. Within the inner membrane reside five enzyme complexes of oxidative phosphorylation. These enzyme complexes, through the process of oxidative phosphorylation (OXPHOS), are responsible for generating the energy unit ATP from the breakdown of carbohydrates and fatty acids. For this reason mitochondria are often called the 'powerhouses of cells'. Mitochondria are a unique feature of eukaryotic cells. They are thought to have arisen from an α -proteobacterium endosymbiont (1). This notion is supported by the fact that mitochondria show reminiscent characteristics of α -proteobacteria including harbouring their own genome and translational system.

1.1.1.2 The mitochondrial genome

Mitochondria contain both mitochondrial DNA (mt-DNA) and the machinery necessary to express this genetic code, including mitochondrial ribosomes (mitoribosomes). However, much of the genetic material within mitochondria has been lost or transferred to the host during evolution, leaving a vestigial genome. Adaptations to the cellular environment have led to inactivation of redundant genes and transfer of essential genes to the nucleus (2). In addition, the mitochondrial proteome has expanded, as a result of the mitochondrion being a beneficiary of imported non-bacterial nuclear encoded and translated proteins. Nuclear gene

transfer to mt-DNA is also known to occur, but the net result remains, of mitochondrial genomes being a fraction of the size compared to their ancestral free-living α -proteobacterium (2). The extent of this reduction in genome size is organism-dependent, with very little correlation between mt-DNA length and the number of genes retained. The coding capability of mt-DNA is an average of 40-50 genes across eukaryotes. At one extreme, jakobid flagellates have as many as 100 genes (3). These genes are largely involved in the fundamental processes of oxidative phosphorylation, translation, transcription, ribonucleic acid (RNA) maturation and protein import. While at the other extreme, *Plasmodium falciparum* have only 5 genes (3). The likely advantages of nuclear centralisation of genetic material, include sex recombination and protection against oxidative stress in the mitochondrial microenvironment. However, in most aerobic eukaryotes, mitochondria retain a set of genes. In these cases, the transfer of genes to the nucleus is not random. Most aerobic eukaryotes have not lost all their genes involved in oxidative phosphorylation (4). The membrane proteins cytochrome *b* (Cytb) and cytochrome oxidase subunit 1 (Cox1) remain present, as do, mitoribosomal RNA (mt-rRNA) genes. These features can be explained by the fact that translocation of large molecules such as mt-rRNA into the mitochondria could be problematic. In the case of Cytb and Cox1, these highly hydrophobic proteins were also thought to be difficult to transport across mitochondrial membranes. However, recent experiments suggest that they are retained in the mitochondria to prevent aberrant targeting to the endoplasmic reticulum if nuclear encoded (5). In addition, protein synthesis within the mitochondria is thought to allow greater control over gene expression in response to the redox state of mitochondria (6). Eukaryotes have therefore, largely retained a separate translation system within mitochondria despite the considerable expense to the cell, at times for the production of only a few proteins. An exception is the aerobic eukaryotic parasite *Amoebophrya ceratii* (*A. cerattii*). A recent study has revealed that no mt-DNA was found in *A. cerattii* (7). Although mitochondrial genomes have been previously found to be lost in anaerobes, this is the first time an aerobic species has been found to completely lose its genome. The explanation, however, is similar for both cases. In anaerobes, the genomes have been lost in conjunction with loss of respiratory complexes that need oxygen to function. The loss of the mitochondrial genome in *A.*

cerattii is in line with loss of certain respiratory complexes and energy adaptation (7).

In the vast majority of species, due to the reduced genome size, almost all the ribosomal proteins and the translation factors vital for this mitochondrial translation system have to be imported in from the cytoplasm. This feature is in addition to the components of the machinery necessary for mt-DNA maintenance, replication, transcription, mt-mRNA processing and maturation. The yeast *Saccharomyces cerevisiae* (*S. cerevisiae*) and mammalian mt-DNA encode for only 8 and 13 proteins respectively, but there is a nearly five-fold difference in their genome sizes (85.8kb and 16.5kb, respectively) (8,9). A representation of the genomes taken from a review by Ott *et al* is shown in Figure 1 (10). An estimated 250-300 nuclear encoded proteins are postulated to be necessary to maintain human mitochondrial gene expression (11). However, both *S. cerevisiae* and mammals synthesise all mt-rRNA and mitochondrial transfer RNA (mt-tRNA) *in situ* (12,13).

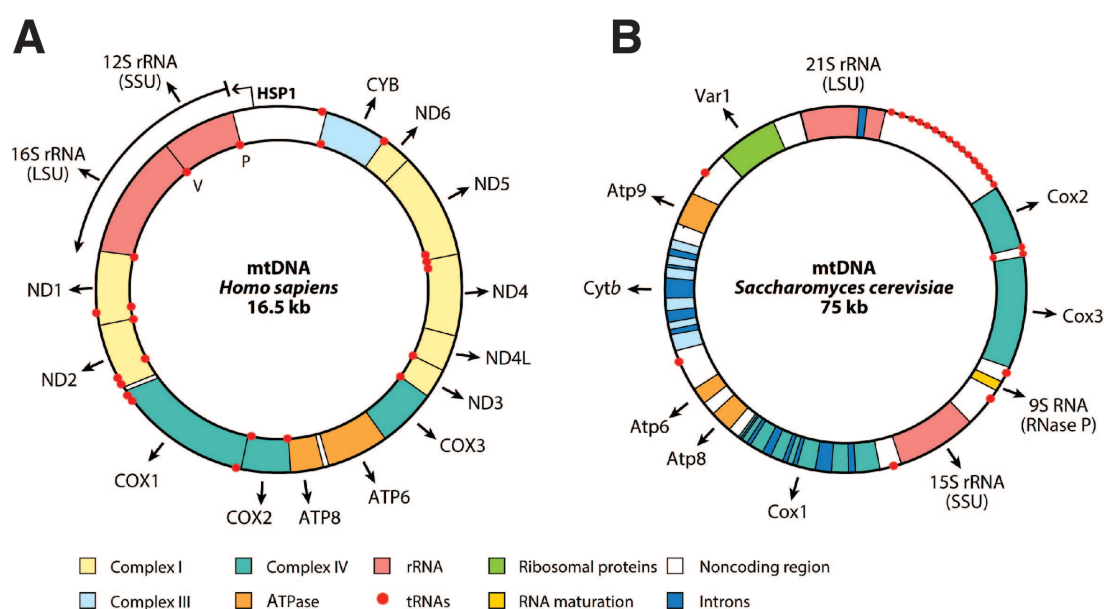


Figure 1 – Taken from Ott M, Amunts A, Brown A. Organization and Regulation of Mitochondrial Protein Synthesis. Annu Rev Biochem. 2016 Jun 2;85:77-101 (10). (A) Human mitochondrial genome. (B) *Saccharomyces cerevisiae* mitochondrial genome. The genes are colour coded according to function as denoted by the legend.

1.1.1.3 Protein translation and ribosome structure

The ribosome is a macromolecule composed of ribosomal RNA (rRNA) and proteins. First discovered in 1955 by George E. Palade as cytoplasmic particles attached to the endoplasmic reticulum (ER) responsible for the production of proteins, for which he shared the Nobel Prize in 1974 (14). The basic ribosome unit consists of a large subunit (LSU) and a small subunit (SSU). In the 70S bacterial ribosome the subunits are designated 50S and 30S for the LSU and SSU, respectively. Ribosomes contain over 50 proteins, in complex with 3 rRNA molecules. It was first postulated that the rRNA might serve as a scaffold for ribosomal proteins, carrying out the protein making functions of the ribosome. However, it was later discovered that the 3'- end of the bacterial 16S rRNA of the SSU was important in forming complementary rRNA base pairing with the 5'- end of messenger RNA (mRNA), close to initiation codons (15). mRNA contains the protein sequence to be decoded by the ribosome for polypeptide production. Shine and Dalgarno later identified this to be a 16S rRNA pyrimidine-rich tract at the 3'- end (16,17). In *E. coli*, the ACCUCC nucleotide sequence at the 3'- end base pairs with complementary mRNA to form the initial mRNA:30S complex (16). The sequence on the mRNA is now known as the Shine-Dalgarno sequence. Thus, the SSU is able to bind the mRNA encoding, via triplet nucleotides (codons), the sequence of amino acids of a polypeptide.

Subsequent sequencing of rRNA allowed secondary structure modelling and subsequent chemical footprinting and crosslinking methods to study specific rRNA interactions with proteins and transfer RNA (tRNA) (18-20). Three binding sites on each of the ribosomal subunits were found to exist (21). The ribosomal A-site (aminoacyl site) is responsible for binding the incoming aminoacylated tRNA. The ribosomal P-site (peptidyl site) harbours the tRNA that holds the nascent polypeptide. The ribosomal E-site (exit site) accepts the deacylated tRNA before it exits the ribosome. Details of the steps in the translation pathway have been mapped out in bacteria, with the help of pre-steady-state kinetic experiments and single-molecule fluorescence resonance energy transfer experiments (22-25). The SSU was found to bind the anticodon stem of the tRNA that recognises the corresponding codon of the mRNA. In this way the SSU is involved in decoding and monitoring of translational fidelity. The LSU binds the acceptor arms of tRNA and

catalyses the formation of a peptide bond, between the incoming amino acid of the A-site tRNA and the polypeptide chain of the P-site tRNA at the peptidyl transferase centre (PTC). Early protease and phenol extraction experiments, to remove the thermophilic eubacterium *Thermus aquaticus* 50S ribosomal proteins, found retention of peptidyl transferase activity pointing to the catalytic role of rRNA (26). Biochemical studies have thus paved the way towards an in-depth understanding of ribosomal translation. However, it would be structural biology that would provide a more detailed picture of the components of the ribosome and with this further mechanistic understanding of translation.

Early work towards understanding the structure of the complete ribosome *in situ* used room temperature electron microscopy (EM). This was followed by early cryo-electron microscopy (cryo-EM), which allowed low resolution visualisation of ribosomes in complex with tRNA and translational factors, although it would be x-ray crystallography that first provided atomic level detail. In 2000, Ban *et al* published, at 2.4 Å, the first high resolution structure of the LSU from the archaean *Haloarcula marismortui* (27). This was followed by a 3.1 Å reconstruction of the bacterium *Deinococcus radiodurans* LSU by Harms *et al* (28). In 2000, the Ramakrishnan and Yonath groups, respectively, reported the structure of the SSU from the bacterium *Thermus thermophilus* to 3.0 Å and 3.3 Å (29,30). These initial structures were significant breakthroughs and were followed by further crystal structures of actively translating ribosomes, that have greatly improved our understanding of the precise mechanisms of protein synthesis (31).

Protein translation by ribosomes is a highly regulated process, directed by the sequence of mRNA codons. Translation occurs in distinct phases; initiation, elongation, termination and ribosome recycling (31). These phases are regulated by a variety of translation factors. This feature is universally conserved across all ribosomal species. Initiation is the stage where mRNA is recognized and loaded onto the SSU of the ribosome with the start codon primed in the ribosomal P-site. During elongation, amino acid residues are added to the carboxyl-terminus (C-terminus) of the growing polypeptide chain. The amino-terminus (N-terminus) at the other end is the start of the polypeptide sequence. The growing polypeptide traverses through

the polypeptide tunnel of the LSU and emerges from the polypeptide exit site at the end of the tunnel. During elongation, coordinated efforts of both ribosomal subunits move the tRNAs and mRNA in their triplet codon units through the ribosome into the different tRNA binding sites, in a process called translocation. Termination of translation occurs when a stop codon reaches the ribosomal A-site and is recognised by release factors (RF). RFs catalyse the release of polypeptides and the ribosome is recycled by ribosome recycling factor (RRF).

1.1.1.4 The mitochondrial ribosome

It has been known since the late 1950s that radiolabelled amino acids can be incorporated into nascent polypeptides, in isolated rat liver mitochondria (32). By the 1960s, ribosome-like particles were visualised by negative-stain electron microscopy within the mitochondrial matrix (33). By 1967, it became possible to purify mitoribosomes from yeast and human cells (34-38). These advances led to more comprehensive negative-stain EM studies of mitoribosomes (39-41). However, progress in high resolution visualisation of mitoribosomes was hampered by the limitations of room temperature EM technology, and the difficulty in crystallising mitoribosomes for X-ray crystallography. With the emergence of cryo-EM, several low resolution structures of the mitoribosome from a variety of species were solved (42-45). Improved purification methods and technological advances in cryo-EM have together provided high resolution cryo-EM structures of the mammalian mitoribosome, and large subunit of the yeast *S. cerevisiae* (46-51). From these structures there is evidence of species-specific specialisation amongst mitoribosomes. Species-specific pressures on the mitoribosome have resulted in mitoribosomes from different species exhibiting individuality, whilst retaining largely conserved functional sites comparing with other ribosomes. The differences may be a reflection of genomic translational requirements and also manifest in unique translational factors, mt-tRNAs and regulation. Progress in our understanding of these peculiarities is still in its infancy and is obstructed by the lack of an *in vitro* reconstitution system for mitoribosomal translation and robust methods for genetic manipulation.

shorter, such that the mammalian ribosome is only 1/3rd rRNA (48,50). The bacterial ribosome by comparison consists of 2/3rds rRNA. Although the exit tunnel in the human mitoribosome follows a similar path to the bacterial tunnel, it has been remodelled to include a lateral polypeptide accessible opening (47,49). These, and other novel structural elements with proposed unique functions, will require further study via biochemical, genetic and structural experimentation.

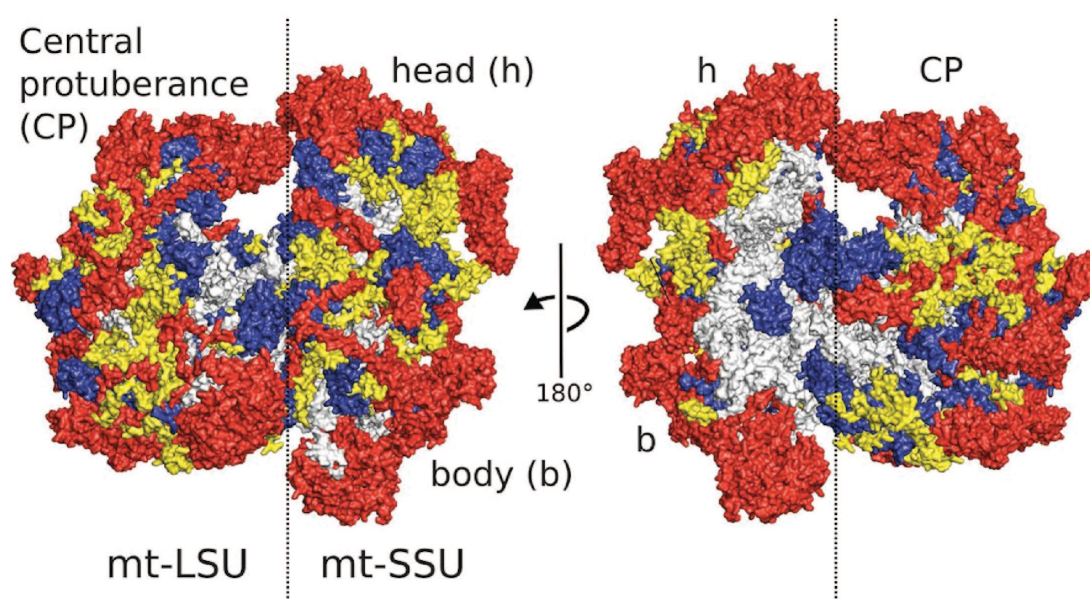


Figure 3 - Taken from Amunts A, Brown A, Toots J, Scheres SHW, Ramakrishnan V. Ribosome. The structure of the human mitochondrial ribosome. From *Science*. 2015;348(6230):95–98/ Reprinted with permission from AAAS (48). Overview of the human mitoribosome. The areas with bacterial conservation are coloured in blue. The extensions of homologous bacterial proteins are coloured in yellow and the mitochondria-specific proteins are coloured in red. mt-rRNA is coloured in grey.

1.1.1.5 Expression, maturation and characteristics of mitochondrial RNA

In order to understand differences in translation in the mitochondrion, it is important to understand the differences in gene expression. The circular human mt-DNA genome encodes only 37 genes, divided into 13 proteins, 22 mt-tRNAs and 2 mt-rRNAs (12S and 16S) (13). The 13 proteins include; apocytochrome b (cob), 3 cytochrome c oxidase subunits (cox1,2,3), 2 ATPase subunits (atp6,8), and 7 NADH dehydrogenase subunits (nad1,2,3,4,4L,5,6). Individual mt-mRNAs are a product of

polycistronic RNAs, generated from promoters from both heavy and light strands of the circular mt-DNA (52). The heavy and light strands reflect the mass of the DNA strands due to differing proportions of heavier nucleotides. Transcription is catalysed by the mitochondrial RNA polymerase mt-RNAP (53). Additional factors required are; mitochondrial transcription factor A (TFAM), mitochondrial transcription factor B2 (TFB2M) and mitochondrial transcription elongation factor (TEFM) (53). Following RNA transcription, processing at the 5' by mitochondrial endonuclease RNase P and at the 3' by ELAC2, liberates the RNA into individual components of mt-tRNAs and polycistronic RNA units (54,55). Where mt-mRNA and mt-rRNA are not flanked by mt-tRNA, the factors FASTK, FASTKD4, FASTKD5 and GRSF1 have been implicated in RNA processing (11). Mt-mRNA, mt-rRNA and mt-tRNA all undergo post-transcriptional modifications including 3' polyadenylation (poly(A)tail) by mitochondrial poly(A) polymerase (mt-PAP) (56). Post transcriptional modifications of mt-tRNA include nucleotide modifications and the addition of a 3' CCA for aminoacylation of cognate amino acids (57).

Although the majority of mt-mRNAs lack 5' untranslated regions (UTRs), some human mt-mRNAs do contain very short 5' UTRs (52). This is in contrast to human cytosolic mRNA that can harbour long 5' UTRs with an average length of 210 nucleotides (58). This long 5' UTR, upstream of the initiation codon, is instrumental for translation regulation of cytosolic mRNAs. The lack or shortened 5' UTRs in human mt-mRNAs presents questions on the mechanism of initiation of translation in these circumstances. In human mitochondria there are 8 transcripts without 5' UTRs, with 3 other transcripts that have between 1 and 3 nucleotides before the initiation start codon (52). The remaining two transcripts, ND4 and ATPase6, have sizeable 5' UTRs of 296 and 161 nucleotides, respectively, which also serve as the 3' UTRs of the upstream sequences of these bicistronic transcripts (52). Thus, the ND4 and ATPase6 start codons are embedded in the middle of mt-mRNA. There are 4 transcripts that contain 3' UTRs, with 3 of these being within the anti-sense of other coding sequences (52). Thus, in addition to the 3' UTRs with overlapping open reading frames, the signal for mt-mRNA processing would be contained in sense or anti-sense coding sequences (52).

Yeast mt-DNA are largely linear molecules, but also contain circular DNA in smaller amounts (59). The *S. cerevisiae* mitochondrial genome encodes 35 genes which represent 8 proteins, 24 mt-tRNAs, 2 mt-rRNAs (21S and 15S) and the 9S RNA subunit of RNase P (12). The 8 proteins include the ribosomal SSU protein (*VAR1*), cytochrome oxidase subunits I, II and III (*COX1*, *COX2*, *COX3*), apocytochrome b (*COB*) and three ATP synthase subunits (*ATP6*, *APT8*, *ATP9*). Transcription is less complex in yeast mitochondria as it requires only two components; a mitochondrial polymerase (Rpo41) and the transcription factor mt-TFB (Mtf1) (60). However, RNA processing is a much more complicated affair. Individual transcripts must first be liberated, with subsequent non-coding introns within transcripts requiring removal by a process called splicing (61). As in human mitochondria, yeast mt-tRNAs are liberated from their position at the end of transcripts by the action of RNaseP and RNase Z (62). Pet127 in addition is important for 5' end trimming of transcripts (63). Following these processing steps, mt-tRNA, mt-rRNA and mt-mRNA to include monocistronic and one discistronic transcript encoding ATP8 and ATP6, are released from the original continuous RNA stretches (64). In contrast to humans, yeast mt-mRNAs contain long 5' and 3' UTRs more akin to canonical cytosolic translation (65). However *S. cerevisiae* mt-mRNA is not subject to 3'UTR polyadenylation, which remains a feature of some human mt-mRNA transcripts (52). The long 5' UTRs present in yeast mt-mRNA also permit mt-mRNA specific nuclear encoded translational activators to promote translation of their cognate mt-mRNAs, as discussed below (65). In general, the paucity of UTRs in the human mitochondria requires that the messages for transcriptional regulators are encrypted within the body of open reading frames (52). This leaves little room for genomic mutations known to be of a higher rate in mt-DNA.

1.1.1.6 Translation initiation

Translation initiation is a highly coordinated process and in bacteria is largely regulated by three SSU binding factors, initiation factor 1 (IF1), initiation factor 2 (IF2) and initiation factor 3 (IF3) (66). IF1 binds the 30S A-site and anchors IF2 and IF3 (66). The 5' Shine-Dalgarno sequence of the mRNA and the 3' anti-Shine-Dalgarno sequence of the 16S mRNA of the 30S mediate mRNA placement and start

codon positioning. The GTPase IF2 recruits formylmethionyl-tRNA (fMet-tRNA^{fMet}) to the start codon and IF3 helps to select tRNA^{fMet} and the start codon (66). Initiation is completed when initiation factors leave and the subunits join to form a 70S ribosome with a P-site fMet-tRNA^{fMet} primed for elongation.

The situation in mitochondria has differences from the bacteria. IF1 is absent in mitochondria, whereas the GTPase mitochondrial IF2 (mt-IF2) is universally present. IF3, previously thought not to exist in *S. cerevisiae*, has now been identified as Aim23p (67). However deletion of Aim23 in *S. cerevisiae* does not affect mitochondrial translation indiscriminately, but instead causes an imbalance in protein production (68). The first step in mitochondrial initiation is recruitment of the mt-mRNA to mt-IF3-bound mt-SSU, thereby positioning the mt-mRNA initiation codon in the mt-SSU P-site and inhibiting premature mt-LSU association. Mt-IF3 has a central region homologous to bacterial IF3, flanked by N and C terminal extensions which have roles in initiator mt-tRNA binding to the 28S mt-SSU and anti-association with the mt-LSU, respectively (69,70). The GTPase mt-IF2 then brings the initiator tRNA, fMet-tRNA^{Met} to this complex (71,72). Unlike in bacteria, there is only one methionyl mt-tRNA in the human mitochondrion and its affinity for mt-IF2 and mt-EF-Tu (the elongator GTPase) is dependent on its formylation status. mt-IF2 is important in the recognition of the formylated fMet-tRNA^{Met} initiator tRNA (71). In yeast, the situation is more akin to the bacteria where there are two methionine mt-tRNA species, the initiator tRNA_i^{fMet} and elongator tRNA^{Met} (64). Formylation of Met-tRNA_i^{fMet} in *S. cerevisiae* increases its affinity for mt-IF2 (64). In addition to binding initiator mt-tRNA, mt-IF2 also performs functions that are usually associated with IF1, owing to the presence of a highly variable insertion (71,72). It has now been shown by cryo-EM in the mammalian system that this insertion functions near the decoding centre, at the A-site, preventing premature elongator mt-tRNA binding and mRNA slippage to ensuring correct reading frame selection (71). This latter point is especially important for leaderless mRNAs (71). Furthermore, the C-terminal domain of the large subunit protein bL12m has been found to interact with mt-IF2 and may be important in promoting subunit joining (71). In addition, human mt-mRNA binding is also facilitated by the RNA-binding ability of mt-SSU protein mS39,

which contains multiple pentatricopeptide repeats that aid the threading of mRNA through the entrance channel (48,50).

AUG, which codes for methionine, is the most common initiation codon in human mitochondria, but AUA and AUU can also be used (52). The mechanism by which the recruited mt-mRNA start codon is positioned in the initiating mitoribosome remains largely elusive and is further confounded by the varying characteristics of mt-mRNA. This opens up the possibility of transcript specific factors guiding not only initiation, but location of translation. Unlike their bacterial ancestors, mitochondrial mRNA does not initiate using a Shine-Dalgarno sequence. This mechanism is lost not just in transcripts with little or no 5' UTR, but even in transcripts containing longer 5' UTRs. In *S. cerevisiae*, it has been shown that mutations of the COX2 start codon that abolish initiation also prevent initiation at a nearby AUG, suggesting that positioning of the AUG and its environment is indeed specific (73).

Unique mt-mRNA motifs or sequences that might aid this process remain largely elusive in the mammalian system. An exception, however, is TACO1, which has been identified as a translational activator of the COX1 transcript (74). Although yeast mitochondrial translational activators are by far the best studied, since human mt-mRNAs on the whole do not contain long 5' UTRs, alternative mechanisms must therefore exist (52). Specific, but not universal, features of translational activators include their ability to interact with; 5' UTRs, proteins of the small and large subunit, the inner membrane surface and, either directly or indirectly, with the nascent polypeptide chain (65). In this way they are able to direct expression of their target mt-mRNA to their site of usage at the inner membrane. The amount translated can thus be coordinated with nuclear encoded products through a negative feedback mechanism, ensuring stoichiometric protein production of macromolecular complexes (65). Translational activators promote translation, but once the polypeptide is synthesised, the same activator binds the polypeptide product and therefore is not able to promote another round of translation elsewhere until it is released, when the translated polypeptide is translocated to the inner membrane (64). Examples of these translational activators with the ability to bind the 5' UTR include; Pet309 and Mss51, which direct the translation of COX1, and Pet53, Pet122

and Pet494, which direct COX3 translation (75-77). Thus, translation initiation in the mitochondrion has unique features and specialised processes, but also follows some general rules of bacterial initiation. Unanswered questions pertain to the order and precise mechanisms of initiation factor binding and release.

1.1.1.7 Translation elongation

Translation elongation on the ribosome is the process by which mRNA codons are decoded by aminoacylated tRNAs to add amino acid residues to the growing polypeptide chain. In humans and *S. cerevisiae*, there are 22 and 24 mitochondrially-encoded amino acid specific tRNAs, respectively. These mt-tRNAs possess diverse structures and non-canonical truncated species are also present in metazoans (78). Adaptations are apparent in both mt-tRNA and mitoribosomal subunit interfaces. Simplified decoding mechanisms, termed wobbling and superwobbling allow for less than the 32 tRNA species normally required by Crick's wobble hypothesis (79). In Crick's wobble hypothesis, tRNAs with a modified uridine (U) in the wobble position of their anticodon compensate for the reduced number of tRNAs by pairing with any of the four bases at the third position of the codon (80). Unmodified uridines in the wobble position base pairing is called 'superwobbling' (80).

Elongation on mitoribosomes is similar to the bacteria. A ternary complex, comprising the mitochondrial elongation factor (mt-EF-Tu), GTP and an aminoacylated mt-tRNA, enters the ribosomal A-site, with the mt-tRNA initially in the A/T conformation (81). Following anticodon:codon recognition between the mt-tRNA and mt-mRNA respectively, GTP is hydrolysed to release GDP:mt-EF-Tu. The mt-tRNA then fully accommodates into the A-site to permit peptide bond formation between the incoming amino acid and the last amino acid in the nascent chain at the peptidyl transferase centre of the mt-LSU. Through an interaction with another GTPase elongation factor (mt-EF-G1), the A-site mt-tRNA, which now bears the nascent chain, translocates the mt-mRNA into the ribosomal P-site, while the deacylated P-site mt-tRNA moves into the ribosomal E-site. Elongation continues in this pattern until a mt-mRNA stop codon is positioned in the A-site. In bacteria, the same elongation factor EF-G mediates translocation during peptide elongation and

during recycling when acting with ribosome recycling factor(31). In mitochondria, however, these two functions are fulfilled by mt-EF-G1 and mt-EF-G2 (81). The yeast and mammalian mitoribosome structures of the mt-LSU confirm that the peptidyl transferase centre, entirely formed of mt-rRNA, is highly conserved and therefore indicates that the mechanism for peptide bond synthesis is identical to cytosolic ribosomes in all kingdoms (46,47,50).

1.1.1.8 Translation termination and recycling

Translation termination is mediated by two classes of release factors in the bacteria, Class I factors; release factor 1 (RF1) and 2 (RF2), harbour specific motifs (SPF or PXT tripeptide motif) for stop codon recognition (31). The Class II factor, release factor 3 (RF3) is a GTPase that binds and dissociates class I release factors from the ribosome. Binding of RF1/2 to the A-site stop codon results in ester bond hydrolysis and peptide chain release from the P-site tRNA. This leads to binding of a GTP bound RF3, which promotes a conformational change that favours dissociation of RF1/2 and subsequent dissociation of RF3 upon GTP hydrolysis (31).

While the canonical codons UAA and UAG serve as stop codons in the human and yeast mitochondria, UGA instead codes for a tryptophan (9,52). In human mitochondria, the stop codon is recognised by a single mitochondrial release factor 1a (mt-RF1a), which positions a conserved GGQ motif in the PTC to hydrolyse the ester bond between the P-site mt-tRNA and the nascent chain (82). The counterpart in *S. cerevisiae* is mt-RF1 (83). This is in contrast to the bacteria where two classes of release factors, RF1 and RF2, are required to recognise the three stop codons (31). Since RF2 recognises UAA and UGA and RF1 recognises UAA and UAG, a lack of an RF2 homologue in mitochondria is understandable as it is unnecessary owing to UGA not encoding a stop codon. In the early 1980s, it was thought that in human mitochondrial translation, AGA and AGG also represented stop codons in the ORFs of proteins; CO1 and ND6 (13). However, it has now been shown that the AGA/AGG was in fact instrumental in creating a -1 frameshift in conjunction with downstream 3' UTR sequences that form a secondary structure (84). This secondary structure has the effect of preventing any downstream translation, thus repositioning the

mitoribosome, which subsequently encounters the canonical UAA and UAG stop codons (84). Of note, eukaryotic cytosolic translation termination also only employs 1 release factor, eRF1 for all the 3 termination codons (85).

Following termination, a deacylated mt-tRNA in the P/E state, and mt-mRNA, remains associated with the ribosome in the post termination complex (PoTC). Two ribosomal recycling factors mt-RRF1 and mt-EF-G2 then bind and promote the dissociation of the subunits and other bound components to be recycled for further use (86). However, unlike the bacterial system, mitochondrial ribosome recycling does not require GTP hydrolysis (87,88).

1.1.1.9 Mitochondrial translation in human health and disease

Aberrant translation within the mitochondria is known to be associated with perturbations of human health. This is not surprising as the products of translation are all components of the electron transport chain, involved in oxidative phosphorylation. Mitochondrial electron transport chain deficiencies are a major cause of metabolic and neurological disorders. However, there is considerable heterogeneity in both the clinical picture and the pathogenesis of the various disorders (89,90). This heterogeneity is in part a reflection of different mutations, but also the burden of different populations of mt-DNA (wild type and mutant) that are present in individual cells, a phenomenon called heteroplasmy (89). During mitosis, lineages can drift towards one type of mt-DNA, thereby individual cells potentially containing increasing amounts of mutant mt-DNA and a consequent bias to expressing a disease phenotype.

Thirteen of the oxidative phosphorylation proteins are mitochondrially encoded and translated. Therefore, any defect affecting the mitochondria's ability to produce a functional product can be involved in the pathogenesis of electron transport chain diseases. Mutations involving mt-DNA protein encoding regions that cause diseases include isolated myopathy and Leber's hereditary optic neuropathy (89). Examples of mitochondrial diseases related to defective translation of the thirteen mt-DNA encoded proteins include MELAS syndrome, characterised by mitochondrial

encephalomyopathy with lactic acidosis and stroke-like episodes, resultant of an A3243G mutation in the tRNA^{Leu(UUR)} (MTTL1) gene (91). Aminoglycoside-induced deafness is associated with mitoribosomal RNA mutations such as the A1555G mutation in the 12S rRNA gene, although the mutation itself appears to be insufficient to produce a clinical phenotype without additional factors, as demonstrated by the variability in clinical penetrance (92). The first discovered nuclear gene mutation, PUS1 encodes a mt-tRNA modification enzyme, pseudouridine synthase, responsible for converting uridine into pseudouridine within mt-tRNA (93). Mutations in this gene appear to affect stability of the mt-tRNA secondary and tertiary structure and the associated clinical syndrome observed is mitochondrial myopathy, lactic acidosis and sideroblastic anaemia (MLASA) (93). Additional mutations affecting mitochondrial translation are found in mitoribosomal proteins, aminoacyl-tRNA synthases, elongation factors, translational activators, translation terminators and proteins regulating mt-mRNA stability (94). Additionally, any defects in the pathway that mediates transport and import of nuclear-encoded mitochondrial proteins associated with translation can be pathogenic. These can include; mutations in either the mitochondrial localisation signal itself, chaperones that assist in the pathway, the import machinery or deficiencies in the assembly and processing of the clients.

On the non-pathogenic side, there has been considerable interest in the mitochondria as a possible chemotherapeutic target. This is based on the identification of tumour vulnerabilities not necessarily related to particular somatic mutations. As the apparent genetic heterogeneity of tumours increases with the presence of clonal subtypes with differing genetic landscapes emerging within single tumours, targeting global tumour vulnerabilities in association with more specific gene targets continues to be an attractive strategy. The mitochondrion, an integral part of cellular metabolism, is beginning to be considered as one of these global targets (95). Alterations to metabolism have long been considered a tumourigenic hallmark (96). The originally described Warburg effect is the idea that tumours use increased aerobic glycolysis and are shifted away from ATP generation through oxidative phosphorylation, even under normal oxygen concentrations (96). ATP production by glycolysis, although more rapid than oxidative phosphorylation, is

comparatively inefficient in generation of ATP per unit of glucose consumed. However, it is apparent that this model is too simplistic and that tumours must be metabolically adapted to provide the crucial requirements of not only increased energy production but generation of sufficient macromolecules and maintenance of redox balance (96). Additionally, it is known that many key oncogenic signalling pathways result in an adaptation of tumour cell metabolism, to allow increased growth and survival. Anti-cancer drugs acting on mitochondria have recently been classified according to their targets within the mitochondria, which include drugs targeting hexokinase on the outer mitochondrial membrane, components of the electron transport chain and mt-DNA (95). Of interest to us is the possibility of chemotherapeutics affecting the translational function of mitochondria. Tigecycline has recently been reported as an effective inhibitor of mitochondrial translation in acute myeloid leukaemia (AML), and selectively killed leukaemic stem and progenitor cells preferentially to normal cells (97). Furthermore, small interfering RNA-mediated knockdown of mt-EF-Tu in leukaemic cells produced a similar effect. The AML cells were found to have increased numbers of mitochondria, coupled with increased mt-DNA copies and an increased oxygen consumption rate compared to normal cells (97). Tigecycline is an FDA-approved antimicrobial and is currently being investigated in clinical trials as a treatment for AML, with the phase 1 dose-escalation study being completed (98).

1.1.1.10 Polypeptide exit tunnel and mitoribosome localisation

Mitochondrial ribosomes, as discussed, translate the hydrophobic components of oxidative phosphorylation and have been found to harbour adaptations to this. The first adaptations involve 1) the characterisation of the polypeptide exit tunnel and 2) the localisation of the tunnel. The mammalian mitochondrial 39S exit tunnel largely follows a similar path to that seen in the bacterial 50S, although aspects of the tunnel may be unique (47,49). In the structure of the human mitoribosome there was density for an endogenous polypeptide interacting with the hydrophobic lining of the tunnel (47). It is hypothesised that helices of mitochondrial OXPHOS proteins may start forming within the exit tunnel, the hydrophobicity of the tunnel slowing the rate of elongation allowing time for domain folding and mimicking the

hydrophobic environment of the mitochondrial membrane. The exit is also remodelled compared to the bacteria with a more proteinaceous character and consists of a conserved ring of polypeptides; uL23m (Mrpl22), uL29m (Mrpl47), uL22m (Mrpl22), uL24m (Mrpl24) and the mitochondrial specific protein mL45 (47,49). Interestingly, in the initiating mitoribosome, the polypeptide tunnel has been found to be occupied by an N-terminal portion of mL45, which later becomes exposed in the elongating mitoribosome, further supporting the role of mL45 in targeting the mitoribosome to the inner mitochondrial membrane (71). In the yeast 54S mt-LSU, the canonical polypeptide tunnel of the bacterial 50S is blocked by a yeast specific extension of uL23m (Mrpl23) (46). A new path is seen and the boundaries of this new tunnel are extensions of uL22m (Mrpl22), uL23m (Mrpl23), and uL24m (Mrpl24), and by rRNA expansion segment 3 (3-ES). The new exit site is roughly 35 Å away from the original bacterial tunnel exit site and has two additional mitochondrial specific proteins, mL44 and mL45, with exciting implications for the unique attachment of the inner membrane bound mitoribosomes (46).

Mitoribosomes have been shown by cryo-electron tomography to be anchored to the inner mitochondrial membrane (Figure 4) (99,100). The concept of co-translational translocation of proteins across membranes is widespread in biology. In the bacterial and eukaryotic system, co-translational protein translocation is a conserved process involving the SecY and Sec61 complexes, respectively, along with their regulatory partners (101). The Sec61 complex, a conserved protein conducting channel, is found on the membrane of the endoplasmic reticulum. It facilitates transport of proteins emerging from membrane bound ribosomes across the membrane or laterally into the lipid bilayer. The structure of the mammalian ribosome-Sec61 complex with its nascent peptide chain and hybrid tRNA was solved to a resolution of 3.4 Å using single particle cryo-EM (102).

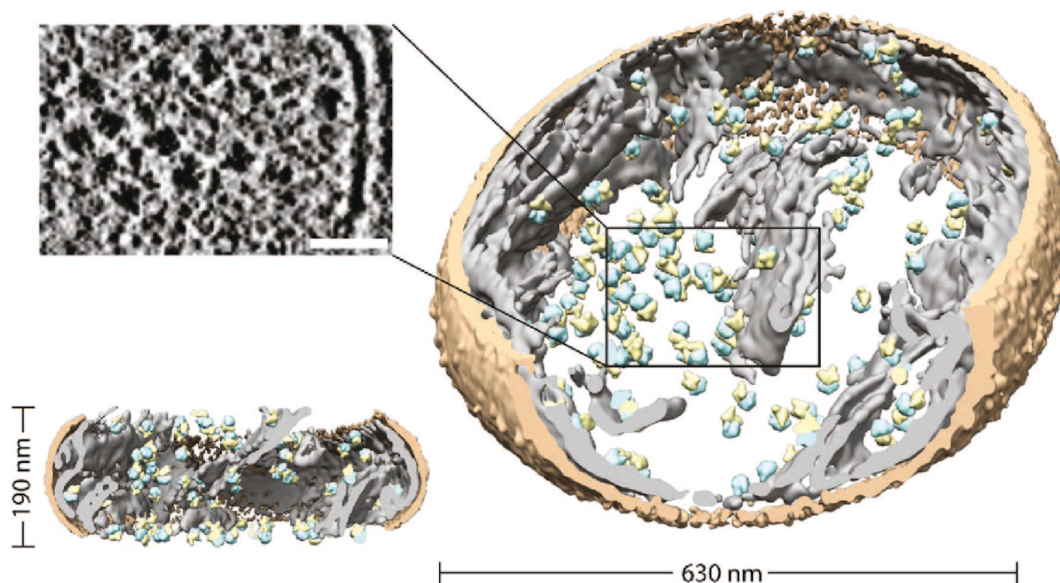


Figure 4 – Taken from Englmeier, Robert et al. “Structure of the Human Mitochondrial Ribosome Studied In Situ by Cryoelectron Tomography.” *Structure* 25 10 (2017): 1574-1581.e2 (100). Top left is a tomographic slice showing a cluster of mitoribosome. Scale bar, 50nM. The coloured images show tomographic reconstructions of mitoribosome distribution. Orange = Outer mitochondrial membrane. Grey = Inner mitochondrial membrane. Blue = Mt-LSU. Yellow = Mt-SSU.

In the mitochondria the cytochrome oxidase assembly (OXA) translocase, OXA1L and OXA1, in the human and yeast, respectively, is a translocase bound to the inner mitochondrial membrane. Mitoribosomes of both human and yeast origin are bound to the inner mitochondrial membrane via a few postulated proteins, of which OXA has been found to be consistently identified (99,103-105). OXA is thought to mediate the co-translational insertion of mitochondrially encoded membrane proteins through an attachment to the mitoribosome. In addition, it also plays a role in the insertion of nuclear encoded proteins that have been imported into the mitochondrial matrix. This process of import of proteins through the translocase of the outer membrane (TOM) and translocase of the inner membrane (TIM) machinery into the mitochondrial matrix and export into the inner mitochondrial membrane through OXA has been termed ‘conservative sorting’ (106). OXA is a member of the highly conserved OXA/YidC/Alb3 protein family in eukaryotes, prokaryotes and plant chloroplasts, respectively, involved in membrane protein insertion (107). In general, OXA contains five hydrophobic transmembrane segments with intervening hydrophobic loops on either sides of the inner

mitochondrial membrane (108). The N-terminus sits within the inter-membrane space and the long C-terminal tail in the mitochondrial matrix. It has also recently been found to be part of an even bigger 'OXA1 superfamily', consisting of the additional endoplasmic reticulum proteins Get1, EMC3 and TMC01 that also facilitate biogenesis of membrane proteins (109). Thus OXA's role in both co-translational insertion of mitoribosome produced proteins and conservative sorting of nuclear encoded proteins from the mitochondrial matrix to the inner membrane establishes its role in global inner mitochondrial membrane protein assembly. The use of OXA by two translational systems also highlights the mitochondrion as a recipient of two distinct translational systems where coordinated cooperation between them is vital for proper functioning of mitochondria.

1.1.1.11 Cooperation between mitochondrial and cytosolic ribosomes

As previously discussed, mt-DNA often encodes for a limited number of proteins. In fact, most mitochondrial proteins across species are nuclear encoded and imported into the mitochondrion. Previous studies have revealed the following characteristics about how mitochondrial proteins are translated: (i) the majority of mitochondrial proteins are nuclear-encoded and are translated by cytosolic ribosomes (110), (ii) proteins destined for the mitochondria often possess a recognisable localisation motif, (iii) mitochondrial targeting typically occurs post-translationally, but can also occur during translation, (iv) most proteins use the classical protein import route that requires a cleavable mitochondrial localisation "pre-sequence" (110), (v) proximity-specific ribosome profiling studies in yeast have shown that most inner membrane proteins are targeted to the mitochondria co-translationally (111), and finally, (vi) recent low-resolution cryo-electron tomographic studies have shown that cytosolic ribosomes actively synthesising mitochondrial proteins associate with the mitochondrial membrane surface (112). Interestingly, ribosomes bearing nascent chains have been shown to bind in the proximity of the TOM complex (112). The TOM complex recognises the nascent chain pre-sequence to facilitate translocation. In the canonical pathway the preprotein is transferred to the TIM23 complex and is ultimately translocated to its correct mitochondrial location (110). A TOM-TIM23

supercomplex tethered by protein–protein interactions has been revealed by cryo-ET, however further mechanistic details remain to be elucidated (113).

The need for tight regulation of mitochondrial import becomes even more critical when concerning the production of proteins from two different translation systems that need to come together and be assembled, for example as an oxidative phosphorylation component. Monitoring of global mitochondrial and nuclear gene expression in *S. cerevisiae* shows that mitochondrial translation is controlled by cytosolic translation in a unidirectional manner allowing orchestration of assembly of the macromolecular complexes of oxidative phosphorylation (114). There is also evidence of translational adaptation to global changes in cellular state in both cytosolic and mitochondrial compartments, allowing the focus of translation to be where it is needed at times of stress (114). Overall, this synchronisation between cytosolic and mitochondrial translation is likely to increase the efficiency of oxidative phosphorylation, reducing the production of unnecessary and potentially harmful subunits if stoichiometry is not retained. The exact role of translational activators in this synchronised response remains to be elucidated. Indeed, it has been shown that human mitoribosomes translating COX1 mRNA have been found to be engaged with cytochrome c oxidase factors in the inner membrane in a stalled ribosome nascent chain complex. This occurs when assembly defects of cytochrome c oxidase are present, such as when the nuclear-encoded COX4 a component of the full unit is not available (115).

1.1.2 Single particle cryo-electron microscopy

The development of techniques in structural biology have been essential in aiding our understanding of the architecture of macromolecular complexes and have complemented the quest in understanding biological and molecular function. Historically, the most widely used technique for obtaining atomic models was X-ray crystallography. However, this technique has limitations, in the challenge of crystallisation of samples, requiring high concentrations and homogeneity. Although cryo-EM was a technique pioneered in the 1970s (*116*), it wasn't until recently that resolution limiting bottlenecks have been overcome, and high resolution biological structures could be obtained.

Cryo-EM is a technique that involves embedding purified biological macromolecules in a thin layer of vitreous ice in random orientations. Using a high voltage electron beam, images representing 2D multiple projections of the 3D molecule are acquired and later computationally combined to obtain a 3D model of the structure to be determined. In 1995, Henderson hypothesised that with macromolecules of 100 kDa and above, we could in theory reach atomic resolution using electron microscopy with $\sim 10,000$ averaged together particles (*117*). Whilst atomic resolution has long been possible with non-biological samples, the radiation induced damage to biological samples has limited resolution (*118*). The electron beam deteriorates the biological specimen during image acquisition. This electron exposure damage occurs at a lower level than that needed for high resolution structural determination (*118*). Minimisation of radiation damage has been obtained through maintenance of low temperatures and techniques to minimise the exposure of the biological specimen to electrons (*116*). Early experiments into the preparation of frozen hydrated samples, followed by the development of rapid vitrification of biological samples in liquid ethane or propane in the 1980s, identified techniques to preserve high resolution features (*119*). However, low contrast of biological specimens in vitreous ice has required that the images be collected with a defocus, thus hampering the resolution potential in this technique.

The recent advances in cryo-EM were made possible by the advent of technology such as the direct electron detectors, high throughput and automated data collection

and software programmes accurately producing 3D reconstructions. This has led to a sharp increase in the number of high resolution structures solved by cryo-EM since 2012 which has not been limited to macromolecular structures but have also included small protein structures as well as membrane proteins. Direct electron detectors, detecting electrons without having to first convert them into photons, as in the charge coupled device (CCD) cameras, have the advantage of fast readouts and limited noise, resulting in higher contrast images. Automated data acquisition packages such as EPU (from FEI) work in line with direct electron detectors, allowing automated collection of images as multi frame movies in 'movie mode' from pre-selected areas. The collection of cryo-EM data in 'movie mode' where several images are recorded successively, allows for tracking of the beam induced motion that can be corrected for to retain higher resolution information *(120)*. Maximum likelihood based image analysis programmes such as RELION (REgularized Likelihood Optimization), have overcome challenges in image processing, including dealing with the inherent background noise of the raw images and the need to identify the relative orientations of the selected particles *(121-123)*. Features include; automated particle selection, pre-processing of the raw images to correct for the microscope contrast transfer function and 2D class averaging to group aligned and similar particles increasing the signal-to-noise ratio for input into 3D refinement where particle orientations alignment allows reconstruction of an initial model. With near atomic resolution now within reach, classical model building and refinement programs have been modified to adapt to the special needs of cryo-EM maps and models. Model building molecular-graphics software packages such as Coot (Crystallographic Object-Oriented Toolkit) have been modified for manual model building in cryo-EM as well as the refinement programme REFMAC used for fitting of models to EM maps *(124,125)*.

Thus, the combined advances in cryo-electron microscopy over the last 40 years have revolutionised the world of structural biology. Examples of the first wave of the single particle cryo-EM 'resolution revolution' structures include the 2013 membrane structure of TRPV1 channels (EMD-5778), the 2014 structure of the Brome mosaic virus (EMD-6000) and the 2014 structure of the large subunit of the yeast mitochondrial ribosome (EMD-2566) *(46,126-128)*. Single particle cryo-EM is a

field that continues to grow with exciting developments in grid preparation methods, data collection, for example phase-plate technology allowing in-focus data acquisition, and data processing such as on the fly motion correction for improve time efficiency (129). Thus, the full potential of cryo-EM as a tool for solving biological structures remains to be realised.

1.1.3 The state of the mitoribosomal structural field

At the onset of the current study, high resolutions structures of mitoribosomes had just begun to emerge. The Ramakrishnan and Ban lab had both elucidated the complete structure of the human and bovine mitoribosome to 3.5 Å and 3.8 Å, respectively (48,50). In addition, the group of V. Ramakrishnan had also solved the structure of the large subunit of the yeast mitoribosome but were unable to obtain a map of high enough resolution to solve the structure of the small subunit and hence the complete yeast mitochondrial ribosome (46). To date these were the only high resolution near-atomic mitoribosome structures but previous work had existed of lower resolution cryo-EM structures (42-45,130). I was interested in exploring the mitoribosome field in 2 particular aspects; 1) the basic structure of mitochondrial ribosomes and 2) the co-translational insertion of mitochondrially translated proteins.

Comparisons between the large subunit structures in yeast and mammals have highlighted stark differences. For example the different locations of the polypeptide tunnel (46). I was therefore interested in exploring further differences between the small subunits and the complete yeast and mammalian mitoribosomes and bacterial ribosome. There was biochemical and low resolution structural evidence that the yeast SSU would have unique features in protein composition and overall structure (45,131,132). In addition, because of differences in regulation of translation between these different species the expectation was that this would be reflected in the overall structure of the yeast mitoribosome (65). Thus the first aim of my PhD was to solve the structure of the complete yeast mitochondrial ribosome.

The mechanism of mitoribosome co-translational insertion of inner membrane proteins is one of the next interesting questions to be answered in mitochondrial translation. Because of the high proportion of mitoribosomes attached to the inner mitochondrial membrane this is thought to be a key aspect of mitochondrial translation (99,100). The OXA translocon mediates this co-translational insertion of mitochondrial proteins and as yet there is no high resolution structure of this protein, in isolation or in conjunction with the mitoribosome. Thus, the second aim of my PhD was to study the co-translational insertion of mitochondrially produced

proteins by trapping an actively translating complex of the mitoribosome with its translocon OXA. In particular, I focussed on the human system for its pathogenic relevance. As a clinician I am interested in the way perturbations to basic mitochondrial translation cause human disease. Thus, studying the normal mechanism of active mitochondrial translation will lay the groundwork for investigating pathological questions and potentially reveal novel drug targets of this.

2 Yeast Mitochondrial Ribosome

2.1 Scientific aims

The aim of this project was to solve the structure of the whole yeast mitoribosome. The large subunit of the yeast mitoribosome had previously been solved to near-atomic resolution by cryo-EM, but as yet there was no structure of the mt-SSU and hence no structure of the full yeast mitoribosome (46). The yeast *S. cerevisiae* has long been used as a tool and model system to understand genetic and biochemical activities of mitochondria, largely aided by our ability to manipulate its mt-DNA (133). Thus, it has also been a model to study mitochondrial disease (134). Mitochondrial ribosomes have been shown to differ in both structure and constituents when compared not only with their bacterial and cytosolic ribosomal counterparts, but also between different eukaryotic species. The mitoribosome within the yeast mitochondrion is an important and integral macromolecule, responsible for translating 7 essential proteins of oxidative phosphorylation and 1 protein integral to the mt-SSU. The fundamental protein and RNA components of the yeast mitoribosome have been well characterised biochemically, but the relative positions of proteins were not well elucidated and best ascertained through a high resolution structure of the whole mitoribosome. In addition, high resolution structural information of the whole mitoribosome may shed light on particular functional aspects of proteins, mt-rRNA and mitoribosomal active sites, as well as evolutionary information particularly from mapping homologous regions of proteins/rRNA.

To gain more understanding of the constituents of the whole yeast mitoribosome and the spatial relationship of the components, in order to try and answer some more mechanistic questions of the translation cycle such as mt-mRNA, mt-tRNA and factor binding sites, we have determined and published the complete structure of the whole yeast mitochondrial ribosome by single particle cryo-electron microscopy to a resolution of 3.3 Å (135). The mt-SSU has been solved to 3.3 Å in the body region and 3.5 Å in the head region and the mt-LSU to 3.2 Å. The previously unsolved

mt-SSU has been built *de novo* and includes 34 proteins of which 7 are yeast specific, as well as unique expansion segments of mt-rRNA. We have improved the modelling of components of the previously published mt-LSU as well as building some previously unmodelled areas due to improved resolution.

2.2 Strategy

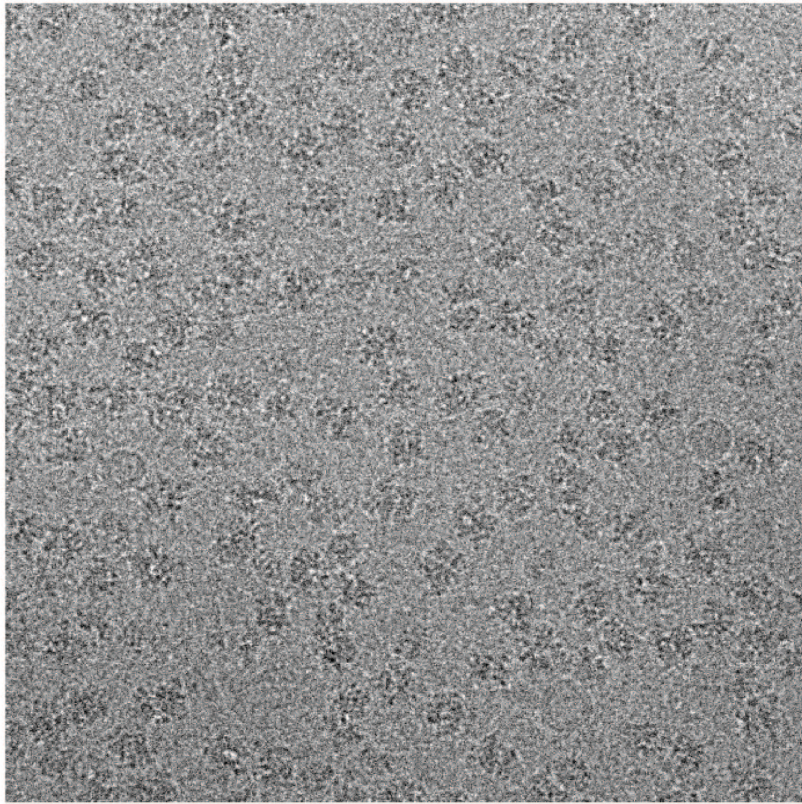
2.2.1 Sample preparation

The general strategy was to prepared a sample of native *S. cerevisiae* mitoribosomes and apply them to cryo-EM grids in order to visualise them using the cryo-electron microscope. To do this, we first purified mitochondria from *S. cerevisiae* and subsequently purified intact mitoribosomes via sucrose gradient density separation. The purified sample was applied onto copper grids lined with a layer of homemade continuous carbon and frozen in liquid ethane. The sample was then stored in liquid nitrogen and subsequently data was collected on these grids on the 300 kV FEI Titan Krios electron microscope. 2525 micrographs were obtained from two days of data collection using the Falcon II detector. A representative micrograph is shown in Figure 5 (A).

2.2.2 Data processing and map generation

Processing was performed using RELION, apart from particle picking which was done using EMAN2 (121,136). After particle picking, extraction and subsequent 2D classification a total of 341,270 particles was retained. 2D classes with different views of the yeast mitoribosomes are shown in Figure 5 (B). The general data processing steps are outlined in Figure 6. Full details of the methods are available in the materials and methods section (2.5).

A



B

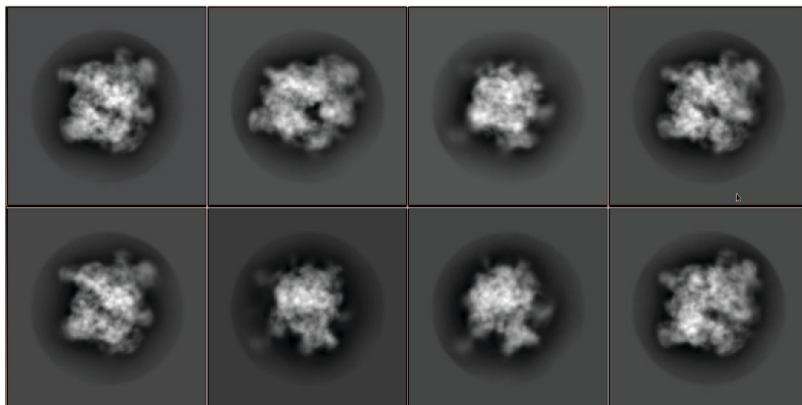


Figure 5 - (A) A representative electron micrograph. (B) Representative 2D classes. Adapted from Desai *et al* (135).

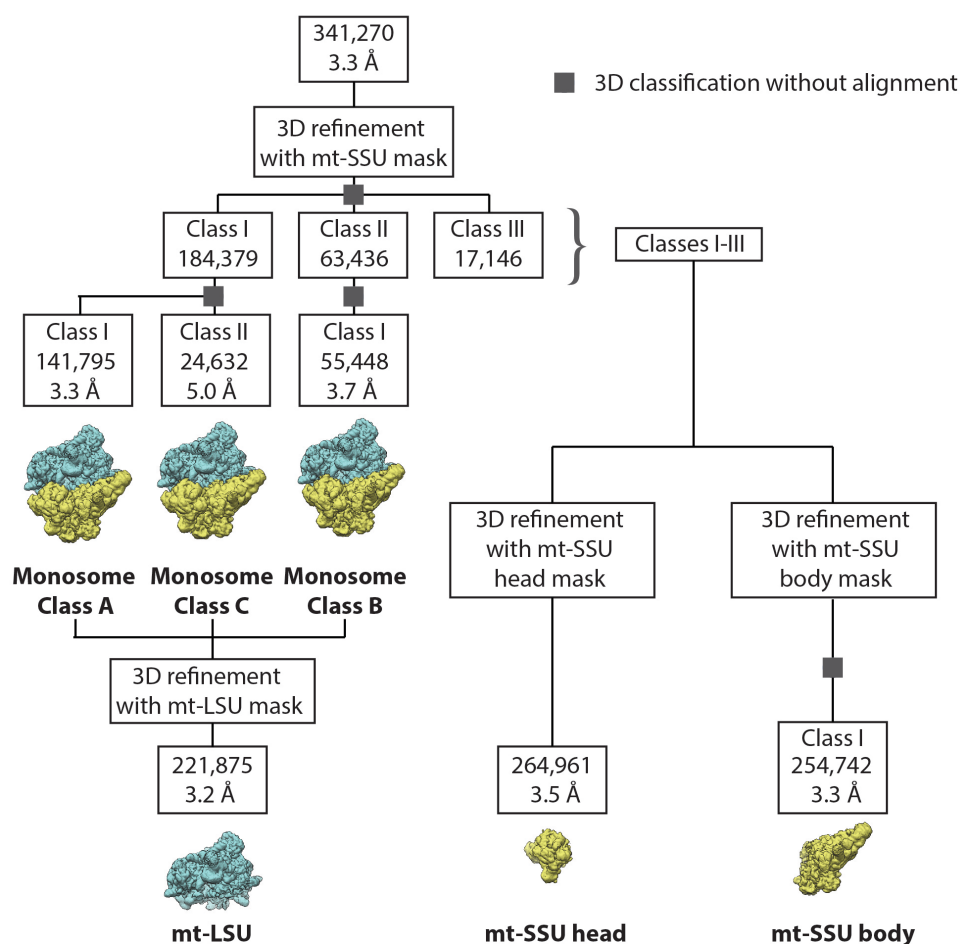


Figure 6 – RELION data processing scheme (135).

After initial 3D refinement a resolution of 3.3 Å was achieved for the reconstruction from the complete dataset as judged by the Fourier-shell-correlation (FSC) 0.143 criterion. After mt-SSU masked 3D refinement, 3 classes were identified following 3D classification without alignments. The most abundant classes, class I and II, were further 3D classified without alignments and overall 3 monosome classes were identified (class A, B and C), which displayed distinctive conformational heterogeneity and resolved to 3.3 Å, 3.7 Å and 4.6 Å, respectively (Figure 7). Due to the flexible movement of the small and large subunits relative to each other it was necessary to further improve the quality of the maps of individual parts of the ribosome to aid *de novo* building by applying specific soft masks during subsequent refinements, in combination with further 3D classification. To improve the resolution of the mt-SSU we went back to the initial 3D classification, pooled these classes and performed 3D refinement with a mt-SSU head mask or mt-SSU body

mask. For the mt-SSU body we also performed an additional 3D classification. For the mt-LSU we combined the final three monosome classes and performed 3D refinement with a mt-LSU mask. Overall, the local resolution improved after these masks, with the mt-SSU body resolved to 3.3 Å, the head to 3.5 Å and the mt-LSU resolved to 3.2 Å. The FSC curves for the 6 different maps are shown in Figure 8.

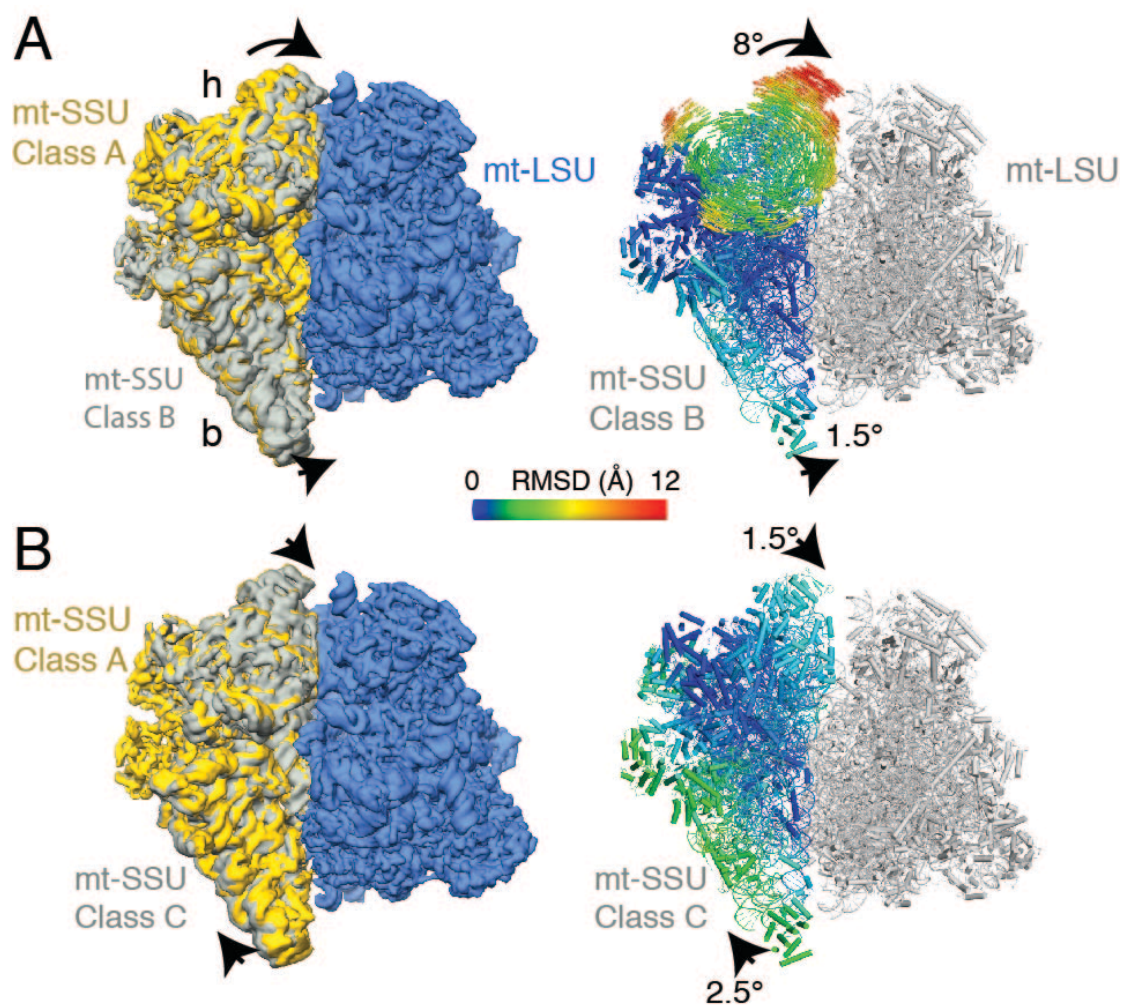


Figure 7 - (A) Class B is related to class A by a small 1.5° rotation of the mt-SSU body and an 8° rotation of the mt-SSU head. (B) Class C is related to class A by small rotations of 2.5° and 1.5° of the mt-SSU body and head respectively. The body atoms and head vectors are coloured by root-mean-square displacement (RMSD), according to the figure legend, from their position in class A and positioned in the right hand images (135).

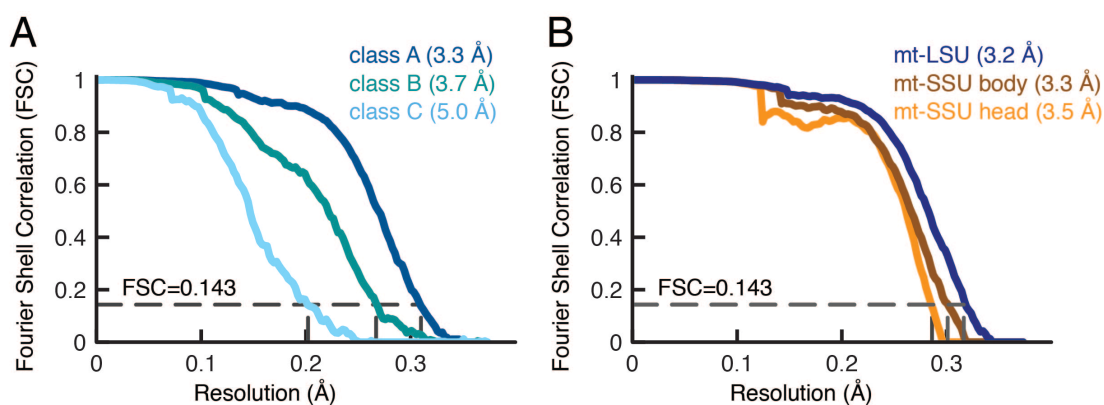


Figure 8 – (A) Fourier-shell-correlation (FSC) curves for the three different conformations of the yeast mitoribosome monosomes. (B) FCS curves for each for the masked maps for the different segments of the mitoribosome. Adapted from Desai *et al* (135).

It is evident from the maps of the monosomes and the masked maps coloured by resolution, that the cores of the maps are of higher resolution compared with the peripheries (Figure 9). This is due to relative flexibility of the peripheral components to include flexible helical segments of mt-rRNA. As expected the overall resolution of the most abundant class, class A, was better than the other monosome classes. Local resolution was further improved in the masked map refinements of individual sections of the mitoribosome (as described above), compared with the whole monosome class refinement due to reduction of the obligate movement between the larger segments of the mitoribosome. In particular the improvements of the mt-LSU maps were crucial for map interpretation and *de novo* model building of previously unbuilt areas (Figure 10). A comparison of the FSC curves between the old (EMD-2566) and the new mt-LSU map showed that, although the overall resolutions were similar at around 3.2 Å at the FSC=0.143 criterion, the new map had higher FSC correlations at lower resolutions compared with the previous map (46).

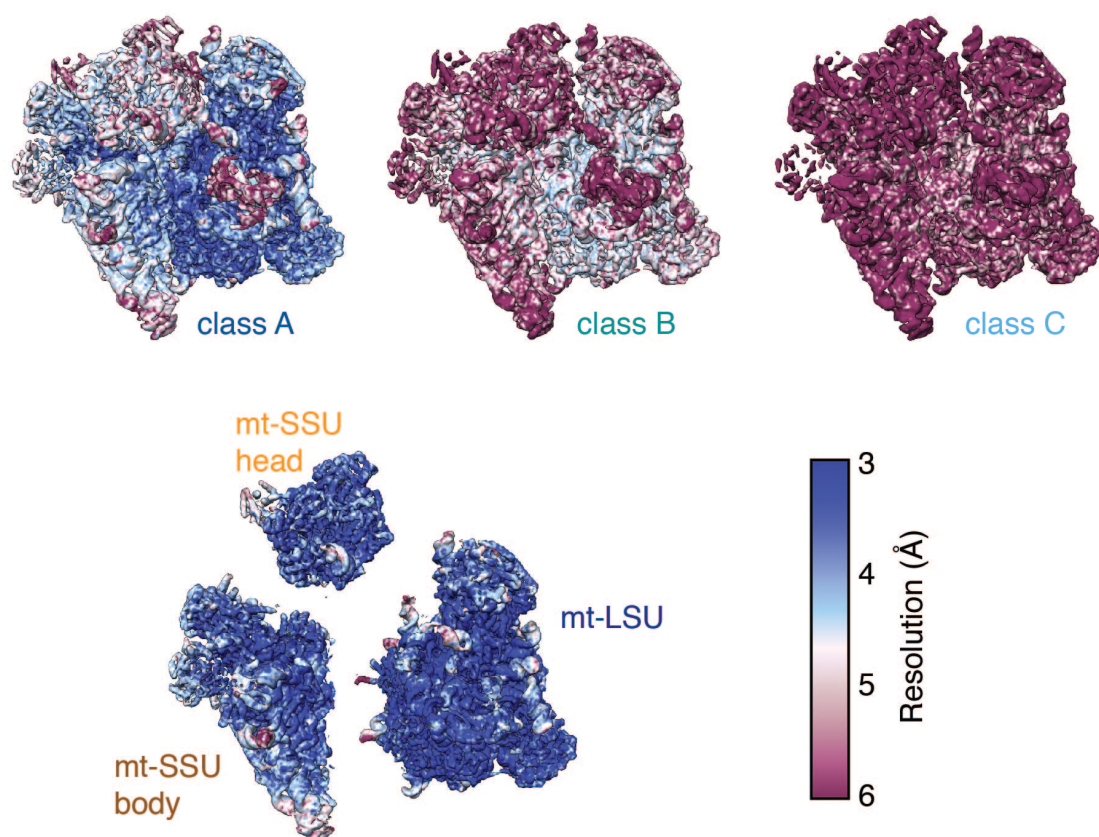


Figure 9 – Maps for each main yeast mitoribosome monosome class A-C, and maps for each masked map coloured by local resolution according to the figure legend. Adapted from Desai *et al* (135).

After obtaining the 3 monosome maps and the focussed maps, *de novo* modelling of the mt-SSU and fitting and further modelling of the mt-LSU was done in the Crystallographic Object-Oriented Toolkit (Coot) software (125). Known structures of the human mitoribosome (PDB 3J9M) and bacteria *Escherichia coli* (*E. coli*; PDB 5IQR) ribosomal proteins were docked into homologous regions using a trace of the main chains of the proteins, representing the α -carbon atoms (48,137). Subsequently the sequence was mutated and *de novo* areas built.

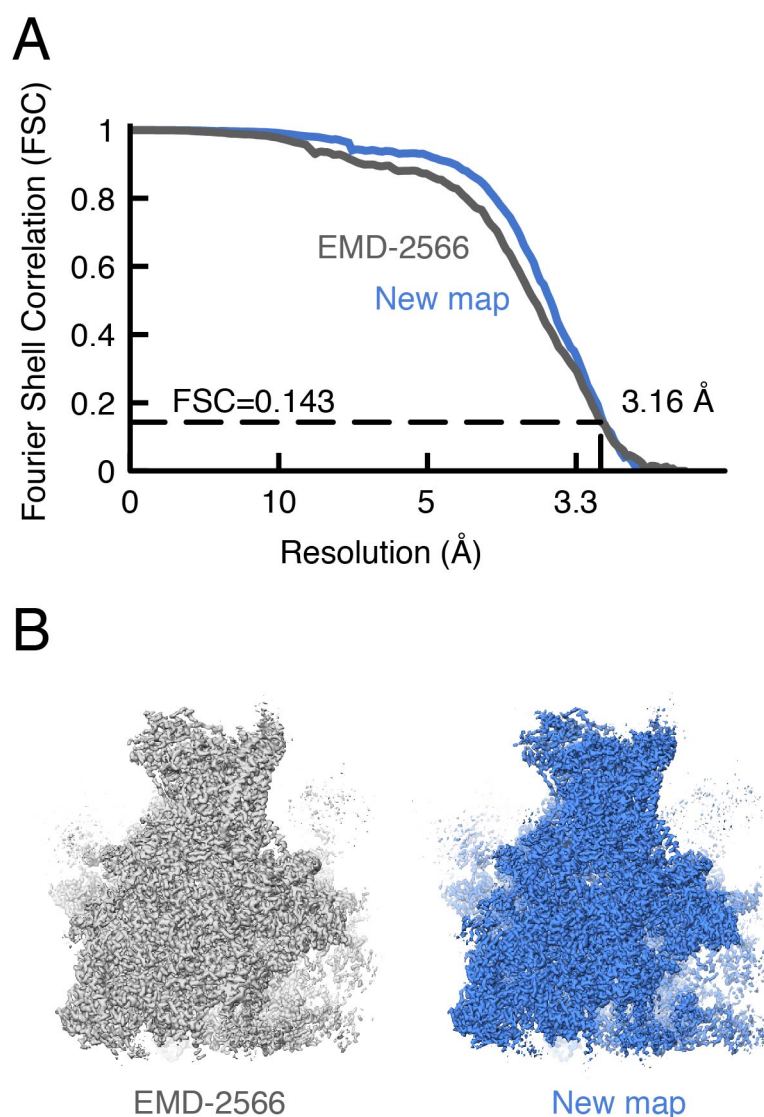


Figure 10 – (A) FSC curves comparing the obtained masked map of the mt-LSU and the previously published map (EMD-2566) (B) Post processed maps (46). Adapted from Desai *et al* (135).

Furthermore, *E. coli* rRNA (PDB 5IQR) was also used as a starting reference to build the mt-SSU mt-rRNA (137). The modelling was done using the higher resolution maps of the mt-SSU head and body, and the mt-LSU. These individually modelled sections were then fitted into the 3 monosome maps, to obtain a model of the complete mitoribosome. The FSC curves of the fit of the refined model to the final map for each of the 3 classes of the monosome are shown in Figure 11. In the mt-LSU, in areas that previously were unable to be confidently built into, we were now able to model in amino acid side chains (Figure 12) (46). Table 1 on page 37

contains the model statistics and data collection information for the three monosome classes. Full details of the methods are listed in 2.5.

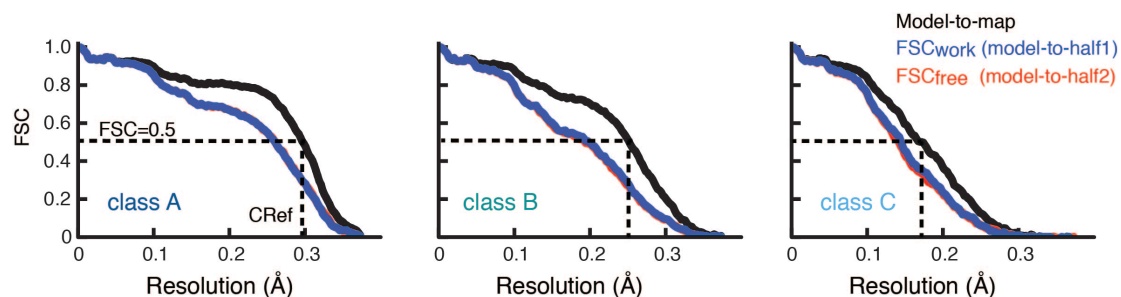


Figure 11 – FSC curves representing the fit of the refined model to the final map (black line) for each of the three yeast mitoribosome conformations. The dashed line indicates the resolution at FSC=0.5. Denoted by blue and red lines are the self- (FSC_{work}) and cross-validated (FSC_{free}) correlations respectively. Adapted from Desai *et al* (135).

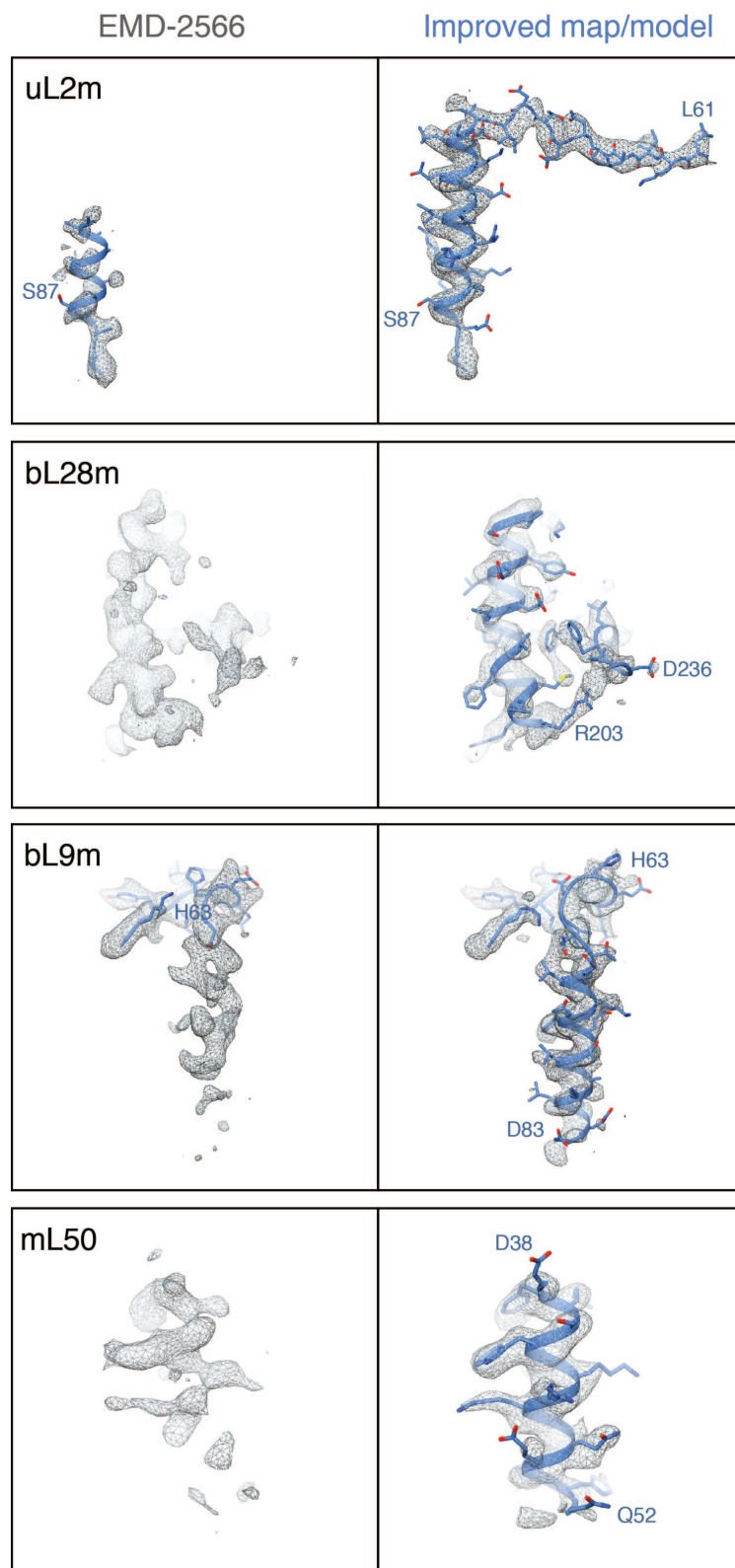


Figure 12 – Examples of regions improved comparing the old map (EMD-2566) with our new map, with newly built amino acids (46). Adapted from Desai *et al* (135).

Data Collection	Class A	Class B	Class C
Particles	141,795	24,632	55,448
Pixel size (Å)	1.34	1.34	1.34
Defocus mean (µm)	2.4	2.5	2.6
Defocus range (-µm)	1.3–4.8	1.3–4.8	1.3–4.8
Voltage (kV)	300	300	300
Electron dose ($e^- \text{Å}^{-2}$)	23.5	23.5	23.5
Model composition			
Non-hydrogen atoms	201,475	201,475	201,475
Protein residues	13,711	13,711	13,711
RNA bases	4,286	4,286	4,286
Ligands ($\text{Zn}^{2+}/\text{Mg}^{2+}/\text{H}_2\text{O}$)	2/301	2/301	2/301
Refinement			
Resolution (Å)	3.25	3.75	4.97
Map sharpening B-factor (Å ²)	-72	-86.6	-138
Average B factor (Å ²)	74.9	87.0	111.0
FSC _{average} CRef (Å)	0.80	0.77	0.72
Rms deviations			
Bond lengths (Å)	0.005	0.005	0.005
Bond angles (°)	1.03	1.02	1.02
Validation (proteins)			
MolProbity score	2.0 (100 th percentile)	2.1 (100 th percentile)	2.0 (100 th percentile)
Clashscore, all atoms	2.4 (100 th percentile)	3.1 (100 th percentile)	2.7 (100 th percentile)
Favoured rotamers (%)	84.8	84.9	84.7
Poor rotamers (%)	6.0	6.0	6.0
Ramachandran plot			
Favored (%)	94.3	94.4	94.3
Outliers (%)	0.4	0.4	0.4
Validation (RNA)			
Correct sugar puckers (%)	95.3	95.3	95.3
Good backbone conformations (%)	74.5	74.7	74.6

Table 1 – Data collection parameters and model statistics. Adapted from Desai *et al* (135).

2.3 Results and Discussion

2.3.1 Overall Structure

The structure of the whole yeast mitochondrial ribosome was determined to 3.2 Å by cryo-electron microscopy (Figure 13) (135). The small subunit head has been determined to a resolution of 3.5 Å, the body to 3.3 Å and the large subunit to 3.2 Å. The complete model of the yeast mitoribosome contains two mt-rRNA molecules (the 21S of the mt-LSU and the 15S rRNA of the mt-SSU), 74 mitoribosomal proteins and an E-site mt-tRNA. The E-site mt-tRNA is presumed to be a mixture of the 24 mt-tRNAs (Figure 14).

The newly built mt-SSU contains the 15S mt-rRNA and 34 proteins, of which 20 have bacterial homologues (Figure 13, Table 2). In fact, only the bacterial SSU protein bS20 was found to be absent. Additionally the yeast mt-SSU was not found to have homologues to the human mitoribosomal proteins mS22, mS25, mS27, mS31, mS34 and mS39. 14 of the mt-SSU proteins have been found to be unique to mitoribosomes and of these, 7 are yeast mitochondrial specific. These have been renamed in accordance with the new classification for the naming of ribosomal proteins (138).

We were unable to locate 2 proteins previously reported in the literature to be constituents of the yeast mitoribosome RSM22 and YMS2 (131,132). It is possible that these proteins are located in the periphery where unaccounted alpha helices were identified. Nevertheless, due to these short segments being of insufficient density no protein could be assigned. However, RSM22 has also been reported as an RNA methyl transferase that only interacts with the ribosome transiently (139,140). The absence of these proteins was further confirmed by tandem mass spectrometry of purified yeast mitoribosomes. Although, 8 other proteins that were identified in the structure were also missing from the mass spectrometry data (Table 3) (46).

The 7 yeast specific proteins, as well as the unique elements of homologous proteins and the mt-rRNA expansion segments largely occupy the peripheral surface of the mitoribosome, creating a distinctive surface conformation compared to other

mitoribosomes. Two new proteinacious protuberances dominate the periphery of the mt-SSU body. mS38 (Cox24) not previously identified as a yeast mitoribosomal protein was assigned by directly interpreting the density and obtaining a sequence that was cross referenced against protein databases (Figure 15). Although not known previously to be a mitoribosomal protein, it had been reported in the literature to have an effect on mitochondrial translation. Cox24 null mutants had been found to have reduced amount of mitochondrially encoded proteins, although its hypothesised role in mitochondrial RNA processing cannot be explained by our structure (141).

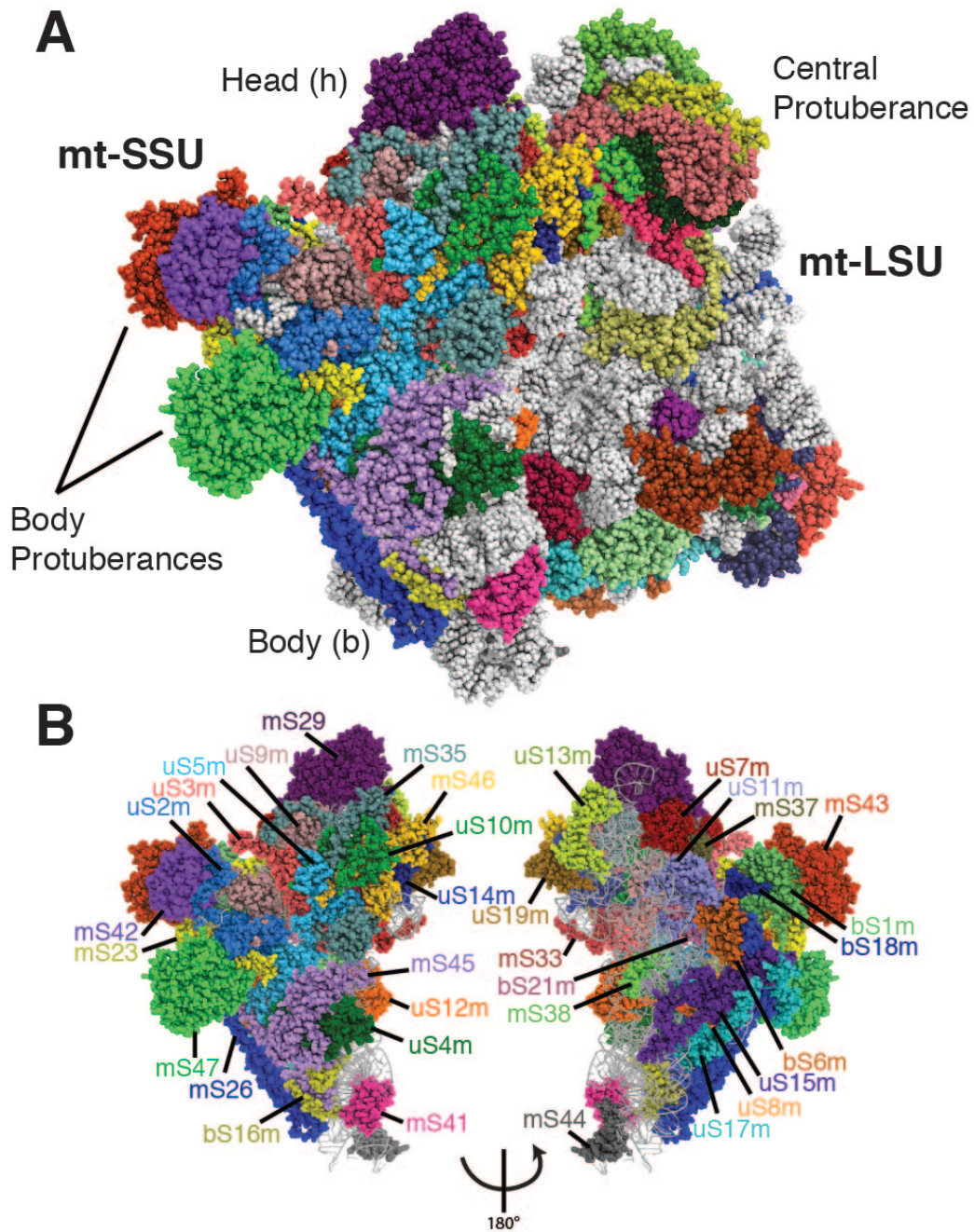


Figure 13 - (A) The overall structure of the yeast mitochondrial ribosome. (B) Protein constituents of the yeast mt-SSU (135). The figures represent the PyMOL surface representations of the model.

MRP	Alias	UniProt ID	Chain ID	Residue range	MW (Da)	Modelled residues	Notes
bS1m	MRP51	Q02950	AA	1-344	39,445	2-109, 195-233, 244-299,	Extensively remodelled when compared to bacterial and human mitochondrial homologs.
uS2m	MRP4	P32902	BB	26-394	44,162	128-393	
uS3m	VAR1	P02381	CC	1-398	47,123	30-68, 78-158, 166-280, 295-398	Yeast mitochondrial genome encoded.
uS4m	NAM9	P27929	DD	35-486	56,356	2-80, 88-192, 384-486	
uS5m	MRPS5	P33759	EE	14-307	34,883	14-113, 119-306	
bS6m	MRP17	P28778	FF	1-131	15,021	1-125	
uS7m	RSM7	P47150	GG	27-247	27,816	87-247	
uS8m	MRPS8	Q03799	HH	1-155	17,471	2-155	
uS9m	MRPS9	P38120	II	11-278	31,925	35-71, 81-134, 144-278	
uS10m	RSM10	Q03201	JJ	15-203	23,424	17-201	
uS11m	MRPS18	P42847	KK	60-217	24,563	70-99, 106-217	
uS12m	MRPS12	P53732	LL	21-153	16,917	29-152	
uS13m	SWS2	P53937	MM	1-143	16,089	2-121	
uS14m	MRP2	P10663	NN	1-115	13,538	1-115	
uS15m	MRPS28	P21771	OO	34-286	33,057	34-112, 128-286	
bS16m	MRPS16	Q02608	PP	1-121	13,639	2-106, 110-120	
uS17m	MRPS17	Q03246	QQ	1-237	27,635	2-117, 124-135, 140-150, 159-208, 218-232	
bS18m	RSM18	P40033	RR	1-138	15,835	40-72, 81-138	
uS19m	RSM19	P53733	SS	1-91	10,275	9-88	
bS21m	MRP21	P38175	TT	18-177	20,395	86-177	

MRP	Alias	UniProt ID	Chain ID	MRR	MW (Da)	Modelled residues	Notes
mS23	RSM25	P40496	UU	1-264	30,513	1-233	
mS26	PET123	P17558	VV	1-318	35,998	2-234	
mS29	RSM23	Q001163	WW	15-450	50,867	50-450	
mS33	RSM27	P53305	XX	1-110	12,393	1-96	
mS35	RSM24	Q03976	YY	31-319	37,393	47-119, 124-319	
mS37	MRP10	O75012	ZZ	2-95	10,691	5-70, 75-95	Certain human homologous domains but different spatial orientation adopted.
mS38	COX24	P32344	11	1-111	12,772	78-111	Not previously identified as a mitoribosomal protein in yeast. Shown to be involved in processing COX1 transcripts (138).

mS41	FYV4P	P38783	22	28-130	15,292	30-128	Sterile alpha motif domain
mS42	RSM26	P47141	33	1-266	30,224	8-100, 112-262	Forms a heterodimer with mS43. Homologous to Fe/Mn superoxide dismutases.
mS43	MRP1	P10662	44	14-421	36,729	18-175, 190-230, 244-313	Forms a heterodimer with mS42. Homologous to Fe/Mn superoxide dismutases.
mS44	MRP13	P12686	55	38-339	38,988	42-78, 115-136	
mS45	MRPS35	P53292	66	27-345	39,575	27-276, 291-345	
mS46	RSM28	Q03430	77	1-359	41,216	197-361	Occupies a similar position to human mS31 however structural similarities appears resultant of environmental constraints rather than shared ancestry.
mS47	EDH3	P28817	88	36-500	56,288	36-449, 455-492	Probable active enzyme. Structural similar to human 3-hydroxyisobutyryl-CoA hydrolase (HIBCH, PDB entry code 3BPT).

Table 1 – Yeast small subunit mitoribosomal proteins. The shading of the background is coloured by protein conservation with the bacterial ribosome (blue) and human mitochondrial ribosome (red), and yeast mitoribosome specific proteins (yellow)(133). MRP – mitochondrial ribosomal protein. MRR - mature residue range. MW – molecular weight

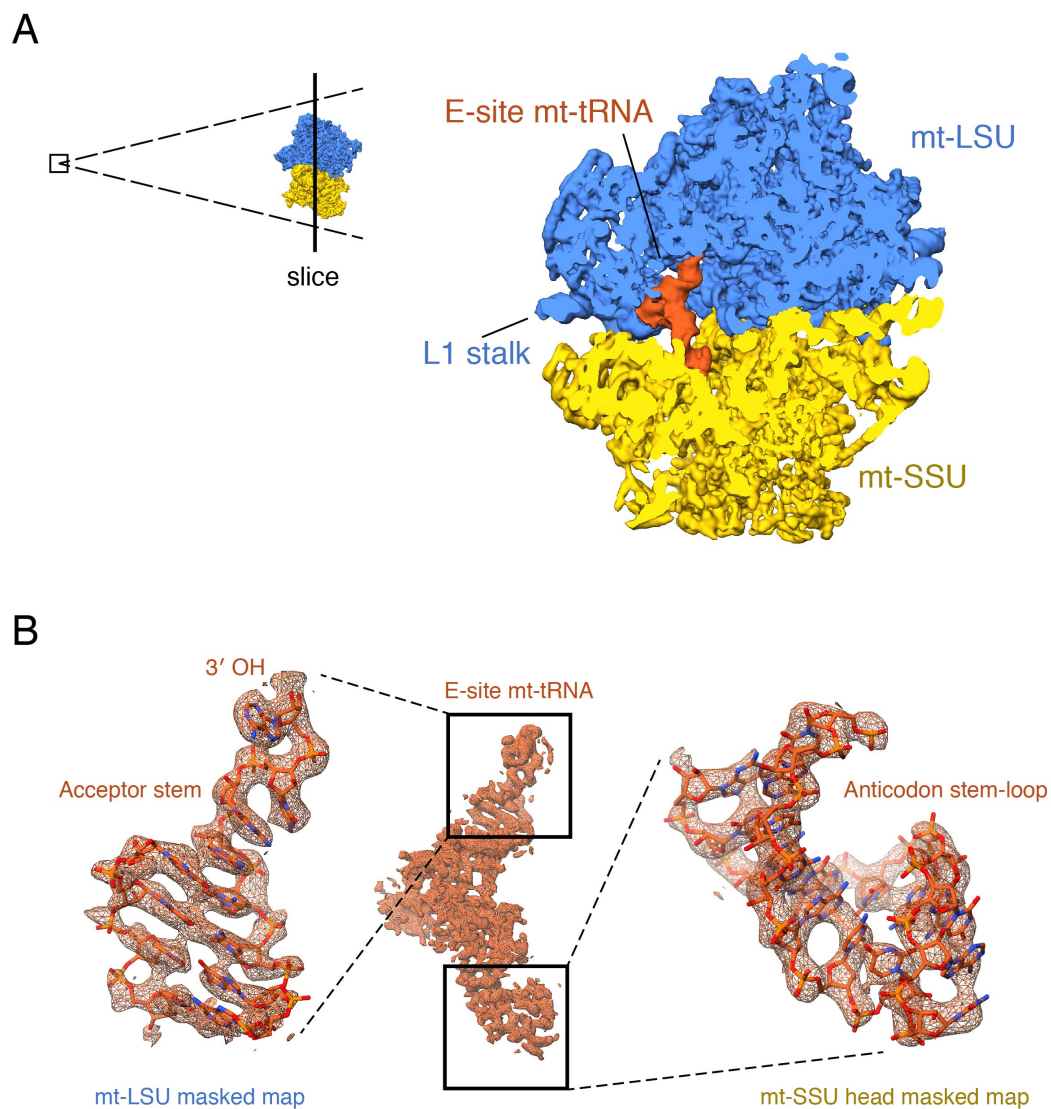


Figure 14 – E-site mt-tRNA (135). (A) E-site mt-tRNA bound in the intersubunit space shown as a slice through the unfiltered map of the yeast mitoribosome. The mt-LSU makes contact with the acceptor stem and elbow of the mt-tRNA and the mt-SSU makes contact with the anticodon stem loop. (B) Masked maps of the subunit were used to model the acceptor stem and anticodon stem-loop of the mt-tRNA .

mt-LSU		mt-SSU	Translational Activators	Others	
uL1m	uL30m	bS1m	Aep1	Ach1	Lpd1
uL2m	bL31m	uS2m	Aep2	Aco1	Lsc2
uL3m	bL32m	uS3m	Atp25	Ald4	Lsp1
uL4m	bL33m	uS4m	Cbp1	Atp1	Mdh1
uL5m	bL34m	uS5m	Cbs2	Atp16	Mic10
uL6m	bL36m	bS6m	Mam33	Atp2	Mir1
bL9m	mL38	uS7m	Ssc1	Atp3	Mss116
uL10m	mL40	uS8m		Atp4	Ndi1
uL11m	mL41	uS9m		Atp5	Om45
bL12m	mL43	uS10m		Atp6	Pda1
uL13m	mL44	uS11m		Atp7	Pdb1
uL14m	mL46	uS13m		Cat2	Pdx1
uL15m	mL49	uS14m		Cit1	Pet9
uL16m	mL50	uS15m		Cor1	Phb1
uL17m	mL53	bS16m		Cox2	Phb2
bL19m	mL54	uS17m		Cox5	Por1
bL21m	mL57	bS18m		Fum1	Pth4
uL22m	mL58	bS21m		Ggc1	Qcr2
uL23m	mL59	mS23m		Gut2	Qcr7
uL24m	mL60	mS26		Hsp60	Rip1
bL27m	mL61	mS29		Idh2	Sdh1
bL28m	MHR1	mS33		Ilv5	Sdh2
uL29m		mS35		Kgd1	Stb1
		mS37		Kgd2	Suv3
		mS41		Krt14	Tim9
		mS42		Lat1	
		mS43			
		mS44			
		mS45			
		mS46			
		mS47			

Table 3 - Analysis of purified yeast mitoribosomes by tandem mass spectrometry (135).

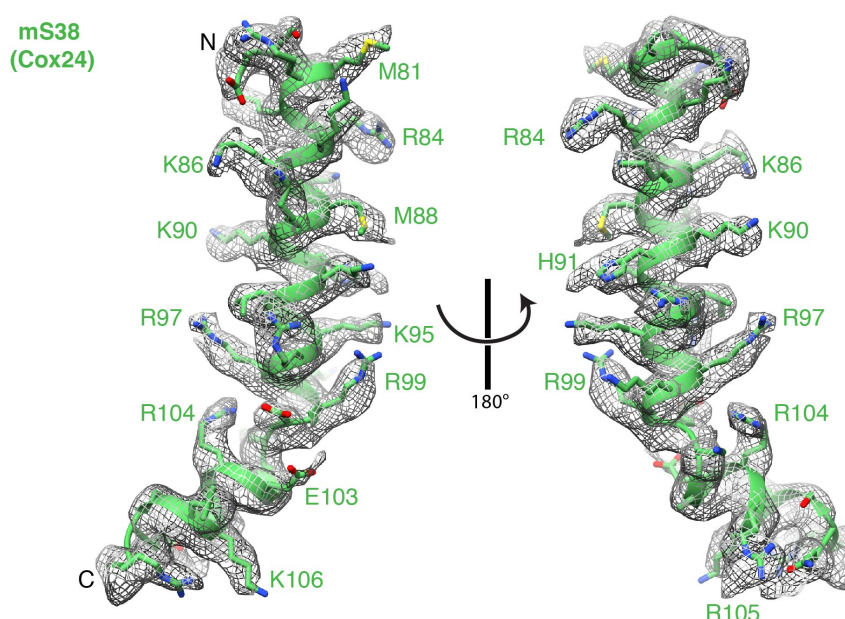


Figure 15 – mS38 (Cox24) (135). Model of S38 (Cox24) fitted to the density. From the density mS38 was identified as being a constituent of the yeast mitoribosomes.

2.3.2 Mt-SSU protein elements and mt-rRNA expansion segments

Of the mt-SSU proteins modelled, the ones found to be homologous with the bacterial ribosome include bS1m (Mrp51), uS2m (Mrp4), uS3m (Var1), uS4m (Nam9), uS5m (Mrps5), bS6m (Mrp17), uS7m (Rsm7), uS8m (Mrps8), uS9m (Mrps9), uS10m (Rsm10), uS11m (Mrps18), uS12m (Mrps12), uS13m (Sws2), uS14m (Mrp2), uS15m (Mrps28), bS16m (Mrps16), uS17m (Mrps17), bS18m (Rsm18), uS19m (Rsm19) and bS21m (Mrp21) (Table 2). The majority of proteins found to be homologous with bacteria are distinguishable by their domain extensions, at times reaching considerable length (Figure 17). The extensions however do not necessarily show good homology with human protein counter-part extensions. Of the proteins homologous only with the human, there is again evidence of variation in tertiary structure and length.

The proteins that have homologues in both the human and yeast mitochondrial system are mS23 (Rsm25), mS26 (Pet123), mS29 (Rsm23), mS33 (Rsm27), mS35 (Rsm24), mS37 (Mrp10) and mS38 (Cox24). Additionally there are 7 proteins that are entirely specific to the yeast mt-SSU, mS41 (Fyv4), mS42 (Rsm26), mS43 (Mrp1),

mS44 (Mrp13), mS45 (Mrps35), mS46 (Rsm28) and mS47 (Ehd3). Overall, the addition of the mitochondrial-specific elements results in a more proteinacious mitoribosome with a conserved core of bacterial proteinacious elements and surrounding mitochondrially unique elements (Figure 16). Figure 16 shows the mt-SSU proteins with the areas homologous to bacteria in blue occupying the inner layer. The red sections represent the areas homologous to human only and not bacteria. These sections largely occupy the peripheral layer. To an even greater proportion, the outer layer is occupied by yeast specific elements (represented in yellow). Figure 18 (A) shows the proteins of the mt-SSU represented by the presence of homologues. The core represents proteins that have bacterial homologues in blue. The mitochondrial specific proteins (red) and the new yeast specific proteins (yellow) are present at the periphery, including two protuberances giving the mitoribosome a unique shape. Accordingly, increased protein-protein interfaces have been observed when compared with the bacteria (Figure 18 (B)). In addition to the new yeast specific protein-protein interfaces, the majority of ancestral bacterial interfaces are still conserved, as well as some interfaces that also occur in the human mitoribosome.

1501 nucleotides of the 1649 nucleotides of the 15S mt-rRNA were modelled in the structure. Using base pairing information from the structure we were able to derive a secondary structure diagram (Figure 19 (A)). The helices that correspond to the known *E. coli* helices are numbered as so. Overall, the core structure of the 15S mt-rRNA maintains good homology with the bacterial 16S mt-rRNA but is longer, 1649 nucleotides compared to 1542 nucleotides.

Discrepancies are mostly found at the mitoribosome peripheries. In comparison with *E. coli*, 6 bacterial helices have been shortened (h6, h8, h17, h21, h33 and h39). However, this is complimented by 3 new expansion segments (h16-ES, h17-ES and h41-ES), as well as extensions of h9, h44 and of the 5' and 3' tails. This is in contrast to the human 12S mt-rRNA which exhibits significant helical contraction compared to the bacterial 16S with which it too shares the core domains (48). We were unable to accurately model two of the expansion segments, h16-ES and h17-ES, which occupy the periphery due to insufficient density. It was however possible to

recognise that they formed helical domains. Overall, these new extension and proteins serve to give the yeast and human mitoribosome and the bacterial ribosome their unique shapes (Figure 20). Human and yeast protein extension disparity supports elongation of these proteins after divergence from the common bacterial ancestor rather than contraction of their bacterial homologues. Bacterial proteins may additionally have further contracted post divergence. Regions of conservation and divergences may help to construct the evolution of mitoribosomes.

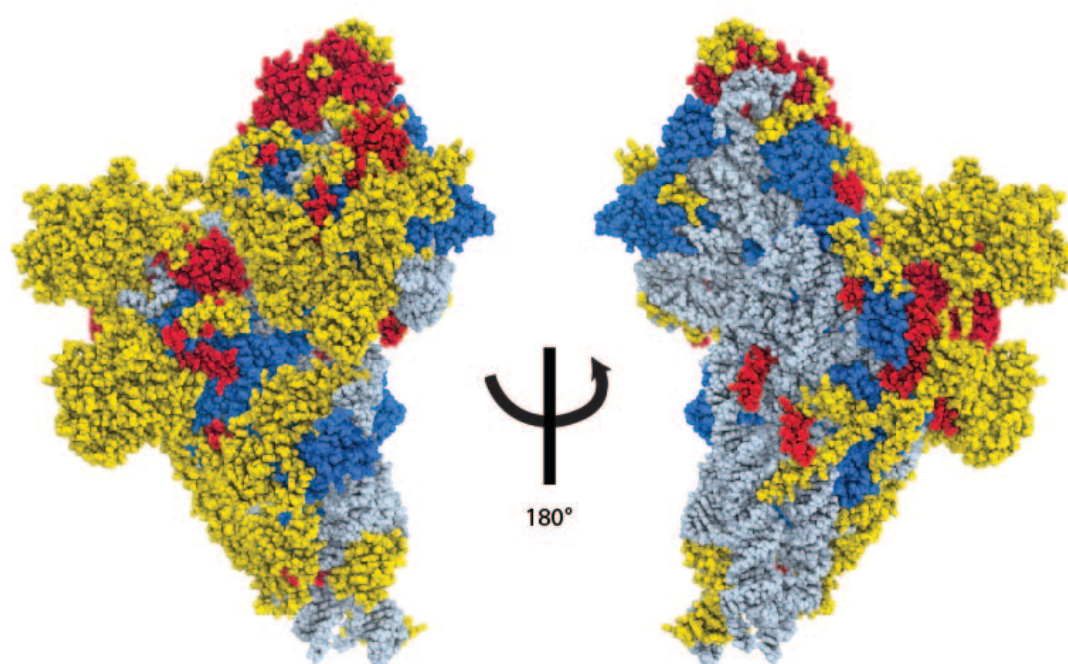


Figure 16 – Protein elements of the mt-SSU coloured by conservation (135). The blue coloured regions are elements conserved with the bacterial ribosome. The red coloured regions are elements conserved with the human mitochondrial ribosome but not the bacterial ribosome. Yeast specific elements are coloured yellow. Mt-rRNA is coloured in grey. The figure represents the PyMOL surface representation of the model.

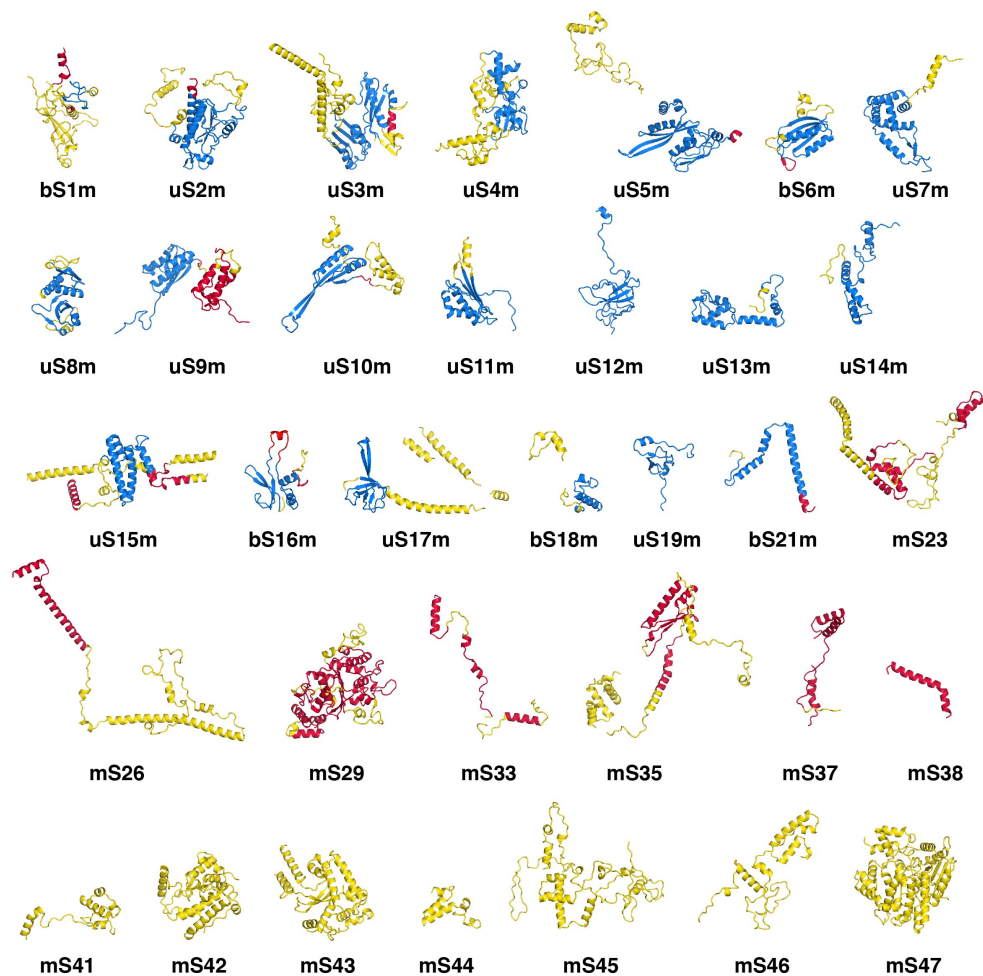


Figure 17 – Mitoribosomal protein expansions (135). (A) Each mitoribosomal protein of the yeast mt-SSU represented by their tertiary folds, coloured by conservation. The blue coloured regions are elements conserved with the bacterial ribosome. The red coloured regions are elements conserved with the human mitochondrial ribosome but not the bacterial ribosome. Yeast specific elements are coloured yellow.

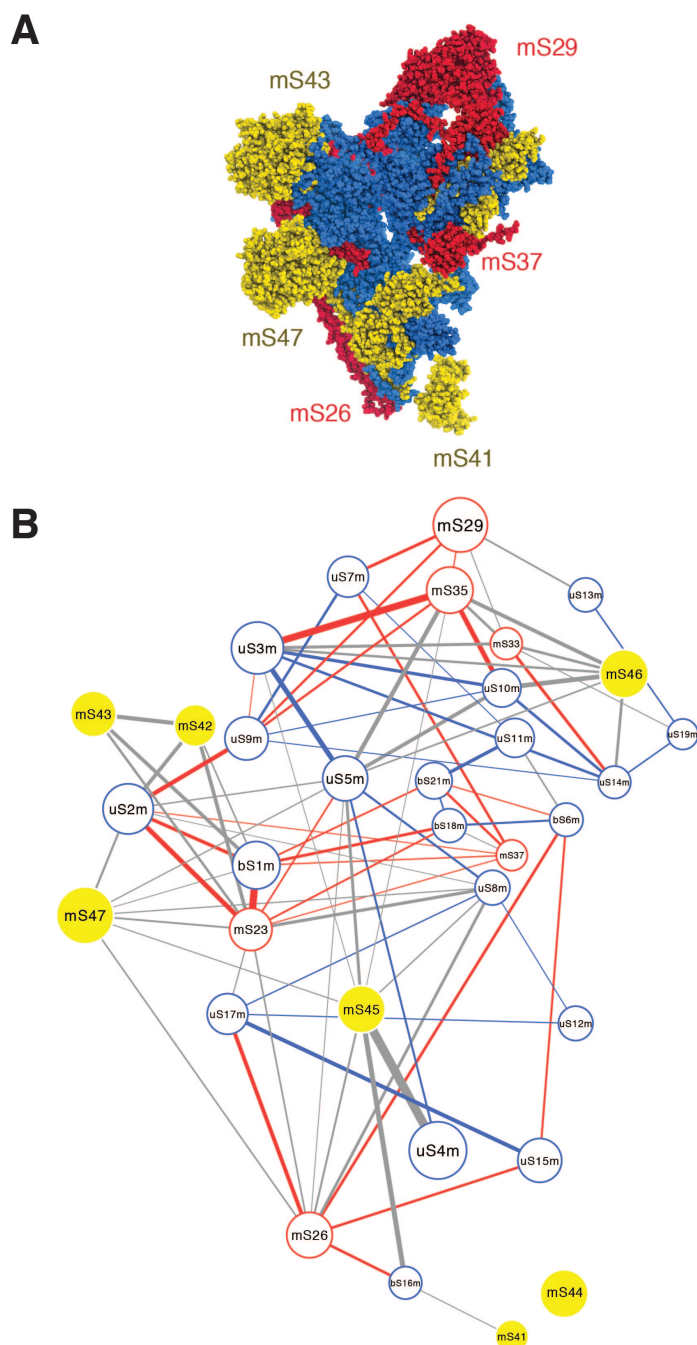
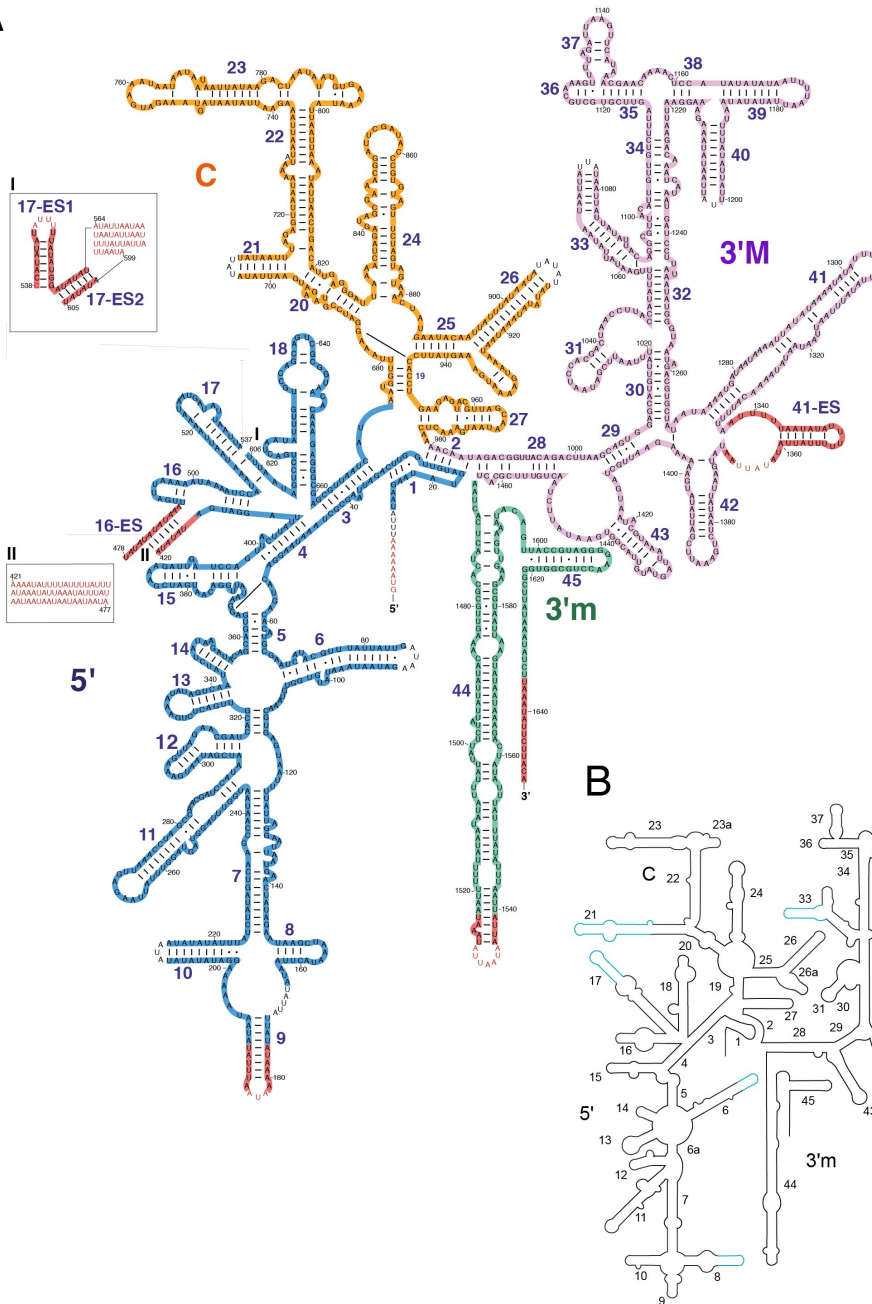


Figure 18 – Interactions between proteins of the yeast mt-SSU. (A) Yeast mitoribosomal proteins with bacterial ribosome homologues are shown in blue. Yeast mitoribosomal proteins with human mitoribosomal homologues are shown in red. Yeast specific proteins are shown in yellow. The figure represents the PyMOL surface representations of the model. **(B)** The protein-protein network of the mt-SSU. The size of the nodes represents the relative molecular masses of the proteins, and the thickness of the edge represents the extent of the interface between the interacting proteins. Interactions also occurring in bacterial and human mitoribosomes are shown in blue and red, respectively. Yeast mitoribosome specific interactions are shown in grey. Edgeless nodes represent proteins that only contact mt-rRNA. Adapted from Desai *et al* (135).

A



B

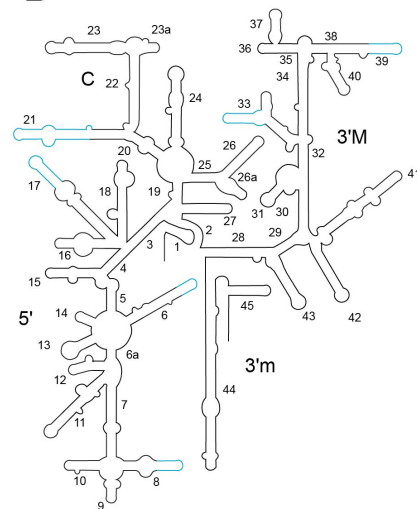


Figure 19 – Secondary structure diagram of the yeast mt-SSU 15S rRNA. (A) The 15S mt-rRNA coloured by the different domains and labelled according to the *E. coli* counterparts when appropriate. The yeast mitoribosome specific expansions are highlighted in red. The nucleotides that could not be modelled are shown with no background colouring. Unmodelled areas specific to the yeast mitoribosome are denoted in red lettering. **(B)** Secondary structure diagram of the *E. coli* 16S rRNA. The helices that are not present in the yeast mitoribosome are coloured in blue. Adapted from Desai *et al* (135).

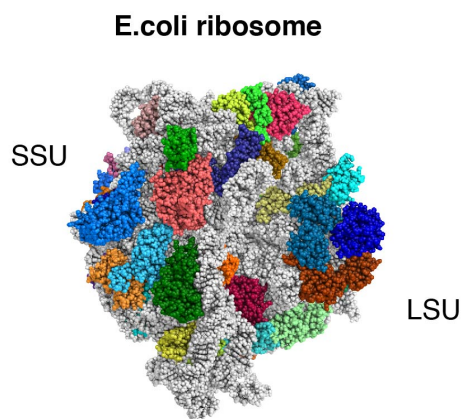
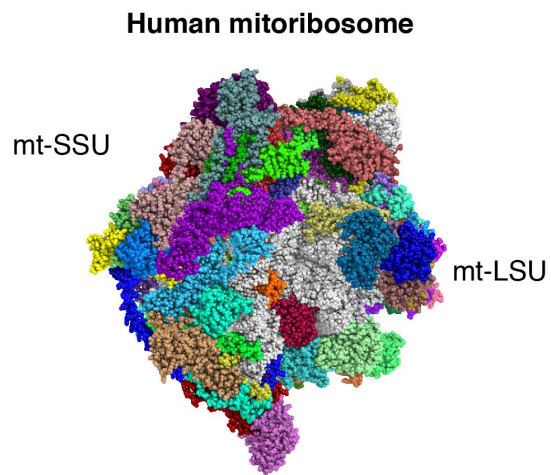
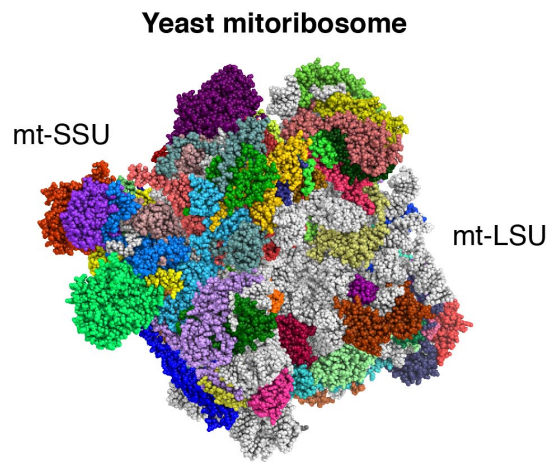


Figure 20 - Comparison between the yeast mitoribosome, human mitoribosome and *E. coli* ribosome. Mt-rRNA is coloured in grey. Homologous proteins are assigned the same colour. Adapted from Desai *et al* (135). The figures represent PyMOL surface representations of the models.

2.3.3 Intersubunit Connections

The subunits of the mitoribosome are connected through a series of intersubunit bridges, which serve to regulate the relative movements of the subunits (Figure 21). Most of the bacterial ribosome bridges are conserved in the yeast mitoribosome with the exception of B1a/b and B4 (Figure 21, Table 4) (142).

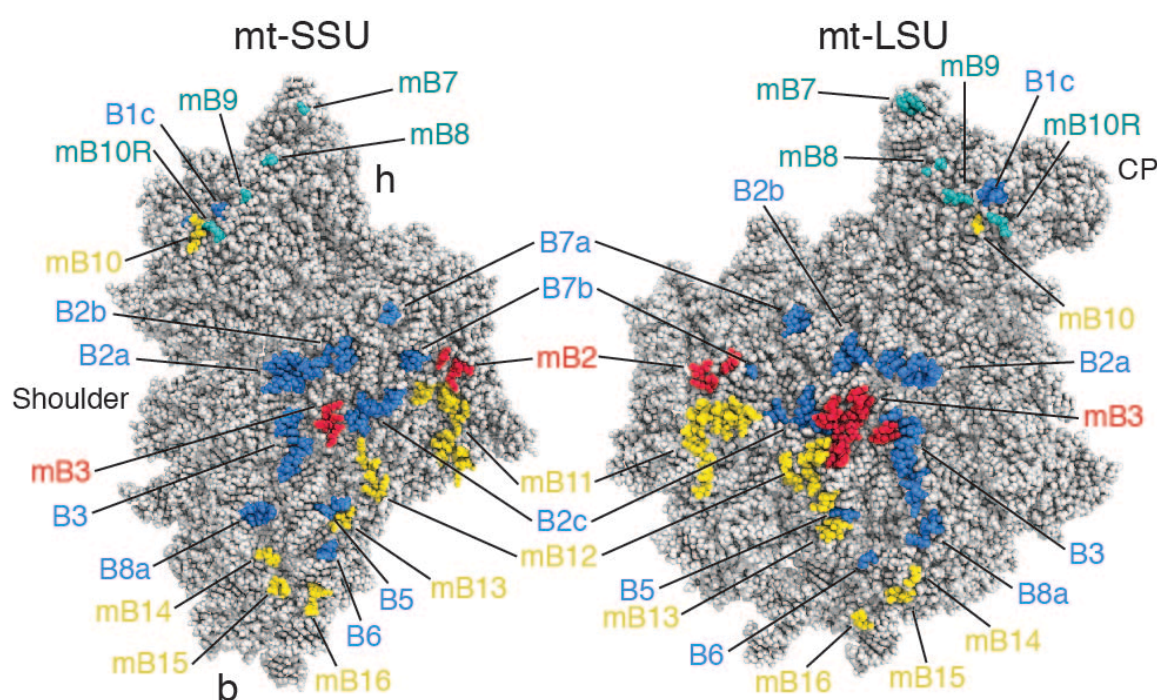


Figure 21 – Intersubunit Bridges (135). (1) The intersubunit interface of the mt-SSU and mt-LSU are shown. Residues involved in intersubunit contacts are coloured and labelled with the respective bridge names. Residues coloured blue represent bridges also present in the bacterial ribosome. Residues coloured red represent bridges present in the yeast and human mitoribosome. Residues coloured yellow represent yeast specific bridges. Yeast specific residues that are found only in class B are coloured in teal. b = body, h = head and CP = central protuberance. The figure represents the PyMOL surface representation of the model.

In class A there are also 7 yeast mitoribosome specific bridges and 2 bridges that are shared with the mammalian mitoribosome (Figure 21, Figure 22, Figure 23, Table 5). Representative density for two of the bridges B5 and B6 are shown in Figure 24. The increased number of intersubunit bridges in the yeast mitoribosome (as

compared to the bacterial ribosome) may limit the intersubunit movement. This is reflected in the relatively subtle movement between the three monosome classes we observed (Figure 7). In the mammalian mitoribosome a remodelled helix 44 has led to comparatively fewer intersubunit contacts (48,50). In our models we were not able to observe the previously seen ‘racheted and ‘rolled’ states of the human mitoribosome or the hyper-rotated state for the yeast mitoribosome captured previously by cryo-electron tomography (48,99).

In Class B, further yeast mitoribosome specific bridges were observed (Figure 21, Table 5). This is mediated by an 8° rotation of the head bringing it into contact with the central protuberance of the mt-LSU (Figure 21, Figure 23). This also has the effect of bringing mS29 (Rsm23) into contact with a 21S mt-rRNA expansion segment of the mt-LSU, H82-ES4 (Figure 25). mS29 in the mammalian mitoribosome has been found to be bound by guanosine 5'-diphosphate (GDP) (48,50). Additionally it has been shown that guanosine 5'-triphosphate (GTP) shows higher affinity to the mt-SSU than to the monosome (143). This has led to the hypothesis that nucleotide association is in some way linked to subunit association. However, in the yeast, mS29 is involved in an alternative subunit bridge contacting a mt-LSU mt-rRNA expansion segment. In the human mitoribosome, this association is mediated instead by two proteins of the mt-LSU mL46 and mL48 (Figure 25 (C)). Additionally, the bridge formed in the yeast is only transitory as it was only observed in Class B and not in Class A or C. The ambiguous density for the nucleotide in our maps meant that we were not able to conclusively assign a nucleotide, although a GDP has been modelled into the density. Thus, the role of mS29 in subunit association remains inconclusive and is likely to be more species dependent.

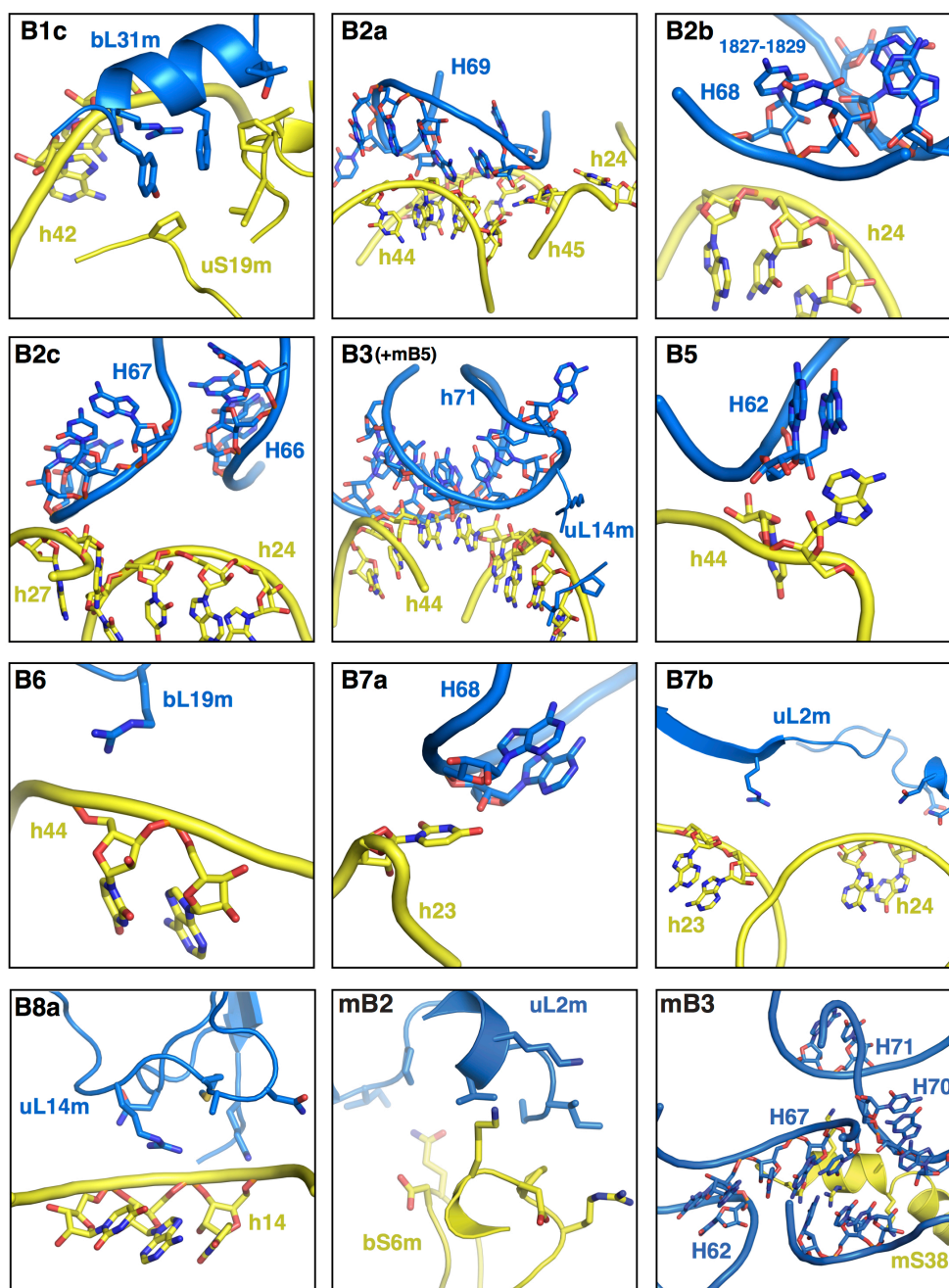


Figure 22 – Conserved Bridges (135). Molecular details of the intersubunit bridges of the yeast mitoribosome that are conserved with the bacterial ribosome or human mitoribosome. When the bridge is only conserved with the human mitoribosome the prefix ‘m’ is given.

Bridge	mt-SSU	mt-LSU
B1c	uS19m: 43-44, 69 h42: 1379-1380	bL31m: 97-98, 101, 104-105
B2a	h44: 1474-1477, 1586-1599 h45: 1609 h24: 858	H69: 1813-1817, 1819-1820
B2b	h24: 848-850	H68: 1744-1745 21S: 1827-1829
B2c	h24: 835-838 h27: 964-965	H66: 1698-1701 H67: 1738-1741
B3	h44: 1575-1577 1487-1490	H71: 1846-1852, 1859-1861 uL14m: 49-50, 65
B5	h44: 1496-1497	H62: 1656-1657
B6	h44: 1556-1557	bL19m: 155
B7a	h23: 768	H68: 1754-1755
B7b	h23: 778-779 h24: 838-839	uL2m: 312, 314-315 274
B8a	h14: 343-345	uL14m: 13, 48, 110, 112-114

Table 4 - Intersubunit-bridge compositions that are conserved with the bacterial ribosome (135).

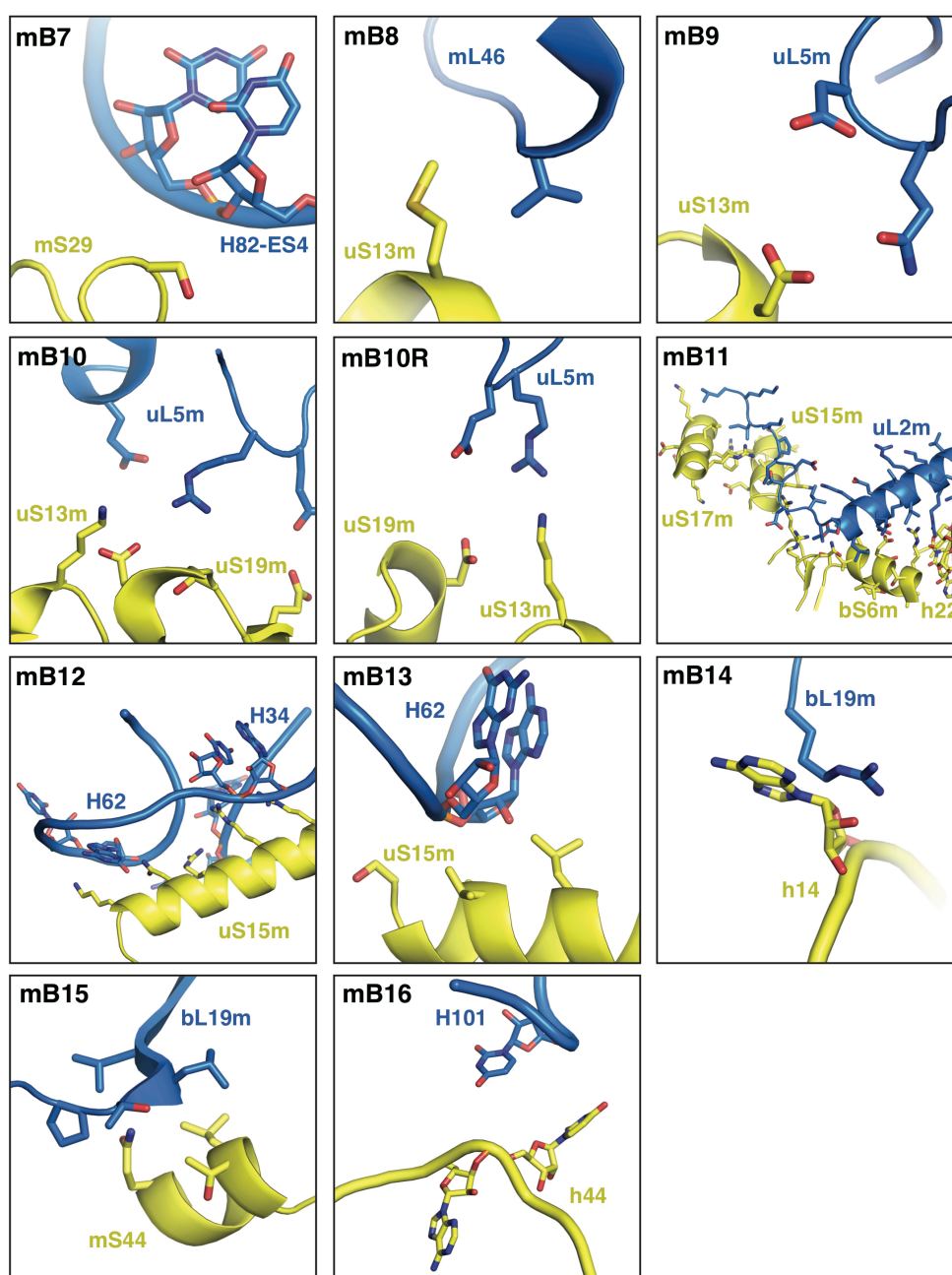


Figure 23 – Yeast mitoribosome specific bridges (135). Molecular details for yeast mitoribosome specific intersubunit bridges. Bridges mB7, mB8, mB9 and mB10R are only present in class B. The 8° rotation of the mt-SSU creates additional contacts with the central protuberance of the mt-LSU. Blue = mt-LSU. Yellow = mt-SSU.

mB2	bS6m: 87-90 57-58	uL2m: 228-229, 232-233 247-248
mB3	mS38: 101-102 105-106 109-110	H70: 1832-1834 H71: 1859-1860 H62: 1643-1644 H67: 1739-1741, 1874-1877,

mB7	mS29: 241	H82-ES4: 2389-2390
mB8	uS13m: 56	mL46: 72, 74
mB9	uS13m: 70	uL5: 253-254
mB10R	uS19m: 67 uS13m: 84	uL5: 218-219

mB10	uS19m: 63-67 uS13m: 84	uL5: 218-219, 241
mB11	uS17m: 105-111 uS15m: 77-84, 145 bS6m: 35-36, 74-83 h22:735-736	uL2m: 61-88
mB12	uS15m: 268, 272, 275, 279, 282-283	H42: 613-614 H62: 1639-1640, 1645-1648
mB13	uS13m: 34, 37-38, 41	H62: 1657-1658
mB14	h14:315	bL19m: 166
mB15	mS44: 72, 75-76	bL19m: 135-138
mB16	h44: 1510-1511	H101-ES: 3172

Table 5 - Intersubunit-bridge compositions coloured by conservation with the human mitoribosome have a red background (135). Bridges only found in class B have a teal background. Bridges only seen in the yeast have a yellow background.

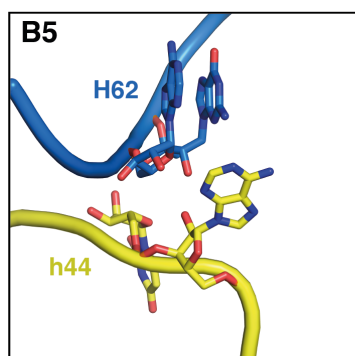
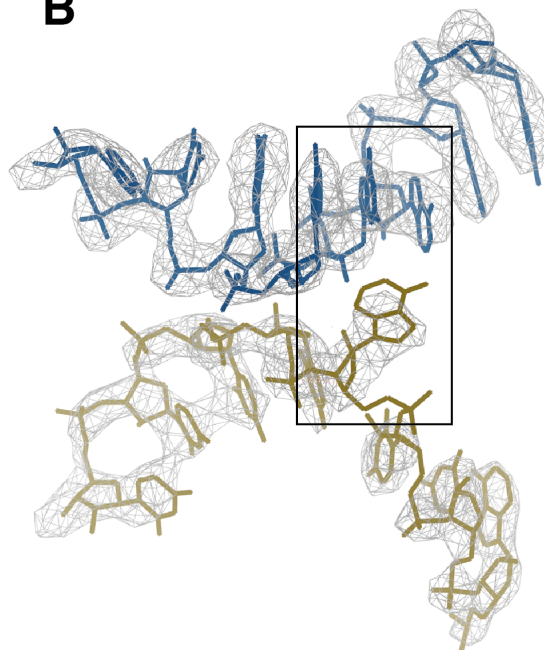
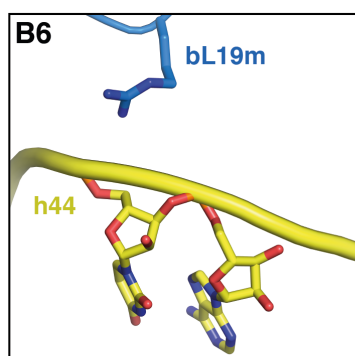
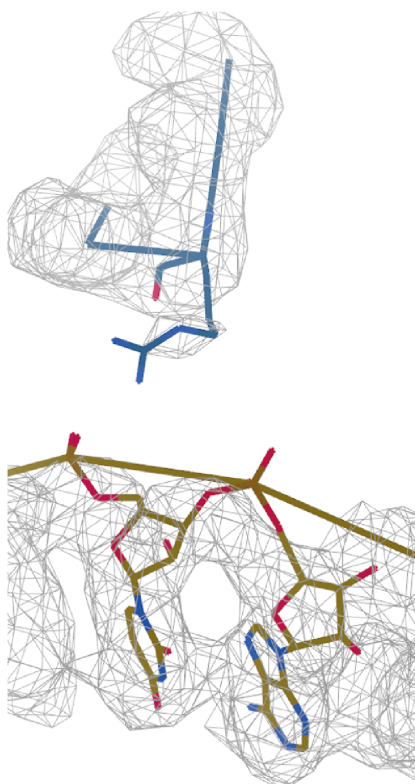
A**B****C****D**

Figure 24 – Figure showing representative density for bridges B5 and B6. (A) Bridge B5. (B) B5 representative density in boxed area. Surrounding density included. (C) Bridge B6. (D) B6 representative density shown.

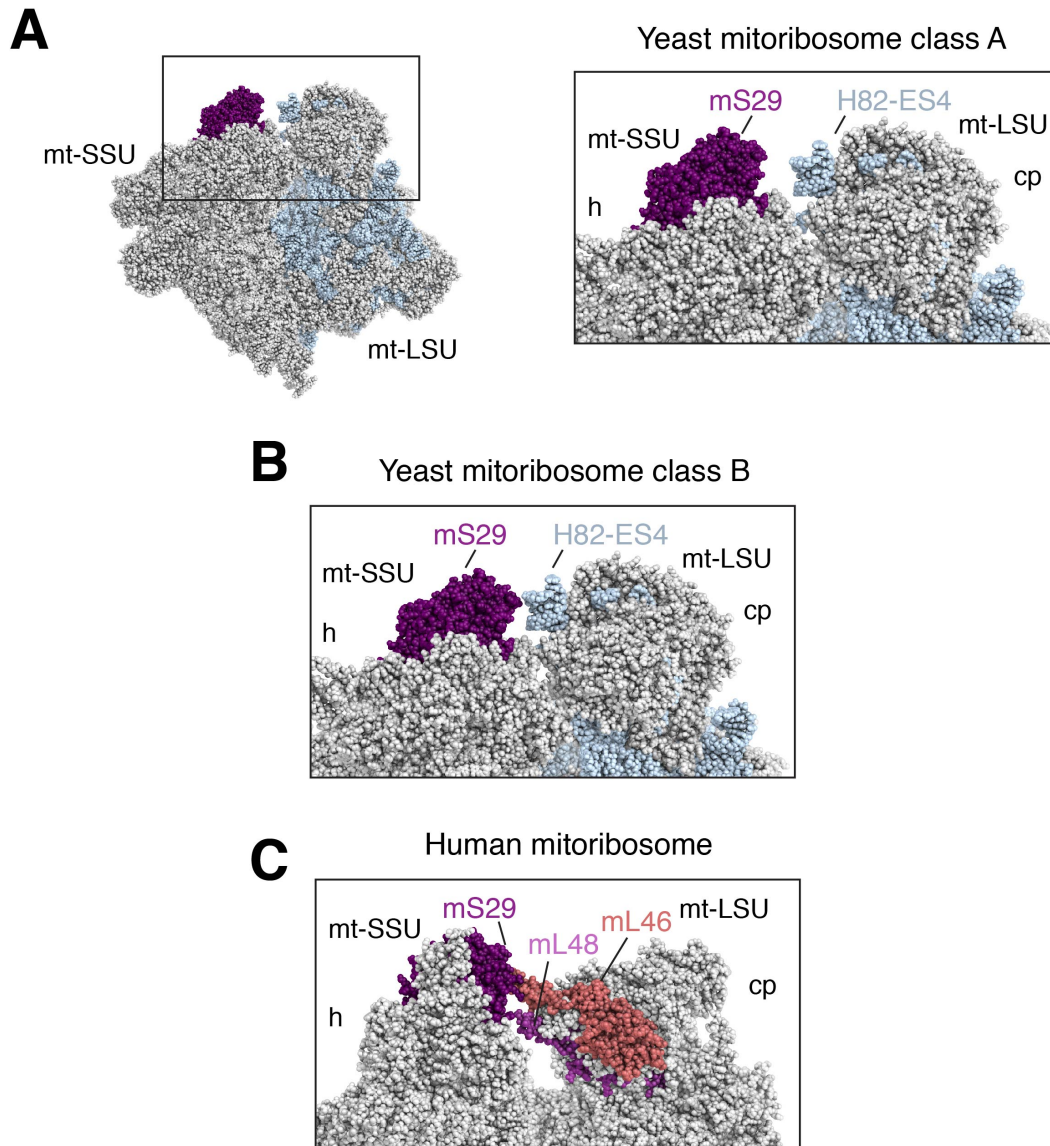


Figure 25 – Position of mS29 in the yeast and human mitoribosome. (A) Position of mS29 shown in purple in the yeast mitoribosome class A. Close up of the boxed section. (B) mS29 contacts H82-ES4 of the mt-LSU mt-rRNA in class B (bridge mB7) in the yeast mitoribosome due to an 8° rotation of the mt-SSU head. (C) The equivalent position in human mitoribosomes where contact with mS29 is mediated by mt-LSU proteins mL46 and mL48. Adapted from Desai *et al* (135). The figures represent PyMOL surface representations of the models.

2.3.4 Features of the yeast mt-SSU

Overall the presence of yeast mitoribosomal specific proteins and extensions appear congregated on the periphery of the mitoribosome. In particular two protuberances

on the lateral part of the mt-SSU body, which contribute to the distinct outline of the ribosome constitute, mS42, mS43 and mS47. mS42 and mS43 (RSM26 and MRP1 respectively) are both homologues of the iron/manganese binding superoxide dismutase, however the catalytic metal binding cores of each of these proteins have diverged in sequence rendering a likely inactive hydrophobic environment (Figure 26(A)(B)). They appear in the model as a hetero-dimer protuberance adjacent to proteins that surround the mt-mRNA exit tunnel.

mS47 (EHD3) forms the other protuberance and is a 3-hydroxyisobutyryl-CoA hydrolase, a member of the enoyl-CoA hydratase/isomerase family. There is good fitting homology with human 3-hydroxyisobutyryl-CoA hydrolase (PDB 3BPT), with an overlap of 240 residues (35% identity) to include the active site, which shows apparent conservation (Figure 26(A)(C)) (144). β -hydroxyisobutyryl-CoA hydrolase is a human mitochondrial protein, (albeit not part of the human mitoribosome) that has a role in valine catabolism and hereditary mitochondrial disease (145). EHD3 has been shown in the literature to catalyse hydrolysis of 3-hydroxyisobutyryl-CoA, part of the valine catabolic pathway, although its *in vivo* substrate is unknown (144). The EHD3 active site on the mitoribosome is a solvent exposed, large cavity, likely capable of accommodating its substrate, and retains a coordinating glutamate at position 172 (146). Active site residues are either preserved or show conservative mutations. We hypothesise that maintenance of such an environment suggests selective pressure. This would be consistent with the ability of EHD3, as part of the mitochondrial ribosome, to be an active enzyme and have potential functions beyond being an integral structural component. As it occupies a peripheral location on the mitoribosome, it is likely that its role in translation is non-essential which is consistent with viable null mutants. Its co-localisation with the mitoribosome may act as a link between translation and the catabolic state of the mitochondrion (144).

uS3m or Var1, the yeast mitoribosomal homolog of uS3 is the only soluble protein encoded by mt-DNA (147,148). Curiously, in contrast to nuclear encoded uS3m in other species, mitochondrially encoded yeast uS3m has a ~30% asparagine content (Figure 26(D)). The asparagines are largely represented on the solvent surface of the protein and is most likely a consequence of the mt-DNA having ~83% AT content.

Asparagine encoded by the AAT codon, is the only hydrophilic residue formed entirely of adenine and thymine nucleotides. Only 2 of the 127 asparagine residues are encoded by AAC the alternative codon.

In conclusion, the yeast mitoribosome specific proteins may not only serve as structural scaffolds for stabilisation but are potentially conveying further regulatory functions.

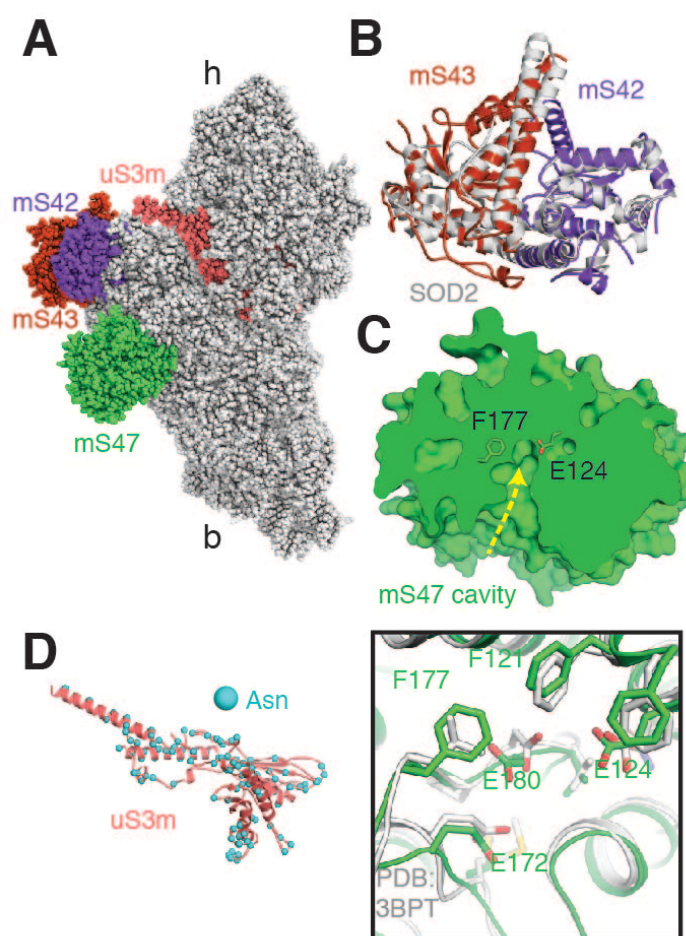


Figure 26 – Features of the yeast mt-SSU. (A) Structure of the mt-SSU with uS3m, mS42, mS43, and mS47 coloured. This figure represents the PyMOL surface representation of the model. (B) mS42 and mS43 form a heterodimer that structurally resembles the yeast mitochondrial superoxide dismutase dimer (PDB 3LSU). The image is related to (A) by a 90° rotation around the y-axis. (C) mS47, catalytic residues conserved with human β -hydroxyisobutyryl-CoA hydrolase (PDB 3BPT). The image is related to (A) by an approximate 180° rotation around the x-axis. (D) uS3m has multiple asparagine residues distributed on its surface. Amino acid residue abbreviations: E, Glu; F, Phe. Adapted from Desai *et al* (135).

2.3.5 The mt-mRNA channel

The path of the mt-mRNA in the yeast mitoribosome can be ascertained by tracing the path of bacterial mRNA from known structures (Figure 27) (149,150). The mRNA in bacteria has been shown to enter between the head and shoulder of the SSU through an entry site surrounded by uS3, uS4 and uS5. The proteins uS3 and uS4 are known to have helicase activity, unraveling the mRNA to a single stranded form required for translation (151). Additionally uS5 has a highly conserved glycine 28 in bacteria, which has been shown to be important for translation fidelity (152).

In the yeast model, the mt-mRNA entrance has been found to have the conserved elements of uS3m (Var1), uS4m (Nam9) and uS5m (Mrps5). Additionally, the mitochondrial specific protein mS35 (Rsm24) and the yeast mitochondrial specific protein mS45 (Mrps35) contribute to the architecture of the outer mt-mRNA entrance, but the large scale remodelling observed in the human mitoribosome is not seen (48). At the mitoribosomal A-site, mt-mRNA threads through the major groove made up of the upper part of helix 44. The decoding centre here, which mediates the interaction of the mt-mRNA and A-site mt-tRNA, is made up of the 15S nucleotides G644, A1584 and A1585 (G530, A1492, and A1493 in bacteria respectively) and a loop of uS12m (Mrps12). The mechanism of decoding appears to be preserved when compared with other ribosomes. The cryo-EM structure of the mammalian 55S mitoribosome with all 3 mt-tRNAs (A-, P-, and E- site) sites occupied confirms the conservation of the decoding centre, comparable to the here reported yeast mitoribosome structure (50). However, the yeast mitoribosome appears to be devoid of a P-site finger extending from the central protuberance to contact the A- and P-site mt-tRNAs as observed in the mammalian mitoribosome, part of an apparent co-evolution of the mammalian mitoribosome to accommodate mt- tRNAs that show considerable elbow region variability (48,50).

The mt-mRNA channel exit, in general, shows substantial remodelling compared to the early and intermediate parts of the mt-mRNA channel. In bacteria the 3' tail of the 16S rRNA contains an anti Shine-Dalgarno sequence that base pairs with the Shine-Dalgarno sequence of the 5'UTR of mRNA, facilitating start codon selection during initiation of translation. Yeast mitochondrial transcripts do not contain a

Shine-Dalgarno sequence and the 3' tail of the 16S mt-rRNA is additionally embedded within the mt-SSU and not accessible to the mt-mRNA. Clearly an alternative mechanism of translation initiation is needed. From our structure we observed a wide V-shaped canyon at the mt-mRNA exit channel (Figure 27). On one side of the canyon lies the heterodimer protuberance composed of mS42-mS43 (Rsm26-Mrp1). The other side is flanked by a series of mitoribosomal protein extensions to include bS6m (Mrp17), uS15m (Mrps28), uS17m (Mrps17), bS18m (Rsm18), and bS21m (Mrp21). Ribosome profiling data has shown that the yeast mitoribosome protects longer stretches of mt-mRNA during translation compare to cytosolic ribosomes (~38 nucleotides compared to 28 nucleotides) (114). This would be consistent with the mt-mRNA occupying the space created by the V-shaped canyon. In ~60% of our particles additional density was visible above the mt-mRNA exit canyon (Figure 27). We employed focussed classification with signal subtraction methods for the unknown density but were not able to resolve it further (Figure 29). A similarly placed density has previously been observed by cryo-electron tomography using subtomogram averaging of *in situ* yeast mitoribosomes (99). In our model the density contacts both walls of the V-shaped mt-mRNA exit canyon. bS1m (Mrp51), bS6m (Mrps17) and mS43 are contacted on one side while on the other side uS15m (Mrps28), uS17m (Mrps17) and mS26 (Pet123) are contacted. Evidence that the canyon is involved in translation initiation includes bS1m being shown to interact with the 5' UTRs of yeast mt-mRNAs, thereby showing similarity to bS1 in the bacterial system where this function is better understood (153,154). Pet122 is a known translational activator for cytochrome c oxidase subunit III and has been shown to functionally interact with the following components of the canyon, bS6m (Mrp17), mS26 (Pet123) and mS43 (Mrp1) (155-157). In the yeast mitochondrial translation system, translational activators are thought to be the factor unifying the 5' UTRs of mitochondrial transcripts, the mitoribosome and the inner mitochondrial membrane, and are found to be transcript specific (10,65). An absence of the Shine-Dalgarno sequence in yeast mt-mRNA transcripts necessitates an alternative method of aligning and priming the mt-mRNA for translation and defining the start codon. However, translational activators are also thought to have functions that extend to establishing tailored translational micro-environments. We hypothesise that the large V-shaped canyon

that is the mt-mRNA exit site acts as a platform capable of binding translational activators and that the density that was captured represents a heterogeneous mixture of such translational activators that co-purified with the monosome (Table 3).

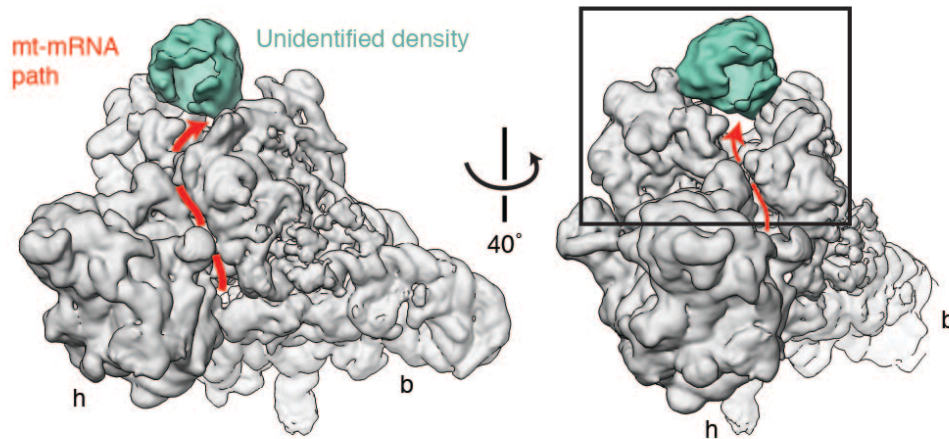
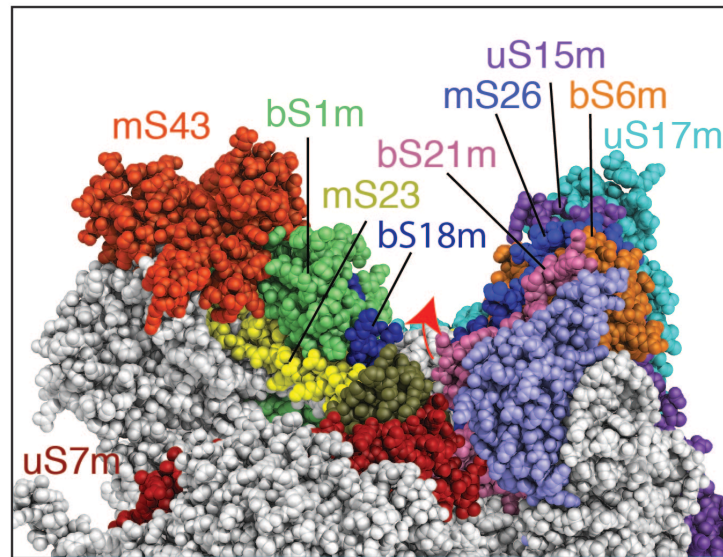


Figure 27 – The extended mt-mRNA exit channel. View from the mt-LSU. The path of the mt-mRNA channel curving around the neck of the yeast mt-SSU is shown by the red arrowed line. Additional unidentified density is located above a canyon at the mt-mRNA exit channel. h = head of SSU, b = body of SSU. Adapted from Desai *et al* (135).

A



B

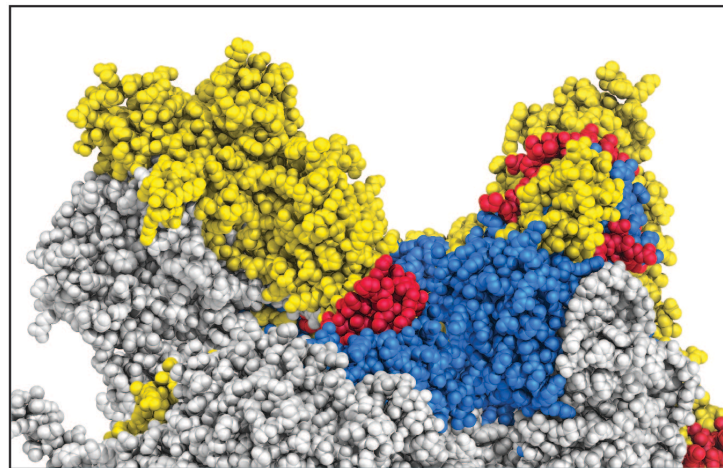


Figure 28 - (A) and (B) represent the boxed area in Figure 27. (B) The proteins that form the mt-mRNA exit canyon. (C) The canyon walls coloured by conservation. Yellow = yeast mitochondrial specific. Red = human and yeast mitochondrial specific. Blue = proteins homologous with the bacterial ribosome. Adapted from Desai *et al* (135). These figures represent the PyMOL surface representation of the model.

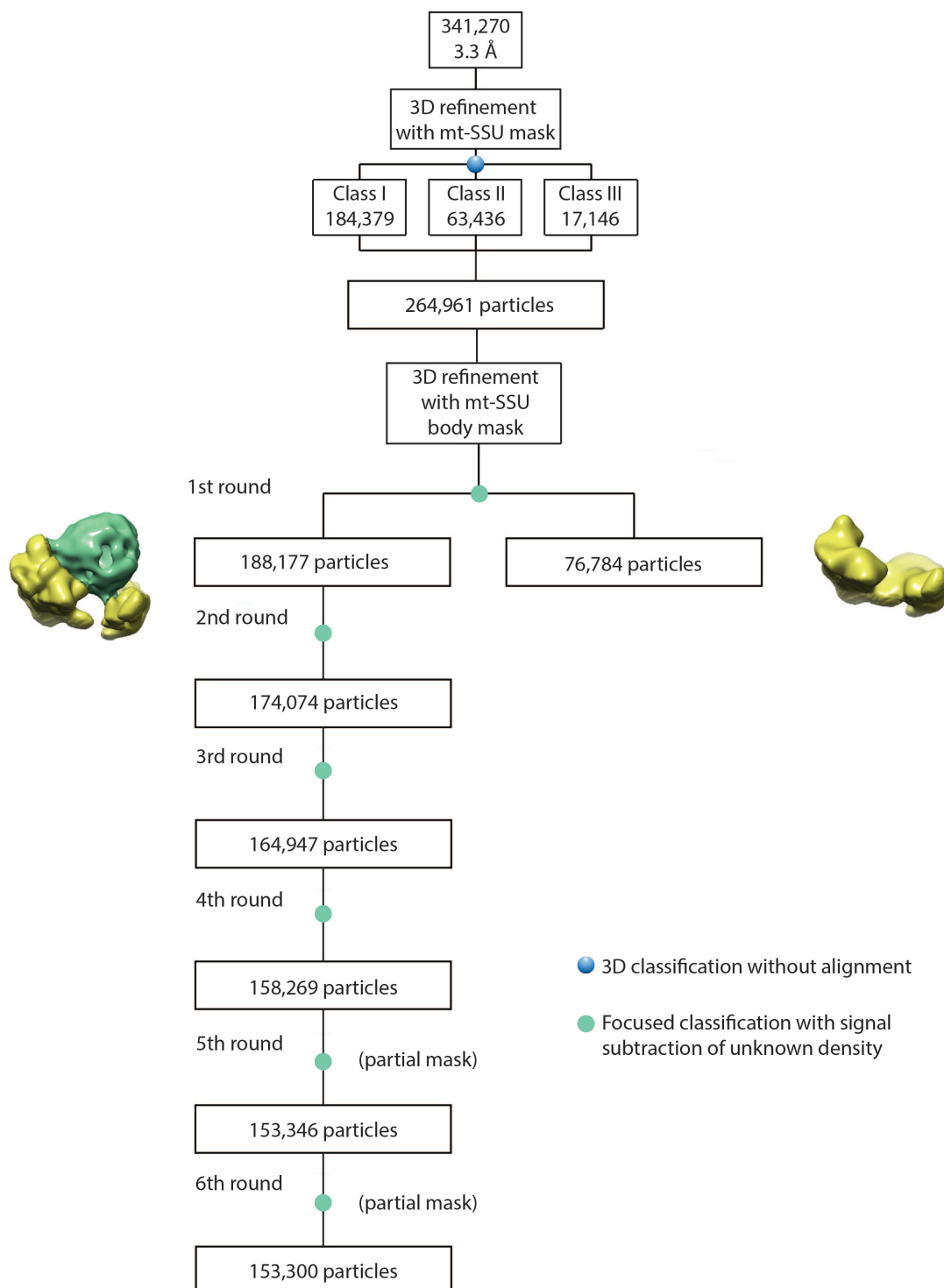


Figure 29 – RELION classification scheme for unknown density at the mt-mRNA exit channel (135). Multiple rounds of focussed classification with signal subtraction (FCwSS) was employed with the aim of separating out particles containing density at the mt-mRNA exit site. A partial mask was used to only mask a section of the unknown density.

2.4 Conclusions

Mitochondria, amongst their other cellular functions, universally carry out the function of aerobic respiration in eukaryotic cells. Their presence is a hallmark of eukaryotic cells and they are descended from a common bacterial endosymbiont ancestor. Yet, there are huge differences between mitochondria from different species and this feature is unsurprisingly reflected in the mitochondrial translation system. The translation requirements of mitoribosomes from different species vary between ~3-100 mitochondrially encoded genes. Yet for any number of genes the entire translation system must exist and be adapted to serve its purpose. The translation system itself in the mitochondrion has been found to have considerable species-specific specialisation. This is likely a response to different evolutionary pressures and a reflection of their different intra-cellular environments.

Translation specialisation has extended to the composition and structures of mitoribosomes. High resolution cryo-EM structures of mitoribosomes have begun to emerge since 2014 and have further posed questions as to the evolutionary cause and functional effects of mitoribosomes being so varied (*46,48-50,158*). From the structures of mitoribosomes from different species, they appear to have diverged from their ancestral bacterial ribosome, and additionally there are divergences between mitoribosomes from different species (Figure 20) (*48,50,135*). The variation in ribosomal RNA:protein ratio is between 2:1 in bacterial ribosomes, to 1:3 and even 1:6 in mitoribosomes, sometimes with comparable molecular weights between the ribosomes. This is also in stark contrast to the chloroplast organelle whose ribosome more closely resembles the bacterial ribosome with good conservation between rRNA and ribosomal proteins; only 6 plastid specific ribosomal proteins are observed (*159-161*).

In general, it has been observed that mitoribosomes have acquired novel proteins and protein extensions compared to bacterial ribosomes, and their mt-rRNA has undergone some remodelling at the peripheries to include shortening in mammalian mt-rRNA and areas of expansion in yeast mt-rRNA (*48,50,135*). It is hypothesised that mitoribosomes have evolved with an initial constructive phase in eukaryotic evolution of protein accumulation, followed by a reductive phase during metazoan

evolution which has resulted in reduction in length of mt-rRNA (45). As non metazoans, plants and fungi have retained the feature of organellar ribosomes being relatively rich in protein as well as in mt-rRNA (45,135,159-161). Further down the eukaryotic tree in metazoan evolution there was a subsequent reduction in mt-rRNA resulting in protein rich mitoribosomes with differing degrees of reduced mt-rRNA (45). Thus, the increase in mitoribosomal protein is not thought to be a reactionary to loss of mt-rRNA, as this happened before the loss of mt-rRNA which appears later in metazoan evolution (45). Interestingly, it is thought that the 5 macromolecular complexes of OXPHOS have evolved in parallel with mitoribosome with the same pattern of construction and reduction during their evolution accordingly (45).

This hypothesis of construction followed by reduction is evident in the mammalian 55S ribosome. Its mt-rRNA has gone through a reductive phase having ~ half the number of mt-rRNA nucleotides, deleted from the periphery while the core analogous to the bacterial is largely conserved (47-50). The protein fraction has gone through a constructive phase however, approximately doubling in mass compared to the bacteria (Figure 20). The mitochondrial specific protein elements largely occupy novel positions on the periphery of the mitoribosome and areas of mt-rRNA reduction remains empty giving it a porous structure (48,50). From our structure of the yeast mitoribosome we can see that the core is similar to the bacterial ribosome with the new mass of proteins and specific yeast protein elements distributed on the periphery (Figure 16). Mt-rRNA however, does display some areas of deletion, but areas of expansions leave an overall mt-rRNA size comparable to the bacterial ribosome (Figure 19). However, due to the increase in protein mass it has comparatively increased in molecular weight by ~30% (46).

It is unclear whether acquisition of these novel mitoribosomal proteins was part of 'non adaptive' evolution implying that they have become part of the mitoribosome and subsequently have evolved to fulfill a function, or whether they are a necessary evolutionary adaptation to fulfill this function, 'adaptive' evolution (45). The constructive phase is hypothesised to arise from slightly deleterious mutations in the mt-DNA encoding mt-rRNA (45,162). Slightly deleterious mutations are thought to cause structural destabilisation and act as the catalyst in the recruitment of new

protein components in early non-adaptive evolution. The pressure for accumulation of mutations in mt-DNA ('mutation pressure hypothesis') are thought to result from their inherent high rates of mutation, low recombination rates and small population numbers (162). In metazoan bilaterians, in particular, the mitochondrial genome mutation rates are thought to be 9-25 times more than their counter part nuclear genomes (163). This is thought to result in a mt-DNA deletion bias, thought to drive the metazoan reductive phase (45).

In our yeast mitoribosome structure, novel mitochondrial proteins are found to be constitutive components of the yeast mitoribosome as well as proteins homologous to other mitochondrial proteins with alternative functions. An example of this is mS47 (EHD3) a putatively active enzyme found at the peripheral location of the mitoribosome whose positioning may not be crucial to mitoribosome function but may serve a co-localisation purpose (Figure 26). Thus, addition of these proteins to the core structure of mitoribosomes may, in some instances, may confer an as yet unidentified advantage. In the yeast mitoribosome an adaptation on the polypeptide exit tunnel, remodelled to have a wider opening site, allows translation and release, into the matrix, of the soluble protein uS3m (Var1) (46). In this way the product to be translated may have had some influence on the structure of the mitoribosome, or the structure of the mitoribosome has allowed the retention of this function to produce a soluble product, which is lost in other mitoribosomes. Similarly, the remodelled V-shaped canyon on the yeast mt-SSU hypothesised to serve the purpose of a binding platform for translational activators, is a mechanism that is not employed in the bacterial or human mitochondrial translation system (Figure 27, Figure 28). Hence, this large mt-mRNA exit canyon is absent in the bacterial and human mitochondrial ribosome.

To conclude, the recent new cryo-EM structural information from mitoribosomes across different species, to include our yeast mitoribosome structure, has revealed the complexity of diversity present. It has particularly highlighted species specific-specialisation of translation and taken together it allows the appreciation of the fine differences and similarities between mitoribosomes. Our yeast mitoribosome

structure, in particular has shown specific features, making it unique compared to other ribosomes.

Overall, future structural studies of mitoribosomes from different species will be a valuable resource for the further construction of the evolution of mitoribosomes and mitochondrial translation to population and evolutionary biologists. The use of high resolution structural information to learn more about the function and assembly of mitoribosomes and the translational system is still in its infancy compared to studies on other ribosome. Further structural and biochemical studies are needed to elucidate the translational cycle in mitoribosomes together with its co-translational insertion of emerging polypeptides into the inner mitochondrial membrane. The control of translation, to include initiation, varies between species and further biochemical and high resolution data will aid in elucidating this finely tuned system in which products of two translational systems are required to work together.

2.5 Materials and Methods

All experimentation was done according to Desai *et al* (135).

2.5.1 Isolation of mitochondria

S. cerevisiae were grown aerobically in YPG media (1% yeast extract, 2% peptone, 3% glycerol) until an OD_{600nm} of 2 was reached. The cells were then centrifuged at 4,500 x *g* for 9 min. The pellet was then washed with pre-cooled distilled water and centrifuged for a further 15 minutes at 4,500 x *g*. The pellet was then weighed and resuspended in pre-warmed (30°C) DTT buffer (100 mM Tris-HCl pH 9.3, 10 mM DTT) and left for 30 min in a 30°C incubator to shake. This was followed by further pelleting by centrifugation at 3,500 x *g* for 10 minutes at room temperature. The pellet was resuspended in Zymolyase buffer (20 mM K₂HPO₄-HCl pH 7.4, 1.2 M sorbitol) to an optical density at OD_{600nm} of 0.6. 1 mg Zymolyase-100T (MP Biomedicals, LLC) was added per gram wet weight as measured earlier. The solution was shaken slowly in a 30°C incubator for 60 minutes. Centrifugation at 4,000 x *g* for 15 minutes at room temperature further pelleted the solution. The pellet was then resuspended in Zymolyase buffer and centrifuged again for another 15 minutes at 4,000 x *g*. The pellet was then resuspended in homogenisation buffer (20 mM Hepes-KOH pH 7.45, 0.6 M sorbitol, 1 mM EDTA) and the pellet homogenised using a glass Dounce homogeniser for 15 strokes. The cell debris and nuclei was separated from the mitochondrial fraction by centrifugation at 2000 x *g* for 20 min. The supernatant was collected and centrifugation for 20 minutes at 4500 x *g*. The collected supernatant was then centrifuged at 13,000 x *g* for 25 minutes. This allowed initial collection of the crude mitochondrial pellet. To further purify the crude mitochondria we employed ultracentrifugation using a 15-60% step sucrose gradient in SEM buffer (250 mM sucrose, 20 mM Hepes-KOH pH 7.5, 1 mM EDTA) at 141,000 x *g* for 1 hour. Mitochondrial samples were then pooled and flash frozen in liquid nitrogen and subsequently stored at -80°C.

2.5.2 Purification of mitoribosomes

3 volumes of Lysis buffer (25 mM Hepes-KOH pH 7.5, 100 mM KCl, 25 mM

MgOAc, 1.7% Triton X-100, 2 mM DTT) with added 0.0075% Cardiolipin and 100 μ g/ml chloramphenicol was added to sucrose gradient purified mitochondria and incubated for 10 minutes on ice. Centrifugation at 30,000 $\times g$ for 20 min pelleted out the membrane fraction. The supernatant was loaded onto a 1 M sucrose cushion in buffer: 20 mM Hepes- KOH pH 7.5, 100 mM KCl, 20 mM MgOAc, 1% Triton X-100, 2 mM DTT, 0.0075%cardiolipin, 0.05% β -DDM and 50 μ g/ml chloramphenicol. The sucrose cushion was centrifuged for 4 hours at 231,550 $\times g$. The pellet was resuspended in the same buffer as above (without Triton X-100) and loaded on 15%-30% sucrose gradient and run for 16 hours at 80,000 $\times g$. Mitoribosome fractions were collected. The sucrose was exchanged with the above buffer (without triton but with added 0.001% cardiolipin) using a 15 ml Vivaspin concentrator (30 kDa). An aliquot of the mitoribosome fraction was sent to mass spectrometry.

2.5.3 Electron microscopy

3 μ l aliquots of purified *S. cerevisiae* mitoribosomes (0.29mg/ml) were applied onto 30 second glow-discharged holey carbon grids (Quantifoil R2/2) coated with home-made continuous carbon (\sim 50 Å thick) at a concentration of \sim 97nM. The grids were blotted for 3.5 seconds using the ThermoFisher scientific Vitrobot™. The conditions were set to 100% ambient humidity and 4°C. The grids were flash frozen in liquid ethane and subsequently stored in liquid nitrogen. The grids were subsequently loaded onto an FEI Titan Krios 300kV electron microscope for data collection. The images were collected in linear mode using FEI's automated single particle acquisition software (EPU). The images were recorded on a back-thinned FEI Falcon II detector at a magnification of 104,478 (pixel size 1.34 Å). For each 1 second exposure, 17 movie frames were collected. Defocus values ranged from -1 to -3.3. Data was collected over a two day period.

2.5.4 Image Processing

MotionCorr was used to align the movie frames of each image, then contrast transfer function parameters were estimated using CTFFIND3(164,165). Particles were

picked using semi-automated particle picking with EMAN2 (136). Subsequent data processing was all performed in RELION and according to Figure 6 (121). A total of 468,858 particles were extracted from 2525 micrographs. 127,588 particles were discarded after 2D classification leaving a total of 341,270 particles. Initial refinement of the data set obtained a resolution of 3.3 Å. Particle polishing in RELION was subsequently used to correct beam-induced particle motion (121). The resolutions quoted were estimated during post-processing using the Fourier-shell-correlation (FSC) 0.143 criterion (166). We subsequently performed a refinement with a mt-SSU mask followed by 3D classifications without alignments. Further refinement of selected classes with soft masks applied over the mt-SSU head, mt-SSU body and mt-LSU was followed with subsequent 3D classification. The masks used were generated using RELION applying a soft edge. Prior to visualisation of the density maps, the modulation transfer function of the Falcon II detector was corrected and the maps sharpened by application of a negative B-factor, estimated using automated procedures (166). The best monosome class (class A) resolved to 3.3 Å. However, due to regions of this map being of insufficient local resolution to model build *de novo* we did further masked refinements with masks created for the mt-SSU head and body and the mt-LSU. The mt-SSU body elucidation went through an additional round of 3D classification. The final resolution of the mt-SSU head reached 3.5 Å, the mt-SSU body 3.3 Å and the mt-LSU 3.2 Å (Figure 8). Figure 9 highlights the improved resolution of these areas. Additionally, multiple rounds of focussed classification with signal subtraction (FCwSS) was performed on the unidentified density above the mRNA exit channel (Figure 29).

2.5.5 Model building

Model building was done in Coot using the generated masked maps which had improved local resolution (125). In regions of poor density Chimera was used to generate Gaussian-filtered maps to aid model building (167). The structure of the human mitoribosome (PDB 3J9M) and the *E. coli* ribosome (PDB 5IQR) were used as aids to building homologous proteins (48,137). This was done by first fitting these models into the yeast mt-SSU map using the Chimera 'fit in map' function (48,137,167). All further modelling was done in Coot (125). Yeast and human

mitoribosome homologous proteins were rigid body fitted in Coot to the density and the sequence and numbering modified to relate to the yeast mitoribosome. To aid this, the sequences from the two different species were aligned using ClustalOmega (168). Real space refinement in Coot was used to fit the new yeast model to the density, and extensions and insertions were built *de novo* (125). Torsion, planar-peptide, trans-peptide and Ramachandran restraints were all applied during model building (trans-peptide restraints removed to model clear *cis*-proline residues). In addition during real-space refinement of α -helices helical restraints were applied.

Poly(alanine) models were built into unknown sections of the map and searched against PDBefold, DALI and Backphyre(169-171). Sequences obtained from interpretation of the map were also estimated and searched against known sets of protein sequences using BLAST (172). In addition, mass spectrometry results were also used to identify yeast proteins without known ribosomal homologs. Seven new ribosomal proteins were named according to the established nomenclature starting with the lowest unassigned number and by increasing molecular weight (138).

The model of *E. coli* 16S rRNA (PDB 5IQR) was used as a template to build the 15S mt-rRNA (137). Secondary structure diagrams were used in conjunction with sequence alignment information using ClustalOmega to rigid body fit conserved section of the 16S rRNA to our map, with subsequent sequence mutation, re-numbering and *de novo* building (168,173). Each individual nucleotide was examined and fitted to the density using real-space refinement in Coot (125). Mt-rRNA helices were labelled when appropriate according to the equivalently numbered 16S *E. coli* helices.

The previously published model of the yeast mt-LSU was improved upon by docking the model into our map in Chimera using fit-in map then in Coot using real space refinement (46,125,167). Issues addressed were previous Ramachandran outliers, *de novo* model building of previously unbuilt areas and correction of any registry and numbering errors.

2.5.6 Model refinement and validation

Mitoribosomal protein secondary structure restraints were derived from the model using ProSMART (174). LIBG was used to obtain mt-rRNA basepair, stacking and sugar-pucker restraints (124). Reciprocal-space refinement in REFMAC v5.8, optimised for cryo-EM maps, was performed using the external restraints obtained as above (175). For each of the domains, mt-SSU body, head and mt-LSU, the models were refined against their respective masked maps. The refined individual domains were then combined and further refined against each of the 3 mitoribosome monosome classes. To maintain the stereochemistry obtained from the refinements with higher resolution maps, tighter restraints were applied to refinements against lower resolution maps. The subsequent fit of the model to the map density was quantified. The post-refinement model statistics obtained using REFMAC and Molprobit as shown in Table 1 on page 37 (176). Cross-validation against overfitting was performed (124). $FSC_{average}$ and CRef was used to evaluate the final model-to map fit, CRef being a measure of the resolution when the FSC between the map and refined model is 0.5 (124).

2.5.7 Figures

Figures were generated using PyMOL ('The PyMOL Molecular Graphics System', DeLano Scientific LLC) and Chimera (167). Estimations of local resolution was generated by ResMap and a map coloured by local resolution generated (177). The secondary structure diagram was modified from the Comparative RNA website and base pair information was ascertained from our model using DSSR (173,178). Using CytoScape we mapped a protein-protein interaction network of the mt-SSU in two-dimension to represent the three-dimension organization of the proteins. Molecular weights from UniProt were used to represent the nodal size, and protein-protein interfaces calculated from our map using PDBePISA is represented by edge thickness (169,179,180).

3 Co-translational insertion of mitochondrial membrane proteins

3.1 Scientific Aims

As all of the proteins translated by the human mitoribosome are membrane proteins, understanding the mechanism of co-translational membrane protein insertion is central to understanding mitoribosome translation. In mitochondria, the oxidase assembly (OXA) translocase plays a central role in membrane insertion of mitoribosome translated products *(181)*. OXA shows conservation with the prokaryotic protein insertase YidC, and is thought to retain functional similarity as an inner membrane protein insertase *(182,183)*. As yet there is no high resolution structure of the human mitoribosome attached to the OXA1L protein. Nor is there a high resolution structure of OXA1L in isolation. As a result, whether OXA1L acts as a monomer or a dimer is still in question, although there is some evidence that it may act as a dimer *(184)*. Cryo-electron tomography data has placed human mitoribosomes on the inner mitochondrial membrane but has lacked the appropriate resolution to determine the structure of the OXA1L translocase *(100)*. To this end, the aim was to trap the human mitoribosome in an actively translating state, capturing the ribosomal nascent chain as it traverses through the exit tunnel binding to its membrane bound translocase OXA1L (Figure 30). The structural elucidation of the interaction sites of OXA1L with the nascent chain, and the mitoribosome, will shed light on the unique characteristics of co-translation insertion of membrane proteins within the mitochondria.

Oxa1, initially identified in 1994, is a member of an evolutionarily conserved family, present in the inner membranes of bacteria (YidC), chloroplasts (Alb3), yeast mitochondrial (OXA1) and mammalian mitochondria (OXA1L) *(183,185-187)*. All members of this family contain a core hydrophobic domain of five transmembrane segments exhibiting the catalytic activity *(186)*. OXA has a C-terminal domain that resides in the mitochondrial matrix *(184)*. Mitochondrial OXA has also been found to be part of the 'OXA1 superfamily' with ER proteins Get1, EMC3 and TMC01 that are involved in membrane protein regulation *(109)*.

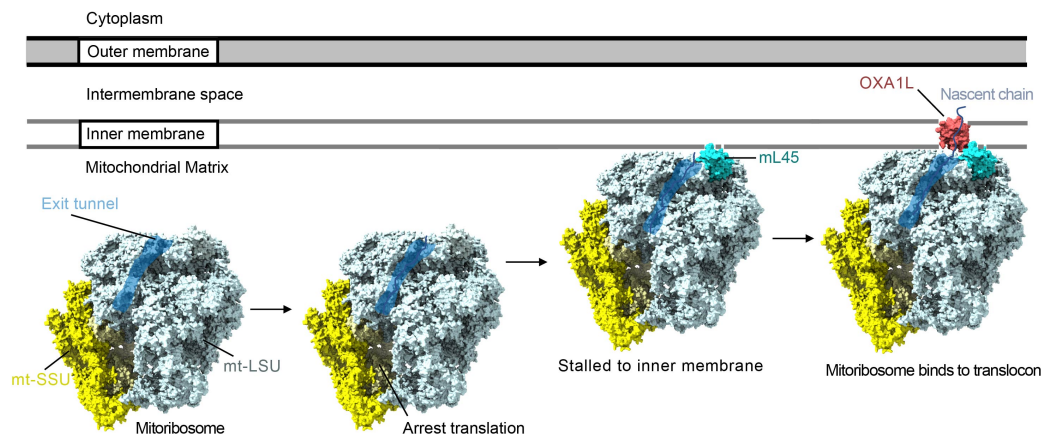


Figure 30 – Schematic for scientific aims. Adapted by Dr Hanting Yang from the structure of human mitochondrial ribosome (PDB 3J9M) (48). The mt-SSU and mt-LSU of the mitoribosome are coloured in yellow and light cyan respectively. The ribosomal exit tunnel is depicted in blue. Mitoribosomes bind to the inner membrane via mitoribosomal protein mL45 (cyan). The nascent chain is transferred to OXA1L (light red) for transport of the nascent peptide across for insertion into the mitochondrial inner membrane.

Most of the biochemical studies on Oxa1 have focussed on the role and function in the yeast model system. The yeast OXA1 protein (Oxa1p) has long been known to be important in the assembly of oxidative phosphorylation components such as complex IV and the ATP synthase complex (185,188). Initially, the yeast Oxa1p, was found to be important in the export of the N- and C-termini of Cox2p, a mitochondrially encoded component of complex IV (cytochrome c oxidase) (189). This was further confirmed by its ability to bind the nascent polypeptide chains of Cox2, and Cox3p, another component of complex IV (190).

In addition, through protein binding, Oxa1p was found to be crucial for export of the N-terminus of conservatively sorted proteins into the inner membrane, resembling bacterial N-tail export (190). It was later found that Oxa1p could also interact with the mitochondrially encoded complex IV components, Cox1p and Cox3p whose N-termini are retained in the matrix (191). This interaction was found to be prior to completion of protein synthesis, suggestive of co-translational insertion into the inner mitochondrial membrane (191). Others later observed that close proximity of

Oxa1p to ribosomes, in addition to improving membrane protein insertion, had a role in the coordinated assembly of complex IV which consists of both mitochondria and nuclear encoded proteins (192). Another important role of Oxa1p was found in the assembly of the mitochondrially encoded components, Atp6 and -9, of the F(1)F(o)-ATP synthase complex (193). Oxa1p is thought to interact with Atp9 in a post-translational manner not dependent on the Oxa1p C-terminus, and be important in the assembly of the Atp9-F(1)-subcomplex with Atp6 (193). Thus, it appears that OXA1 is not only important for co-translational insertion of membrane proteins, but has a more global and complex role in oxidative phosphorylation complex formation. In humans, complex I, IV and V assembly have been found to be perturbed by OXA1L deletion (194). In addition OXA1L genetic variants have been found to segregate with human disease with patients displaying variable phenotypes to include encephalopathy with hypotonia and developmental delay (194).

Interest in the co-translational insertion of polypeptide chain capabilities of OXA has led to work on the attachment of OXA to the mitoribosome. The C-terminal tail of Oxa1p resides in the mitochondrial matrix. Yeast Cox2, a product of the mitoribosome, was found to be inefficiently integrated into the mitochondrial membrane following deletion of the C-terminal end of Oxa1p (103). The C-terminal domain was found to be a ~100 amino acid element with the ability to bind mitoribosomes (103-105). Oxa1p has been found to crosslink to uL23m a protein of the yeast mitoribosome exit tunnel (104). Studies in human found the C-terminal domain of OXA1L able to crosslink to the mitoribosomal proteins uL13m, bL20m, bL28, mL48, mL49 and mL51 (105). However, these proteins have not been found to be proteins of the conserved polypeptide ring surrounding the exit tunnel or indeed on the exit tunnel surface of the mt-LSU (48,50).

Further studies have been done into the inner membrane contact points of the mitoribosome. The general surface of the mt-LSU attachment to the inner membrane appears, as expected, by cryo-electron tomography in the vicinity of the polypeptide exit tunnel (99,100). The specific protein/rRNA interactions of this appear different in the human and yeast systems. In the human mitoribosome, cryo-electron tomography data suggests that mL45 contacts the inner membrane (100). In the

yeast, the inner membrane contacts of the mitoribosome are mediated by the expansion segment 96 ES-1 and the Mba1, an adapter protein that is not a main constituent of the yeast mitoribosome (99). It is thought that mL45 and Mba1 have evolved to provide similar functions. Figure 31 shows a graphical representation of the likely membrane attachment (195). Thus, although information is available on the membrane attachment of mitoribosomes, the exact protein or mt-rRNA interactions of OXA to the mitoribosome remains to be revealed.

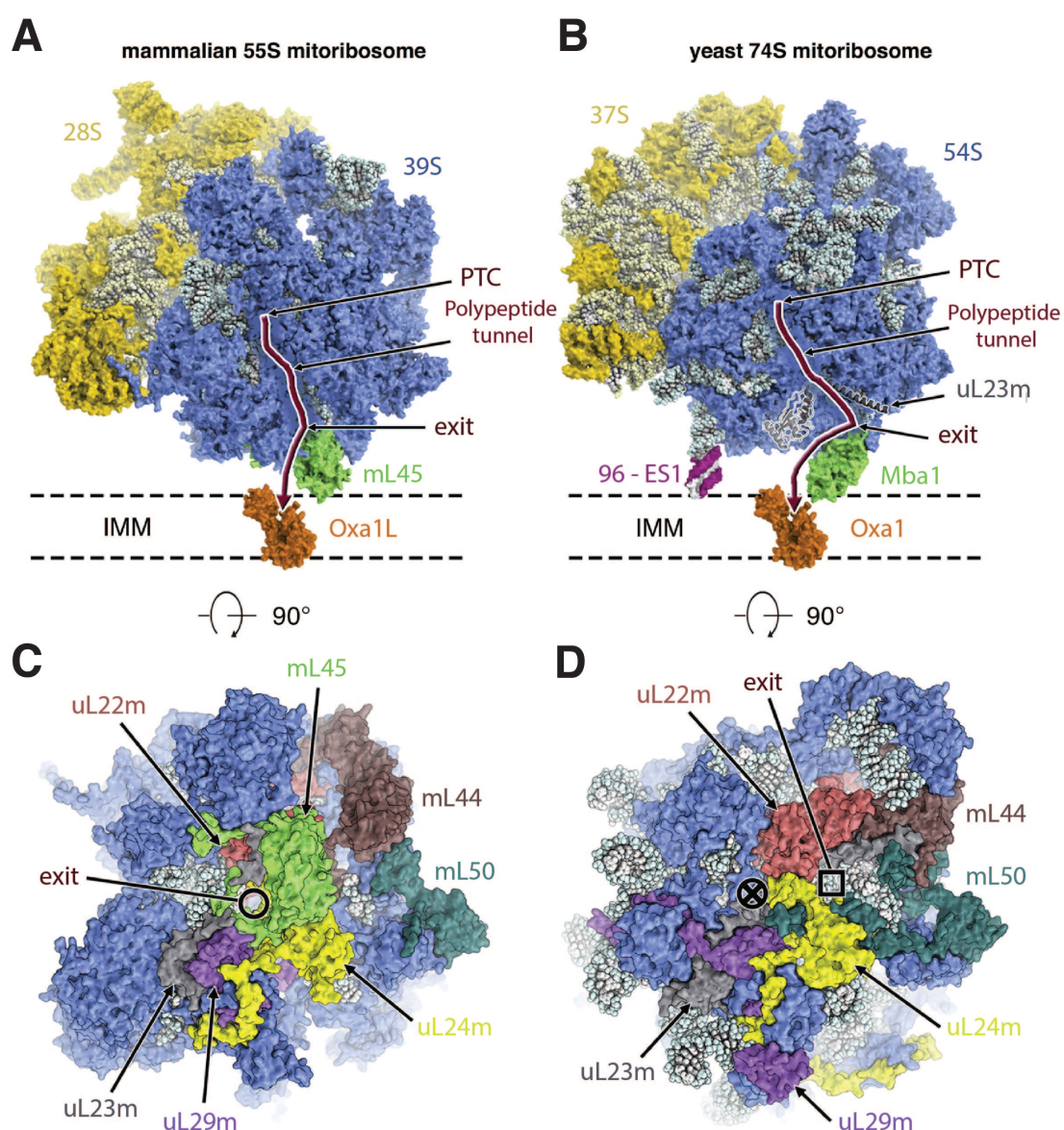


Figure 31 - Adapted from High-resolution structures of mitochondrial ribosomes and their functional implication. Bieri P, Greber BJ, Ban N. Curr Opin Struct Biol. 2018 Apr;49:44-53 (195). PTC = peptidyl transferase centre.

3.2 Strategy

To address the questions raised above regarding the mechanism of co-translational insertion of membrane proteins by the mitoribosomes, we aimed to determine the structure of OXA1L bound to actively translating mitoribosomes. Thus, the general strategy was to purify human mitoribosomes with the use of detergents and phospholipids to simulate an environment in which OXA1L would be stably bound to the mitoribosome. To ensure the binding of OXA1L in a physiologically relevant state, we aimed to trap, by using antibiotics, an actively translating mitoribosome with its polypeptide chain attached. We hypothesised that the presence of a polypeptide chain may help to increase the stability of the interaction of the mitoribosome with its translocase OXA1L, as well as being of biological interest. In addition, we also experimented with using the non-hydrolysable GTP analogues aimed at trapping GTPase translational factors to aid stalling. A panel of antibiotics was tested for effectiveness of stalling and trapping of OXA1L.

According to the endosymbiont hypothesis of mitochondrial origin, mitochondria were derived from their prokaryotic ancestor, and thus the basic mechanisms of a variety of mitochondrial activities are conserved with prokaryotes. Included in this conservation are many of the catalytic site targets between bacterial and mitochondrial ribosomes. This results in a number of bacterially targeted antimicrobials also affecting human mitoribosomes, inducing toxicity (196). Our strategy was to harness the ability of antibacterial agents to bind the mitoribosome to affect translation in the mitochondria. Assumptions were made that the antibiotics would affect mitoribosomes in a similar conformation. However, as yet no antimicrobials have been visualised structurally on the mitoribosome.

Examples of antibiotic classes known to bind the mitoribosome include oxazolidinone, amphenicols, aminoglycosides and tetracyclines. The oxazolidinone class of antibiotics, of which linezolid is a member, acts on the PTC of the large ribosomal subunit (197). Crystal structures have shown that linezolid binds to the bacterial A-site pocket of the PTC of the ribosome, which causes significant overlap with an A-site bound tRNA at the aminoacyl moiety (197). Linezolid has been found

clinically to cause life-threatening myelosuppression due to its effects on the mitoribosome.

Amphenicols, such as chloramphenicol, inhibit ribosomal elongation by its ability to inhibit the PTC and overlapping with the tRNA A-site binding on the 50S subunit. Unwanted effects of chloramphenicol on the mitochondrial ribosome include aplastic anaemia, bone marrow suppression and neurotoxicity *(198)*.

Aminoglycosides, such as streptomycin and gentamicin, act on the bacterial SSU and have also been found to interfere with mitochondrial protein synthesis. Streptomycin binds to the SSU and crystal structures have revealed that this causes local distortion favouring a near-cognate anticodon stem-loop analogue complex to a cognate stem-loop analogue complex *(199)*. The main side effect of streptomycin to mitoribosomes is sensorineural hearing loss, but toxicity appears to be dependent on host genetic susceptibilities, with mutations in mt-rRNA being one of the possible reasons *(92)*.

Tetracyclines have been found by x-ray crystallography to bind the 30S subunit, thus preventing binding of the anticodon step-loop of an A-site tRNA binding during elongation *(200)*. Tigecycline is a tetracycline derivative that has increased affinity and efficacy against the bacterial ribosome. The enhanced tigecycline action is through to be, via its 9-t-butylglycylamido moiety which forms a stacking interaction with nucleotide C1054 of the 16S rRNA increasing its binding affinity to the 30S and conferring an ability to overcome the tetracycline resistance protein TetM-mediated resistance *(201)*. TetM works by binding ribosomes stalled by tetracyclines and displacing the drug. Tigecycline has been found to be useful in inhibiting mitochondrial translation in acute myeloid leukaemia (AML) cell lines. Tigecycline has the ability to selectively kill leukaemic stem cells and clinical trials in AML are currently underway *(97,98)*. Additionally there is evidence that other cancer types may also be targets to include MYC driven lymphomas *(202)*.

The tuberactinomycin class of antibiotics is used in multiresistant tuberculosis. Viomycin belongs to this class and functions by inhibiting bacterial protein synthesis

by preventing EF-G mediated translocation on the ribosome (203). A common side effect of viomycin, owing to its effect on the mitochondrial ribosome, is ototoxicity (204). Viomycin has been found in crystal and EM structures to bind the bacterial ribosomal interface between helix 44 (h44) of the SSU and Helix 69 (H69) of the LSU (205-207). It is thought to compete with EF-G for binding to the pre-translocated ribosome and maintain it in this state, but it has also been found to stabilise EF-G binding in the pre-translocation state (203,207).

Thus, a variety of antibacterials are thought to effect mitoribosomes at different stages of the translation cycle. We aimed to use this side effect to stall the human mitoribosome. In the initial purifications, the antibiotics chloramphenicol, viomycin and tigecycline were selected bases on their different mechanisms of action as described above. In addition, non-hydrolysable GTP analogues were also added in some instances to aid mitoribosome stalling by trapping GTPases.

Once an effective stalling mechanism is ascertained the subsequent steps were to create an environment in solution in which the membrane protein OXA1L remained intact and bound to the mitoribosome. A biological membrane is a hydrophobic barrier between two aqueous compartments such as intermembrane space (IMS) and mitochondrial matrix. To create a membrane-like environment of OXA1L, we aimed to use different detergents and phospholipids. Detergents are amphiphilic compounds that typically have a polar hydrophilic head and a non-polar hydrophobic tail. Detergents are useful in the extraction and purification of membrane proteins (208). Their interaction with hydrophobic membrane proteins, provide a water-soluble environment for their manipulation. At high concentrations, the non-polar hydrophobic tails of the detergent can associate with the hydrophobic surfaces of membrane proteins. The polar hydrophilic regions are orientated towards the polar solute, forming stable micelles with hydrophobic cores. The concentration of detergent at which micelles start to form is called the critical micelle concentration (CMC). In general, detergents with low CMC values form micelles more easily and stably. Higher CMC values are associated with weaker binding, with these detergents being easier to remove by dialysis. The most commonly used detergents for membrane protein purification are non-ionic

detergents that are characterised by uncharged hydrophilic head groups (209). Examples of these detergents include maltosides, glucosides and polyoxyethylene glycols. These detergents work in a mild non-denaturing fashion to disrupt protein-lipid and lipid-lipid interactions, while preserving protein-protein interactions (209). In this way, detergents are able to disrupt the bilayer of phospholipid molecules in biological membranes. The general architecture of a lipid bilayer has the polar hydrophilic phosphoester head groups pointing outwards with the lipid acyl tails pointing towards each other creating a hydrophobic centre. Mitochondrial membranes are composed of an inner and outer membrane with varying lipid compositions. The inner membrane has been found to contain low levels of triglycerides and high levels of cardiolipin (CL) (210). Cardiolipin is an evolutionarily conserved dimeric phospholipid that is specifically found in this organelle (211). CL is found almost exclusively in mitochondrial membrane and constitutes approximately 15% of total mitochondrial phospholipids (212). In contrast, the outer membrane had higher levels of lipids to include phosphatidylcholine (PC), phosphatidylinositol (PI), plasmalogen and triglyceride (210). Our plans for purification included the use of the non-ionic detergents n-Dodecyl β -D-maltoside (β -DDM) and digitonin which have been used extensively in mitochondrial membrane protein purification. In addition, 18:1 cardiolipin (TOCL) has been used to try and mimic the inner membrane environment.

Thus, through the use of a variety of antibiotics, detergents, phospholipids and non-hydrolysable GTP analogues, we hoped to achieve our aim of trapping the human mitoribosome with its translocon OXA1L.

3.3 Results and Discussion

3.3.1 Purification 1 - Actively translating mitoribosome with mt-tRNA

Initial mitoribosome purification was done in the presence of the detergent β -DDM, cardiolipin (TOCL) and chloramphenicol. Mitochondria were lysed with 1.5% β -DDM containing lysis buffer. Additionally this lysis buffer contained 0.15mg/ml TOCL and 500 μ g/ml of chloramphenicol. The full protocol is described in the methods section (3.5.3).

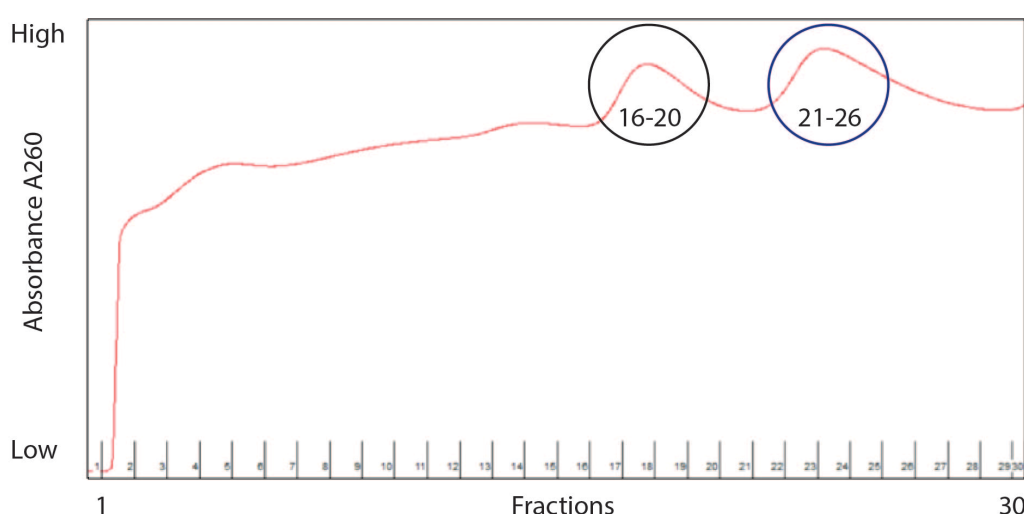


Figure 32 – Purification 1. 15-30% sucrose gradient fractions. Peak 1 was composed of fractions 16-20 and peak 2 composed of fractions 21-26 as circled.

Once the mitochondria were lysed, the mitoribosomes were crudely pelleted through a sucrose cushion and fractionated after ultracentrifugation on a 15-30% sucrose gradient (Figure 32). From the sucrose gradient fractionation, there were two visible A_{260} peaks, peak 1 and 2. These were thought to represent mitoribosomal subunits and monosomes, respectively. To assess the protein/RNA ratio, the ratio of the absorptions at 260nm and 280nm (A_{260}/A_{280}) were determined for each collected fraction using a nanodrop spectrophotometer.

The A_{260}/A_{280} ratio for pure RNA is ~ 2.0 and mammalian mitoribosomes are thought to be approximately 2:1 protein:RNA, in contrast to 1:2 for bacterial and eukaryotic

cytosolic ribosomes. Thus, mitoribosomes have a typical A_{260}/A_{280} of >1.6 . The A_{260}/A_{280} was found to be an average of 1.85 for fractions 16-20 (peak1) and 1.86 for fractions 21-26 (peak 2) that were pooled together. These two pooled fractions were concentrated by pelleting and resuspending in final buffer (3.5.3). The final measured A_{260}/A_{280} was 1.9 for both peaks and the samples were applied onto R2/2 copper grids coated with homemade continuous carbon.

In addition, the two peaks were sent for tandem mass spectrometry. The results of the tandem mass spectrometry showed an abundance of mitoribosomal proteins and in addition OXA1L was present in both the samples. However, there were also mitochondrial proteins not known to be related to mitochondrial translation found in the sample, probably a result of the mitoribosome purification being imperfect with contaminations. Mass spectrometry was therefore used as a tool to confirm that OXA1L was present in the sample but could not confirm that OXA1L was co-purifying exclusively with the mitoribosome. The results of the tandem mass spectrometry data from peak 2 is shown in Table 6.

To obtain biochemical evidence of OXA1L co-migrating with mitoribosomes, aliquots of both samples (peak 1 and 2) were tested for migration on a 10-15% sucrose gradient by centrifugation and collected as 11 equal fractions (Figure 33). The collected fractions were subjected to western blotting with primary antibodies against the mt-SSU protein mS27 (MRPS27) and OXA1L. Peak 1 showed signal for the mitoribosomal protein mS27 in fractions 3, 4 and faintly in 5, whilst the signal for OXA1L was seen in fractions 4, 5 and faintly in 6. Under these conditions from previous experiments in the lab and published data, fractions 4 and 5 are thought to represent monosomes with polysomes running in the heavier fractions of 6 onwards when intact ribosomes are loaded (213). Given that peak 1 was hypothesised to be a mixture of subunits it seems that fraction 3 could represent isolated mt-SSU, in which case it is expected that OXA1L would not be present. OXA1L being present in fractions 4, 5 and 6 are suggestive of an association with mt-LSU in isolation. It is expected that there is cross contamination between the two pooled peak fractions as consecutive fractions were taken. Peak 2 showed signal for mS27 predominantly in fractions 4,5,6 and 7 and signal for OXA1L in fractions 5,6 and 7. For mS27 a shift to

the heavier monosome fractions was consistent with peak 2 being hypothesised to be monosomes (or disomes). These fractions also had signal for OXA1L, suggesting that OXA1L and the mitoribosome are co-migrating together. What we couldn't conclude was the stoichiometry between the two.

mt-LSU		mt-SSU	Translationally Related proteins	Others	
uL1m	bL32m	bS1m	MALSU1	DLAT	HSPD1
uL2m	bL33m	uS2m	OXA1L	PDHB	CELA1
uL3m	bL35m	uS3m	TUFM(mtEF-Tu)	PDHA1	POLRMT
bL12m	mL41	uS10m		PDHX	CAD
uL13m	mL42	uS11m		GTPBP10	PRDX3
uL14m	mL43	uS12m		NDUFAB1	XRCC5
uL15m	mL44	uS14m		TFAM	TFB1M
uL16m	mL45	uS15m		DLST	CHCHD1
bL17m	mL46	bS16m		PHB2	GLUD1
uL18m	mL48	uS17m		DBT	POLG
bL19m	mL49	bS18m		SSBP1	HIST1H1C
bL20m	mL50	bS21m		MRM3	FTH1
bL21m	mL51	mS22		DLD	HSPA9
uL22m	mL52	mS23		PHB	ATAD3A
uL23m	mL53	mS25		NOA1	HK1
uL24m	mL54	mS26		HSPD1	HMGA2
bL27m	mL55	mS27		CELA1	TTN
bL28m	mL62	mS29		POLRMT	ABCC8
uL29m	mL66	mS31		DDX28	LAMC1
uL30m	mL65	mS33		AURKAIP1	MCAT
		mS34		ERLIN2	YBX1
		mS35		HADHA	POLG2
		mS39		HSPA5	DHX30
		mS40		C1QBP	BANF1
				HERC2	

Table 6 – Tandem mass spectrometry analysis. Purified human mitoribosomes from preparation 1, peak 2 were analysed.

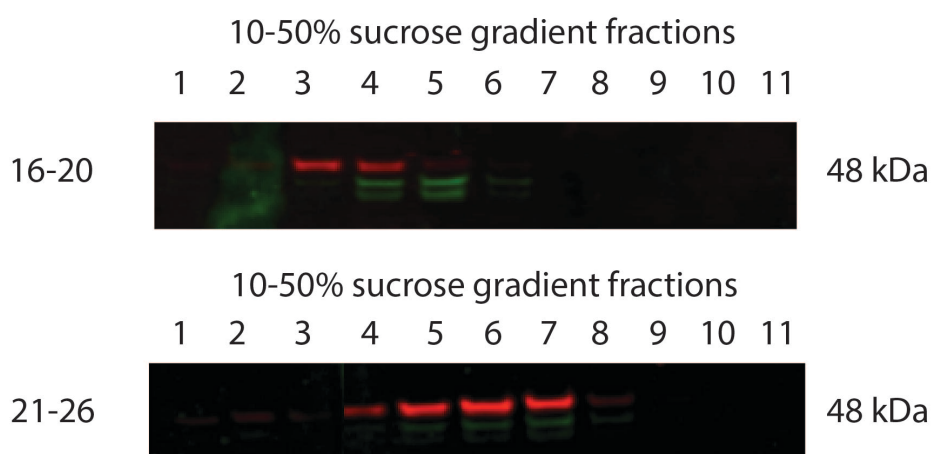


Figure 33 – Purification 1 - western blotting results. Pooled fractions 16-20 (peak 1) and 21-26 (peak 2) were run on a 10-50% sucrose gradient and 11 equal fractions collected. Red bands represent anti-mS27 signal. Green bands represent anti-OXA1L signal. Predicted band size of both antibodies was 48kDa.

Peak 2 was chosen for data collection as it likely represented whole monosomes and had signal for OXA1L in the corresponding fractions. The sample that was collected on was blotted for 5.5 seconds and collected in linear mode on the FEI Titan Krios using the Falcon III detector at a magnification of 75,000 and pixel size of 1.06 Å (Table 7 – page 139).

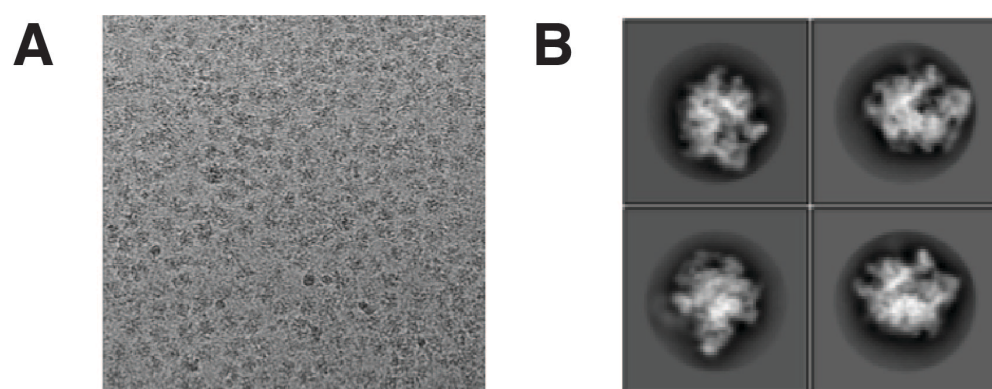


Figure 34 – Purification 1. (A) Representative micrograph. (B) Representative 2D classes.

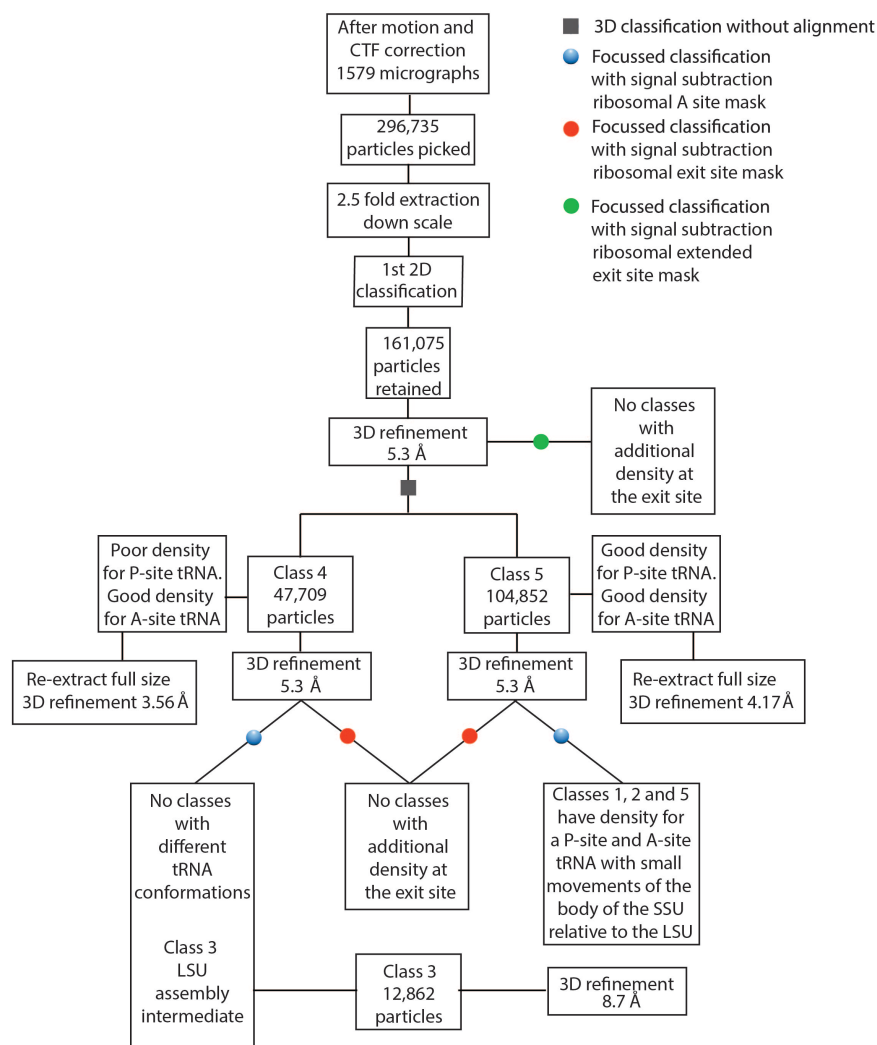


Figure 35 - Purification 1. RELION processing classification scheme.

A representative micrograph and representative 2D classes are shown in Figure 34. This sample was processed according to the scheme in Figure 35. The processing was done with 2.5X downsampled extracted particles to optimise the efficiency of processing. The initial first downsampled 3D refinement reached nyquist at 5.3 Å (Figure 36). In all cases, unless otherwise stated the unsharpened map is used in Chimera figure preparation for clarity. At this stage P-site and A-site mt-tRNA were clearly visible, coloured green and dark blue respectively. The P-site and A-site mt-tRNAs were docked in from the structure of the mammalian mitochondrial ribosome (PDB 5AJ4), confirming the presence of our map in the canonical state (50). In addition, density was visible for a nascent polypeptide chain at the mitoribosomal polypeptide exit site.

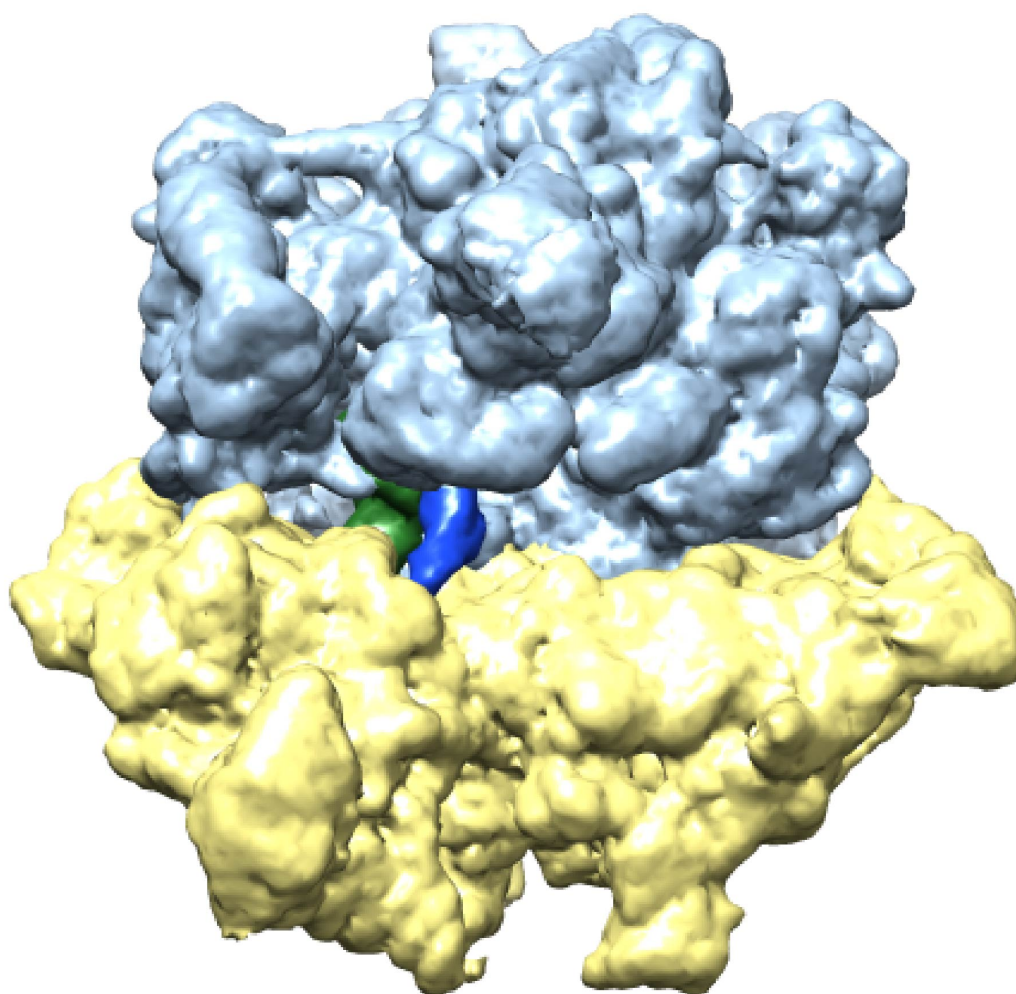


Figure 36 – Purification 1 – 5.3 Å unsharpened map. 1st 3D refinement. Light blue = mt-LSU, yellow = mt-SSU, green = P-site mt-tRNA and dark blue = A-site mt-tRNA

Unmasked 3D classification without alignments resulted in two predominant classes, class 4 consisting of 47,709 particles and class 5 consisting of 104,852 particles. After refinement both classes reached an initial resolution of 5.3 Å. Class 4 had clear density for an A-site mt-tRNA and an E-site mt-tRNA with relatively poor density for the P-site mt-tRNA (Figure 37). Class 5 had strong density for both the A- and P-site mt-tRNA with weak E site mt-tRNA density. It also had density for a nascent polypeptide chain visible at the polypeptide exit site. Between the two

classes there was evidence of a ratcheting movement of the mt-SSU relative to the mt-LSU, but both were still in the canonical state.

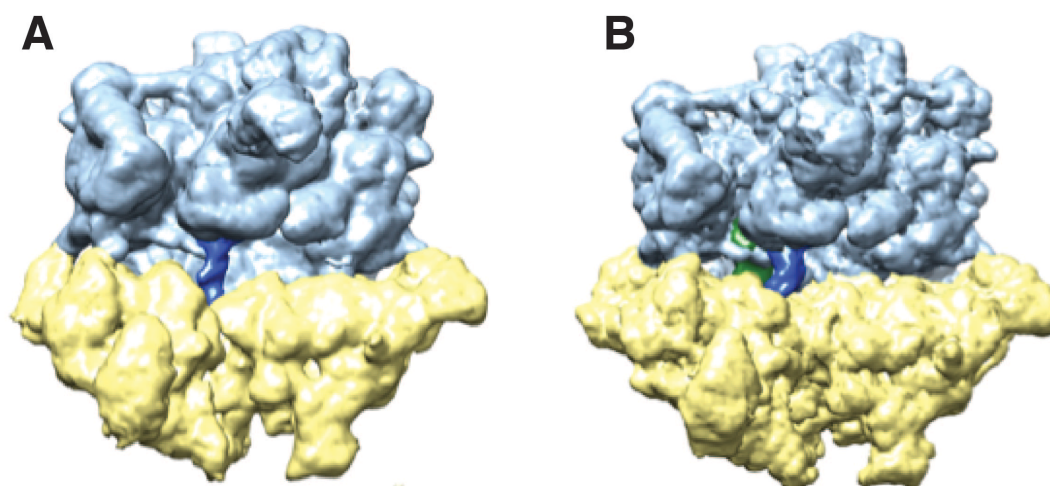


Figure 37 – Purification 1 - 5.3 Å unsharpened maps. (A) Class 4 from 1st 3D classification. (B) Class 5 from 1st 3D classification. Light blue = mt-LSU, yellow = mt-SSU, green = P-site mt-tRNA, Dark blue = A-site mt-tRNA.

Furthermore, for each of these classes, focussed classification with signal subtraction (FCwSS) on the A-site and the polypeptide exit site was performed. For the A-site FCwSS, the aim was to identify classes of actively translating mitoribosomes that might reveal density at the exit site. The polypeptide exit site mask FCwSS aimed to use the bigger pool of particles to try and extract mitoribosomes that may have a translocon attached, but may not necessarily be actively translating. Both of these strategies on the two above classes did not yield any density for the translocon OXA1L. Nor were there any classes with new conformations of mt-tRNA. However, A-site FCwSS on class 5 separated it into 3 classes that had both the P-site and A-site mt-tRNA, but with the mt-SSU in slightly different conformations compared to the mt-LSU. Additionally, the A-site FCwSS on class 4 revealed a mt-LSU subclass in class 3. This mt-LSU subclass was comparable to the late mt-LSU assembly intermediate seen by Brown *et al* (214). Further data collections on other sample preparations also revealed this class of mt-LSU and I will expand on the discussions surrounding this in the subsequent sections.

One concern was that the initial mask used for the exit tunnel FCwSS was too restrictive. Therefore FCwSS was re-performed encompassing the polypeptide exit site, the polypeptide tunnel and the P-site mt-tRNA in one continuous mask on the 1st 3D refinement. However, the results did not reveal any extra density for the translocon.

Thus, what we were able to conclude from this preparation was that under these conditions, we were able to extract actively translating mitoribosomes with a with P- and A- site mt-tRNAs and a polypeptide chain. It is hypothesised that the nascent chain presence may strengthen the interaction between the mitoribosome and translocon. However, despite having a density for a nascent chain we were not able to see a translocon attached. Class 4 and Class 5 were further re-extracted at full scale (pixel size of 1.06 Å) and after post processing reached resolutions of 3.56 Å and 4.17 Å respectively (Figure 37).

3.3.2 Purification 2 - Mitoribosome mt-LSU

While the method discussed above, yielded actively translating mitoribosomes, no OXA1L could be identified. Thus, an alternative strategy to stall the actively translating complex with bound OXA1L was employed in the hope that with a more stable stall OXA1L might have more chance of being bound. Since OXA1L did appear to co-migrate with monosomes according to our western blotting analysis for purification 1 (Figure 33), we decided to try using glutaraldehyde as a crosslinker in this next purification in the final step before grid making for cryo-EM. The aim was for OXA1L to be covalently crosslinked to the mitoribosome with the hope of strengthening its interaction. In addition to using a crosslinker, we also added the non-hydrolysable GTP analogue GDPNP (5'-Guanylyl imidodiphosphate). The aim was to trap GTPase translation factors such as mt-EF-Tu and mt-EG-G1 on the mitoribosome, thereby stalling the mitoribosome in a state of elongation. The general experimentation procedure remained the same as in purification 1 with the changes just discussed and the omission of chloramphenicol (3.5.3).

The UV absorbance profile at 260nm allowed the identification of 2 peaks, fractions 17-20 as peak 1 and fractions 23-27 as peak 2 (Figure 38). The fractions per pooled peak resulted in a final A_{260} of 8.7 and 8 respectively. Furthermore, aliquots of the individual fractions were analysed by western blotting with primary antibodies against OXA1L and mS27 (Figure 39).

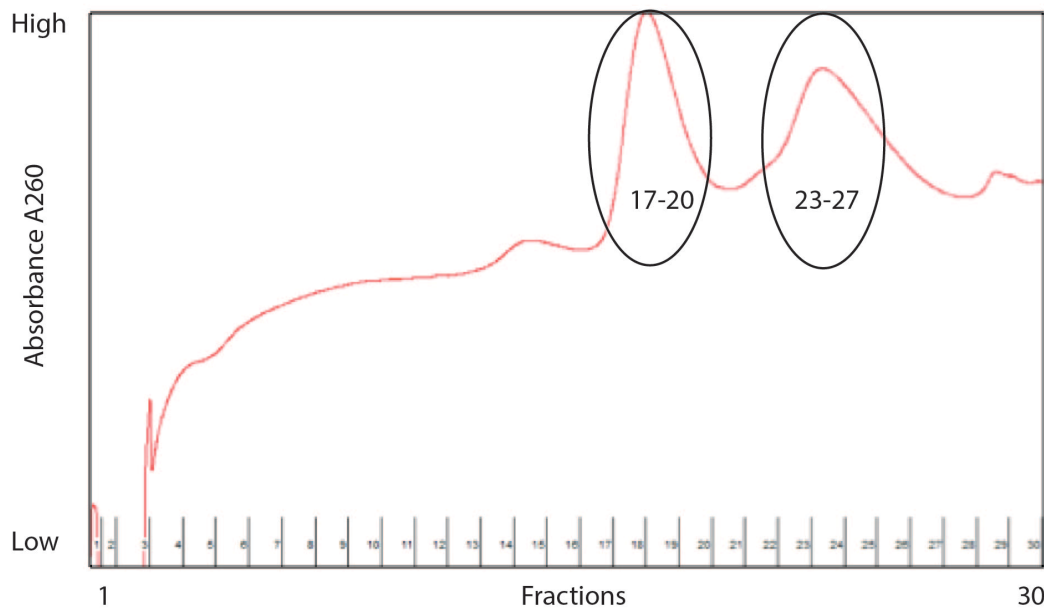


Figure 38 - Purification 2. 15-30% sucrose gradient fractions. Peak 1 composed of fractions 17-20 and peak 2 composed of fractions 23-27 highlighted.

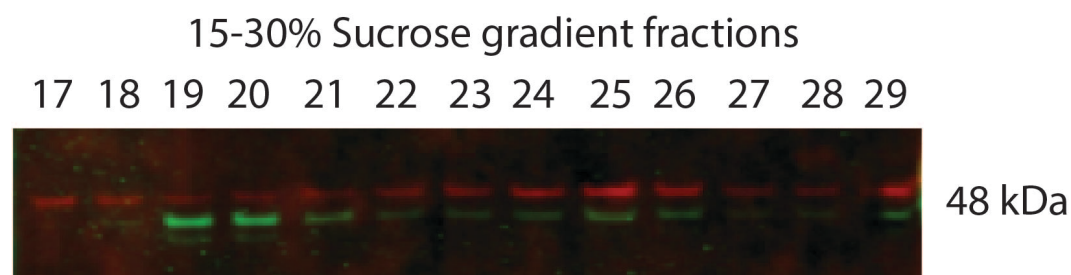


Figure 39 - Purification 2 western blotting results. Fractions 17-30 from the 15-30% sucrose gradient were run on a protein gel and subjected to western blotting. Red bands represent anti-mS27 signal. Green bands represent anti-OXA1L signal. Predicted band size of both antibodies is 48kDa.

The western blotting revealed signal for mS27 across the fractions shown 17-29, with increased signal around fraction 25 in the middle of peak 2 which we expected to be the monosome peak (Figure 39). There was corresponding widespread signal for OXA1L with increased signal in fractions 19-21 thought to represent the subunit fractions. There was also increased signal in fraction 25 corresponding to the monosome fraction. As the signal for OXA1L was strongest in the fractions constituting peak 1, the pooled fractions of peak 1, we decided to analyse this further by single particle cryo-electron microscopy data collection. We were curious to see if OXA1L was able to be trapped on the large mitoribosomal subunit alone. Mt-LSU bound OXA1L would deliver valuable information to supplement any monosome-OXA1L interactions seen and could guide a more directed search. The sample was collected on the FEI Titan Krios, Falcon III detector in linear mode at a magnification of 75,000, 1.06 Å pixel size. Full details are in the methods section in Table 7.

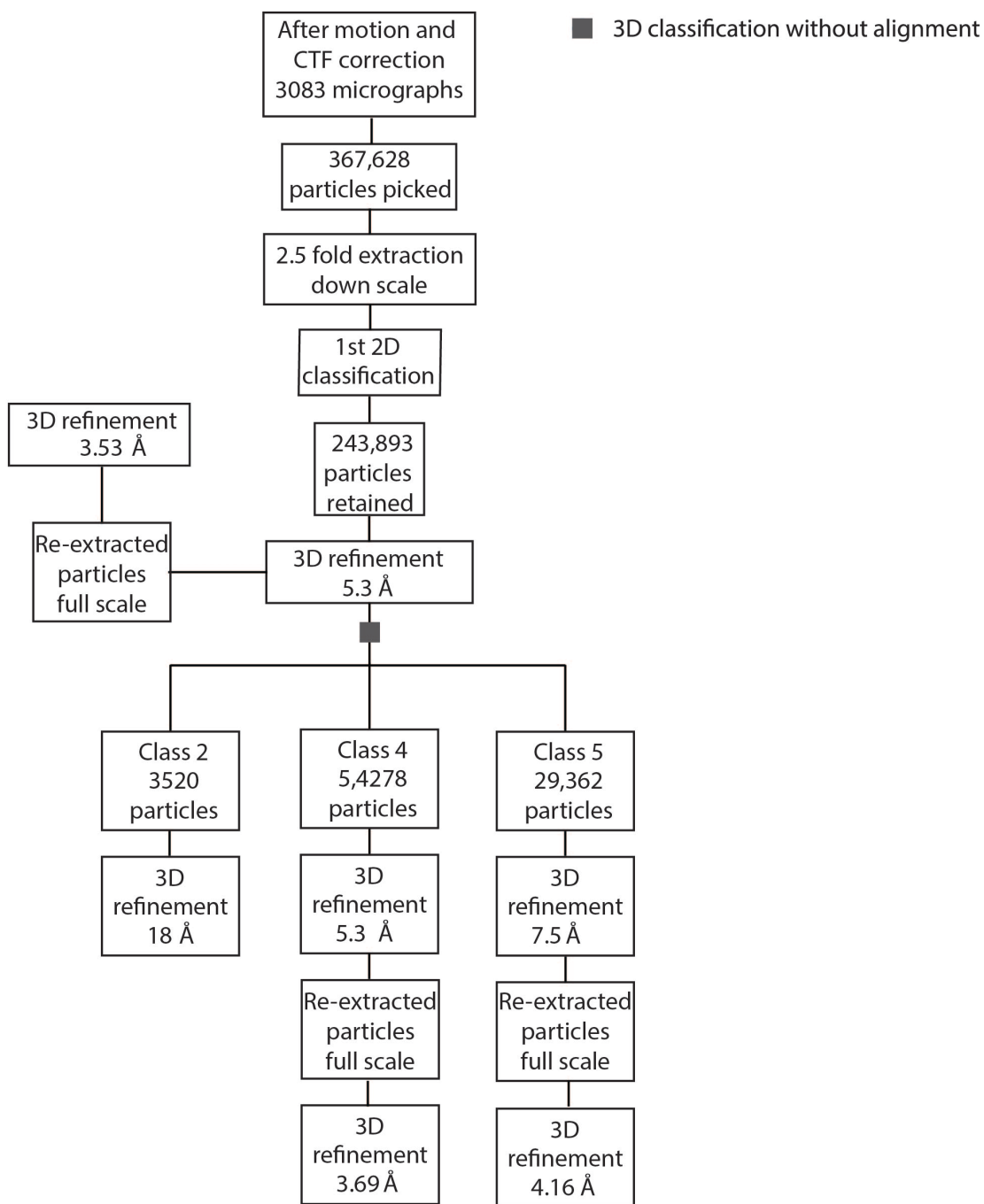


Figure 40 – Purification 2. RELION classification scheme.

The data was processed using RELION according to Figure 40. The particles were processed after 2.5X downscaling. After 2D classification there were 243,893 particles remaining. The initial 3D refinement went to nyqvist at 5.3 Å and revealed a map of the large subunit (Figure 41). However, it was evident that it was a variation of the mt-LSU, usually associated with the monosome, as there was an extra density that would clash in space with the platform of the body of the large subunit (Figure 42).

3D classification without alignment of the initial 3D refinement yielded 3 distinct classes. Class 2 consisted of the monosome but there were only 3,520 particles present at a resolution of 18 Å. Class 4 (54,278 particles) and class 5 (29,362) resolved to 5.3 Å and 7.5 Å respectively. Both class 4 and 5 represented the mt-LSU with the extra density with subtle differences in the subunit interface. All maps were examined for the presence of a nascent chain and OXA1L translocon at the polypeptide exit channel but neither of these was observed.

Though the presence of a nascent chain was unlikely from the onset due to the absence of a P-site mt-tRNA in any of the map, it remains possible that OXA1L could be associated to the mt-LSU in the absence of a nascent chain (although we hypothesise that the association would be strongest in the presence of a nascent chain).

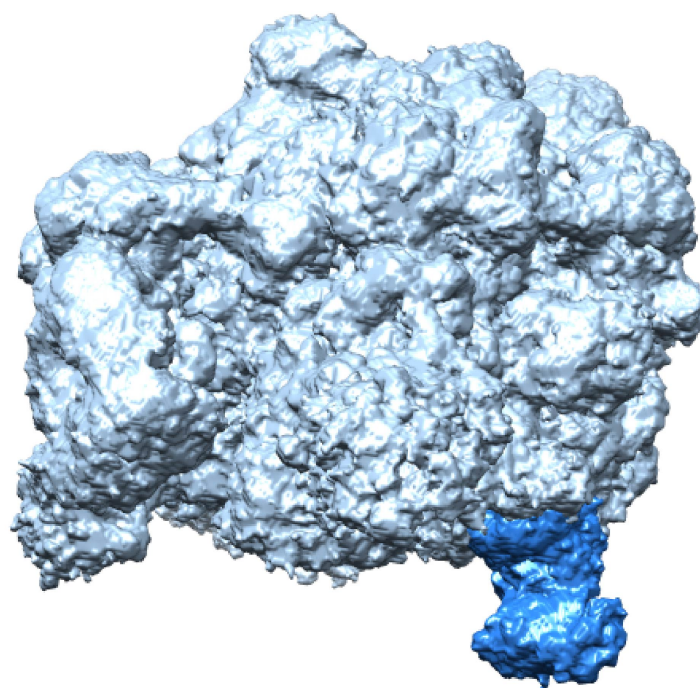


Figure 41 – Purification 2 - 5.3 Å unsharpened map. 1st 3D refine. Mt-LSU late assembly intermediate. Light blue = mt-LSU. Dark blue = MALSU1-L0R8F8-mt-ACP module.

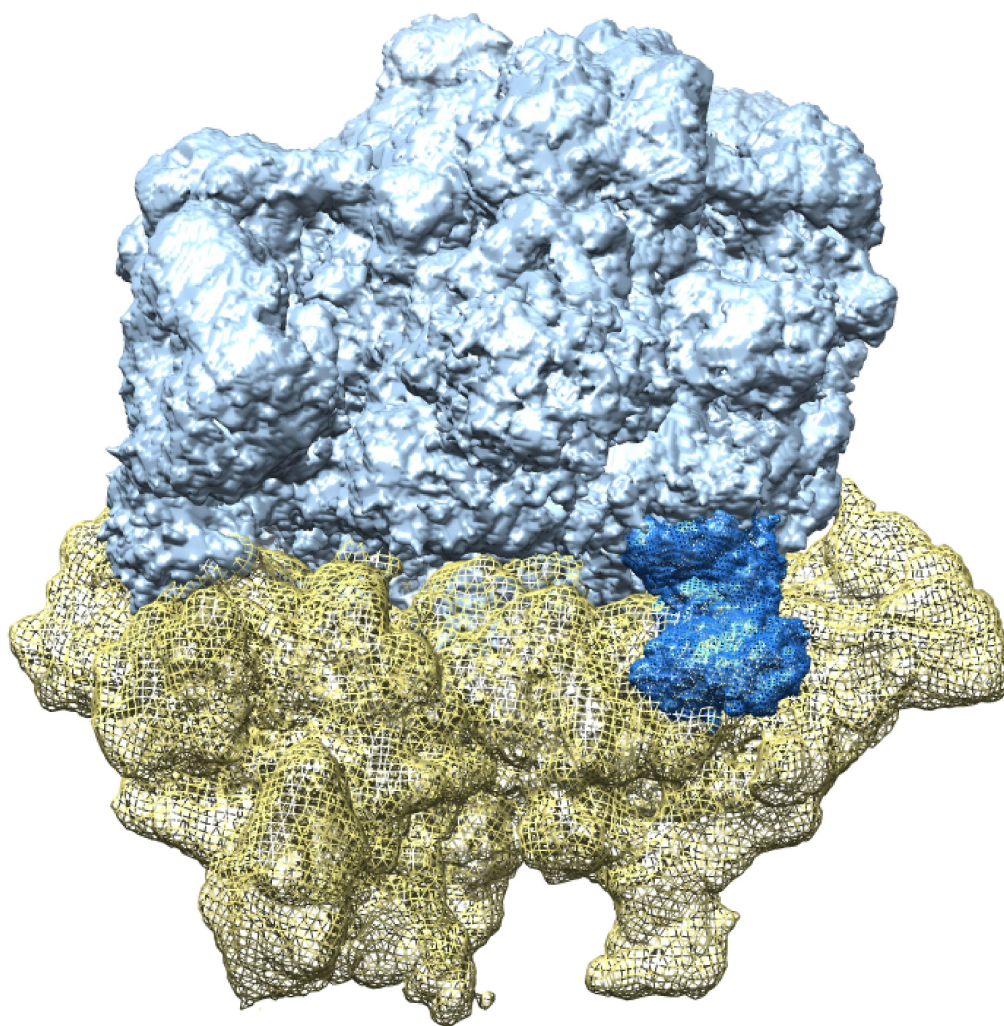


Figure 42 – Purification 2. 1st 3D refinement - 5.3 Å unsharpened map. Mt-LSU late assembly intermediate with mt-SSU model docked to demonstrate clash with new module. Light blue = mt-LSU. Dark blue = MALSU1-L0R8F8-mt-ACP module. Yellow mesh = mt-SSU.

Modelled structures corresponding to the class 4 and 5 maps of the mt-LSU have recently been published (214). In this paper the structures were identified as 2 late stage assembly intermediates of the mt-LSU and have been determined to ~3.0 Å. In general, mitoribosome assembly is a finely tuned process involving proteins and rRNA encoded by 2 different genomes, nuclear and mitochondrial respectively (90). Known assembly factors with bacterial homologues are thought to mediate this effort with the help of at present unknown axillary factors (90). It is thought that in general mitoribosomal proteins are recruited to the folding mt-rRNA in a dynamic process featuring active remodelling of the mt-rRNA (215).

In the published structure they identified the same additional density adjacent to uL14m that we observed, in their 2 classes. Their 2 classes composed of one showing the interfacial region adopting a fully folded mt-rRNA at 3.1 Å resolution, with the other class at 3.0 Å resolution seemingly lacking interfacial mt-rRNA explained by multiple adopted conformations of the mt-rRNA rather than cleavage (214). The lacking helices that could not be placed are H34–H35, H65, H67–H71, and H89–H93 which comprise the peptidyl transferase centre. All mt-LSU proteins were found to be present except bL36m in the unfolded interfacial mt-rRNA class. bL36m functions in stabilisation of interactions of H89, H91 and H97 and has been found to be one of the last recruited proteins in bacterial ribosome biogenesis (216,217). This suggests that recruitment of bL36m and folding of the peptidyl transferase centre occurs late in mt-LSU biogenesis.

The extra density adjacent to uL14m was found to be mitochondrial assembly of ribosomal large subunit 1 (MALSU1) a member of the RsfS family of proteins known to be associated with mitoribosomal assembly, along with mt-ACP and L0R8F8 (Figure 43) (214).

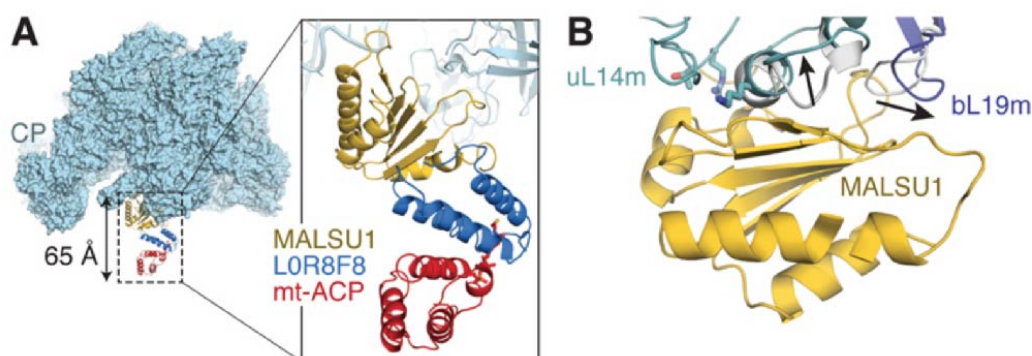


Figure 43 – Taken from (214). (A) Shows the MALSU1-LOR8F-mt-ACP module in context of the mt-LSU in light blue. (B) Shows MALSU1 adjacent to uL14m and bL19m.

Both mt-ACP and the LYR-motif protein LOR8F8 were found to be novel components of mitoribosome assembly. It is thought that they may link fatty acid and iron-sulphur synthesis to mitoribosome assembly. However, a probable function of the

MALSU1–L0R8F8–mt-ACP module would be to prevent binding of the mt-SSU to the mt-LSU. MALSU1 on its own would be insufficient to fulfil this function, owing to deletions of the mt-SSU compared to the bacterial ribosome, including loss of h14. Therefore, additional proteins have joined the module. The module would cause clashes with h5, h15 and the N-terminus of mS26 in the mt-SSU. The observation that the module is present in both the unfolded and folded mt-rRNA conformations that we have also observed in our structure, suggests that loss of the module is not directly linked to rRNA folding. We were able to dock the published model from the paper into our maps. MALSU1, L0R8F8 and mt-ACP all fit our density well (Figure 44). On examination of the intersubunit interface class 4 is most consistent with the folded interface previously observed (EMD-3842) and class 5 with the unfolded interface (EMD-3843) (214).

Thus, this purification and data collection of the mt-LSU assembly intermediate did not reveal any density for OXA1L. Of note we did not observe any mt-LSU species that did not have the extra density adjacent to uL14m. As the assembly intermediate has not partaken in any rounds of translation and therefore co-translational insertion it is not entirely unexpected that OXA1L was not visualised. However, western blotting analysis did show evidence of OXA1L in the subunit peak. Possible explanations for this include the mt-LSU assembly intermediate being tethered to the membrane to OXA1L during assembly. We decided not to collect on the monosome peak of this purification, as the signal for OXA1L was weaker in this peak than for the subunit peak.

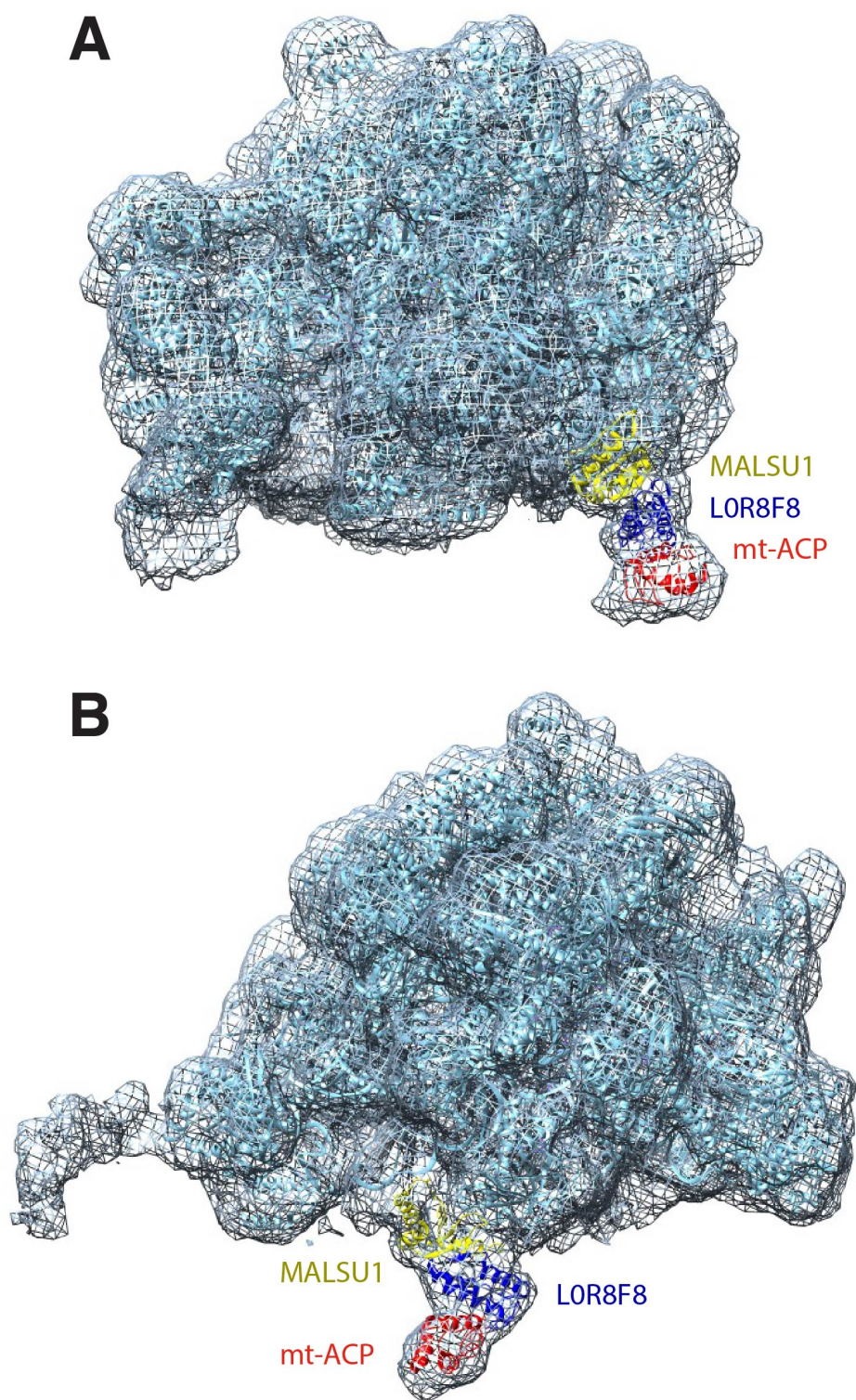


Figure 44 - Purification 2. Mt-LSU late assembly intermediate 1st 3D refinement. The assembly proteins are shown in colour (PDB 500M) (214). (A) Front view. (B) Side view.

3.3.3 Purification 3 – P-site mt-tRNA and density in factor site

To try to improve upon the stalling of actively translating mitoribosomes we also utilised the antibiotic viomycin and GDPNP with the aim of specifically trapping the GTPase mt-EF-G. The aim was to try and explore another method by which a mt-tRNA could be stably trapped in the P-site. We also attempted to actively stimulate mitoribosome translation in the mitochondria before stalling. This was attempted by heating the mitochondria preparation to 32°C for 5 minutes in a water bath with addition of 100mM KCl, 5mM Mg(OAc)₂, 0.1mM amino acid mix, 0.02mM methionine and 1mg/ml of bovine serum albumin. After 5 minutes incubation, 0.5mM viomycin and 0.5mM GDPNP were added to arrest translation along with 1mM Mg(OAc)₂ for a further 5 minutes at room temperature. Another modification that was made to the sample preparation compared with purification 1 was the omission of the overnight sucrose gradient step. We omitted this step to minimise the time and steps between mitochondrial lysis and grid preparations. Our previous western blotting results had shown OXA1L and the mitoribosome to be co-migrating after the sucrose gradient step but as we are unable to work out the stoichiometry there may be some dissociation during this step that we were unable to quantify. Therefore, mitochondria were lysed and after the initial centrifugation step to remove debris the mitoribosomes were pelleted through a sucrose cushion. At this stage the resuspended mitoribosome samples were used for grid preparation. An aliquot of the sample was further run on a 10-50% sucrose gradient and subjected to western blotting with antibodies against OXA1L and mS27. Our western blotting results showed migration of OXA1L with the ribosomal protein across fractions 2-11 with the strongest signal for both antibodies being in fractions 6-10 (Figure 45). In addition the intensities of the two bands appear to follow a corresponding pattern across the fractions, suggesting co-migration of OXA1L and the mitoribosome.

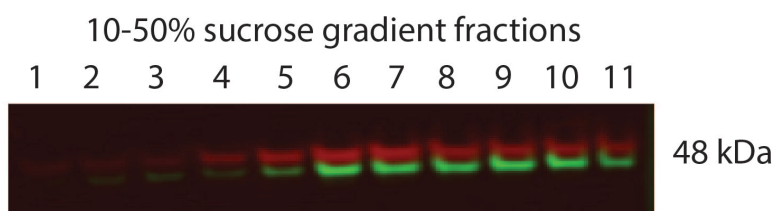


Figure 45 – Purification 3 western blotting results. The sample was run on a 10-50% sucrose gradient and 11 equal fractions collected. Red bands represent anti-mS27 signal. Green bands represent anti-OXA1L signal. Predicted band size of both antibodies is 48kDa.

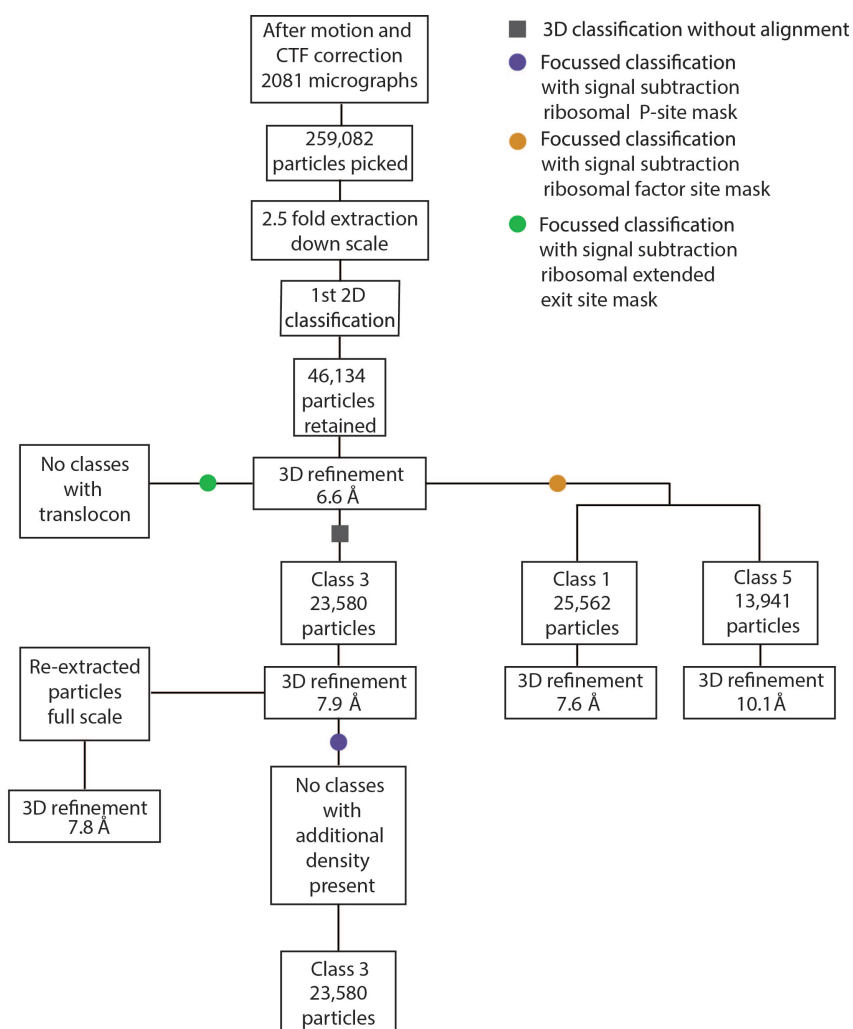


Figure 46 – Purification 3. RELION classification scheme.

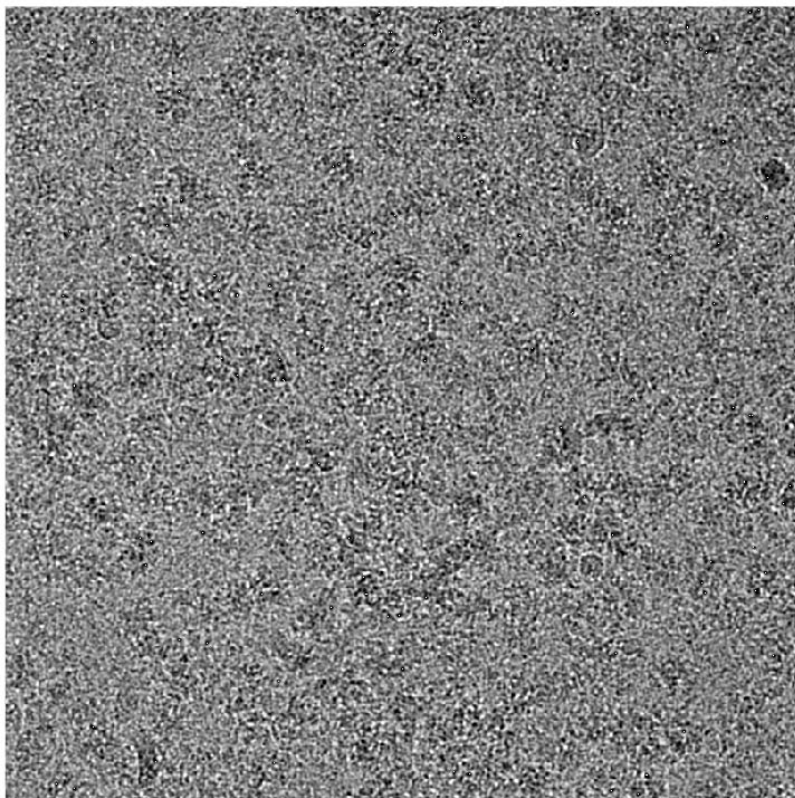
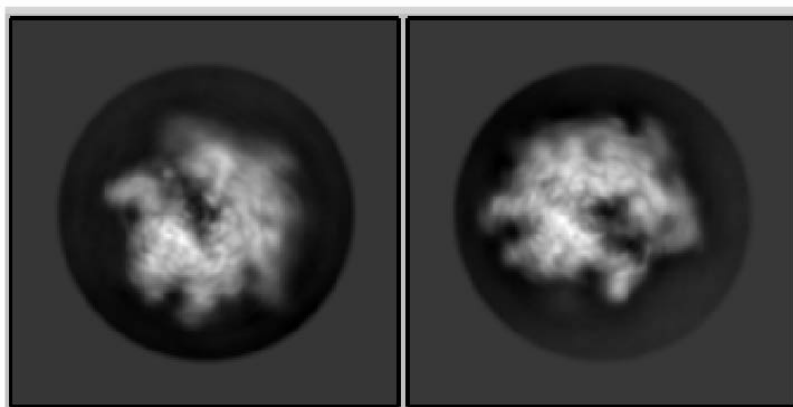
A**B**

Figure 47 – Purification 3. (A) Representative micrograph and (B) Representative 2D classes.

The cryo-EM data was collected according to Table 7 in the methods sections. The grid used was blotted for 6.5 seconds. The data was processed according to Figure

46. After motion and CTF correction 2081 micrographs were retained. 259,082 particles were picked initially but after a 2.5X downsampled 2D classification only 46,134 particles were retained (Figure 47). Due to ice contamination on the grid acquired as a consequence of unforeseen fluctuations in the microscope temperatures, there was huge over picking of particles that were not ribosomes initially, but these were discarded after 2D classification. The initial 3D refinement achieved a resolution of 6.6 Å. 3D classification without alignments revealed class 3 consisting of 23,580 particles which had a P-site mt-tRNA and weak density in the factor site. On examination of the polypeptide exit channel there was also density present for a nascent chain. In order to obtain better density for the factor, a FCwSS was performed on the mitoribosomal factor site. This revealed 2 classes with density in the factor site, class 1 and class 5, which resolved to 7.6 Å and 10.1 Å respectively. Neither of these classes however have a concurrent P-site mt-tRNA. FCwSS on the expected translocon site was also performed on the 1st 3D refinement but OXA1L was not identified. Thus, this purification has provided us with another purification strategy in which to trap a P-site mt-tRNA with a nascent chain. In addition we have seen density in the factor binding site that may represent mt-EF-G which is what we might expect with viomycin trapping. However, this more likely represents non-specific binding of mt-EF-G, as the same particles do not contain a P-site mt-tRNA, than any physiological step in translation. Again OXA1L was not found to be present on the 3D reconstructions despite OXA1L on the western blotting co-migrating with mitoribosomes. The omission of a sucrose gradient step with resultant decrease in handling time did not appear to make a difference in OXA1L binding. However, this omission also did not increase the cytosolic ribosome contamination in the final sample. No cytosolic ribosome classes were seen during processing of the data set.

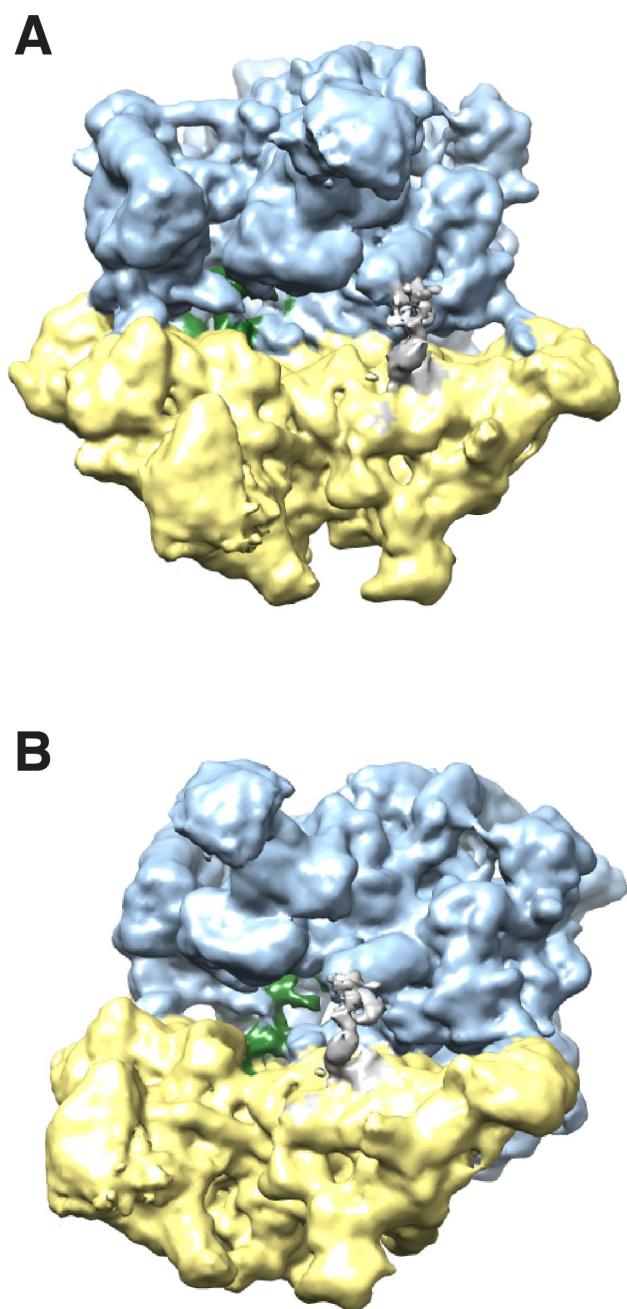


Figure 48 – Purification 3. 1st 3D classification class 3 - 6.6 Å unsharpened map. (A) Front view. (B) Side view. Light blue = mt-LSU. Yellow = mt-SSU. Green = P-site mt-tRNA. Grey = unknown density in factor site.

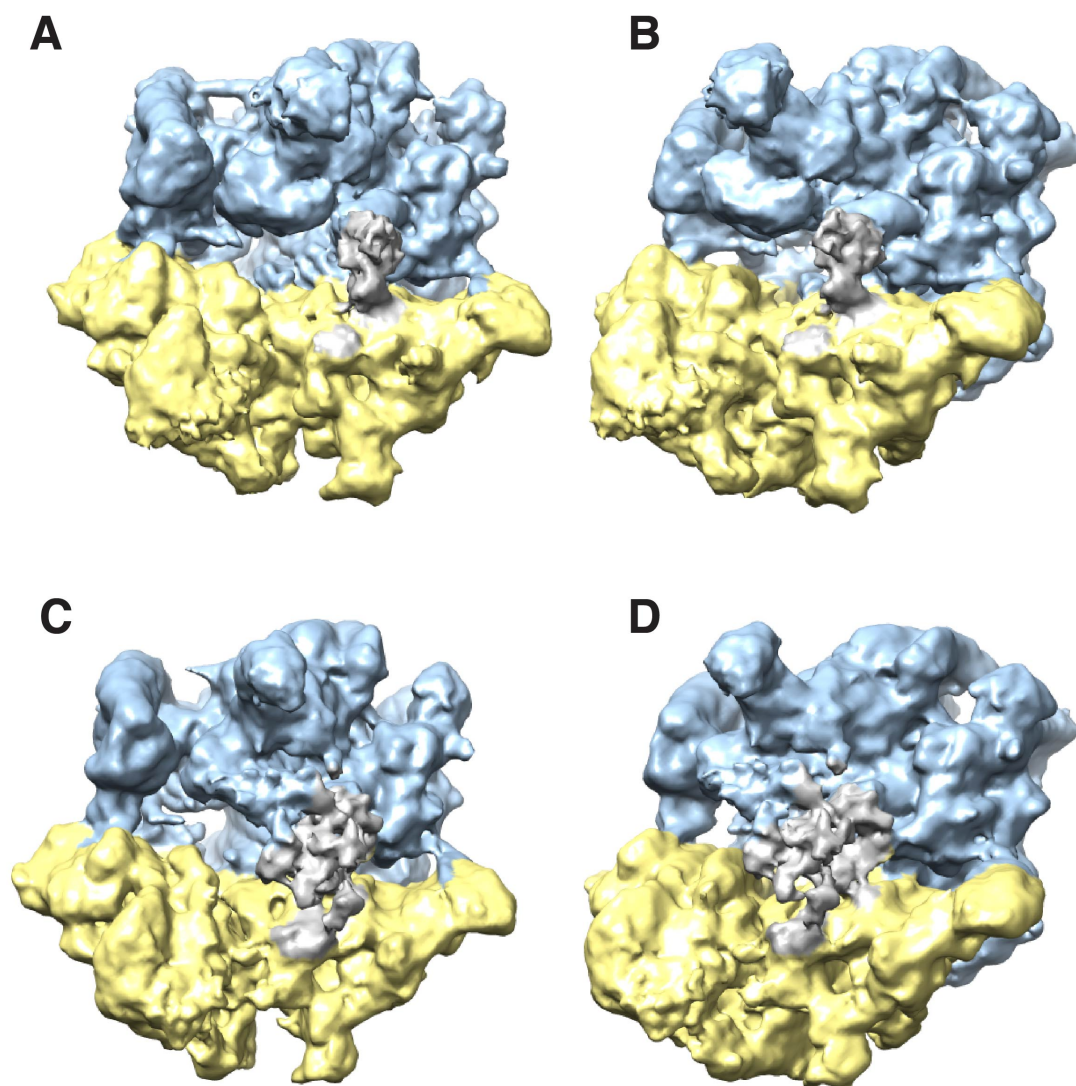


Figure 49 – Purification 3. (A) FCwSS class 1 front view. 7.6 Å unsharpened map. (B) FCwSS class 1 side view. (C) FCwSS class 5 front view. 10.1 Å unsharpened map. (D) FCwSS class5 side view. Light blue = mt-LSU. Yellow = mt-SSU. Grey = unknown density in factor site.

3.3.4 Purification 4 – extended factor site density

Following on from the above purifications we wanted to try out a third antibiotic tigecycline on its ability to stall actively translating ribosome. 0.5mM tigecycline with the non-hydrolysable GTP analogue GDPCP (5'-guanosyl-methylene-triphosphate) was used in the lysis buffer. The traditional method of obtaining mitochondria was used. Full details on sample preparation are found in the methods section (3.5.3). From the 15-30% sucrose gradient fractions 15-17 were taken for peak 1 and 20-24 for peak 2 and concentrated to an average A_{260} of 3.56 and 3.44

respectively (Figure 50). 0.1% glutaraldehyde as a cross linker was added just before putting these samples on grids. The fractions were run on a protein gel and probed for OXA1L and mS27 during western blotting (Figure 51). This showed good signal for the mS27 in peak 2 with virtually no signal in peak 1. This is expected as peak 1 from previous experiments has been found to be mostly large subunit confirmed by data processing. We decided to collect on the monosome peak 2. We collected on the sample that was blotted for 6.5 seconds. As previously, this was collected using linear mode at a magnification of 75,000 on the FEI Titan Krios, Falcon III, pixel size 1.06 Å (Table 7). Particle density on the micrographs was excellent (Figure 52).

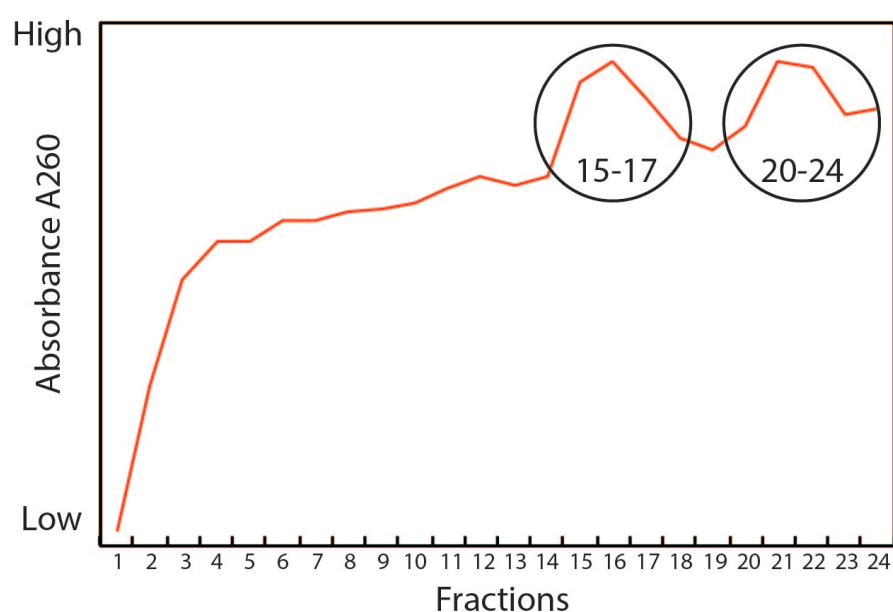


Figure 50 - Purification 4. 15-30% sucrose gradient fractions. Peak 1 is composed of fractions 15-27 and peak 2 is composed of fractions 20-24 as highlighted.



Figure 51 - Purification 4 - western blotting results. Fractions 13-24 from the 15-30% sucrose gradient were run on a protein gel and subjected to western blotting. Red bands represent anti-mS27 signal. (A) Green bands represent anti-OXA1L signal. Predicted band size of both antibodies is 48kDa. (B) Alternative representation of the anti-OXA1L signal.

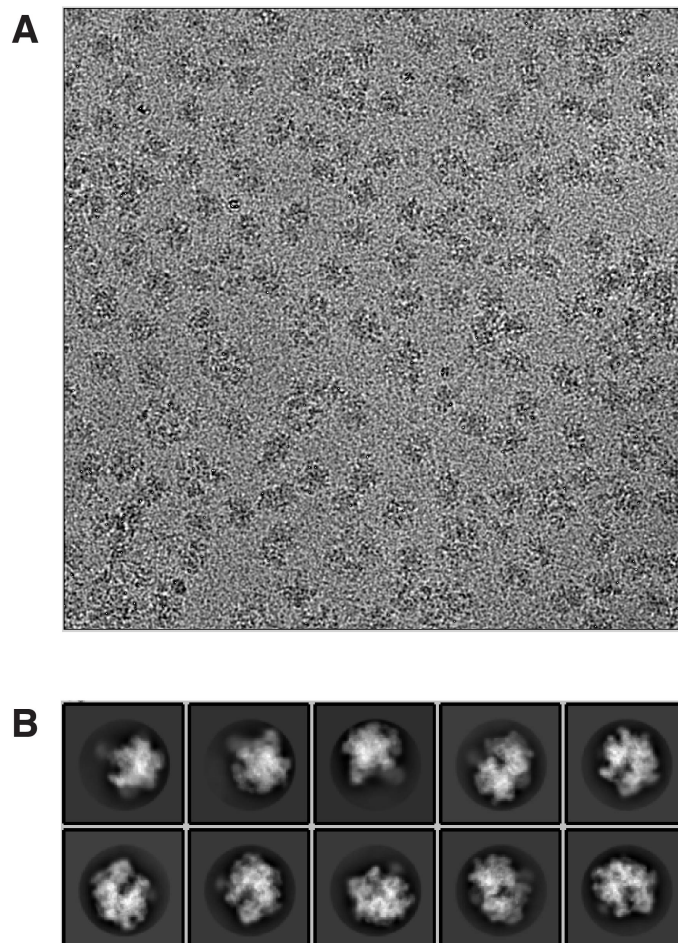


Figure 52 - Purification 4. (A) Representative micrograph. (B) Representative 2D classes.

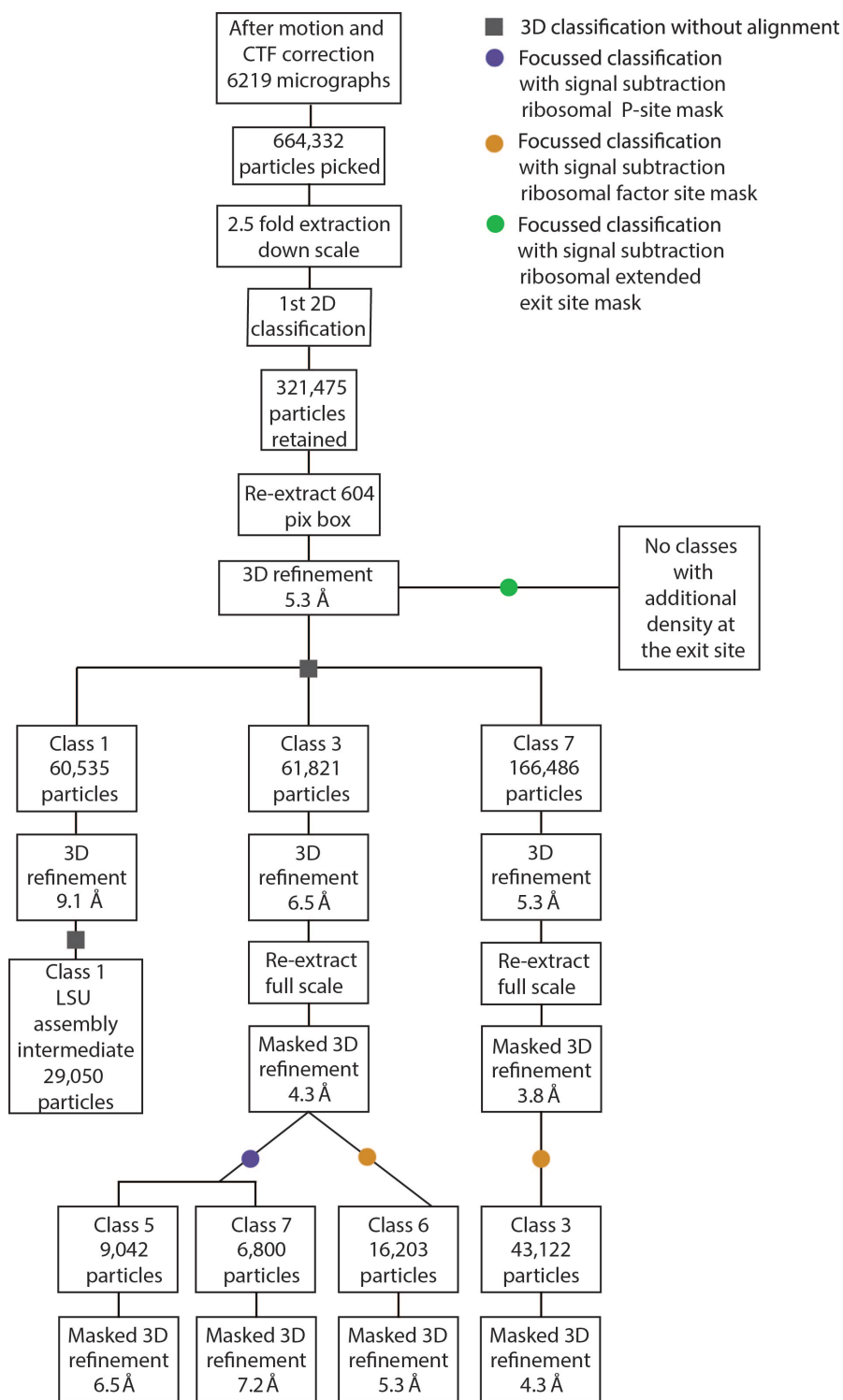


Figure 53 – Purification 4- RELION processing scheme.

After motion and CTF correction 6219 micrographs were retained. After 2D classification after 2.5X downscaling 321,475 particles were kept. The first 3D refinement reached a resolution of 5.3 Å. On this refinement FCwSS was performed using an extended ribosomal exit site mask. However, no classes were found with

additional density at the exit site. On the same refinement a 3D classification without alignment was performed separating the data into 8 classes. 3 dominant classes were identified. Class 1 contained 60,535 particles which had strong density for the mt-LSU and refined to 9.1 Å. Further 3D classification on class 1 identified a class of mt-LSU late assembly intermediates with 29,050 particles, as seen in previous preparations. The first 3D classification on the 1st refinement also revealed classes 3 and 7 with 61,821 and 166,486 particles respectively. The 3D refinements of these classes reached a resolution of 6.5 Å and 5.3 Å respectively. Class 3 was found to have density in the factor site which also extended into A-site. In addition there was density for a P-site mt-tRNA and a possible nascent chain. There was however, no density for a translocon. Class 7 had density in the factor site but not reaching into the A-site. In addition, there was no density for a P-site mt-tRNA. These classes were re-extracted full scale and a repeat 3D refinement was performed with monosome masking. Class 3 reached a resolution of 4.3 Å and class 7 a resolution of 3.8 Å. To further investigate these classes FCwSS was performed on the ribosomal factor site. From class 3 FCwSS, class 6 consisting of 16, 203 particles was identified. This class refined to 5.3 Å. This class 6 has density in the factor site and the A-site but no density for a P-site mt-tRNA. The same FCwSS of class 7 revealed class 3 with 43,122 particles that has density in the factor site extending into the A-site but again had no P-site mt-tRNA. This class refined to 4.3 Å. Thus, from these rounds of FCwSS we have seen binding of a factor in mostly likely non-translating ribosomes evidenced by the lack of P-site mt-tRNA.

Class 3 from the 1st round of 3D classification was also subjected to FCwSS on the P-site mt-tRNA. Class 5 with 9,042 particles was identified. This class has density for a P-site mt-tRNA and in addition density in the factor site although this density did not extend into the A-site. This class refined to 6.5 Å. Class 7 was also identified that had 6,800 particles and had density in the P-site, A-site and also in the factor site. From the resolution of 7.2 Å achieved it is difficult to clearly make out the exact nature of the density in the area of the P-site which does not have a clear tRNA outline.

Class 3 from FCwSS of the factor site mask from class 7 of the 1st 3D classification had the most promising density for the factor. However, a local resolution map

(Figure 56) showed that although the overall resolution of the core mitoribosome reached 3.5 Å the unknown factor density was ~7 Å. Of note the head of the mt-SSU was also of lower resolution highlighting the flexibility of the head compared to the body of the mt-SSU and the mt-LSU.

Overall from this purification we have a purification scheme capable of stalling a P-site mt-tRNA concurrently with a possible nascent chain and with an unknown factor in the factor site, at a resolution that could be improved upon with further data collection. Unfortunately the translocon continued to remain elusive at this stage.

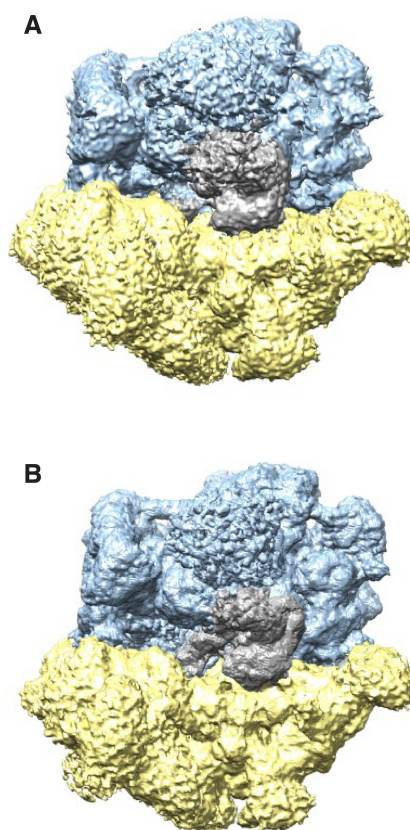


Figure 54 – (A) Class 6 from FCwSS of the ribosomal factor site mask from class 3 of the 1st 3D classification. 5.3 Å unsharpened map. (B) Class 3 from FCwSS ribosomal factor site mask from class 7 of the 1st 3D classification. 4.3 Å unsharpened map. Light blue = mt-LSU. Yellow = mt-SSU. Grey = unknown density in factor site.

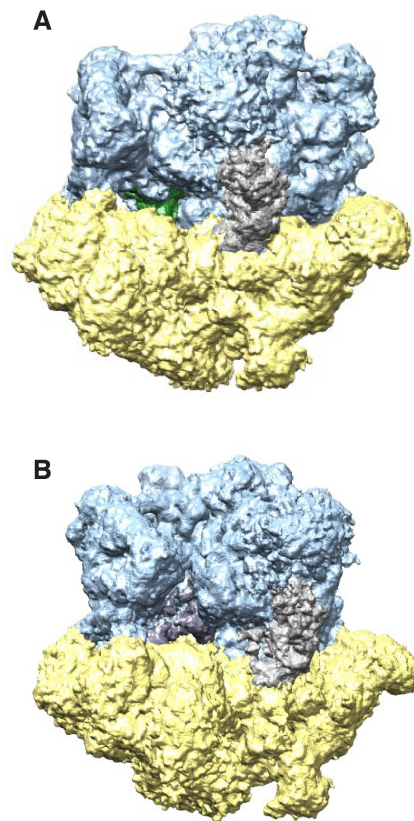


Figure 55 - (A) Class 5 (6.5 Å unsharpened map) and (B) class 7 (7.2 Å unsharpened map) from FCwSS of the exit site from class 3 of the initial 3D refinement. Light blue = mt-LSU. Yellow = mt-SSU. Green = P-site mt-tRNA. Grey = unknown density in factor site. Dark grey = unknown density in P-site.

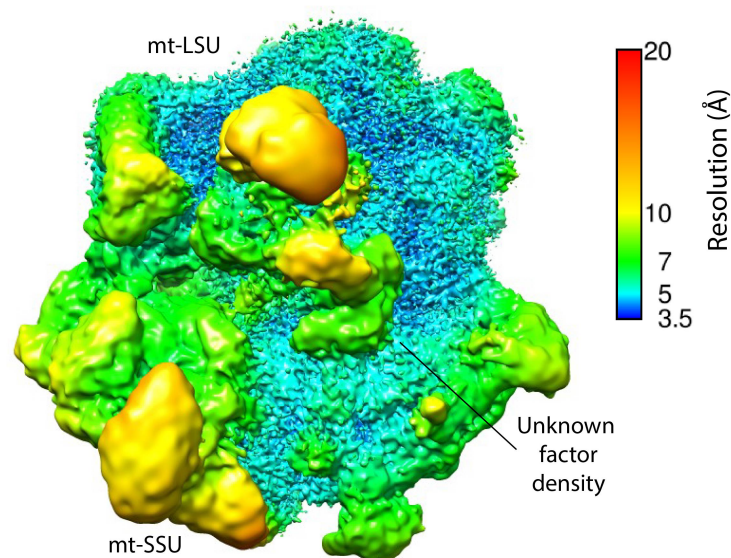


Figure 56 - Local resolution map of Class 3 from FCwSS ribosomal factor site mask from class 7 of the 1st 3D classification.

3.3.5 Purification 5 – Density at the polypeptide exit site on the mt-LSU

Stalling mechanisms that we have tried thus far have involved the use of antibiotics and non-hydrolysable GTP analogues aimed at stalling the ribosome in active translation. Our methods thus far have appeared to achieve stalling by visualisation of good P-site mt-tRNA density and by trapping of a presumed GTPase in the mitoribosomal factor site, but have not yet yielded any density for the translocon. Thus, alternative methods have been explored with the aim of increasing the strength of the stalling to promote translocon association. A cell line was developed in the Minczuk lab that has demonstrated increased mitoribosomal stalling at specific mRNA codons (218). The poly(A)-specific exoribonuclease, phosphodiesterase 12 (PDE12) has been found to be important for the regulation of 3' polyadenylation of mt-rRNA and mt-tRNA by removal of the poly(A) in a 3' to 5' direction (218). The PDE12^{-/-} cell line demonstrated aberrant adenylation of 16S mt-rRNA although not affecting mitoribosomal assembly. In addition, aberrant polyadenylation of mt-tRNA was found to interfere with mt-tRNA aminoacylation, in particular of the lysine specific mt-tRNA. Thus, lack of mature aminoacylated mt-tRNAs has been found to lead to stalling particularly at mRNA codons encoding a lysine.

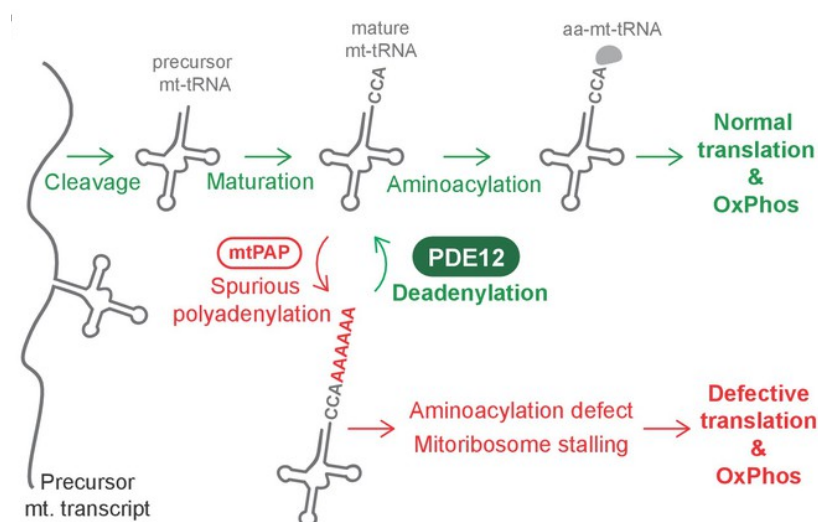


Figure 57 – Taken from Pearce SF, Rorbach J, Van Haute L, *et al.* Maturation of selected human mitochondrial tRNAs requires deadenylation. *Elife*. 2017;6:e27596 (218).

We therefore explored the PDE12^{-/-} cell line as a possible alternative for mitoribosome stalling. The PDE12^{-/-} cell line was cultured and mitochondria extracted as per previously. The conditions used to solubilise the mitochondria involved 1.5% β -DDM, 0.15mg/mL TOCL and 0.5mM GDPCP. The GDPCP was added to further aid stalling of GTPases involved in translational elongation. Additional changes to the preparation detailed in the methods section included the 15-30% sucrose gradient step being run over 1.5 hours on a smaller scale instead of this being an overnight step, and concentration of the mitoribosomes by buffer exchange instead of pelleting. The shortened time from lysis of the mitochondria to obtaining mitoribosomes and buffer exchange step were trialled as a way of minimising disruption to the mitoribosomes and potentially its translocon. The 15-30% sucrose gradient was separated into 15 equal fractions and mitoribosome absorption at A_{260} was measured. Figure 58 shows the A_{260} absorbance for the different fractions. Fractions 10-14 with an A_{260}/A_{280} ratio of above 1.5 were pooled together and concentrated with additional buffer exchange to lower the final β -DDM concentration to 0.05% and obtain an A_{260} of 5 and applied to grids as per previously. In order to maximise sample preparation for grid making, smaller aliquoted fractions were not taken to run on a protein gel for western blotting on this occasion. Instead an aliquot of the final concentrated sample was run on a 10-50% sucrose gradient to look for co-migration of the anti-OXA1L and anti-mS27 signal as in previous experiments. This is shown in Figure 59 (A). Unfortunately the quality of the western blot was poor, but it is still faintly visible that there is co-migration in lanes 4, 5 and 6. The preparation was therefore repeated with identical conditions. Figure 59 (B) shows the 15-30% sucrose gradient fractions and (C) shows the corresponding western blot, showing co-migration and corresponding intensities of the bands throughout.

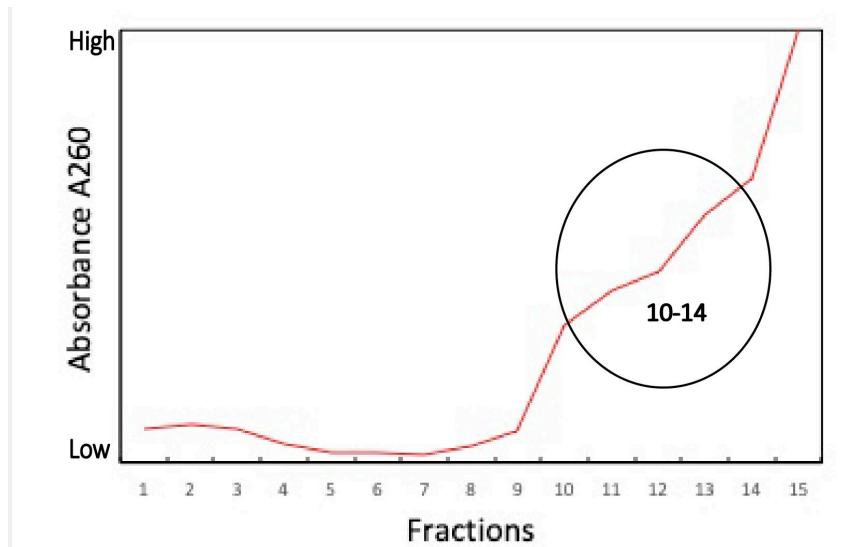


Figure 58 - Purification 5. 15-30% sucrose gradient fractions. Peaks 10-14 were pooled together.

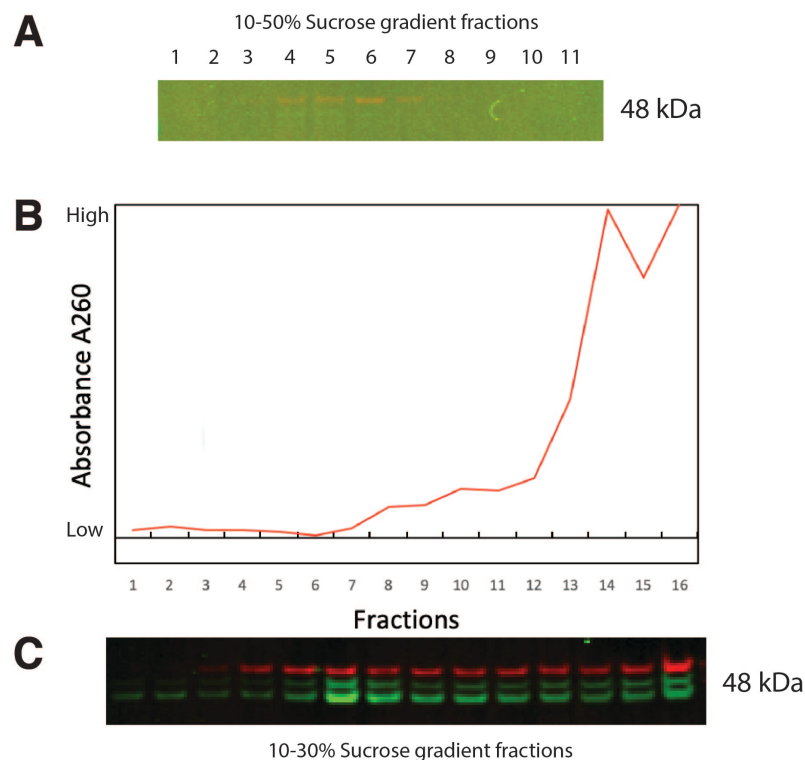


Figure 59 - (A) Purification 5 western blotting result. Fractions 1-11 from the 10-15% sucrose gradient. (B) Repeat of purification 5. 15-30% sucrose gradient fractions. (C) Fractions from (B) subjected to western blotting. Red bands represent anti-mS27 signal. Green bands represent anti-OXA1L signal. Predicted band size of both antibodies is 48kDa.

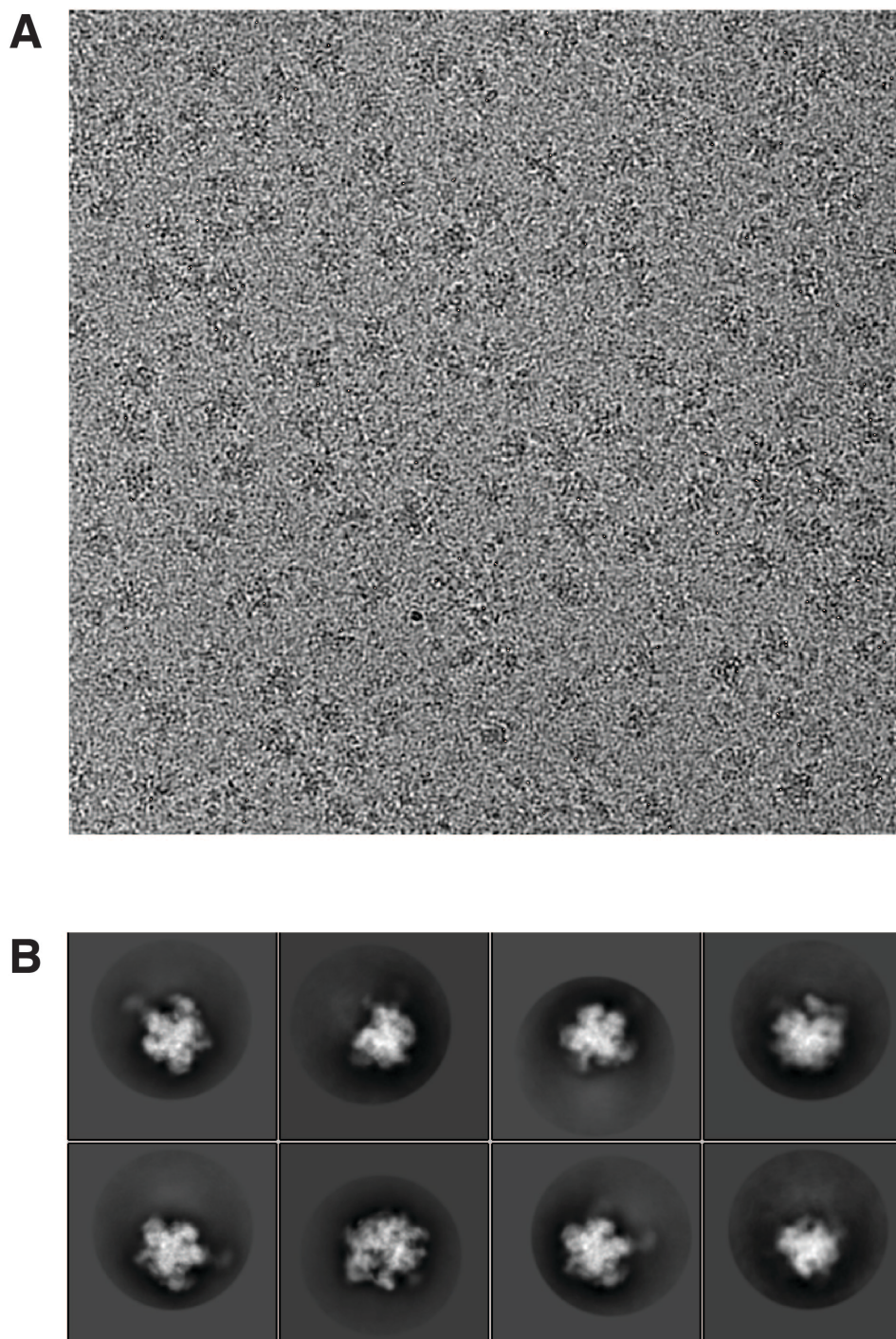


Figure 60 - Purification 5, 1st collection. (A) Representative micrograph and (B) 2D classes.

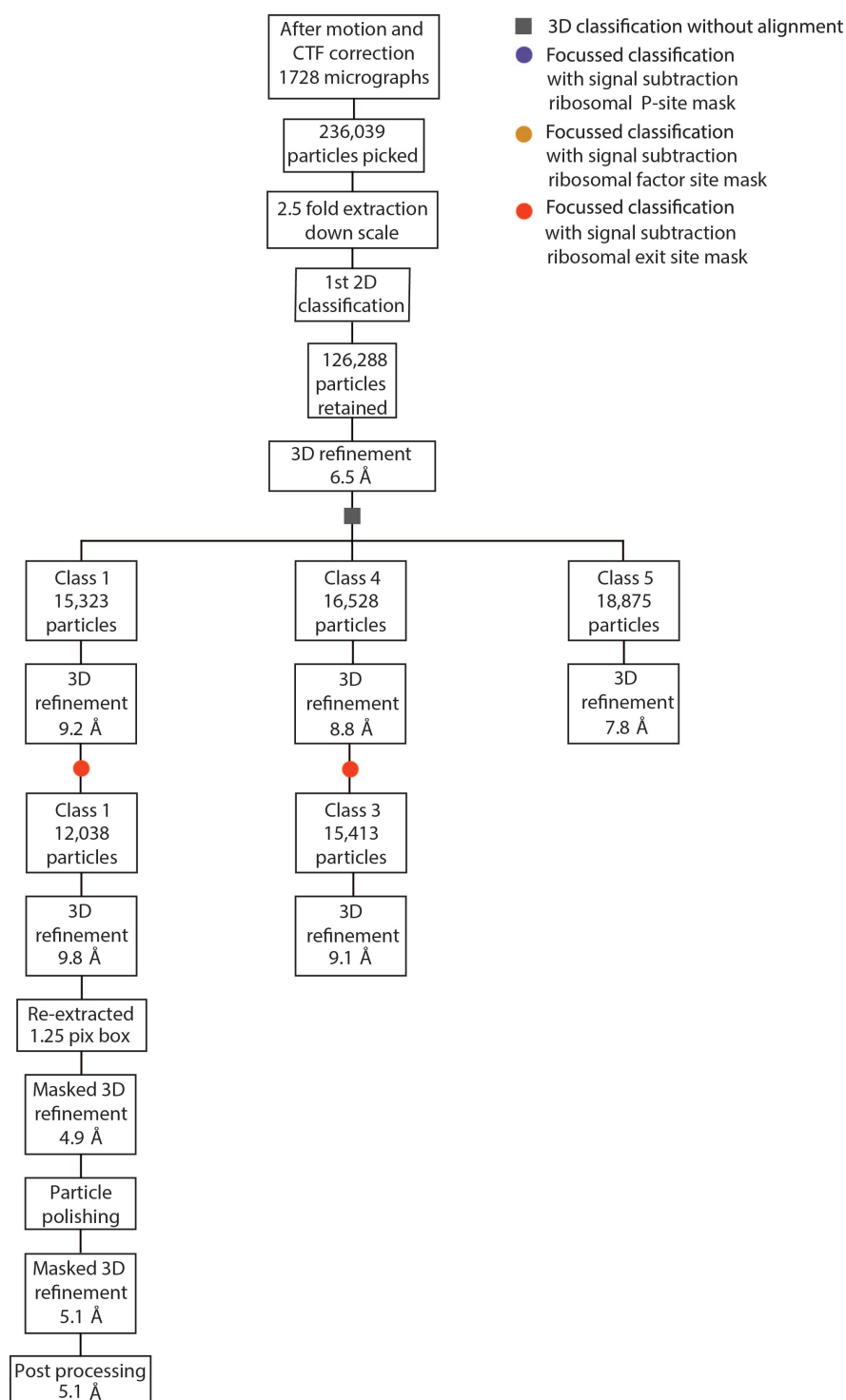


Figure 61 – Purification 5, 1st collection, RELION processing scheme.

For cryo-EM, we collected on the sample that was blotted for 4.5 seconds on the grid. The collection was at a magnification of 75,000 on the FEI Titan Krios, Falcon III detector, pixel size 1.04 Å in linear mode (Table 7). A representative micrograph is shown in Figure 60, along with the 2D classes. After CTF and motion correction

1728 micrographs were retained. After 2.5X downscaling and 2D classification, 126,288 particles were remaining. The initial 3D refinement achieved a resolution of 6.5 Å. The initial 3D classification revealed 3 distinct classes. Class 1 was an mt-LSU class. Classes 4 and 5 were monosome classes. Class 1 had 15,323 particles and resolved to 9.2 Å. There was clear density at the mitoribosomal exit site although not at 100% occupancy. Interestingly, there was also excellent density for the MALSU1-L0R8F8-mt-ACP module that is a part of the published late stage assembly intermediate described above (214). With promising density at the exit site, FCwSS at the exit site was performed on class 1 which revealed class 1, consisting of 12,038 particles which resolved to 9.8 Å. We re-extracted this with a pixel size of 1.25 Å and proceeded with particle polishing, masked refinements and post processing. The final resolution reached was 5.1 Å for the whole map with poorer resolution in the peripheries as shown in the map coloured by local resolution (Figure 62).

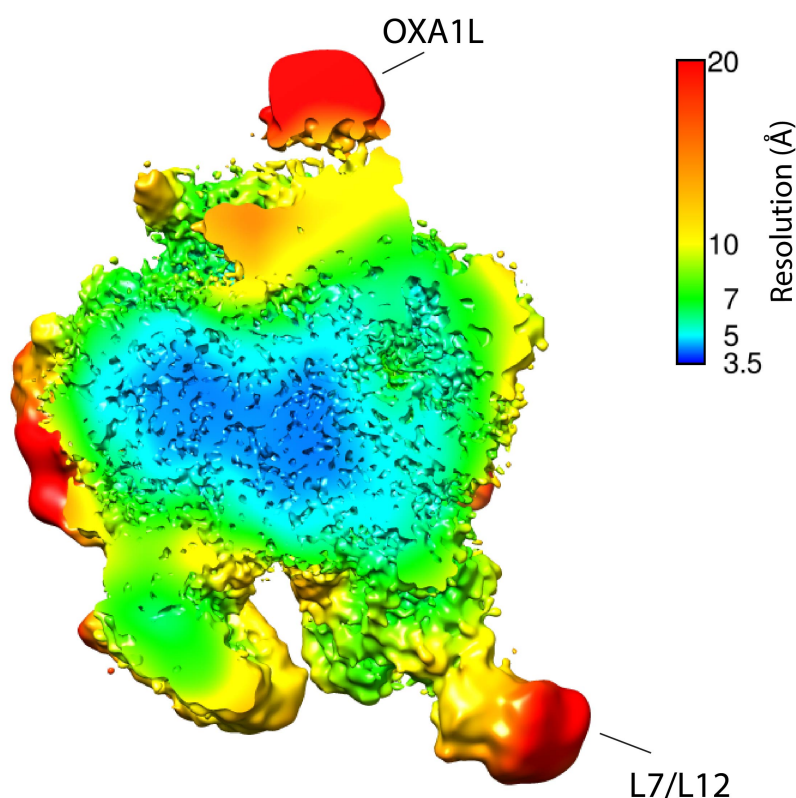


Figure 62 - mt-LSU. Re-extracted (pixel size 1.25 Å) FCwSS class 1 on the exit site of class 1 from the 1st 3D refinement coloured by local resolution.

Figure 63 represents the masked 3D refinement of the same class 1 at 5.1 Å. There was clear density at the exit tunnel likely representing OXA1L as labelled. Also labelled for reference is the L7/L12 stalk. The MALSU1-L0R8F8-mt-ACP module is also visible in this orientation.

Furthermore, class 4 monosome of the initial 3D classification had clear density for a P-site mt-tRNA and patchy density at the polypeptide exit site. However, after FCwSS on the exit site of this class no classes emerged with any density for a translocon. Class 3 of the FCwSS was the most abundant class but no translocon was apparent. Class 5 monosome from the initial 3D classification did not have any early indication of a translocon density and was not pursued further.

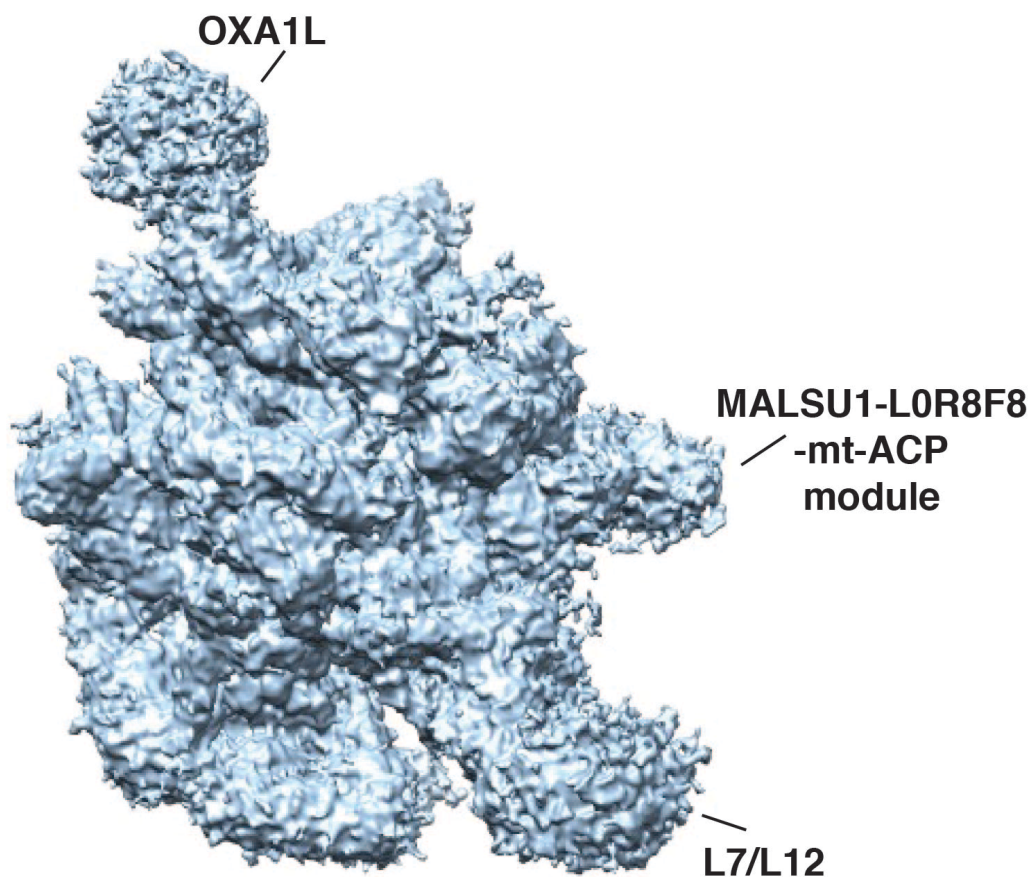


Figure 63 – mt-LSU. Class 1 from focussed classification with signal subtraction on the exit site of class 1 from the 1st 3D refinement. 5.1 Å post processed map.

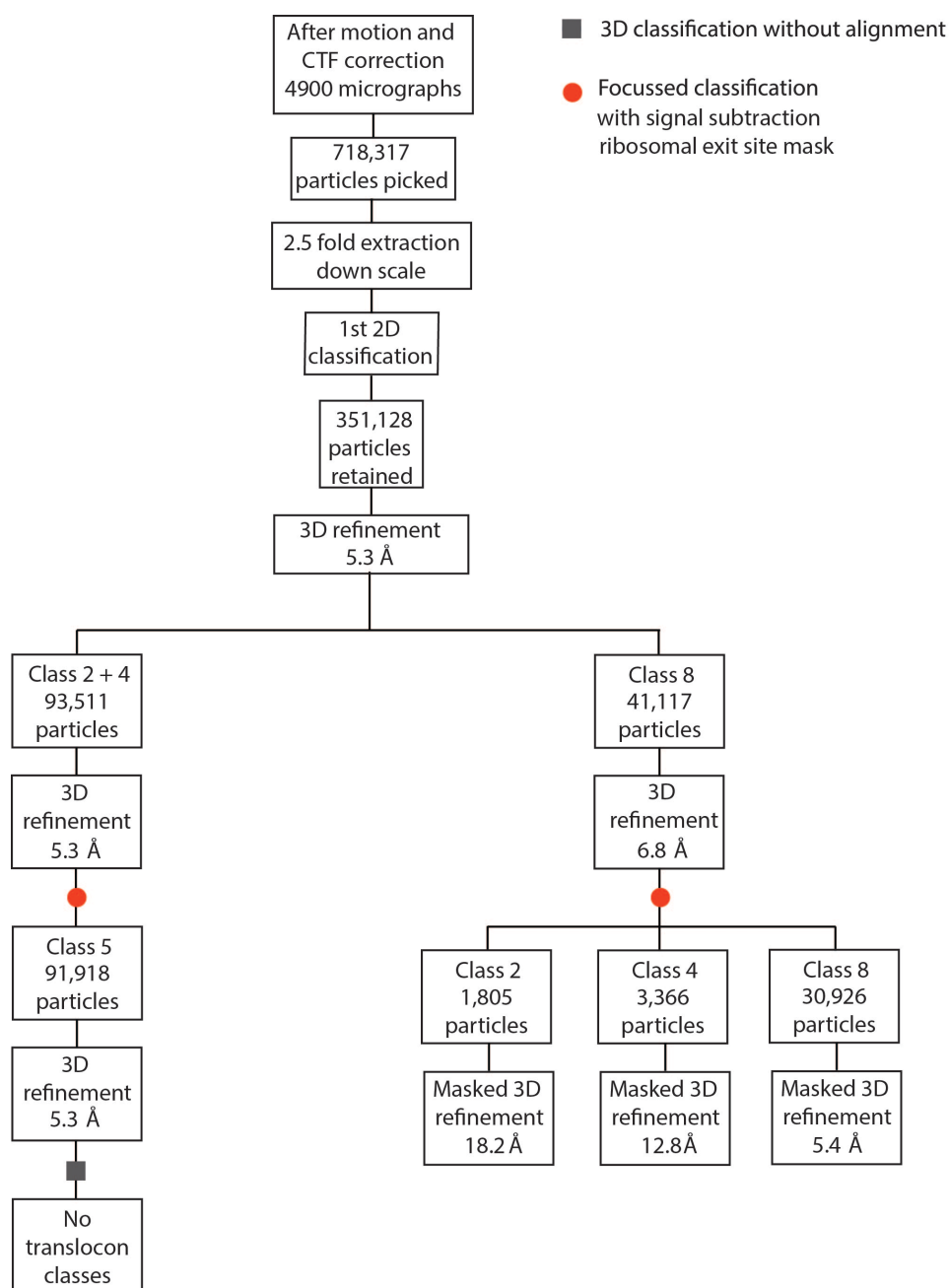


Figure 64 – Purification 5, 2nd collection RELION classification scheme.

A further cryo-EM data set was collected on the same purification to see if the resolution of the density at the exit tunnel could be improved. The collection details are the same as the previous collection (Table 7). The RELION classification scheme is outlined in Figure 64. From this second data collection 4900 micrographs were obtained. After downscaling 2.5X and 2D classification 351,128 particles were retained. Initial 3D refinement the resolution reached 5.3 Å. The 1st round of 3D

classification revealed class 8 representing the mt-LSU class with density at the translocon site as previously seen (Figure 65 (A, B)). This class consisted of 41,117 particles. However, although this mt-LSU class was seen in the previous collection, the improvement in resolution in this data collection revealed a number of new features not previously elucidated.

Figure 65 (C) shows the density present for a P-site mt-tRNA. Modelled in yellow is a mt-tRNA occupying the P/P mt-tRNA space in the mitoribosome. However, in this map the mt-tRNA (yellow) fits the density in this orientation in the acceptor stem, but the anticodon stem loop is deviated towards the E-site. In Figure 66 a mt-tRNA (green) has been modelled into this density in the orientation that fits this map. When we looked at the polypeptide exit site we were able to see density suggestive of a nascent chain, which would be plausible given the position of the mt-tRNA. Additionally, there is density coming from the L1 stalk towards this mt-tRNA density that may represent an E-site mt-tRNA with the anticodon stem loops of the two abutting mt-tRNA's having a contact site. It is difficult to say conclusively at this resolution if this second density is occupied by a mt-tRNA. A mt-tRNA (purple) has been modelled into Figure 66, but using a rigid body fit but the mt-tRNA did not fit the density perfectly.

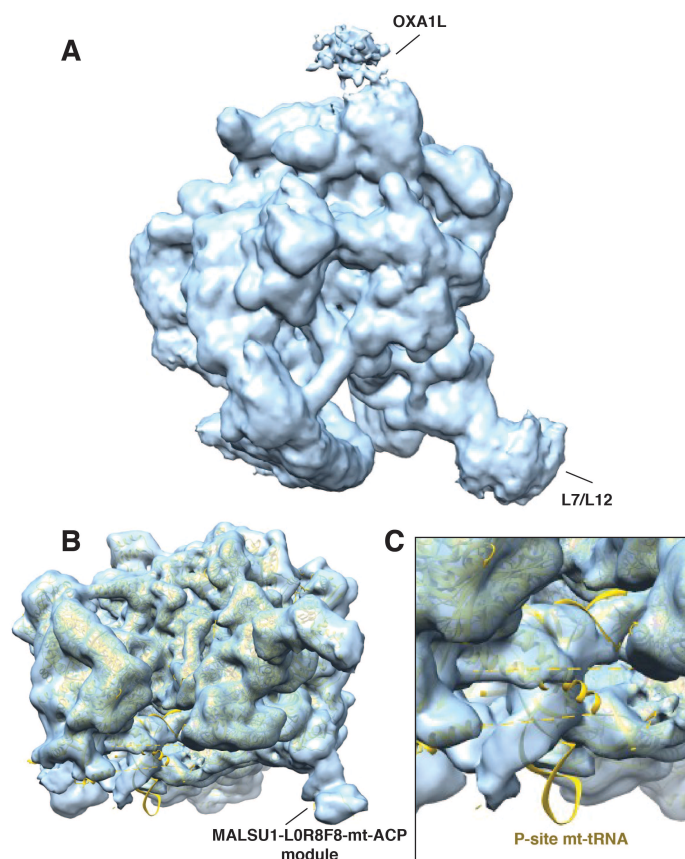


Figure 65 – Purification 5, 2nd collection (A) mt-LSU class 8 (6.8 Å unsharpened map) from initial 3D classification showing a hint of density for OXA1L. (B) Different view of same class to show density for the MALSU1-L0R8F8-mt-ACP module. PDB 5AJ4 docked in to include position of P-site mt-tRNA (50). (C) Enlarged image from (B) showing the position of the P-site mt-tRNA in the monosome and adjacent density to the left in this structure for a mt-tRNA.

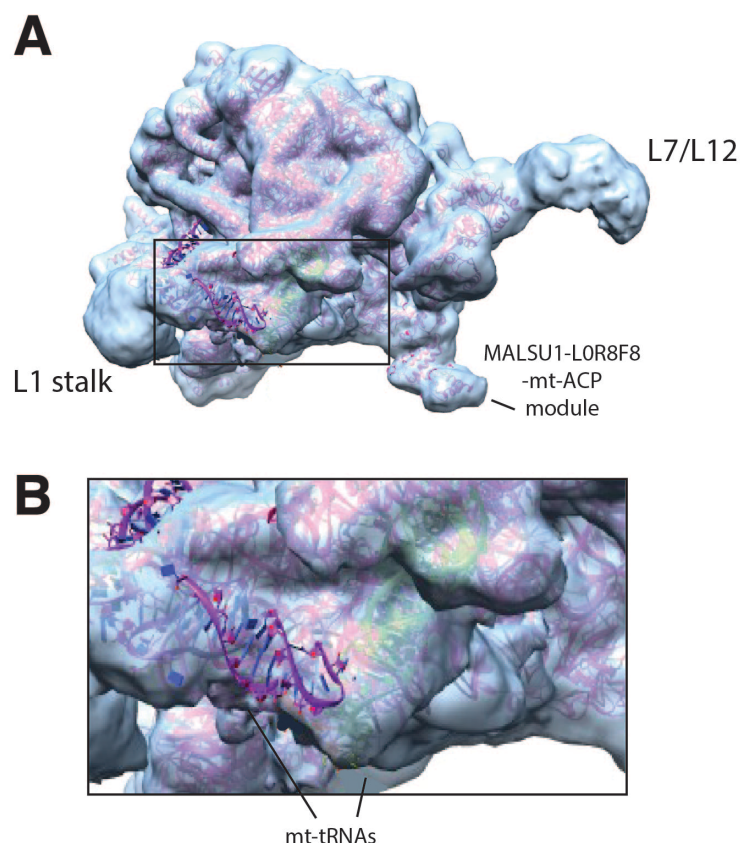


Figure 66 – Purification 5, 2nd collection. FCwSS at the exit site of class 8 (5.4 Å unsharpened map). (A) mt-LSU. PDB 500M (214). (B) Enlarged representation of figure (A). Two mt-tRNAs have been modelled into the density, purple and green.

What is curious about this map is that it is evident that the mt-LSU has split following active translation. This is supported by the presence of a mt-tRNA with its acceptor stem binding in the P-site position, and the presence of a nascent chain. A post termination complex mitoribosome is one in which the mt-tRNA is in the P/E position with the nascent chain having been released, waiting for subsequent mitoribosome splitting through the coordinated effort of mt-RRF1 and mt-EF-G2. However, in this map, splitting of the mitoribosome appears to have occurred prior to nascent chain cleavage allowing for a P-site mt-tRNA to remain *in situ* with apparent stabilisation either from the E-site mt-tRNA or an as yet unidentified factor. In addition, the MALSU1-L0R8F8-mt-ACP module, thought to be part of late stage mt-LSU mitoribosome assembly is also present. It is likely that the MALSU1-L0R8F8-mt-ACP module has a wider role and plays a part in mitoribosome recycling

and prevention of premature mt-SSU subunit joining. The presence of OXA1L in this map is suggestive of the possibility that mitoribosome recycling can take place on the mitochondrial inner membrane when stalled. In this situation, lack of PDE12 possibly together with the used of GDPCP, appears to have caused stalling, and it is likely that the presence of the mt-tRNA and nascent chain have strengthened the interaction of the mitoribosome with OXA1L. However, other changes in the preparation such as a shorter sucrose gradient step with buffer exchange centrifugation is likely to have also played a role.

After the initial 3D classification, classes 2 and 4 emerged which were monosome classes that had a small hint of density at the polypeptide exit site. However, following FCwSS at the exit site followed by a 2nd round of 3D classification, there were no classes with any density for a translocon and this was therefore not pursued further.

To further improve class 8 we performed FCwSS on the polypeptide exit site. This revealed 3 different classes with density at the polypeptide exit site (Figure 67). Class 4 was the most promising for OXA1L density and had 3,366 particles with a down scaled resolution of 12.8 Å. Class 2 also had density in the polypeptide exit site that might represent OXA1L. Class 8 had the most number of particles at 30,926, however the OXA1L density was the weakest in this class. Further 3D classification to this class was not able to separate the mt-LSU into particles containing OXA1L and those without OXA1L.

Thus, from these two collected data sets on the same preparation, we could see that although exit tunnel density on the mt-LSU was a small proportion of our total particles, convincing density suggestive of OXA1L at the polypeptide exit site represented a significant breakthrough in this project. However, density for OXA1L could still only be seen on the mt-LSU. Thus our efforts continued to focus on not only trying to improve the density of mt-LSU - OXA1L through collecting more data but also to try and 1) improve the density by trialling different detergents and 2) aiming for better separation of the peaks when collecting the 15-30% sucrose gradient fractions to separate mt-LSU and monosome particles.

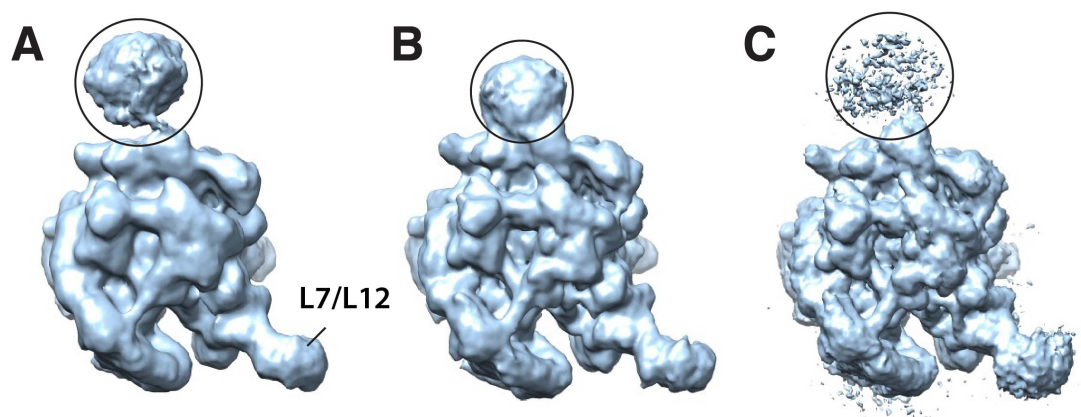


Figure 67 – Purification 5, 2nd collection. Classes from FCwSS at the exit site of class 8. (A) Class 2 (18.2 Å unsharpened map) (B) Class 4 (12.8 Å unsharpened map) (C) Class 8 (5.4 Å unsharpened map).

3.3.6 Purification 6 – Density at the polypeptide exit site on the monosome

Purification 5 was repeated as previously to obtain mitoribosome, but in the final buffer exchange/concentration step β -DDM was exchanged with 0.05% β -DDM/0.005% CHS or 0.05% digitonin for peak 2. Both the ionisable anionic detergent cholesteryl hemisuccinate (CHS) and the non-ionic digitonin, are detergents widely used in the membrane biology field. Blends of CHS and β -DDM have been used for the stabilisation of membrane proteins due to the ability of CHS to mimic cholesterol. The 15-30% sucrose gradient for this purification produced two A_{260} peaks (Figure 68). The second peak consisting of fractions 13-15 was pooled together and halved. In the final buffer exchange concentration step, one half was exchanged with 0.05% β -DDM/0.005% CHS and the other with 0.05% digitonin. Peak one consisting of fractions 8-11 was concentrated with 0.05% β -DDM buffer as in the previous purification. All samples were concentrated to an $A_{260} \sim 5$. The three concentrated samples were run on a protein gel for western blotting. The β -DDM/CHS and digitonin samples had proportional signal against mS27 compared to OXA1L. However, the β -DDM only sample had an apparent increase intensity of the anti-OXA1L band compared to the anti-mS27 band.

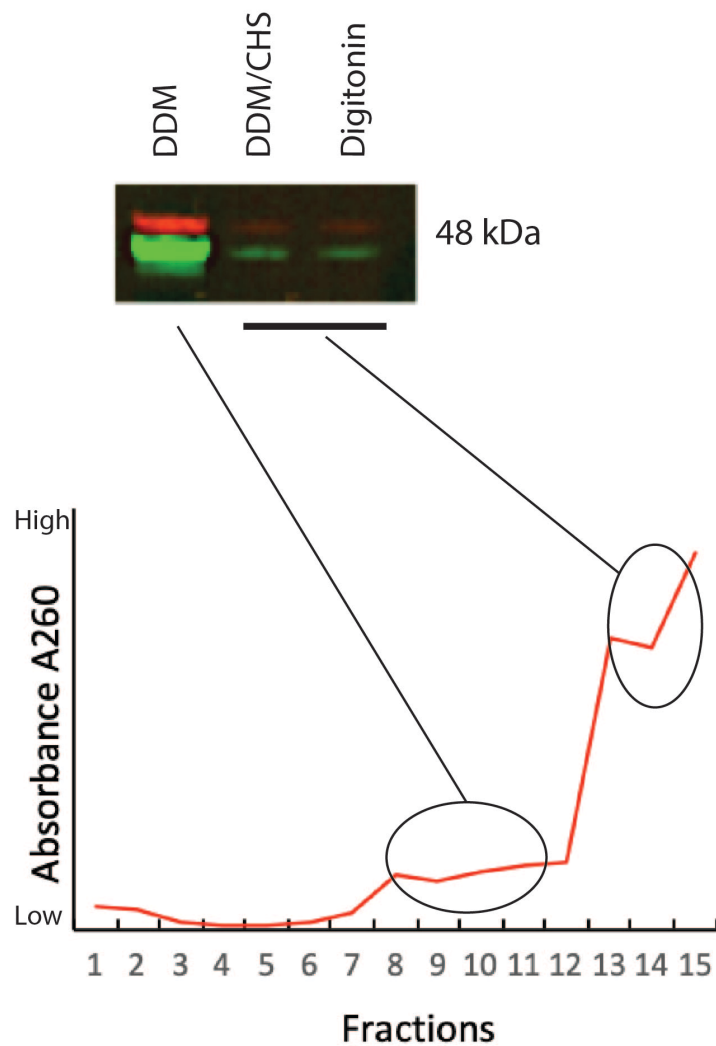


Figure 68 - Purification 6. Figure shows the 15-30% sucrose gradient fractions. Fractions 8-11 (peak 1) were pooled and buffer exchanged in 0.05% β -DDM buffer. Fractions 13-15 (peak 2) were pooled and divided into two and buffer exchanged with either 0.05% β -DDM/0.005% CHS or 0.05% digitonin. Pooled fractions from the three concentrated samples were subjected to western blotting. Red bands represent anti-mS27 signal. Green bands represent anti-OXA1L signal. Predicted band size of both antibodies is 48kDa.

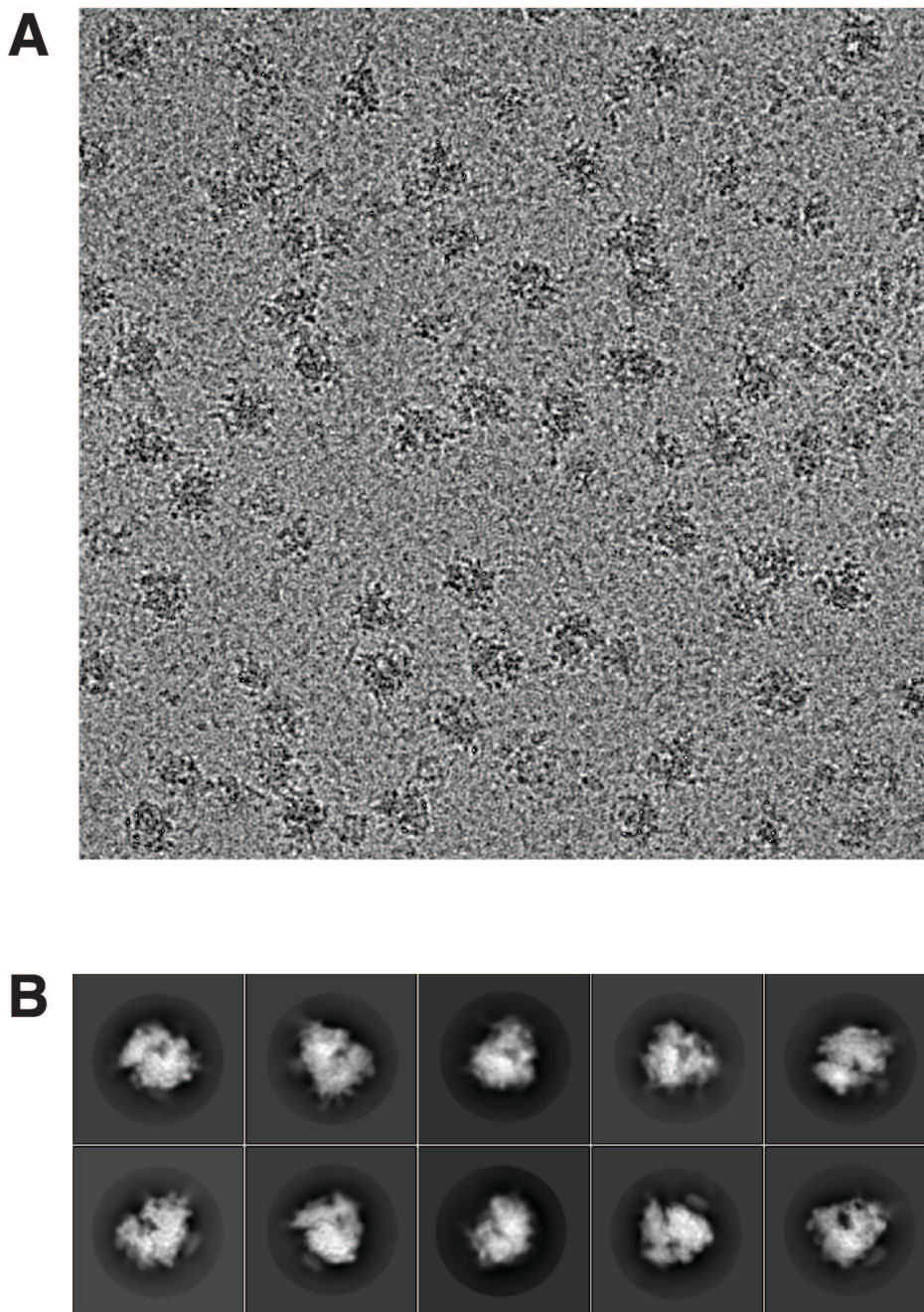


Figure 69 – Purification 6 – digitonin buffer (A) A representative micrograph. (B) Representative 2D classes.

We decided to collect cryo-EM data initially from the peak 2 samples. Cryo-EM collection on the sample buffered exchanged with digitonin was collected in linear mode on the 300kV FEI Titan Krios, Falcon III detector at a pixel size of 1.04 Å (Table 7). 2204 micrographs were retained after motion and CTF correction. The classification scheme is shown in Figure 70. 200,647 particles were picked initially but only 112,176 particles were retained after 2D classification. The extraction was

2.5X downsampled. The initial 3D refinement achieved a resolution of 5.4 Å. 3D classification revealed 3 clear monosome classes. Unfortunately two of the classes, class 2 and class 5 were in fact cytosolic ribosomes which had contaminated our preparation (Figure 71). We do see cytosolic contamination of our mitochondrial ribosome preparations occasionally. This is likely to be resultant of contamination of mitochondrial harvest with rough endoplasmic reticulum. Usually this is easily separated at the 15-30% sucrose gradient stage but in this case the fractions with the mitochondrial monosomes and the cytosolic ribosomes were pooled together. Curiously the cytosolic ribosome has excellent density for the previously published Sec61 (Figure 71), the endoplasmic reticulum translocon that contacts the cytosolic ribosome for co-translational transport of proteins into the endoplasmic reticulum (102).

From the 1st 3D classification class 4 was revealed that showed promise for a translocon on a mitoribosome and further FCwSS revealed class 1 consisting of 5,606 particles. Figure 72 shows the map for class 1 with a visible P-site mt-tRNA and an unidentified factor. A side view shows the density for the possible translocon as previously only seen on the mt-LSU. Thus, this data collection has likely revealed OXA1L in the monosome. We now had a sample in which the mitochondrial monosomes showed promising OXA1L density at the mitoribosomal exit site with grids made using different detergents.

We therefore also collected data on the other peak 2 sample (β -DDM/CHS) and the peak 1 sample (β -DDM). Our rationale was that OXA1L has the potential to be visible in all of the samples as it has been seen in one of the samples. Therefore data collection on each of these samples would act as a trial of different detergent conditions. A one day cryo-EM data collection was done on the β -DDM/CHS sample using the same microscope conditions and pixel size as above. However, after processing through to the 1st round of 3D classification it was apparent that most of the particles in this data set were cytosolic ribosome with no promising mitoribosome particles with any density at the exit site. This data set was therefore not pursued further (results not included).

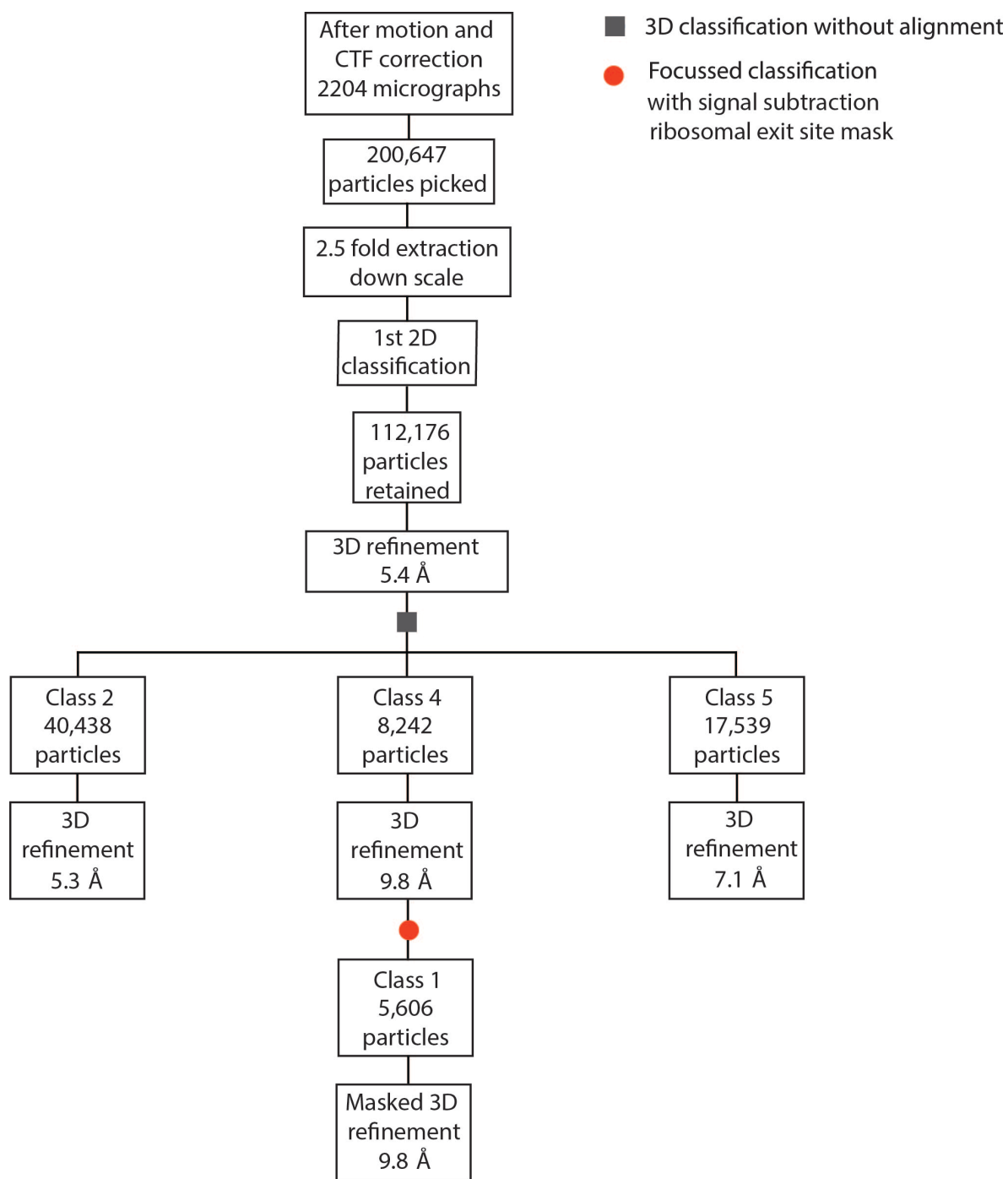


Figure 70 – Purification 6 – digitonin buffer. RELION processing scheme.

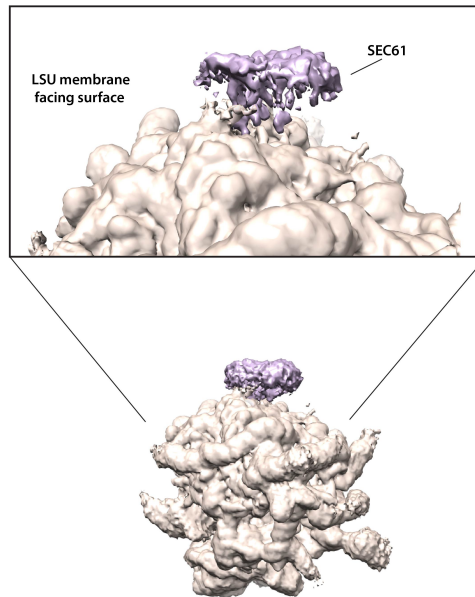


Figure 71 – Purification 6 – digitonin buffer. Class 2 of initial 3D classification. Cytosolic ribosome coloured in taupe. Sec61 is coloured in mauve. The top image features a zoomed in representation showing the LSU membrane facing surface with clear density for Sec61.

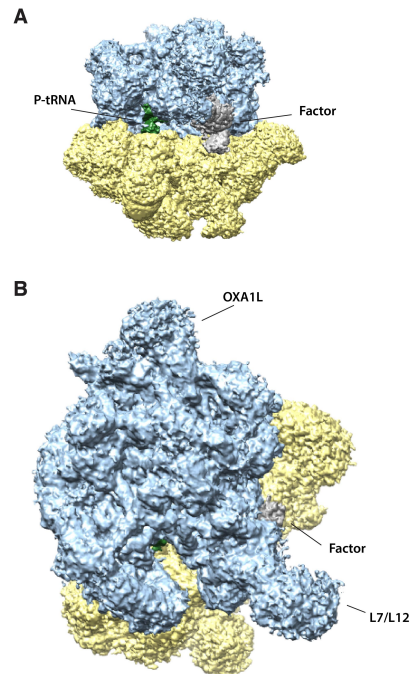


Figure 72 – Purification 6 – digitonin buffer. Class 1 from FCwSS of class 4. 9.8 Å unsharpened map (A) Front view showing the Psite mt-tRNA in green and the unknown factor in grey. (B) Side view showing density for OXA1L. Light blue = mt-LSU. Yellow = mt-SSU.

Cryo-EM data collection in linear mode on the 300kV FEI Titan Krios Falcon III, 1.04 Å pixels was also done on the peak 1 β-DDM sample (Table 7). We expected that this peak would contain mt-LSU and monosomes. 4961 micrographs were retained after motion and CTF correction and 419,657 particles picked initially and extracted downsampled 2.5X (Figure 74). After 2D classification, 180,939 particles were retained and 3D refinement reached a resolution of 5.2 Å. There were two classes of interest after 3D classification, class 3 and class 6. Class 3 containing 28,965 particles, represented the monosome, and class 6 containing 19,304 particles, the mt-LSU. Both classes had signs of density at the mitoribosomal exit site. Their 3D refinements went to resolutions of 6.8 Å and 7.6 Å respectively. FCwSS on the exit site was performed with both of these classes. From FCwSS of class 3, class 4 containing 2,650 particles was obtained that refined to 15.7 Å (Figure 75). Although containing relatively few particles, the density at the exit site for this class was convincing for a translocon like structure with a ~100% occupancy of this class (the exit site density showing up at a low threshold). Of the total monosome particles from the 1st 3D classification this represented 5%. From FCwSS of class 6, class 2 was obtained that showed promise. Class 2 had only 1,677 particles and refined to 18.4 Å but again this largely mt-LSU class showed ~100% occupancy of the translocon density. This mt-LSU class was still contaminated with monosome classes as evident in Figure 76 by the patchy mt-SSU density, but it is clear that the predominant particle is the mt-LSU. Curiously this is the LSU particle without the MALSU1-L0R8F8-mt-ACP module that was previously seen. Therefore, this may represent another instance in which OXA1L can be associated with the LSU possibly without being in active translation. From the initial 3D classification class 4 and class 6 were both mt-LSU and together contained 45,907 particles. Therefore, as a percentage of the total mt-LSU classes, 3.5% of mt-LSU particles contained the translocon density.

Due to the low number of particles this data set was not taken any further with regards to re-extraction and continued processing. To conclude, from this data set we have been able to classify the particles to obtaining a high occupancy of translocon density, albeit in a limited number of particles. It may be that there are other particles with the translocon density in a slightly different orientation that are

not able to be classified due to low particle numbers. Our plan moving forward is therefore to try and improve the resolution through improving the number of particles which will be discussed below.

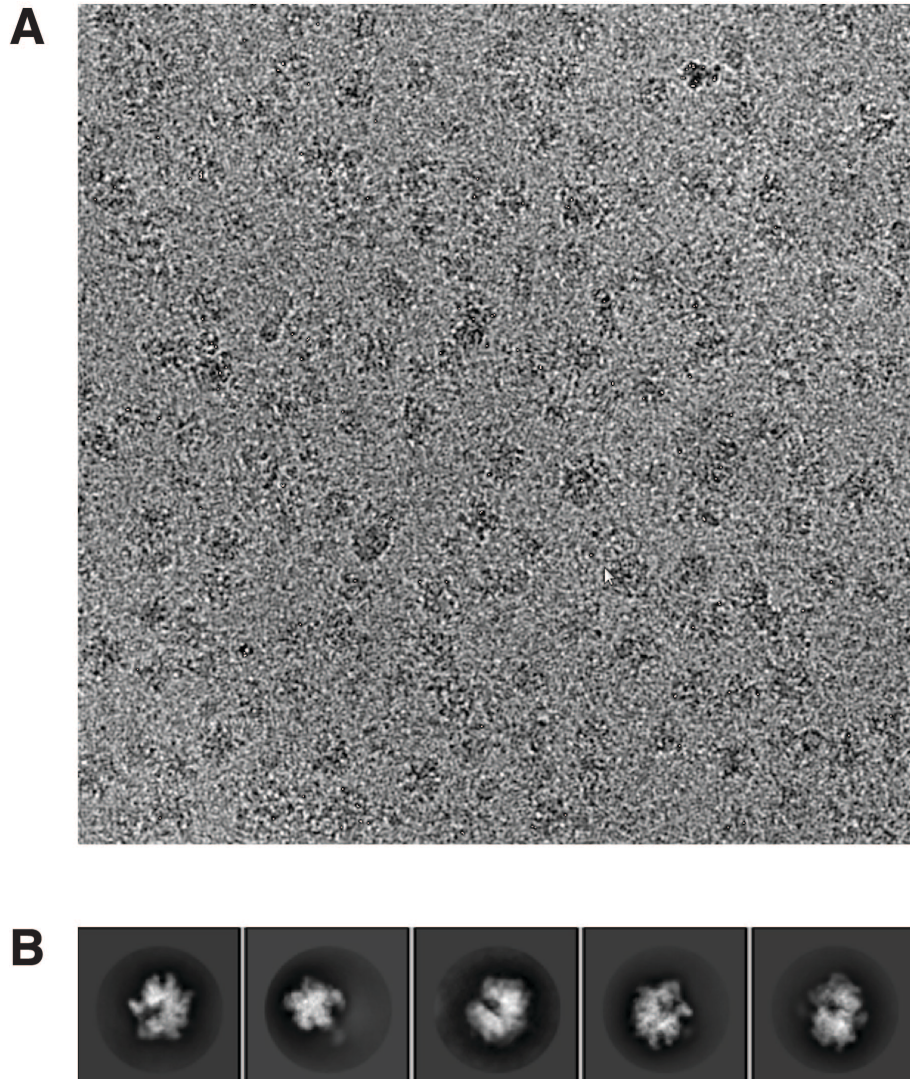


Figure 73 - Purification 6 - β -DDM buffer. (A) A representative micrograph. (B) Representative 2D classes.

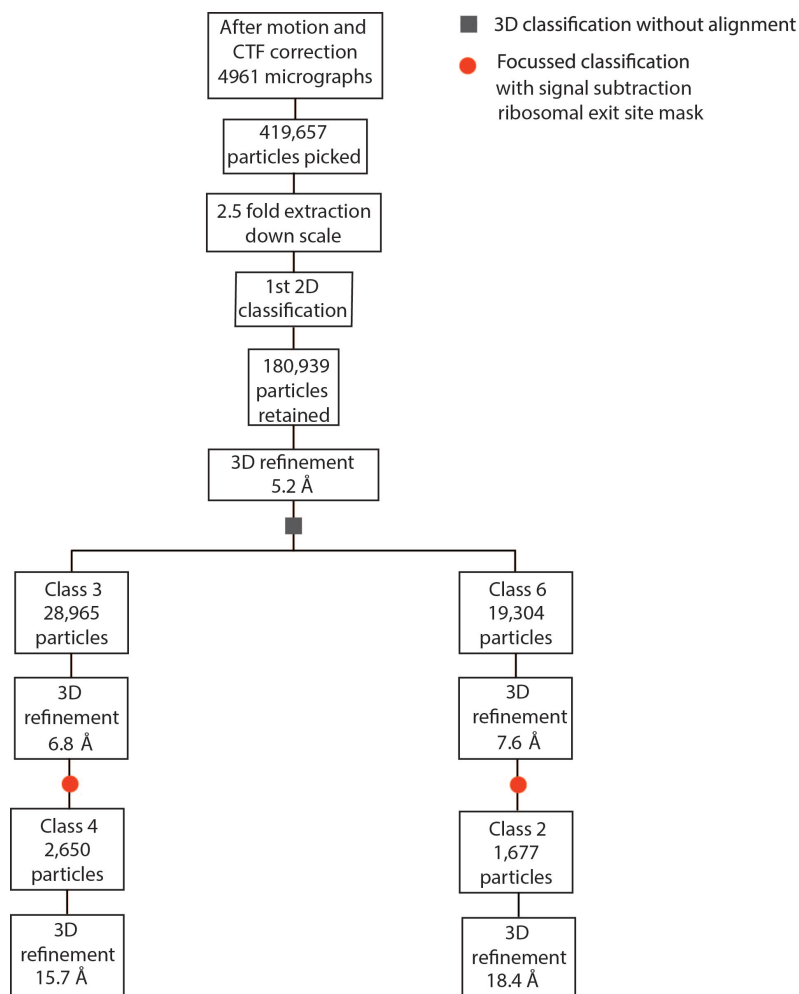


Figure 74 - Purification 6 – β -DDM buffer. RELION classification scheme.

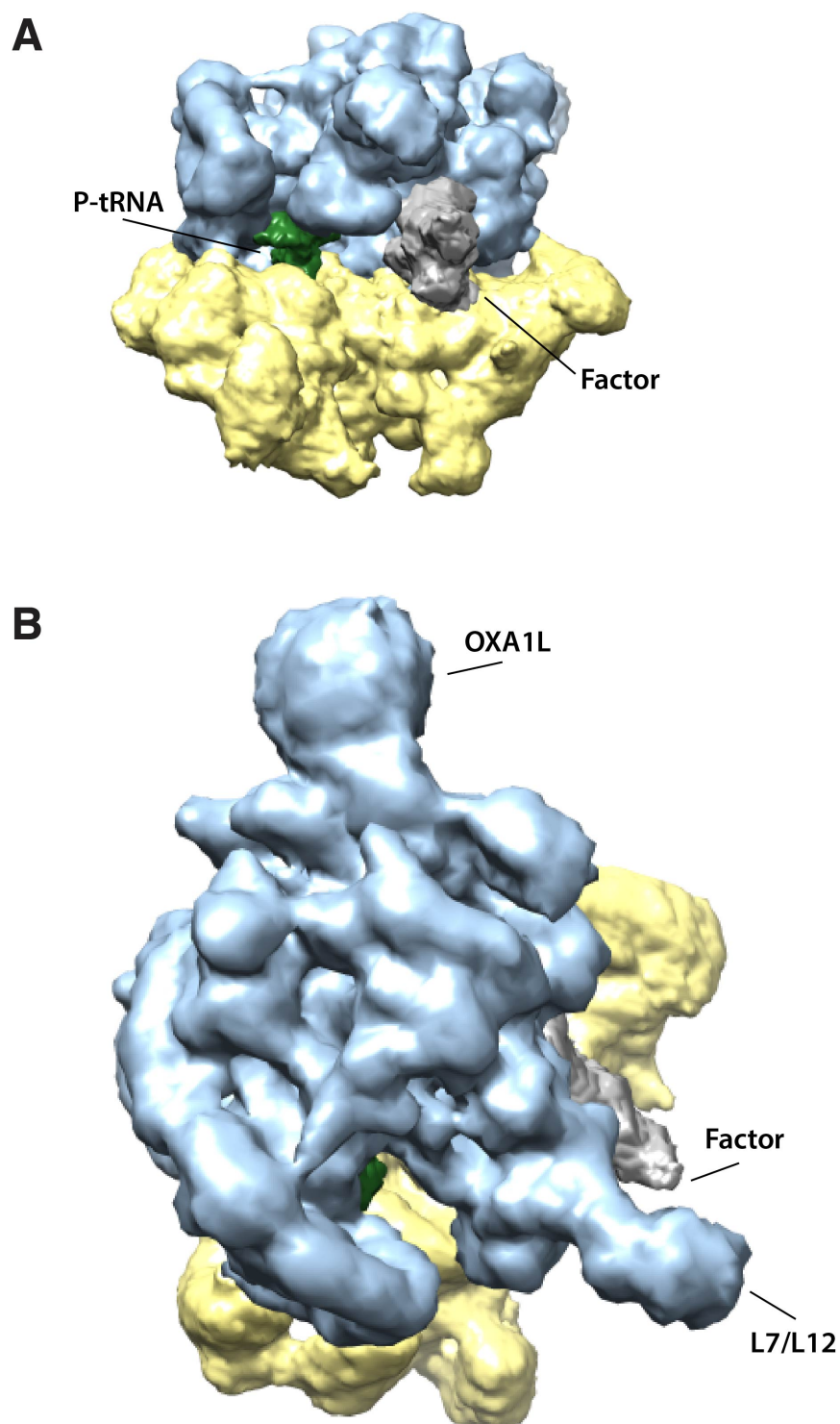


Figure 75 – Purification 6 – β -DDM buffer. FCwSS class 4 of class 3 of the initial 3D classification. 15.7 Å unsharpened map (A) Front view showing the P-site tRNA in green and the unknown factor in grey. (B) side view showing OXA1L density. Light blue = mt-LSU. Yellow = mt-SSU.

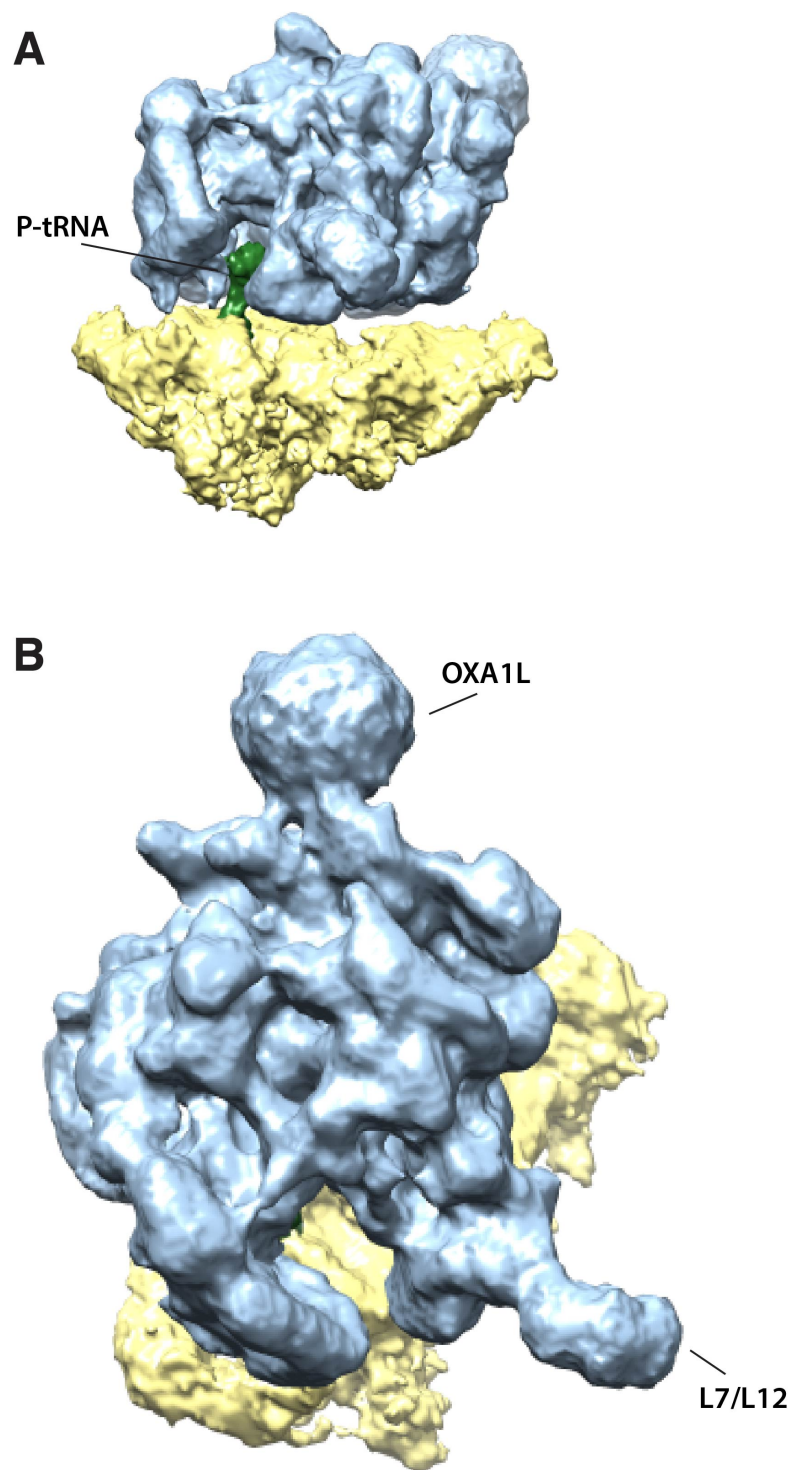


Figure 76 – Purification 6 – β -DDM buffer. FCwSS class 2 of class 6 of the initial 3D classification. 18.4 Å unsharpened map (A) Front view showing the P-site tRNA in green and the unknown factor in grey. (B) side view showing OXA1L density. Light blue = mt-LSU. Yellow = mt-SSU.

3.4 Further work and conclusions

OXA1 (OXA1L and OXA1p in humans and yeast respectively) is the inner mitochondrial membrane translocase that is instrumental in insertion of proteins translated by both mitochondrial and cytosolic ribosomes. From our experiments thus far we believe we have made significant incremental steps towards the aim of obtaining a single particle cryo-EM structure of the human mitoribosome-OXA1L complex. We have found a number of ways to stall an actively translating mitoribosomes using a variety of antibiotics. However OXA1L remained elusive under these conditions. The use of PDE12 Δ cells however revealed a density at the exit tunnel site likely to be OXA1L when using either of the two detergents β -DDM or digitonin. β -DDM is the detergent that was used in the antibiotic stalled purifications, so the assumption is that if OXA1L had remained bound under these conditions β -DDM would have been a suitable detergent. Therefore, it is likely, that although the mitoribosomes were stalled in an actively translating state, this stall may not have been robust enough to trap the translocon. Although, we also have to take into account the changes to the latter stages of sample preparation to include the shortened time of the sucrose gradient and the buffer exchange step. The detergent conditions we have used however appeared to be optimal for the purification of the ER membrane bound Sec61 translocase. This may be a positive step for mitoribosomal membrane protein purification albeit the two membrane compositions have significant differences.

We are reasonably confident that the density we see belongs to OXA1L owing to its location, size and contact points. What we can learn from our maps of OXA1L and the mitoribosome thus far is the probable contact sites being uL24m and mL45. Our current resolution is too low to infer any further details, but with higher resolution of the currently trapped structures we should be able to trace the path of the nascent chain through the polypeptide tunnel and elucidate its engagement with OXA1L. Owing to inherent flexibility, it may be difficult to obtain high resolution information for the complete OXA1L, but areas that contact the mitoribosome will likely be of a higher resolution as already seen in our local resolution map (Figure 62). Our plan at this stage is to collect further data concentrating on the β -DDM

solubilised samples. We aim to collect data on both the mt-LSU and monosome peaks in the PDE12-/- sample, with the end goal of combining the data to achieve higher resolution. This may pose a difficult challenge due to the low abundance of the mitoribosome particles with OXA1L. However, it is likely that due to the current sizes of the data sets, particles are being missed and discarded at the classification stage that would otherwise have been retained if the classification was done on a larger starting population. There may be a population of particles with the translocon in slightly different orientations that are not able to be classified effectively into a translocon containing class due to low numbers. Combining the particles before the classification stage may help to retain subpopulations that could contain our structure of interest and increase the size of the main translocon class.

It is evident from our western blot results and the subsequently seen maps that OXA1L-mitoribosome binding is likely present in our samples even if the apparent occupancy by cryo-EM is low. However, we have been unable to quantify the stoichiometry without purified OXA1L. In the PDE12-/- data sets, the mitoribosomal particles that do not have OXA1L still have a P/P mt-tRNA indicating active translation. The issues may be that OXA1L is dislodged during sample handling and grid preparation, or the nascent chain being translated by that particular mitoribosome does not have a strong enough interaction with OXA1L to encourage interaction with the mitoribosome. However, we have also seen in our data set binding of OXA1L to a presumed inactive mt-LSU subunit. Additionally as only a proportion of mitoribosomes are attached to the membrane, as seen by cryo-ET, this decreases the chance of purifying a mitoribosome attached to the inner membrane (100). To complement data collection, further experiments trialling different detergents as well as detergent and phospholipid combinations will also be explored to aid OXA1L stabilisation. Alternative such as amphipol or nanodisc technology will also be considered.

To conclude, we have made significant initial progress towards elucidating the structure of OXA1L bound to the human mitochondrial ribosome but further work remains to be done to reveal high resolution information.

3.5 Materials and Methods

Experimentation was done in collaboration with Dr Hanting Yang.

3.5.1 Purification of human mitochondria

Human mitochondria was obtained from HEK293S TetF GnTI or PDE12(-/-) HEK293 cells. PDE12 -/- HEK293 cells were kindly gifted by Dr Michal Minczuk and Dr Sarah Pearce (218). HEK293S TetF GnTI were gifted and initially grown by Pat Edwards. HEK293S TetF GnTI cells were grown in freestyle media (Gibco, Life technologies) with 5% fetal calf serum (Gibco, Life technologies) at 37°C with 5% carbon dioxide, in 10L Wave bioreactors (GE Healthcare) to $\sim 2\text{-}3 \times 10^6/\text{ml}$. The PDE12-/- HEK293 cells were initially grown adherently in Dulbecco's Modified Eagle Medium (DMEM), supplemented with 10% bovine serum (FBS) at 37°C and 5% CO₂. The cells were subsequently adapted to suspension cells grown in Freestyle media with 1% FBS at 37°C, 8% CO₂. The cells were harvested at a concentration of no more than 1×10^6 cells/ml. The cells were harvested by centrifuging at 1,000 x g for 7 minutes. They were then washed in 1L of cold phosphate buffered saline (PBS) and centrifuged at 1,200 x g for 10 minutes. The supernatant was decanted carefully and the pellet weighed. Every 100g of pellet was resuspended in 600 ml MIB buffer (50 mM HEPES-KOH pH7.5, 10 mM KCl, 1.5 mM MgCl₂, 1 mM EDTA, 1 mM EGTA, 1 mM DTT, Proteinase Inhibitor (PI, 1 tablet/50ml)) and stirred for 15 minutes in the cold room. The nitrogen cavitation chamber was placed on ice and subsequently the sample was transferred to the chamber. ~ 230 mL SM4 buffer (281mM sucrose, 844mM mannitol in MIB buffer; 1/3 of the final volume of resuspended cells, yielding a final concentration of 70 mM sucrose and 210 mM mannitol) was added to the sample. The nitrogen cavitation chamber was filled with nitrogen until a pressure of 500 psi and kept on ice for 20 minutes. After 20 minutes the pressure in the nitrogen cavitation chamber was slowly released and the sample collected. This was followed by two consecutive centrifugation steps, at 800 x g for 15 minutes, to remove cell debris and nuclei. The supernatant was collected through a cheese cloth. After a further two centrifugation steps at 10,000 x g for 15 minutes, the pellet was resuspended in 50mls ($\sim 2\text{mg}/\text{ml}$) MIBSM buffer (3:1 MIB:SM). 1KU of RNase free DNase was added per 100g of cell pellet and mixed in the cold room for 20 minutes. This was followed by centrifuged at 10,000 x g for 15 minutes and resuspension in

10mls of SEM buffer (250mM sucrose, 20mM Hepes-KOH pH 7.45, 1mM EDTA) and Dounce homogenisation 5 times. The sample was then layered onto a sucrose gradient (60%, 32%, 32%, 15%) and run on the Beckman Coulter SW28 Ti rotor at 28,000 RPM for 1 hour at 4 °C. The brown mitochondrial layer was carefully collected and flash frozen in liquid nitrogen.

3.5.2 Preparation of Cardiolipin

18:1 Cardiolipin (TOCL, 710335C, Avanti) dissolved in chloroform was dried under vacuum in a CentriVap Concentrator (Labconco). The dry lipid sample was then solubilised at 25 mg/ml concentration in a low-salt buffer (1 mM HEPES-KOH pH 7.4, 5 mM KCl) with the detergent required. The sample was then sonicated in a bath sonicator for three cycles (10 s on/20 s off for 1 min).

3.5.3 Purification of human mitoribosome OXA1L complex from HEK293S cells

Frozen mitochondria purified from HEK293S TetF GnTI cells was defrosted on ice. 2-3 volumes of lysis buffer (25 mM HEPES-KOH pH7.4, 100 mM KCl, 25 mM Mg(OAc)₂, 1.5% β -DDM (D310, Anatrace), 0.15 mg/ml TOCL, 1 tablet/50ml PI, 2 mM DTT) was added to the crude mitochondria and homogenized 5 times using a Dounce homogenizer. In all purifications, antibiotics and/or GDPxP was added to the lysis buffer and the subsequent sucrose cushions, 15-30% sucrose gradients and the final buffer. The sample was stirred for 30 minutes at room temperature. It was subsequently centrifuged at 30,000 x g at 4 °C for 20 minutes to remove the insoluble material. The supernatant was collected and layered onto a sucrose cushion (1 M sucrose, 20 mM Hepes-KOH pH 7.4, 100 mM KCl, 20 mM Mg(OAc)₂, 0.6% β -DDM(D310), 0.06mg/ml TOCL, , 2mM DTT) , approximately resulting in a sample:cushion ratio of 2.5:1. The sucrose cushion was centrifuge at ~ 231, 550 x g for 4 hours at 4 °C. In the 3rd purification, the pellet from the sucrose cushion was resuspended in final buffer (20mM Hepes-KOH pH7.4, 100mM KCl, 20mM Mg(OAc)₂, 0.3% β -DDM(D310), 0.03mg/ml TOCL, 2mM DTT) to obtain an absorption of mitoribosomes at A₂₆₀ >5. In all the other preparations the resuspended pellet was loaded onto a 15-30% linear sucrose gradient (15%/30% sucrose, 20mM Hepes-

KOH pH7.4, 100mM KCl, 20mM Mg(OAc)₂, 0.15% β -DDM(D310), 0.015mg/ml TOCL, 2mM DTT) and ultracentrifuged at 80,000 x g for 16 hours. Mitoribosomal fractions were collected using the Biocomp gradient station with the Bio-rad Econo UV monitor. Fractions were pooled according to UV A₂₆₀ absorption and pelleted in Beckman Coulter TLA-120.2 rotor at 100,000 RPM, 4°C for 1 hour and resuspended in final buffer to obtain an absorption at A₂₆₀ >5. In the 2nd and 4th purification, 0.1% (v:v) glutaraldehyde was added at the time of grid making.

3.5.4 Trial of initiation of translation in mitochondria (Purification 3)

Defrosted mitochondria was heated in a water bath to 32°C for 5 minutes at pH 7.2 with mitoribosome translation buffer (100mM KCl, 5mM Mg(OAc)₂, 0.1mM amino acid mix, 0.02mM methionine, 1mg/ml BSA). Following this, mitoribosome translation arrest buffer (0.5mM viomycin, 1mM Mg(OAc)₂, 0.5mM GDPNP) was added and incubated at room temperature for 5 minutes. The subsequent lysis has been described above.

3.5.5 10-50% sucrose gradients

A sucrose gradient of 10-50% sucrose in PS buffer (50mM Hepes-KOH pH 7.4, 100mM KOAc, 2mM Mg(OAc)₂) was used to separate protein and ribosomal fractions. A Beckman Coulter TLS-55 rota was used with adapters and the sample centrifuged for 20 minutes at 55,000 RPM. 20ul of sample was extracted sequentially from the bottom of the tube after piercing a hole. 11 samples were collected numbered from 1 at the top to 11 at the bottom.

3.5.6 Western Blotting

Western blotting was performed after electrophoresis on NuPAGE™ 4-12% Bis-Tris gels (Invitrogen) and transfer to Immobilon®-FL membranes (Merck). The membrane was incubated with the primary antibodies rabbit anti-mS27 (1/750, Abcam) and mouse anti-OXA1L (1/1000, Abcam). After incubation with Alexa FluorAlas conjugated secondary antibodies, Goat anti-mouse 800 and Goat anti-

rabbit 680 (1/40,000, ThermoFisher), blots were visualized with the LI-COR Odyssey® Imaging system, and represented with green and red bands respectively.

3.5.7 Purification of ribosomes from PDE12 -/- HEK293 cells

Mitochondria were harvested using the traditional methods above from 10L of PDE12 -/- HEK293 cells at a concentration of $\sim 0.5 \times 10^6$ cells/ml. 2 volumes of lysis buffer (25mM Hepes-KOH pH7.4, 100mM KCl, 25mM Mg(OAc)₂, 1.5% β -DDM(D310), 0.15mg/ml TOCL, 0.5mM GDPCP, 1 tablet/50ml PI, 2mM DTT) was added to the crude mitochondria and homogenised 5 times using a Dounce homogeniser. The solution was stirred for 20 minutes at 4°C, followed by centrifugation at 30,000 x g 4°C for 30 minutes. The supernatant was collected and loaded onto a sucrose cushion (1M sucrose, 20mM Hepes-KOH, pH 7.4, 100mM KCl, 20mM Mg(OAc)₂, 0.6% β -DDM(D310), 0.06mg/ml TOCL, 0.1mM GDPCP, 2mM DTT) resulting in a sample cushion ratio of 2.5:1 and centrifuged at 231,550 x g for 60 minutes at 4°C. The pellet was then resuspended in resuspension buffer (20mM Hepes-KOH, pH7.4, 100mM KCl, 5mM Mg(OAc)₂, 0.3% β -DDM(D310), 0.03mg/ml TOCL, 0.25mM GDPCP, 2mM DTT). The sample was then loaded onto a 15-30% sucrose gradient and centrifuged in the Beckman Coulter TLS-55 rota at 213,626 x g for 90 minutes at 4°C. After fractionation of the gradient, the optical density at A₂₆₀ was determined by nanodrop and the fractions were pooled together according to the peaks obtained. The pooled fractions were diluted with 5-10 volumes of final buffer (20mM Hepes-KOH, pH7.4, 100mM KCl, 5mM Mg(OAc)₂, 0.05% β -DDM(D310), 0.03mg/ml TOCL, 0.25mM GDPCP, 2mM DTT), slightly rotated, then put through a 30,000 concentrator spun at 1500 x g at 4°C. The buffer was exchanged to minimize the concentration of sucrose. The samples were adjusted to an A₂₆₀ of 4-5. In some of the preparations 0.05% β -DDM (D310) was supplemented with 0.005% Cholesteryl Hemisuccinate (CHS, CH210) or substituted for 0.05% digitonin.

Purification	1	2	3	4	5 (Collection 1 and 2)	6 (Collection 1 and 2)
Magnification	75,000	75,000	75,000	75,000	75,000	75,000
Pixel size (Å)	1.06	1.06	1.06	1.06	1.04	1.04
Defocus range (-μm)	1.2-3.0	1.1-3.2	1.2-3.0	1.1-3.2	1.1-3.2	1.1-3.2
Voltage (kV)	300	300	300	300	300	300
Exposure (s)	1.79	1	1.79	1	1	1
Frames	71	39	71	39	39	39
e/Å ² /frame	0.8	2.5	1.5	1.5	1.3	1.3

Table 7 – Cryo-EM data collection on the FEI Titan Krios, Falcon III detector.

3.5.8 Electron microscopy

3μl aliquots of samples were applied to 30 second glow-discharged holey carbon grids (Quantifoil R2/2) coated with home-made continuous carbon (~50 Å thick) prior to blotting using the FEI ThermoFisher Scientific Vitrobot™. The FEI ThermoFisher Scientific Vitrobot™ conditions were set to 100% ambient humidity and 4°C. Subsequently the grids were flash frozen in liquid ethane and transferred for storage into liquid nitrogen for storage. All cryo-EM data was collected in linear mode on an FEI Titan Krios 300kV electron microscope using the FEI Falcon III detector and EPU. The data collections were done according to Table 7.

3.5.9 Image processing and figures

All data processing was done in RELION (121). All map figures were made in Chimera (167).

4 Final remarks

Since embarking on my PhD there have been further single particle cryo-EM breakthroughs of mitochondrial ribosomes to include my own project on the structure of the yeast mitochondrial ribosome (135). Other structures include the human mt-LSU late assembly intermediate; the structure of the *Trypanosoma brucei* mitoribosome; human mitochondrial initiation complexes, the human mitoribosome in complex with mt-RRF and a recent structure on *Trypanosoma brucei* mt-SSU assembly (69,71,158,214,219,220). However, the structural study of mitochondrial translation and mitoribosome assembly remains a young field compared to other ribosomes such as the eukaryotic cytosolic or the bacterial ribosome. As such, this remains an exciting area with much more to be explored.

5 Appendix

5.1 A specialised case of elongation

5.1.1 Background

5.1.1.1 Selenium, Selenocysteine and Selenoproteins

Selenium is a non-metal trace element that is an essential requirement for selenocysteine (Sec) synthesis, and hence production of selenoproteins. The two main dietary sources of selenium are selenocysteine and selenomethione from animal food products, and selenomethionine from cereal products grown in selenium rich soils. There are around 25 selenocysteine containing proteins termed selenoproteins. These selenoproteins have been found to be important in human health and disease. Examples of selenoproteins are enzymes to include glutathione peroxidases responsible for the breakdown of hydro and lipid peroxides and thioredoxin reductases catalysing thioredoxin regeneration. Known functions of selenoproteins include, the protection of membranes, proteins and nucleic acid from cumulative oxidative damage, as well as roles in male fertility and thyroid hormone homeostasis. Oxidative damage has been linked with cancers, diabetes, Alzheimer's and Parkinson's disease. Health implications can be resultant of dietary selenium deficiency, mutations in selenoproteins and also aberrations in the pathway of selenoprotein synthesis. Disease such as Keshan's disease, Kashin-Beck disease and myxedematous cretinism are caused by severe selenium deficiency (221). Mutations in selenoproteins and enzymes are linked to disorders of the endocrine, nervous, muscular, cardiovascular and immune systems (222,223). The importance of selenoproteins in health is demonstrated in mouse models where knockout of the Sec tRNA^{[Ser]Sec} gene (*Trsp*) or SECIS binding protein 2 (SECISBP2), of the selenocysteine incorporation pathway, is embryonically lethal (224-226).

5.1.1.2 Eukaryotic Translation Termination

Incorporation of selenocysteine into polypeptides on the ribosome is dependent on recoding of UGA. In eukaryotes canonical termination of protein synthesis occurs when a translating ribosome encounters one of the three universal triplet

nucleotides, UAA, UAG and UGA, encoding a stop codon. When any of the stop codons are present in the A-site of a translating ribosome, they are recognized by the release factor eRF1 that binds the ribosomal A-site and mediates the release of the nascent chain and subsequent ribosome recycling. eRF1 binds in a ternary complex of eRF1-eRF3-GTP, with GTP hydrolysis by eRF3 inducing a conformation change that leads to its dissociation and allows eRF1 to fully accommodate into the A-site, as well as bringing its universally conserved GGQ motif in close proximity to the ester bond between the nascent polypeptide and tRNA, promoting hydrolysis of this bond. A recent study by Brown *et al* presented cryo-EM structures at 3.5-3.8 Å of eRF1 interacting with each of the stop codons in the A-site (85). Consequently the ATPase ABCE1 is also recruited to the ribosome and together with eRF1 catalyses ribosome splitting and recycling. The structure of this was trapped by *in vitro* translation reactions in rabbit reticulocyte lysate exploiting the highly conserved GGQ motif and substituting this with AAQ (eRF1(AAQ)) which inhibits peptide release and allows trapping and visualisation of a pre-hydrolysis termination complex (85,227).

5.1.1.3 Ribosome Sec Incorporation

The 21st amino acid selenocysteine whose codon is UGA requires a specialised system for its polypeptide incorporation. Incorporation of selenocysteine into selenoproteins relies on mechanisms that identifies a particular UGA as a specific Sec-tRNA^{[Ser]Sec} (delivering selenocysteine) target rather than a target for eRF1 that recognises all the stop codons including UGA. Specifying a particular UGA to encode for selenocysteine requires a stem-loop structure cis-acting Sec insertion sequence (SECIS) element in the 3'UTR of the encoding mRNA and the coordination action of specific elongation factors (228-230). Features identified in some selenoprotein mRNAs are I) a conserved AUGA at the 5', and a GA at the 3' of the stem bases, as well as, II) a conserved AAR motif in the stem loop. In addition, in a subset of selenoprotein mRNAs there is also a selenocysteine codon redefinition element (SRE) down stream of the UGA further modulating selenocysteine insertion. The SECIS element is bound by the SECIS binding protein 2 (SECISBP2). Consequently a Sec-specific GTPase translation elongation factor (EEFSEC) binds selenocysteine

aminoacylated tRNA (Sec-tRNA^{(Ser)Sec}) and SECISBP2 in a complex (231-233). EEFSEC on its own cannot bind the SECIS element. SECISBP2 can also bind to the ribosome on an expansion segment of the 28S rRNA (234). SECISBP2 therefore steers the above complex into the proximity of the UGA stop codon, which is recognised by Sec-tRNA^{[Ser]Sec} (Figure 77). GTP hydrolysis of EEFSEC allows accommodation of Sec-tRNA^{[Ser]Sec} into the ribosomal A-site. Regulators of the SECISBP2-SECIS binding interaction include the ribosomal protein L30 which has been shown to interact with the SECIS element in a position which would clash with SECISBP2 binding (235). Magnesium has also been found to play an important role in SECISBP2 binding to the SECIS element. In conditions of high magnesium, the ability of magnesium to introduce a kink-turn in mRNA containing two tandem G·A pairs, decreases the SECISBP2-SECIS complex in favour of the L30-SECIS interaction (235). It is thought that once the SECISBP2-SECIS containing complex is anchored onto the ribosome, SECISBP2 may be displaced by L30 which may have a further role in Sec-tRNA^{[Ser]Sec} placement in the ribosomal A-site (235). In addition, nucleolin and eukaryotic translation initiation factor 4A3 (EIF4A3) has also been found to regulate this system (236,237). Nucleolin probably via its ability to bind the SECIS element (236).

Most selenoproteins contain only one selenocysteine to be inserted. However an exception is the protein selenoprotein P. Its mRNA comprises 10 UGA's coding for selenocysteine and contains two SECIS elements in the 3'UTR (238). With this increased numbers of selenocysteine encoding UGA's there is thought to be an increased level of insertion efficiency. This is in keeping with the already complexly regulated process of obtaining Sec-tRNA^{[Ser]Sec}.

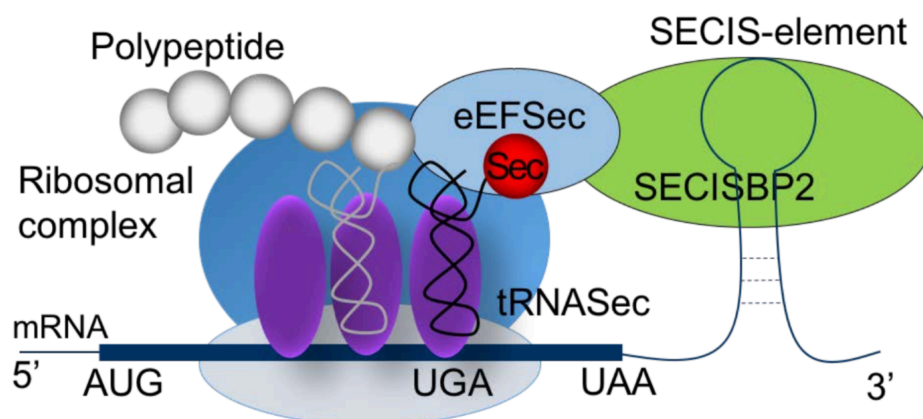


Figure 77 – Adapted image courtesy of Professor Krishna Chatterjee (IMS-MRL) (239). Graphical representation of selenocysteine incorporation into the growing polypeptide by the delivery of Sec-tRNA^{[Ser]Sec} to the A-site UGA on the mRNA by EEFSEC (eEFSEC) with the help of SECISBP2 (SBP2) through its binding to the SECIS element.

5.1.1.3.1 Selenocysteine biogenesis

Selenocysteine is a unique amino acid in that its biosynthesis occurs on its tRNA. The pathway to obtaining the aminoacylated Sec-tRNA^{[Ser]Sec} involves the initial tRNA^{[Ser]Sec} being aminoacylated with a serine by seryl-tRNA synthetase (SARS) (240). *O*-phosphoseryl-tRNA kinase (PSTK) converts the serine to a phosphoserine forming *O*-phosphoseryl-tRNA^{[Ser]Sec}. *O*-phosphoseryl-tRNA:Sec tRNA synthase (SEPSECS) uses selenophosphate to convert *O*-phosphoseryl-tRNA^{[Ser]Sec} finally to Sec-tRNA^{[Ser]Sec} or mcm⁵U/Sec-tRNA^{Sec}, which is partially methylated by an unidentified Um34 methylase (240). The required selenophosphate for the last step of the biogenesis is synthesised by selenophosphate synthetase 2 (SEPHS2) from selenide and ATP (240). An intermediate complex is subsequently formed containing Sec-tRNA^{[Ser]Sec} tRNA selenocysteine 1 associated protein 1 (TRNAU1AP) and EEFSEC on the pathway to forming the SECISBP2, EEFSEC, Sec-tRNA^{[Ser]Sec} complex.

5.1.1.3.2 Pathogenesis of selenocysteine incorporation

The importance of regulation at every step of Sec-tRNA^{[Ser]Sec} formation and selenocysteine incorporation into proteins is highlighted by the clinical manifestations of perturbations (Figure 78). A tRNA^{[Ser]Sec} mutation has been described that diminishes 2'-*O*-methylribosylation at uridine 34, presenting

clinically with low plasma levels of selenium, reduced expression of tRNA^{[Ser]Sec} with muscle weakness, fatigue and abdominal symptoms (239). SEPSECS defects have been found to cause progressive cerebellocerebral atrophy (241). A range of mutations have been identified in SECISBP2 families causing a complex phenotype to include male infertility, muscular dystrophy and photosensitivity and progressive dilatation of the ascending aorta due to cystic medial degeneration (242). In addition, observations in peripheral blood include impaired T-lymphocyte proliferation and mononuclear cell cytokine secretion (242). This diversity reflects the involvement of selenoproteins in different tissues. Lack of antioxidant selenoenzymes glutathione peroxidases (GPxs) and thioredoxin reductases (TrxRs) results in increases reactive oxygen species (ROS). Selenoprotein N (SEPN1) deficiency results in myopic features and selenoprotein deiodinase deficiency culminates in thyroid dysfunction (243). Mutations have also been found in the selenoprotein N gene's SRE element causing decreased levels of the protein and a resultant myopathy (244).

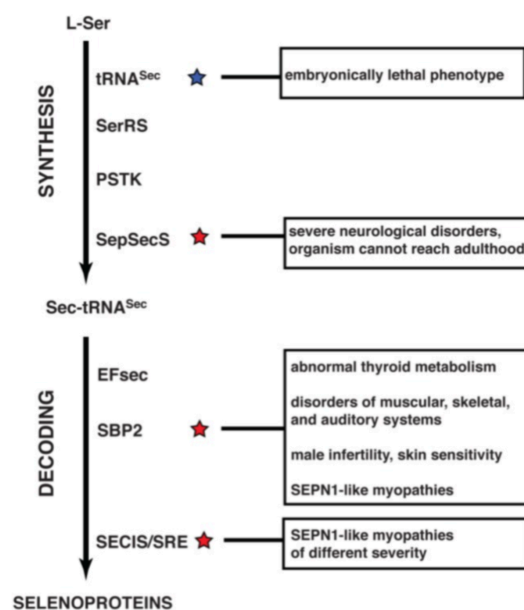


Figure 78 – Taken from Schmidt RL, Simonović M. Synthesis and decoding of selenocysteine and human health. *Croat Med J.* 2012;53(6):535–550 (222). Clinical abnormalities according to the perturbations along the pathway.

5.1.1.3.3 Structural studies of the selenocysteine incorporation pathway

Much of what we know structurally about the final incorporation step of selenocysteine into polypeptides is from prokaryotes. However the systems have some key differences. In prokaryotes the function of EEFSEC and SECISBP2 is encompassed into a GTPase called SelB. In 2016 Fischer *et al* published cryo-EM structures of six intermediates on the pathway of UGA recoding in *E. coli* to selenocysteine to include codon reading of Sec-tRNA^{Sec} with SelB bound(245). In the mammalian systems there are crystal structures of human selenocysteine tRNA and EEFSEC but as yet there is no ribosomal structure of recoding of a UGA to a selenocysteine in the mammalian system (246,247).

5.1.2 Scientific Aims

The aim of this project was to obtain the structure and conformation of different states during selenocysteine incorporation on the eukaryotic ribosome and thus reveal the underlying mechanism of selenoprotein translations. By single particle cryo-EM we aimed to image trapped Sec-tRNA^{[Ser]^{Sec}} in the process of recoding a UGA bound to EEFSEC and SECISBP2 bound to the SECIS element. Additional intermediates along this pathway may include SECIS binding of L30 and adoption of an alternative conformation of L30 to the canonical ribosomal state. Knowledge of the structure will enable us to gain more mechanistic insights into this unique situation of translation elongation. We will also be able to gain a better understanding of how certain mutations affect the function of the components involved.

5.1.3 Strategy

The strategy used by other groups to obtain the bacterial complex was to form a ribosome initiation complex with a UGA in the A-site(245). However, bacterial initiation is much less complicated and has been investigated in greater detail than eukaryotic initiation, and with the current knowledge the assembly of a mammalian initiation complex with an empty A-site would not be feasible. Previous work by the Hegde lab (MRC-LMB) has shown that ribosome nascent chain complexes could be affinity purified using a FLAG-tag on the nascent chain encoded for on a programmed mRNA (248). This strategy together with the use of eRF1(AAQ) was used in a collaboration by the Hegde and Ramakrishnan lab to elucidate the mechanism of termination in mammals on all three of the stop codons (85). We hypothesised that a similar strategy could be used to trap the selenocysteine elongation complex as the codon to be recoded as selenocysteine is the UGA stop codon.

To this end we designed an mRNA construct encoding an N-terminal FLAG peptide, a UGA stop codon down stream of this, with a SECIS element further downstream towards the 3' end of the mRNA. The stop codon would initially be bound by eRF1(AAQ) in the initial *in vitro* translation step, later to be high salt washed to leave

the UGA stop codon of the mRNA primed in the ribosomal A-site. Following FLAG affinity purification of this ribosome nascent chain complex, purified EEFSEC, Sec-tRNA^{[Ser]^{Sec}}, SECISBP2 and GDPPCP a non-hydrolysable GTP analogue would be added to the mix. We hypothesised that SECISBP2 would initially form a complex with EEFSEC and Sec-tRNA^{[Ser]^{Sec}} followed by binding to the SECIS element in the 3' of the mRNA.

5.1.4 Results and Discussion

5.1.4.1 Preparation of materials

SECISBP2 was cloned into a pET28a vector with a twin strep tag, 3X FLAG-tag and PreScission protease at the N-terminus by Dr Erik Schoenmakers (IMS-MRL, Chatterjee group) using the method developed by Gibson (249). A His-tag was subsequently added at the C-terminus using round the horn mutagenesis. EEFSEC was Gibson cloned into the same two vectors as for SECISBP2. EEFSEC isoform 1 was used which is 596 amino acids in length. Purification of EEFSEC and SECISBP2 was a collaboration with Dr Yuliya Gordiyenko (MRC-LMB, Ramakrishnan Group). Details of the cloning and protein purification can be found in the methods section 5.1.6. Additionally eRF1(AAQ) was obtained from lab stocks prepared by Dr Yuliya Gordiyenko and Dr Viswanathan Chandrasekaran (MRC-LMB, Ramakrishnan group).

A total of 3 different sequences encoding for mRNA was designed, 2 from the human sequence of PHGPX (GPX4) and 1 from the rat PHGPX sequence. PHGPX encodes for the protein phospholipid hydroperoxide glutathione peroxidase that plays a role in protecting membranes against lipid peroxidation. Its high abundance in mammalian testis is suggestive of efficiency of selenocysteine incorporation (238).

The final mRNA design contained a 3X FLAG sequence at the 5' end followed by β -VHP-3 x leucines, a linker sequence and a stop codon. The β -VHP protein sequence is a tightly folded domain just outside the ribosomal exit tunnel used previously by other groups to anchor the 3X FLAG at the end of the sequence in the vicinity of the ribosome (248).

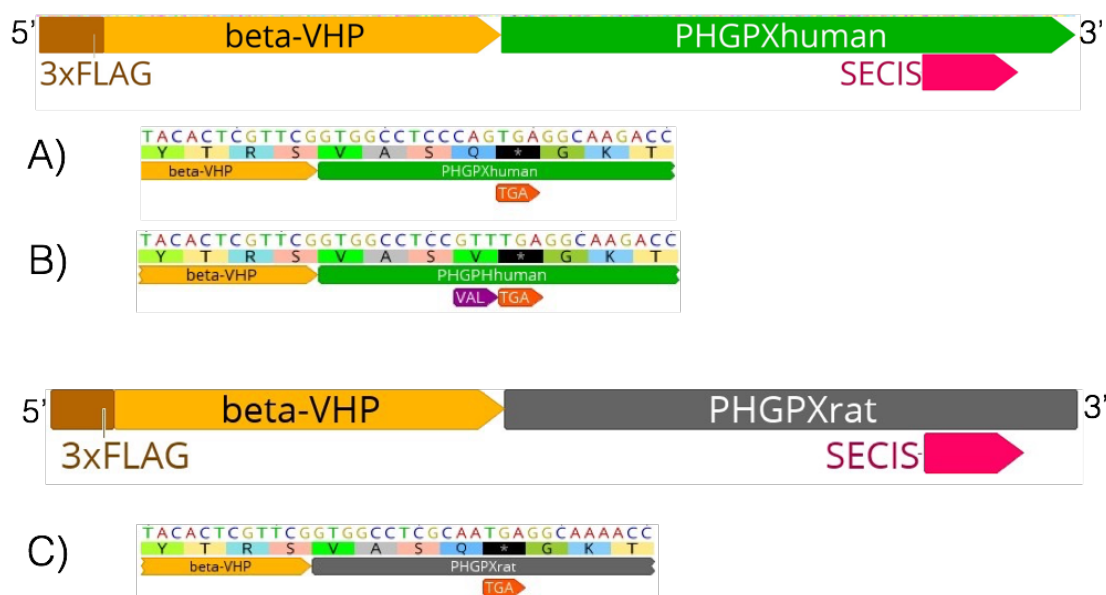


Figure 79 – mRNA designs. 3X FLAG-tag followed by a β -VHP (villin head piece) and the PHGPX gene to include the SECIS element. (A) Human PHGPX. (B) Human PHGPX modified to have a valine codon before the selenocysteine incorporating TGA. (C) Rat PHGPX.

The human constructs differed from each other in that in one of the constructs the glutamine upstream of the TGA was mutated to a valine to increase nascent chain stability within the ribosome, while the other retained the glutamine (250). In all constructs the TGA was followed by the gene sequence to include the SECIS element. However, stop codons in the non coding region down stream of the TGA were mutated to alanine's to minimise interference with eRF1(AAQ) binding to the STOP codon of interest in 3 of the constructs. The mRNA geneblocks were Gibson cloned into a pSP64-3X FLAG-beta-VHP-3Lcommon. Following this, the desired DNA fragment was obtained by PCR and *in vitro* transcribed using the SP6 promoter to obtain the mRNA.

To obtain the aminoacylated Sec-tRNA^{[Ser]Sec}, total tRNA from fresh pigs liver or testis was obtained from fresh products. Once total tRNA was purified we used FLAG tagged EEFSEC to affinity purify Sec-tRNA^{[Ser]Sec} in the presence of GTP, and subsequently purified the Sec-tRNA^{[Ser]Sec} bound to the EEFSEC. To liberate the Sec-tRNA^{[Ser]Sec} a phenol extraction and ethanol precipitation was performed. We performed a non-quantitative test of our ability to purify Sec-tRNA^{[Ser]Sec} by performing a reverse transcription experiment, followed by PCR amplification of the

cDNA which was subsequently sent for sequencing. Sequencing results yielded tRNA^{[Ser]^{Sec} however this does not give us an indication of the whether or not the tRNA was aminoacylated.}

The function of the purified SECISBP2 and EEFSEC was tested by Dr Erik Schoenmakers using a luciferase luminescence measuring assay (251). Increased relative light units measured in the assay correlated with increased rates of translation. Thus, the translation rates were determined in the presence of a UAA control and UGA mRNA with increasing amounts of EEFSEC and SECISBP2. The results showed that with increasing concentrations of SECISBP2 translation rates increased accordingly (Figure 80). This was not the case with addition of EEFSEC where the rates did not appear to increase. These results are consistent with rabbit reticulocyte lysate being devoid of SECISBP2, and EEFSEC being present in non-limiting quantities.

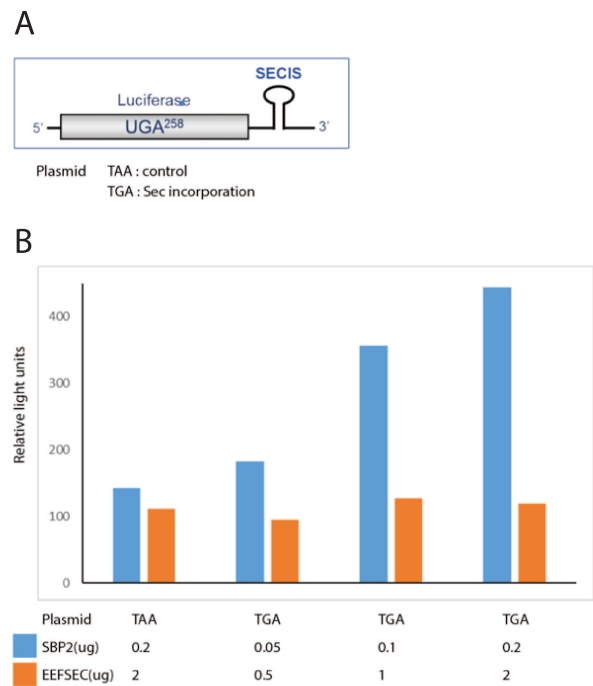


Figure 80 - Courtesy of Dr Erik Schoenmakers. Luciferase assay. (A) UGA or UAA at position 258 in luciferase gene followed by a SECIS element sequence. (B) Results of luciferase assay after adding increasing amounts of SECISBP2 or EEFSEC. TAA (UAA) represents the control.

The competence of the components to form a stalled complex was evaluated with an *in vitro* translation experiment was set up using S^{35} methionine with and without eRF1(AAQ). The results of the crude *in vitro* translation experiment showed that without eRF1(AAQ) the polypeptide was largely detected at ~17 kDa (as predicted by the molecular weight of the full released nascent chain) and that with addition of eRF1(AAQ) the radioactive band was largely detected at ~37 kDa suggesting the trapped nascent chain tRNA complex (Figure 82 (A)). This showed, that without eRF1(AAQ), there was limited read through and the transcript terminated at the UGA stop codon. However, termination at this stop codon would also result in ribosome dissociation. In the presence of eRF1(AAQ) there was the same termination at the stop codon but in addition the polypeptide was likely still attached to the ribosome as evidenced by the polypeptide chain being detected in complex with the tRNA at ~37 kDa. To further test this, the crude samples were run on a 10-50% sucrose gradient and 11 equal fractions taken. Aliquots of these fractions were run on a protein gel and the S^{35} methionine radioactivity detected (Figure 81 B-D). The results showed that without eRF1(AAQ), for all the mRNA transcripts, the majority of the polypeptide was in the free fractions in lanes 1-4. There was also some evidence of stalling on the ribosome too as evidenced by the higher ~37 kDa band being present in the ribosome fractions, approximately lanes 6-9. With eRF1(AAQ), for all the transcripts, there was an increase in the polypeptide chain in fractions 6-9 representing ribosomes with tRNA bound polypeptides.

Thus, the mRNA transcripts have been shown to have the ability to translate, and increased stalling can be achieved at the UGA using eRF1(AAQ). So with this and the purified EEFSEC, SECISBP2 and Sec-tRNA^{[Ser]^{Sec}} an initial complex formation experiment was set up.

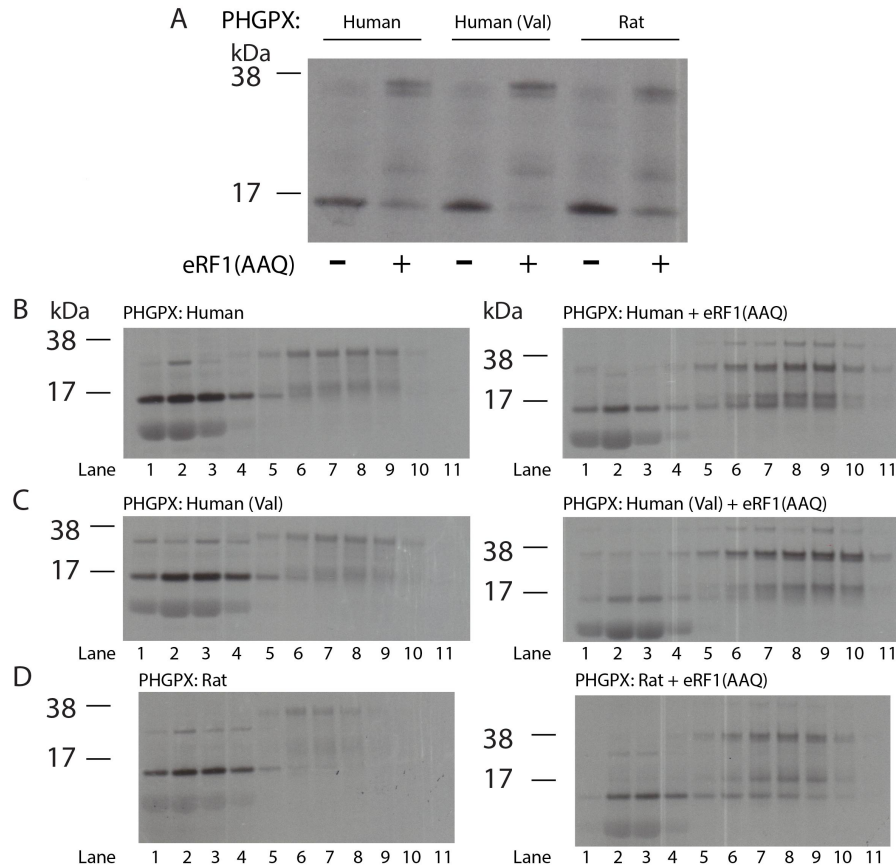


Figure 82 - *In vitro* translation experiments using S^{35} methionine. (A) Using the 3 PHGPX transcripts human, human (val) and rat, with or without eRF1(AAQ). (B-D) Aliquots from the experiments were run on a 10-50% sucrose gradients with and without eRF1(AAQ) and 11 equal aliquots taken for analysis.

5.1.4.2 Initial complex formation

We set up a 2ml *in vitro* translation reaction in the presence of 0.5uM eRF1(AAQ) to trap the termination complex using the standard human PHGPX mRNA sequence. After 25 minutes *in vitro* translation the translation reaction was adjusted to a high salt environment with 750mM KOAc and 15mM Mg(OAc)₂ at room temperature for 5 minutes to remove the bound eRF1(AAQ). The reaction was then spun on a high salt 0.5M sucrose cushion to pellet the ribosomes. The pelleted ribosomes were resuspended in RNC buffer (5.1.6.10) and mixed with anti-FLAG M2 beads for 1 hour at 4°C to allow the FLAG motif on the nascent chain to bind to the beads. After sequential washes the ribosome nascent chain complex was eluted from the beads using 3X FLAG peptide and pelleted. For resuspension 1360nM Sec-tRNA^{Sec}, 500nM EEFSEC, 475nM SECISBP2 and 28 fold excess of GMPPCP were added with RNC

buffer to then pellet to reach an A_{260} of 6. Grids were made as described section 5.1.6.11 and the data was collected on the 300 kV FEI Titan Krios on a Falcon II detector.

Though initially planned, the final sample was not tested by 10-50% sucrose gradient centrifugation with subsequent western blotting (to assess for co-migration with ribosomes) as the amount of obtained sample proved to be limiting. In future experimentations we would either run western blots or the initial protein gels in parallel with the purified protein to correlate the bands.

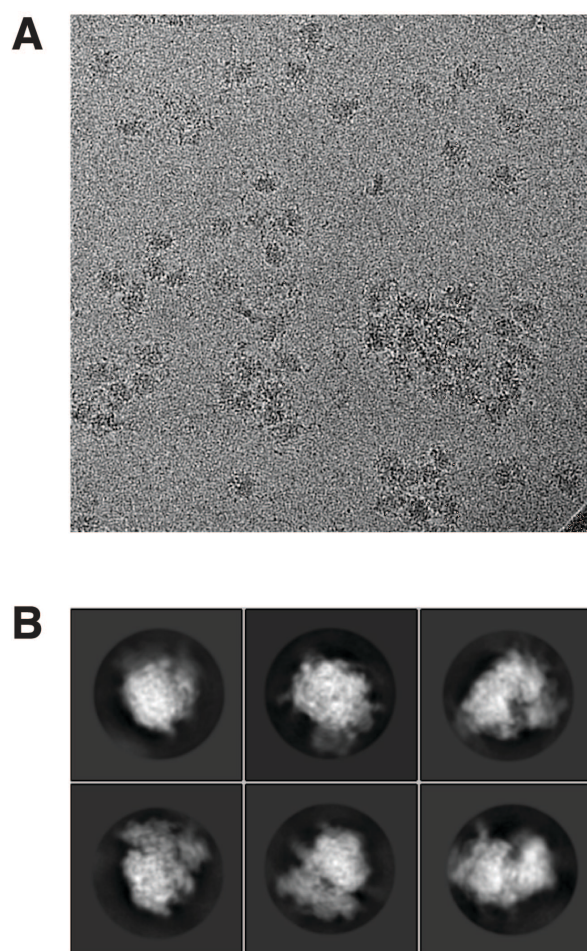


Figure 83 - Data collection. (A) Representative micrograph. (B) Representative 2D's.

An initial data set was collected to ascertain binding of the complex components to the ribosome under the chosen conditions. In particular the data set was evaluated as to whether it contained the predicted ribosome nascent chain complex with a P-

site tRNA. The data collection over 1 day resulted in 108,611 particles being initially picked. The particles were then extracted with a 2.5 fold downscale and after subsequent 2D classification 66,705 particles were retained. The initial 3D refinement achieved a resolution of 8.4 Å. Focussed classification with signal subtraction was performed on the ribosomal factor site to determine whether there was a subclass of particles that contained a factor that was being averaged out in the complete refinement. After several rounds of focussed classification one class was found (class 3 – 3883 particles) that contained density in the factor site. After 3D refinement this yielded a map at a downscaled resolution of 17.4 Å (Figure 84). However contrary to the prediction of an actively translating insertion complex there was no tRNA in the ribosomal P-site. However, the presence of other classes that contained a tRNA in the P-site suggested that the first half of the preparation (pull down of actively translating ribosomes with a tRNA in the ribosomal P-site and an empty A-site) was successful (Figure 85). At this resolution it is difficult to know if the factor bound is EEFSEC with Sec-tRNA^{[Ser]_{Sec}}. It may also represent non specific EEFSEC binding or eRF1(AAQ) binding that has not been removed by the salt wash. Although on docking in eRF1(AAQ) the model does not fit the map well, albeit the resolution of the map is currently low.

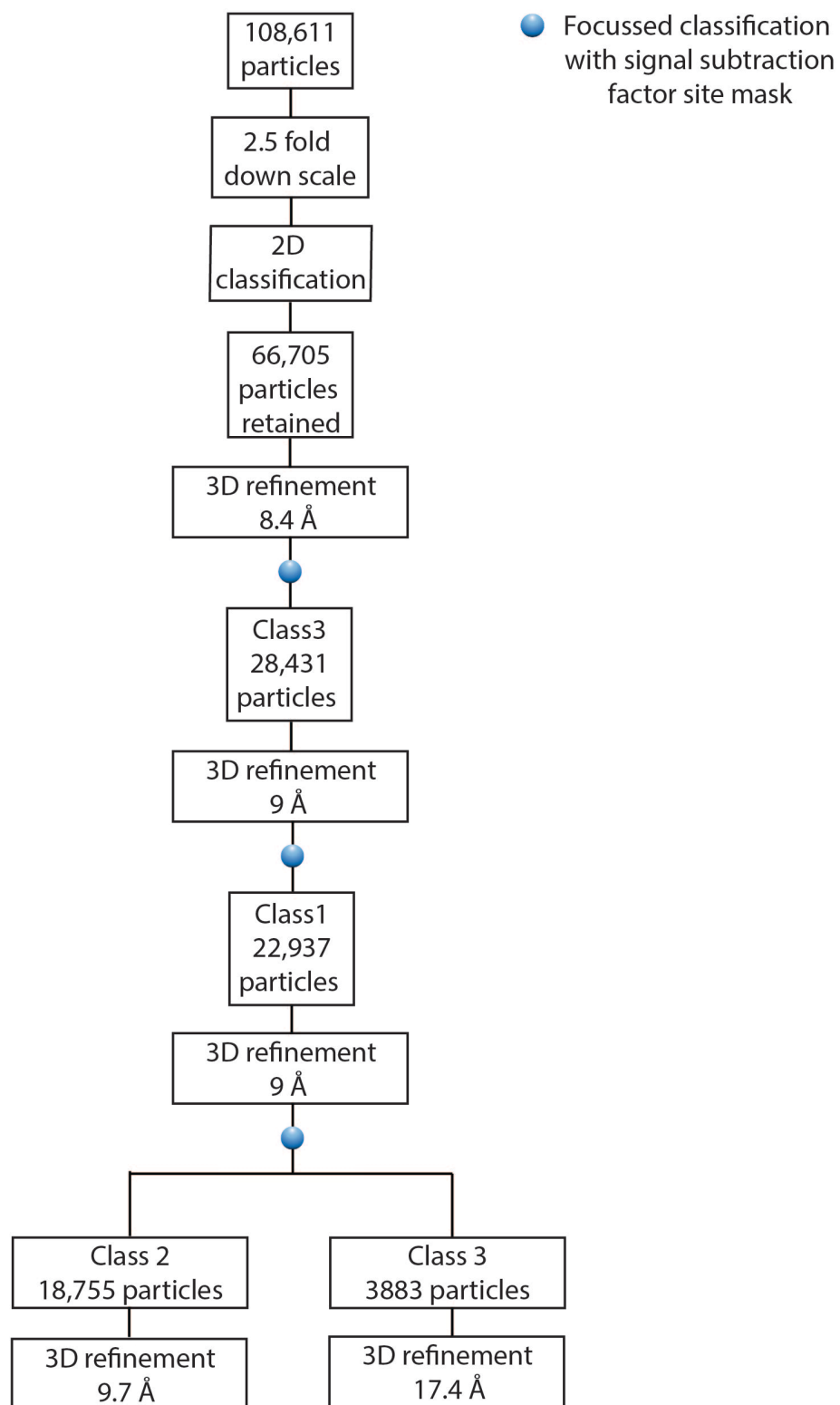


Figure 84 – RELION classification scheme of selenocysteine data collection

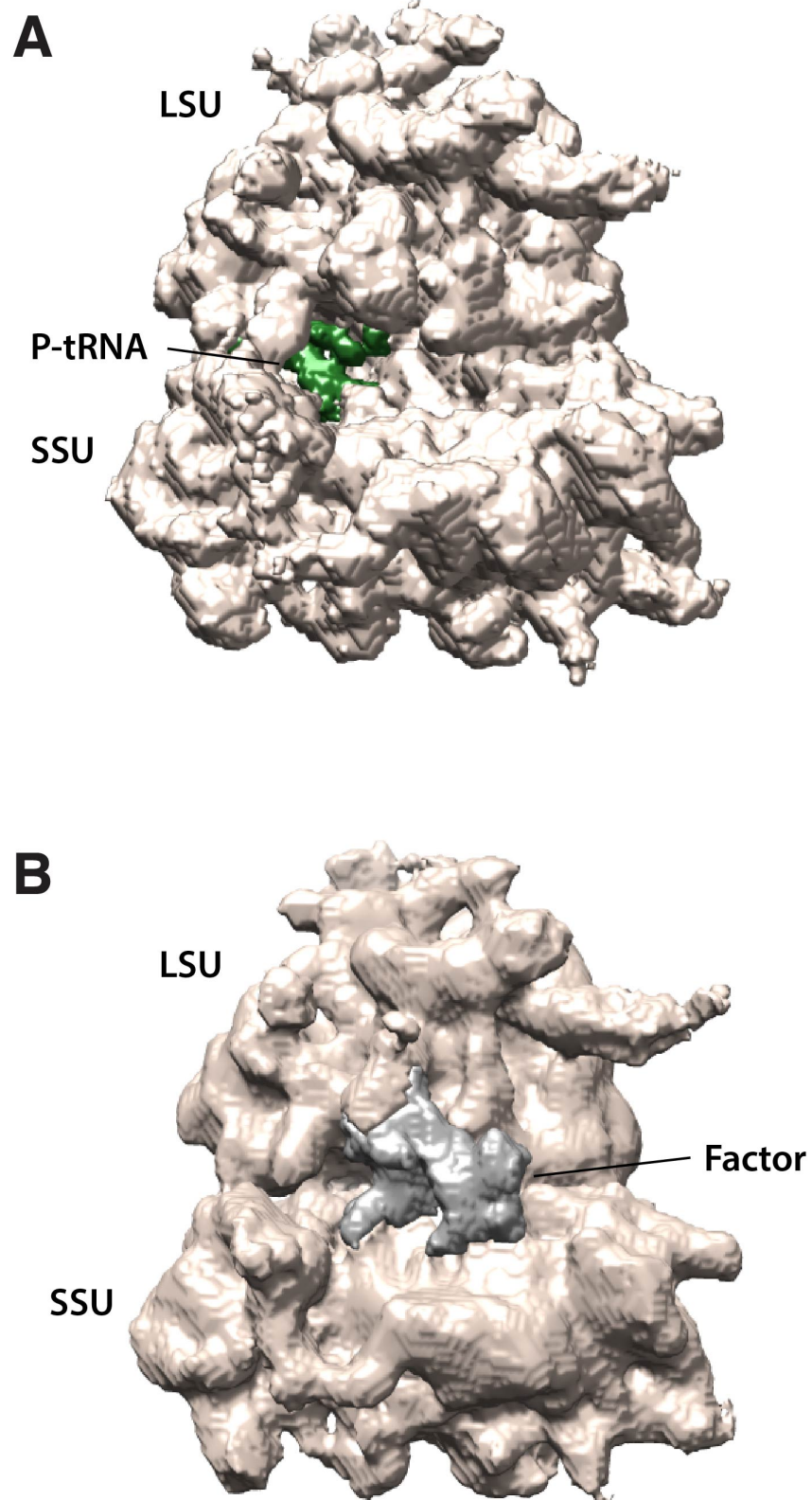


Figure 85 – Post 3 rounds of focussed classification with signal subtraction on ribosomal factor site. (A) Class 2 (B) Class 3.

5.1.5 Conclusions

Thus far, we have purified the components for an initial trial of complex assembly. Radioactivity experiments have confirmed that the specially designed mRNA can be translated in our rabbit reticulocytes lysate *in vitro* translation system. In addition, there is evidence that the polypeptide produced runs in the ribosomal fractions of our sucrose gradient and there is further evidence provided by its association with tRNA. Furthermore, the presence of actively translating ribosomes is confirmed by the presence of P-site tRNA bearing classes in the collected dataset.

The luciferase assays have confirmed that the SECISBP2 protein purified is functional and able to regulate selenocysteine incorporation into the growing polypeptide. The purified EEFSEC could not be verified as functional in this assay as EEFSEC is not in limiting amounts in rabbit reticulocyte lysate. To address this problem we are in the process of setting up a wheat germ based *in vitro* translation system, which in the wild type does not contain selenocysteine-incorporating abilities, but adding SECISBP2, Sec-tRNA^{[Ser]Sec} and EEFSEC has been described to initiate Sec incorporation (252).

We have verified that Sec-tRNA^{[Ser]Sec} is available in the purified sample by reverse transcription. However, this does not tell us if the tRNA is aminoacylated and functional. Additionally our initial yield of purified Sec-tRNA^{[Ser]Sec} was small. In order to increase the yield of Sec-tRNA^{[Ser]Sec} we also obtained total tRNA from pig testis known to be a rich source of Sec-tRNA^{[Ser]Sec}. The Sec-tRNA^{[Ser]Sec} obtained from this method has not yet been used in experiments.

Currently the EEFSEC is stalled by the non-hydrolysable GDPCP during complex formation. Additional ideas to enhance both stalling and promote complex formation have not yet been explored experimentally. Additional strategies would include the addition of spermidine, and didemnin B elongation inhibitor, to support complex formation (253,254). Spermidine is a polyamine known to have positive effects on translational efficiency and fidelity (255). Didemnin B has been found to trap eEF1A in a post-hydrolysis GDP-bound state. eEF1A being the eukaryotic

elongation factor responsible for bringing aminoacylated tRNA's that show sequence and structural similarities with EEFSEC (233,247).

Furthermore, it has been found that magnesium plays an important role in selenocysteine incorporation owing to its ability to regulate RNA secondary structure (256). Thus, we aim to optimize magnesium levels in the sample buffers.

Although SECISBP2 and EEFSEC have been found to be the only necessary components for selenocysteine incorporation via Sec-tRNA^{[Ser]^{Sec}}, it may well be that there are other factors affecting the efficiency of the process that may be vital for trapping the structure (251). One idea discussed is to produce rabbit reticulocyte lysate devoid of eRF1 and add this lysate at the complex formation stage. Removal of eRF1 would ensure that there is no competition with EEFSEC- Sec-tRNA^{[Ser]^{Sec}} for A-site binding when the lysate was added. This modified rabbit reticulocyte lysate could provide the additional factors and aid complex formation efficiency.

Two further strategies have been envisaged. 1) A selenocysteine containing protein selenoprotein P (SELENOP) is unusual in that it contains multiple UGA codons (256). In addition SELENOP is unique in that it contains two SECIS elements. It is therefore hypothesised that, as many selenocysteine residues need to be incorporated into selenoprotein P, the process of doing so is likely to be more tightly regulated. Thus, we aim to repeat the experiments already performed with the SELENOP transcript cloned into our vector for mRNA production. 2) The second strategy is to generate a mutant EEFSEC that does not permit GTP hydrolysis, thereby keeping EEFSEC on the ribosome without the need for GDPCP. It has been found that in EEFSEC the residues threonine 48, aspartate 92 and histidine 96 are important for GTP hydrolysis but mutation does not effect the structure of EEFSEC or its ability to bind GTP/GDP (247). On addition of the mutant EEFSEC to the *in vitro* translation reaction it would compete with wild type eRF1. The aim would be to add an excess of EEFSEC that would bind endogenous or supplemented Sec-tRNA^{Sec}. Then, after *in vitro* translation, the ribosome nascent chain complex would be enriched for by a 15-30% sucrose gradient. The monosome fraction would be the presumed complex as the ribosomes that had bound wild type eRF1 would likely have split for recycling.

Thus, to conclude, this project is currently an ongoing study with multiple exciting avenues that remain to be explored on the path to achieving the structure. This project remains an ongoing collaboration with lab of Dr Krishna Chatterjee.

5.1.6 Materials and Methods

5.1.6.1 Cloning

SECISBP2 was Gibson cloned into a pET28a vector with a twin strep tag, 3X FLAG-tag and PreScission protease (pET28a-TST-3X-FLAG-PP) at the N-terminus by Dr Erik Schoenmakers (249). A C-terminus His-tag was subsequently added by round the horn mutagenesis (257,258). EEFSEC was also cloned into the same vectors with and without a C-terminus His-tag. EEFSEC isoform 1 was used which is 596 amino acids in length. The primers used for obtaining the linear vectors and inserts for Gibson cloning and the round the horn mutagenesis are in (Table 8).

Primer (PCR extension time in minutes)	Direction	Sequence
Gibson Vector: pET28a-TST-3X-FLAG-PP (3.5)	Forward	5' TGAGATCCGGCTGCTAAC 3'
	Reverse	5' GGGCCCCTGGAACAG 3'
Insert: EEFSEC (3.5)	Forward	5' CTGGAAGTCCTGTTCCAGGGGCCCATGG CAGGGCGGCG 3'
	Reverse	5' GGCTTTGTTAGCAGCCGGATCTCAGGGA GACTGAACCATGCGC 3'
Phos-RTH-pET28a	Forward	5'-/5Phos/TGA GAT CCG GCT GCT AAC-3'
SECISBP2: Phos-RTH—His (4)	Reverse	5'-/5Phos/GTG GTG GTG GTG GTG GTG TAA ATT CAA ATT CAT CAT TTG AGA G-3'
EEFSEC: Phos-RTH—His (3.5)	Reverse	5'-/5Phos/GTG GTG GTG GTG GTG GTG GGG AGA CTG AAC CAT GCG -3'GTG GTG GTG AGA CTG AAC CAT GCG -3'
Gibson Vector: pSP64-3XFLAG-betaVHP-TAG-3L (3.5)	Forward	5'- CGA ACG AGT GTA CTT GCC CC -3'
	Reverse	5'- GAA TTC GTA ATC ATG GTC ATA GCT G -3'

Table 8 – The primers used for obtaining the linear vector and inserts for cloning and the round the horn mutagenesis.

PCR reaction		
Component	Volume /50µl	Concentration
water	32.5	
5x HF buffer	10	1x
50x dNTPs	1	1x
Template plasmid 10 ng/µl	1	10ng
Forward primer 10nM	2.5	25pmol
Reverse primer 10nM	2.5	25pmol
Phusion enzyme 2units/µl	0.5	1 unit

Table 9 – Polymerase chain reaction components and concentrations.

PCR cycling parameter			
Cycle step	Temp (°C)	Time	N.o of cycles
Initial denaturation	98	30s	1
Denaturation	98	10s	1
Annealing	55	30s	1
Extension	72	variable	30
Final extension	72	10m	1
Hold	4	-	1

Table 10 – Polymerase chain reaction cycling parameters.

PCR has been performed according to Table 9 and Table 10. The extension times are as in Table 8. 1ul of 1M Tris-HCl pH7.5 and 0.5ul Dpn1 was added per 50ul of PCR reaction and incubated for 37°C for 90 minutes. The size of the product was then verified using agarose gel electrophoresis. 100mls of 0.5x TBE was heated for 2 minutes in the microwave with 1g agarose to produce a 1% agarose gel. This mixture was cooled to room temperature and 10ul of GelRed nucleic acid stain 10,000X (Biotium 41002) was added. The mixture was poured into an Owl™ EasyCast™ B1 Mini Gel Electrophoresis to cast the gel. The samples were mixed with loading dye and together with the DNA ladder loaded onto the cast gel and run at 150V (Pharmacia Biotech EPS3500 XL) for 50 minutes at room temperature in 0.5X TBE. The PCR product was purified using QIAquick® PCR Purification Kit. The eluted products were quantified using UV absorption. For Gibson cloning 3-20X molar excess of insert PCR was added to 150ng of vector PCR. 2X Gibson assembly master mix E2611-NEB was added to the same volume of the above mixture and incubated at 50°C for 15 minutes in a water bath. A proportion of the mixture was diluted in water and transformed in 100µl of DH5α cells. The mixture was tapped

gently before sitting on ice for 20 minutes, followed by heat shocking at 42°C for 45 seconds and recovering on ice for 2 minutes. 300µl of LB was added and agitated at 37°C for 1 hour. For cloning into pET28a-TST-3XFLAG-PP, the mixture was plated on Kanamycin + TYE plates and incubated at 37°C for 24 hours. 5mls of LB with 1X kanamycin was inoculated with single colonies from the plates and shaken at 37°C for 24 hours and mini prepped using QIAquick Spin Miniprep Kit. After mini prepping, 2µl of the prepped plasmid was added to 8µl of restriction digest master mix (1µl smart buffer, 0.2µl restriction enzyme, 6.8µl water) and incubated at 37°C for 10 minutes. BAMH1 and NCO1 restriction enzymes were used for SECISBP2 and EEFSEC plasmids respectively. The products were run on a 1% agarose DNA gel. Promising clones were sent off for sanger sequencing with GATC biotech using GATC T7 as a forward primer, PET RP as the reverse primer and an additional forward primer to sequence the central part of SECISBP2 (SECISBP2 central-GATC-fwdprimer-2168818).

For round the horn mutagenesis (RTH) ligation 100ng concentration of RTH PCR was added to 1X T4 DNA ligase buffer and 200U of T4 DNA ligase and the reaction allowed to proceed for 1 hour at room temperature. The whole reaction was transformed in 100µl of DH5α cells and continued on as above.

Specifically designed geneblocks based on native rat or human selenocysteine containing proteins were purchased from Integrated DNA Technologies (Table 11). The geneblocks were subsequently Gibson cloned into the pSP64-3X FLAG – βVHP-TAG-3L in place of the TAG. The gene blocks were subsequently Gibson cloned into the vector according to the scheme above. Plating was onto ampicillin plates and inoculation into LB supplemented with 1X ampicillin. Once cloned the plasmid was subjected to DNA restriction digest using NCO1 HF and run on a DNA gel and the plasmids sent off to GATC biotech for Sanger sequencing using the SP6 forward primer and M13 reverse primer.

Name	Sequence	Description
Rat PHGPX	5'- CATTTGGGGCAAGTACACTCGTTCGGTGGCCTCGCAATGAGGCAAAACCGA CGTAAACTACACTCAGCTAGTCGATCTGCATGCCCGATACGCCGAGTGTGG TTTACGAATCCTGGCCTTCCCTTGCAACCAAGTTCGGGAGGCAGGAGCCAGG AAGTAATCAAGAAATCAAGGAGTTTGACGCCGCTACAATGTCAGGTTTG ACATGTACAGCAAGATCTGTGTAAATGGGGACGATGCCACCCACTGTGG AAATGGATGAAAGTCCAGCCCAAGGGCAGGGGCATGCTGGGAAATGCCAT CAAATGGAATTTACCAAGTTTCTCATTGATAAGAACGGCTGCGTGGTGA AGCGCTATGGTCCCATGGAGGAGCCCCAGGTGATAGAGAAGGACCTGCCGT GCTATCTCCCTACAAGTGTGTGCCCTGCACCGAGCCCCCTGCCCTGTGA CCCCGGAGCCTTCCACCCGGCACTCATGACGGTCTGCCTGAAAACCAGC CCGCTGGTGGGGCAGTCCCGAGGACCTGGCGTGCATCCCCGCCGAGGAAG GTCCAGAGGCCTGTGGCCCCGGGCTCGAGCTTCACCTTGGCTGCCTTGTGG GAATAAAGAATTCTGTAATCATGGTCATAGCTG -3'	sequence 5' to VASQ- TGA deleted. TAG in 3' end deleted if not part of the SECIS element. Part of the 3'UTR and poly A tail deleted. Overhangs for cloning purposed added
Human- PHGPX	5'- CATTTGGGGCAAGTACACTCGTTCGGTGGCCTCCAGTGAGGCAAGACCGA AGTAAACTACACTCAGCTCGTCGACCTGCACGCCGATACGCTGAGTGTGG TTTGGCGATCCTGGCCTTCCCGTGTAAACCAAGTTCGGGAAGCAGGAGCCAGG GAGTAACGAAGAGATCAAAGAGTTCCGCCGGGCTACAACGTCAAATTCG ATATGTTTCAGCAAGATCTGCGTGAACGGGGACGACGCCACCCGCTGTGGA AGTGGATGAAGATCCAACCAAGGGCAAGGGCATCCTGGGAAATGCCATC AAGTGGAATTCACCAAGTTCCTCATCGACAAGAACGGCTGCGTGGTGAA GCGCTACGGACCCATGGAGGAGCCCTGGTGATAGAGAAGGACCTGCCCCA CTATTTCTCCACAAGTGTGTGGCCCCGCCGAGCCCTGCCACGCCCTTG GAGCCTTCCACCGGCACTCATGACGGCCTGCCTGCAAACCTGCTGGTGGGG CAGACCCGAAAATCCAGCGTGACCCCGCCGAGGAAGGTCCCATGGCCTG CTGGGCTTGGCTCGGCGCCCCACCCCTGGCTACCTTGTGGGAATAAACAG ACAAATGAATTCGTAATCATGGTCATAGCTG - 3'	sequences 5' to VASQ- TGA deleted. Poly A tail deleted as well as a small portion of the 3' UTR. Overhangs added
Human- PHGPX (VAL)	5'- CATTTGGGGCAAGTACACTCGTTCGGTGGCCTCCGTTTGAGGCAAGACCGA AGTAAACTACACTCAGCTCGTCGACCTGCACGCCGATACGCTGAGTGTGG TTTGGCGATCCTGGCCTTCCCGTGTAAACCAAGTTCGGGAAGCAGGAGCCAGG GAGTAACGAAGAGATCAAAGAGTTCCGCCGGGCTACAACGTCAAATTCG ATATGTTTCAGCAAGATCTGCGTGAACGGGGACGACGCCACCCGCTGTGGA AGTGGATGAAGATCCAACCAAGGGCAAGGGCATCCTGGGAAATGCCATC AAGTGGAATTCACCAAGTTCCTCATCGACAAGAACGGCTGCGTGGTGAA GCGCTACGGACCCATGGAGGAGCCCTGGTGATAGAGAAGGACCTGCCCCA CTATTTCTCCACAAGTGTGTGGCCCCGCCGAGCCCTGCCACGCCCTTG GAGCCTTCCACCGGCACTCATGACGGCCTGCCTGCAAACCTGCTGGTGGGG CAGACCCGAAAATCCAGCGTGACCCCGCCGAGGAAGGTCCCATGGCCTG CTGGGCTTGGCTCGGCGCCCCACCCCTGGCTACCTTGTGGGAATAAACAG ACAAATGAATTCGTAATCATGGTCATAGCTG - 3'	sequences 5' to VASQ deleted. Q changed to VAL to increase stability. Otherwise all else same as Human PHGPX

Table 11 – Selenoprotein human and rat PHGPX geneblocks.

5.1.6.2 In vitro transcription

PCR reactions of the cloned mRNA geneblocks were set up using P2 and P3 primers with an extension time of 2 minutes. The PCR products were used in *in vitro* transcription reactions. Aliquots of 10X SP6 buffer (40mM Hepes-KOH pH 7.4, 60mM MgCl₂, 20mM spermidine, 100mM DTT) were prepared. The T1 mixture (1.32X of 10X SP6 buffer, 0.66mM ATP-NaOH, 0.66mM CTP-NaOH, 0.13mM GTP-NaOH, 0.66mM UTP-NaOH, 0.66mM 7-methyldiguanosine triphosphate) was also prepared and flash frozen in liquid nitrogen and stored at -80°C. *In vitro* transcription reactions were set up accordingly for a 10µl reaction (7.6µl T1 mix, 2µl 50ng/µl PCR reaction, 0.2µl RNA pol SP6, 0.2µl RNase In). The mixture was incubated at 40°C for 1 hour. The products of the *in vitro* transcription and the PCR product used for the *in vitro* transcription were run together on a 1% agarose DNA gel.

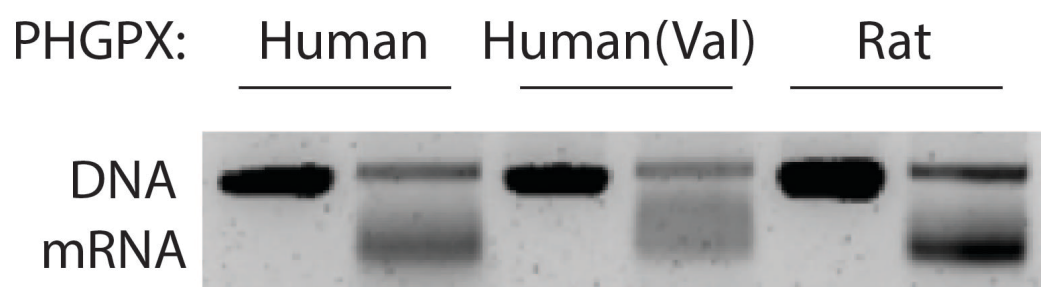


Figure 86 – PCR DNA and in vitro transcription mRNA of human, human(Val) and rat PHGPX.

5.1.6.3 Protein Purification

Protein purification was done initially in collaboration with Dr Yuliya Gordiyenko (MRC-LMB, Ramakrishnan group) . Subsequent purifications were undertaken by Dr Yuliya Gordiyenko.

5.1.6.3.1 EEFSEC for complex formation

The protein was expressed in 12L of *E. coli* Rosetta cells. Cells were induced at an OD₆₀₀ ~ 1 with 0.2mM IPTG (isopropyl β-d-1-thiogalactopyranoside) for 16 hrs at 18°C. The cells were then pelleted and resuspended in 50mls of buffer A (20mM

Tris-HCl, pH 7.5, 20mM KCl, 0.5mM EDTA, 500mM NaCl, 25% glycerol, 1% Tween) + 0.5mM PMSF. The suspension was sonicated for 5 minutes (5sec on, 10 sec off, 60% amplitude) and centrifuged at 38,000 x g for 15 min at 4 °C and filtered through a 45 µm filter. The lysate was then incubated with equilibrated in buffer A anti-FLAG M2 resin for 2h at 4°C. The beads were spun at 1000 x g for 5 minutes and washed in a small column 5 times with buffer A and 3 times with PreScission protease buffer (50mM Tris-HCl, pH 7, 150mM NaCl, 1mM EDTA, 1mM DTT, 10% glycerol). The tag was removed by cutting overnight with 5g of PreScission protease on the beads in the column in the cold room. The column was subsequently spun to collect the flow through. The flow through was mixed with 20µl of glutathione sepharose beads for 1 hour in the cold room to remove the PreScission protease. The protein was concentrated using a 30K concentrator in PreScission buffer and run on a protein gel (Figure 87). The measured concentration using Nanodrop 2000 spectrophotometer (Thermo Scientific) at A₂₈₀ was 1.3 µg/µl (~ 20 µM). 5 µl aliquots were stored at -80°C.

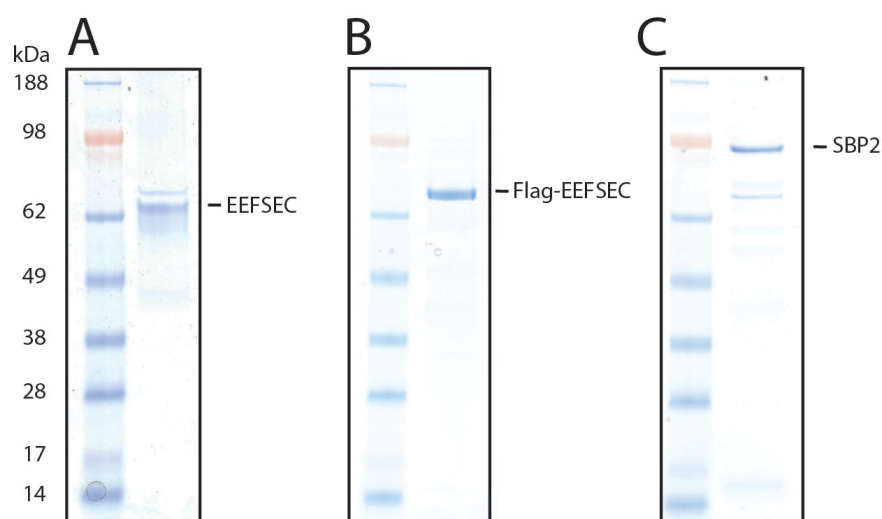


Figure 87 – Protein gels courtesy of Dr Yuliya Gordiyenko. (A) EEFSEC (B) FLAG-EEFSEC (C) SECISBP2

5.1.6.3.2 EEFSEC for Sec-tRNA^{[Ser]^{Sec}} purification.

FLAG-EEFSEC was expressed in 12L of *E. coli* Rosetta cells. The cells were induced at OD₆₀₀ ~0.64 with 0.25mM IPTG for ~16 h at 18°C. The cells were pelleted (~60g) and resuspended in 100mL of buffer A + 0.5mM PMSF. The solution was sonicated for 5 minutes (5 sec on, 10 sec off, 60% amplitude), then centrifuge at 38000 x g for 15 min at 4°C and filtered through a 45 µm filter. The lysate was equilibrated with anti-FLAG resin (2x300ul) for 2 hours at 4°C. The beads were then spun at 1000g for 5 minutes, washed in a small column 5 times with buffer A and twice with RNC+G buffer (50mM Hepes-KOH, pH 7.4, 100mM KOAc, 5mM Mg(OAc)₂, 1mM DTT + 20% glycerol). The protein was eluted with 100ug/ml 3X FLAG peptide in 500ul RNC+G buffer followed by dialysis in 1L RNC+G buffer for 1 hour and a subsequent dialysis in 1L RNC+G buffer overnight using a 14 MWCO membrane to remove the 3X FLAG peptide. Protein concentration measured by A₂₈₀ using Nanodrop 2000 spectrophotometer (Thermo Scientific) was 0.65 mg/ml = 9.4 µM (~0.32 mg total).

5.1.6.4 SECISBP2

Human SECISBP2 was expressed in 12L of *E. coli* Rosetta cells and induced at OD₆₀₀ ~1 by adding 0.5mM IPTG for 1.5 hour at 30°C. The cells were pelleted and resuspended in 50mls of lysis buffer (buffer B (50mM Tris pH8, 150mM NaCl, 5% glycerol, 2mM DTT) + 1% Triton X-100, PI, 1mM PMSF). Cells were then lysed by sonication at 60% amplitude for 5 minutes (5 sec on/10 sec off cycle). Cell debris was removed by centrifugation 38,000 x g for 30 minutes. The lysate was filtered through Mira cloth and a 45µm filter. The filtered lysate was then loaded onto a pre-equilibrated in buffer B Strep trap HP 5ml column (2ml/min) and washed with buffer B, buffer X (50mM Tris-HCl, pH8, 1M NaCl, 5% glycerol, 2mM DTT) and buffer B again. The protein was eluted with elution buffer (buffer B + 2.5mM D-desthiobiotin). The eluted protein was concentrated to 2ml and treated with 32µg PreScission protease overnight. The concentration of the protein by A₂₈₀ was 2.87µg/µl. The cleaved protein was diluted in 20ml of Ni-A buffer (50mM Tris-HCl, pH 8, 500mM NaCl, 50mM imidazole, 5% glycerol, 5mM β-mercaptoethanol) and loaded onto a pre-equilibrated 1ml Ni-column which was then washed with Ni-A buffer, followed by protein elution with Ni-B buffer (50mM Tris-HCl, pH 8, 500mM

NaCl, 500mM imidazole, 5% glycerol, β -mercaptoethanol). The eluted protein was concentrated and buffer exchanged in a 0.5ml 30 MWCO Amicon concentrator into storage buffer (50mM Hepes-KOH, pH 7.45, 200mM KOAc, 5mM Mg(OAc)₂, 5% glycerol, 1mM DTT). The concentration measured by A₂₈₀ was 0.179 μ g/ul.

5.1.6.5 Pig liver tRNA purification

This purification was done in collaboration with Dr Sebastian Kraatz (LMB-MRC, Ramakrishnan group). 1.8kg of fresh pigs liver was obtained from a local butcher's. The liver was cut into small pieces in the 4°C room and homogenized in a Waring blender using 2L ice-cold homogenisation buffer in deionised water (20mM Tris-HCl, pH 7.5, 100mM KCl, 1mM DTT). A proportion of the sample was then snap frozen in liquid nitrogen and stored at 80°C. 430g of the solid weight was processed further by centrifugation for 10 minutes at 12,000 x g at 4°C. The supernatant was collected into a flask and an equal volume of phenol was added followed by stirring for 30 minutes at room temperature in the chemical fume hood. This was then centrifuged at 4,000 x g for 15 minutes at room temperature.

The aqueous phase was collected into a new flask. An equal volume of chloroform was then added with repeated stirring for 30 minutes at room temperature in the chemical fume hood. This was followed by centrifuged at 4,000 x g for 15 minutes at room temperature. Total RNA was precipitated by 1/10 volume of 3M NaOAc (pH 5) and two volumes of reagent grade 95% ethanol at -20°C overnight. The sample was mixed and incubated overnight at -20°C. The next morning the mixture was centrifuged at 12,000 x g for 15 minutes at 4°C to pellet the precipitated nucleic acids. The pellet was air dried and resuspended in 200mls of homogenisation buffer. At this point crude tRNA was obtained. To further purify we prepared a 20ml DEAE (diethylaminoethyl) Sepharose column at room temperature and equilibrated with 400mL homogenisation buffer at room temperature. The crude tRNA was loaded onto the column, allowing the tRNA to bind to the resin, and the flow through discarded. The column was washed with >200ml of homogenisation buffer until the A₂₆₀ of the wash flow was <0.3. The tRNA was eluted by passing elution buffer (40mM Tris-HCl, pH 7.5, 50mM KCl, 500mM NaCl, 0.5mM DTT) until the eluate A₂₆₀

~ 0.1. Subsequently, the column was regenerated using high salt buffer and stored in 20% ethanol at 4°C after regeneration. Two volumes of ethanol was added to the eluate and kept at -20°C overnight. The tRNA was then pelleted at 12,000 x g at 4°C for 25 minutes, the pellet was washed with 70% ethanol, air dried and resuspended in DEPC (diethyl pyrocarbonate water). The A₂₆₀ absorbance was measured by Nanodrop 2000 spectrophotometer (Thermo Scientific) for tRNA quantification. Our total yield was 271mg of tRNA.

5.1.6.6 Sec-tRNA^{[Ser]^{Sec}} purification from pig Liver

Anti-FLAG M2 beads were equilibrated with RNC+G buffer (50mM Hepes-KOH pH7.4, 100mM KOAc, 5mM Mg(OAc)₂, 5% glycerol, 1mM DTT). 195µg (0.65µg/ul) of purified FLAG-EEFSEC was immobilized on 150µl of packed volume anti-FLAG M2 beads rotated in the 4°C cold room for 1 hour. The mixture was then transferred to small columns and spun for 30 seconds 0.1 x g and the flow through discarded. The beads in the column were washed with 300µl RNC+G buffer. 300µl of 22µg/µl total tRNA and GTP (0.5mM final concentration) were added to the column and rotated in the 4°C cold room for 1 hour to allow binding of Sec-tRNA^{[Ser]^{Sec}} from total tRNA to immobilized FLAG-EEFSEC. Washes with RNC+G buffer were repeated. The Sec-tRNA^{[Ser]^{Sec}}-FLAG-EEFSEC complex was eluted with 100µg/ml 3X FLAG peptide incubated for 30 minutes at 4°C in the cold room. The eluate was collected by tabletop centrifugation at maximum speed. To obtain Sec-tRNA^{[Ser]^{Sec}} a phenol extraction and ethanol precipitation was done as described in more detail above (5.1.6.5). Sec-tRNA^{[Ser]^{Sec}} was obtained at 54 µM.

5.1.6.7 Sec-tRNA^{[Ser]^{Sec}} purification from pig testis

1kg of fresh pigs testis (Leech's Butchers, Melbourne) was diced and flash frozen in liquid nitrogen, aliquoted into 50g portions and stored at -80°C. A 500g aliquot was taken and tRNA purification proceeded. Testis lysis buffer (20mM Tris-HCl, 100mM KCl, 2.5mM MgCl₂, 2mM DTT, 0.4mM GTP, 0.25mM spermidine, 20% glycerol, EDTA-free PI) was added and the tissue homogenized using a Waring blender in the cold room, followed by centrifugation at 12,000 x g for 30 minutes at 4°C using the JSP

F500 rotor. The supernatant was transferred to phenol resistant tubes. The supernatant and reagents were added in the following ratio 5:3:2:5, supernatant:water:5X buffer T (50mM NaOAc, 3.25mM NaCl, 50mM MgCl₂, 5mM EDTA, pH4):phenol. The mixture was inverted and centrifuged at 4000 x g for 10 minutes at 4°C. The aqueous layer containing total RNA was transferred to a clean tube and an equal volume of phenol added, vortexed and centrifuged as above for 10 minutes. The aqueous layer was removed again and mixed with 2.5 volumes of 100% ethanol and chilled at -20°C overnight. The next morning the total RNA was pelleted by centrifugation for 15 minutes at 12,000 x g at 4°C. The supernatant was removed and the RNA pellet washed gently with cold 70% ethanol. The ethanol was removed and the RNA pellet was air dried at room temperature until all the liquid has evaporated. Total RNA was resuspended in 10mM NaOAc water.

Purification of Sec-tRNA^{[Ser]Sec} from total pig testis RNA was performed as described before for pig liver Sec-tRNA^{[Ser]Sec}. To FLAG-EEFSEC immobilized on anti-FLAG beads in a gravity flow column, starting from 6L of cells, 45mg of total pig testis RNA (13.44mg/ml) was added. 10X TB buffer (20mM Tris-HCl, pH 7.5, 100mM KCl, 2.5mM MgCl₂, 2mM DTT, 0.5mM GTP) and water to reach a concentration of 1X TB buffer and incubated at 4°C for 30 minutes. The column was washed 5 times with cold 1X TB buffer. The FLAG-EEFSEC- Sec-tRNA^{[Ser]Sec} complex was then eluted with elution buffer (20mM Tris-HCl, pH 7.5, 100mM KCl, 2.5mM MgCl₂, 2mM DTT, 100 µg/ml 3X FLAG peptide). The Sec-tRNA^{[Ser]Sec} was phenol extracted from the eluate as above by first mixing with 5X bufferT in water (1X buffer T final).

Primer	Direction	Sequence
Reverse transcription Sec-tRNA ^{[Ser]Sec}	reverse	5' TGG CGCCCGAAAGGT 3'
PCR cDNA Sec- tRNA ^{[Ser]Sec}	forward	5' TGG CGCCCGA AAGGTGG 3'
	reverse	5' GCCCGGATGATCCTCAGTGG 3'

Table 12 - Primers used for reverse transcription of Sec-tRNA^{[Ser]Sec} experiment.

5.1.6.8 Reverse transcription Sec-tRNA^{[Ser]Sec}

Reverse transcription of Sec-tRNA^{[Ser]Sec} using SuperScript IV Reverse Transcriptase Thermo Fisher Scientific. The primers utilized are in Table 12. The resultant cDNA was sent off for Sanger sequencing with GATC biotech.

5.1.6.9 In Vitro Translation radioactive and 10-50% Sucrose gradient

In vitro translation was performed for each for the 3 mRNAs using S³⁵ methionine. See below for *in vitro* translation description. The products were run on a 200µl 10-50% sucrose gradient (3.5.5) and the fractions collected and analysed on a 4-12% gradient Nupage gel.

5.1.6.10 Complex formation

A 2ml *in vitro* translation reaction in rabbit reticulocyte lysate was set up in the presence of 0.5µM eRF1(AAQ) for 25 minutes at 32°C. The *in vitro* translation reaction contained 1/20 *in vitro* transcription reaction, 1/2 CT2 mix and 0.5 µCi/µL S³⁵-methionine (Perkin Elmer EasyTag). The CT2 mix contained nuclease-treated crude rabbit reticulocyte (Green Hectares), 20 mM Hepes-KOH, pH 7.4, 10 mM KOH, 40µg/mL creatine kinase (Roche), 20µg/mL pig liver tRNA, 12mM creatine phosphate (Roche), 1mM ATP (Roche), 1mM GTP (Roche), 50mM KOAc, 2mM MgCl₂, 1mM glutathione, 0.3mM spermidine, and 40µM of individual amino acids except for methionine (Sigma). After 25 minutes the reaction was adjusted to 750mM KOAc and 15mM Mg(OAc)₂ and incubated at room temperature for 5 minutes. The reaction was then centrifuged on a 0.5M sucrose cushion (50mM Hepes-KOH, pH7.4, 750mM KOAc, 15mM Mg(OAc)₂, 1mM DTT) at 100,000 RPM for 1 hour at 4°C in TLA100.3 rotor (Beckman Coulter). The ribosome pellet was resuspended in 500ul RNC buffer (50mM Hepes-KOH, pH7.4, 100mM KOAc, 5mM Mg(OAc)₂, 1mM DTT) and incubated with 100ul (packed volume) of anti-FLAG M2 beads. The beads were washed sequentially with 3ml 50mM Hepes-KOH, pH 7.4, 100mM KOAc, 5mM Mg(OAc)₂, 0.1% triton X-100, 1mM DTT; 3mls 50mM Hepes-KOH ,pH7.4, 250mM KOAc, 5mM Mg(OAc)₂, 0.5% triton X-100, 1mM DTT and 3mls RNC buffer. The complex was eluted from the beads in two sequential elutions with 100ul 0.1mg/ml

3X FLAG peptide (Sigma) in RNC buffer incubating at room temperature for 25 minutes. A further 200 μ l of RNC buffer was added to the combined eluates and centrifuged at 100,000 RPM for 20 minutes in the TLA 120.1 (Beckman Coulter). The pelleted ribosomes were incubated with 1360nM Sec-tRNA^{[Ser]^{Sec}} (12.7X excess of tRNA over ribosomes, 475nM SECISBP2 (4.4X excess), 500nM EEFSEC (4.6X excess), 28 fold excess of GMPPCP and RNC buffer to a final A₂₆₀ of 6.

5.1.6.11 Grid preparation

3 μ l sample were applied to continuous carbon coated (~50 Å) copper Quantifoil R2/2 grids. Grids were blotted for 4.5 seconds after a 30 second wait using a -15 offset at 4°C and 100% humidity using a ThermoFisher Scientific Vitrobot™. The grids were flash frozen in liquid ethane and subsequently stored in liquid nitrogen.

5.1.6.12 Electron microscopy and Image Processing

Data was collected in linear mode on a FEI Titan Krios 300kV electron microscope equipped with a back-thinned FEI Falcon III detector at a magnification of 75,000 and pixel size of 1.06 Å. 71 frames and fractions were collected per 1.79 sec exposure. 5 images were collected per hole with defocus values ranged from -1.4 to -3.2. Subsequent image processing was done using RELION and map figures generated in Chimera (121,167).

6 References

1. Gray MW. Mitochondrial evolution. *Cold Spring Harb Perspect Biol. Cold Spring Harbor Lab*; 2012 Sep;4(9):a011403–3.
2. Kurland CG, Andersson SG. Origin and evolution of the mitochondrial proteome. *Microbiol Mol Biol Rev. American Society for Microbiology (ASM)*; 2000 Dec;64(4):786–820.
3. Burger G, Gray MW, Lang BF. Mitochondrial genomes: anything goes. *Trends in Genetics. Elsevier*; 2003 Dec 1;19(12):709–16.
4. Gray MW. Mosaic nature of the mitochondrial proteome: Implications for the origin and evolution of mitochondria. *Proceedings of the National Academy of Sciences*. 2015 Aug;112(33):10133–8.
5. Bjorkholm P, Harish A, Hagstrom E, Ernst AM, Andersson SGE. Mitochondrial genomes are retained by selective constraints on protein targeting. *Proceedings of the National Academy of Sciences*. 2015 Aug;112(33):10154–61.
6. Allen JF. Why chloroplasts and mitochondria retain their own genomes and genetic systems: Colocation for redox regulation of gene expression. *Proceedings of the National Academy of Sciences. National Academy of Sciences*; 2015 Aug 18;112(33):10231–8.
7. John U, Lu Y, Wohlrab S, Groth M, Janouškovec J, Kohli GS, et al. An aerobic eukaryotic parasite with functional mitochondria that likely lacks a mitochondrial genome. *Sci Adv*. 2019 Apr 1;5(4):eaav1110.
8. Langkjaer RB, Casaregola S, Ussery DW, Gaillardin C, Piskur J. Sequence analysis of three mitochondrial DNA molecules reveals interesting differences among *Saccharomyces* yeasts. *Nucleic Acids Research. Oxford University Press*; 2003 Jun 15;31(12):3081–91.
9. Taanman J-W. The mitochondrial genome: structure, transcription, translation and replication. *16th European Bioenergetics Conference 2010*. 1999;1410(2):103–23.
10. Ott M, Amunts A, Brown A. Organization and Regulation of Mitochondrial Protein Synthesis. *Annu Rev Biochem. Annual Reviews*; 2016 Jun 2;85(1):77–101.
11. Pearce SF, Rebelo-Guiomar P, D'Souza AR, Powell CA, Van Haute L, Minczuk M. Regulation of Mammalian Mitochondrial Gene Expression: Recent Advances. *Trends Biochem Sci*. 2017 Aug;42(8):625–39.

12. Foury F, Roganti T, Lecrenier N, Purnelle B. The complete sequence of the mitochondrial genome of *Saccharomyces cerevisiae*. *FEBS Lett.* John Wiley & Sons, Ltd; 1998 Dec 22;440(3):325–31.
13. Anderson S, Bankier AT, Barrell BG, de Bruijn MH, Coulson AR, Drouin J, et al. Sequence and organization of the human mitochondrial genome. *Nature.* 1981 Apr;290(5806):457–65.
14. Palade GE. A SMALL PARTICULATE COMPONENT OF THE CYTOPLASM. *J Cell Biol.* 1955 Jan 25;1(1):59.
15. STEITZ JA. Polypeptide Chain Initiation: Nucleotide Sequences of the Three Ribosomal Binding Sites in Bacteriophage R17 RNA. *Nature.* 1969;224(5223):957–64.
16. Shine J, Dalgarno L. The 3'-terminal sequence of *Escherichia coli* 16S ribosomal RNA: complementarity to nonsense triplets and ribosome binding sites. *Proceedings of the National Academy of Sciences.* 1974 Apr;71(4):1342–6.
17. Shine J, Dalgarno L. Terminal-sequence analysis of bacterial ribosomal RNA. Correlation between the 3'-terminal-polypyrimidine sequence of 16S RNA and translational specificity of the ribosome. *Eur J Biochem.* 1975 Sep;57(1):221–30.
18. Moazed D, Noller HF. Transfer RNA shields specific nucleotides in 16S ribosomal RNA from attack by chemical probes. *Cell.* 1986 Dec;47(6):985–94.
19. Moazed D, Noller HF. Intermediate states in the movement of transfer RNA in the ribosome. *Nature.* 1989 Nov;342(6246):142–8.
20. Döring T, Mitchell P, Osswald M, Bochkariov D, Brimacombe R. The decoding region of 16S RNA; a cross-linking study of the ribosomal A, P and E sites using tRNA derivatized at position 32 in the anticodon loop. *EMBO J.* John Wiley & Sons, Ltd; 1994 Jun 1;13(11):2677–85.
21. Rheinberger HJ, Sternbach H, Nierhaus KH. Three tRNA binding sites on *Escherichia coli* ribosomes. *Proceedings of the National Academy of Sciences.* 1981 Sep;78(9):5310–4.
22. Rodnina MV, Savelsbergh A, Katunin VI, Wintermeyer W. Hydrolysis of GTP by elongation factor G drives tRNA movement on the ribosome. *Nature.* 1997;385(6611):37–41.
23. Pape T, Wintermeyer W, Rodnina MV. Complete kinetic mechanism of elongation factor Tu-dependent binding of aminoacyl-tRNA to the A site of the *E. coli* ribosome. *EMBO J.* 1998 Dec 15;17(24):7490.

24. Pape T, Wintermeyer W, Rodnina M. Induced fit in initial selection and proofreading of aminoacyl-tRNA on the ribosome. *EMBO J.* 1999 Jul 1;18(13):3800–7.
25. Blanchard SC, Gonzalez RL, Kim HD, Chu S, Puglisi JD. tRNA selection and kinetic proofreading in translation. *Nat Struct Mol Biol.* 2004;11(10):1008–14.
26. Noller HF, Hoffarth V, Zimniak L. Unusual resistance of peptidyl transferase to protein extraction procedures. *Science.* 1992 Jun;256(5062):1416–9.
27. Ban N, Nissen P, Hansen J, Moore PB, Steitz TA. The complete atomic structure of the large ribosomal subunit at 2.4 Å resolution. *Science.* 2000 Aug;289(5481):905–20.
28. Harms J, Schluenzen F, Zarivach R, Bashan A, Gat S, Agmon I, et al. High resolution structure of the large ribosomal subunit from a mesophilic eubacterium. *Cell.* 2001 Nov;107(5):679–88.
29. Wimberly BT, Brodersen DE, Clemons WMJ, Morgan-Warren RJ, Carter AP, Vonrhein C, et al. Structure of the 30S ribosomal subunit. *Nature.* 2000 Sep;407(6802):327–39.
30. Schluenzen F, Tocilj A, Zarivach R, Harms J, Gluehmann M, Janell D, et al. Structure of functionally activated small ribosomal subunit at 3.3 angstroms resolution. *Cell.* 2000 Sep;102(5):615–23.
31. Ramakrishnan V. Ribosome structure and the mechanism of translation. *Cell.* 2002 Feb;108(4):557–72.
32. McLEAN JR, COHN GL, BRANDT IK, SIMPSON MV. Incorporation of labeled amino acids into the protein of muscle and liver mitochondria. *Journal of Biological Chemistry.* 1958 Sep;233(3):657–63.
33. Stoeckenius W. SOME OBSERVATIONS ON NEGATIVELY STAINED MITOCHONDRIA. *J Cell Biol.* 1963 May 1;17(2):443.
34. O'Brien TW, Kalf GF. Ribosomes from rat liver mitochondria. I. Isolation procedure and contamination studies. *Journal of Biological Chemistry.* 1967 May 10;242(9):2172–9.
35. O'Brien TW, Kalf GF. Ribosomes from rat liver mitochondria. II. Partial characterization. *Journal of Biological Chemistry.* 1967 May 10;242(9):2180–5.
36. KÜNTZEL H, NOLL H. Mitochondrial and Cytoplasmic Polysomes from *Neurospora crassa*. *Nature.* 1967;215(5108):1340–5.
37. Rifkin MR, Wood DD, Luck DJ. Ribosomal RNA and ribosomes from mitochondria of *Neurospora crassa*. *Proc Natl Acad Sci USA.* 1967 Sep 1;58(3):1025–32.

38. *Grivell LA, Reijnders L, Borst P. Isolation of yeast mitochondrial ribosomes highly active in protein synthesis. Biochim Biophys Acta. 1971 Sep;247(1):91–103.*
39. *Kleinow W, Neupert W, Miller F. Electron microscope study of mitochondrial 60S and cytoplasmic 80S ribosomes from *Locusta migratoria*. The Journal of cell biology. The Rockefeller University Press; 1974 Sep 1;62(3):860–75.*
40. *Tait A, Knowles JK. Characterization of mitochondrial and cytoplasmic ribosomes from *Paramecium aurelia*. J Cell Biol. 1977 Apr 1;73(1):139.*
41. *Curgy JJ, Ledoigt G, Stevens BJ, Andre J. Mitochondrial and cytoplasmic ribosomes from *Tetrahymena pyriformis*. Correlative analysis by gel electrophoresis and electron microscopy. J Cell Biol. 1974 Mar;60(3):628–40.*
42. *Sharma MR, Koc EC, Datta PP, Booth TM, Spremulli LL, Agrawal RK. Structure of the Mammalian Mitochondrial Ribosome Reveals an Expanded Functional Role for Its Component Proteins. Cell. 2003;115(1):97–108.*
43. *Sharma MR, Booth TM, Simpson L, Maslov DA, Agrawal RK. Structure of a mitochondrial ribosome with minimal RNA. Proc Natl Acad Sci USA. 2009 Jun 15;106(24):9637.*
44. *Mears JA, Sharma MR, Gutell RR, McCook AS, Richardson PE, Caulfield TR, et al. A structural model for the large subunit of the mammalian mitochondrial ribosome. J Mol Biol. 2006 Apr;358(1):193–212.*
45. *van der Sluis EO, Bauerschmitt H, Becker T, Mielke T, Frauenfeld J, Berninghausen O, et al. Parallel Structural Evolution of Mitochondrial Ribosomes and OXPHOS Complexes. Genome Biol Evol. Oxford University Press; 2015 May;7(5):1235–51.*
46. *Amunts A, Brown A, Bai X-C, Ll  cer JL, Hussain T, Emsley P, et al. Structure of the yeast mitochondrial large ribosomal subunit. Science. 2014 Mar 28;343(6178):1485–9.*
47. *Brown A, Amunts A, Bai X-C, Sugimoto Y, Edwards PC, Murshudov G, et al. Structure of the large ribosomal subunit from human mitochondria. Science. American Association for the Advancement of Science; 2014 Nov 7;346(6210):718–22.*
48. *Amunts A, Brown A, Toots J, Scheres SHW, Ramakrishnan V. Ribosome. The structure of the human mitochondrial ribosome. Science. 2015 Apr 3;348(6230):95–8.*
49. *Greber BJ, Boehringer D, Leitner A, Bieri P, Voigts-Hoffmann F, Erzberger JP, et al. Architecture of the large subunit of the mammalian mitochondrial ribosome. Nature. 2014 Jan 23;505(7484):515–9.*

50. Greber BJ, Bieri P, Leibundgut M, Leitner A, Aebersold R, Boehringer D, et al. Ribosome. The complete structure of the 55S mammalian mitochondrial ribosome. *Science*. 2015 Apr 17;348(6232):303–8.
51. Bai X-C, Fernández IS, McMullan G, Scheres SHW. Ribosome structures to near-atomic resolution from thirty thousand cryo-EM particles. *Elife*. eLife Sciences Publications, Ltd; 2013 Feb 19;2:e00461–1.
52. Temperley RJ, Wydro M, Lightowlers RN, Chrzanowska-Lightowlers ZM. Human mitochondrial mRNAs—like members of all families, similar but different. *Biochimica et Biophysica Acta (BBA) - Bioenergetics*. Elsevier Pub. Co; 2010 Jun;1797(6-7):1081–5.
53. Hillen HS, Temiakov D, Cramer P. Structural basis of mitochondrial transcription. *Nat Struct Mol Biol*. 2018;25(9):754–65.
54. Holzmann J, Frank P, Löffler E, Bennett KL, Gerner C, Rossmanith W. RNase P without RNA: identification and functional reconstitution of the human mitochondrial tRNA processing enzyme. *Cell*. 2008 Oct;135(3):462–74.
55. Brzezniak LK, Bijata M, Szczesny RJ, Stepień PP. Involvement of human ELAC2 gene product in 3' end processing of mitochondrial tRNAs. *RNA Biol*. 2011 Jul;8(4):616–26.
56. Slomovic S, Laufer D, Geiger D, Schuster G. Polyadenylation and degradation of human mitochondrial RNA: the prokaryotic past leaves its mark. *Mol Cell Biol*. American Society for Microbiology; 2005 Aug 1;25(15):6427–35.
57. Suzuki T, Suzuki T. A complete landscape of post-transcriptional modifications in mammalian mitochondrial tRNAs. *Nucleic Acids Research*. Oxford University Press; 2014 Jul 1;42(11):7346–57.
58. Mignone F, Gissi C, Liuni S, Pesole G. Untranslated regions of mRNAs. *Genome Biol*. BioMed Central; 2002;3(3):REVIEWS0004–4.
59. Maleszka R, Skelly PJ, Clark-Walker GD. Rolling circle replication of DNA in yeast mitochondria. *EMBO J*. 1991 Dec;10(12):3923–9.
60. Deshpande AP, Patel SS. Mechanism of transcription initiation by the yeast mitochondrial RNA polymerase. *Biochim Biophys Acta*. 2012 Sep;1819(9-10):930–8.
61. Turk EM, Das V, Seibert RD, Andrulis ED. The mitochondrial RNA landscape of *Saccharomyces cerevisiae*. *PLoS One*. 2013;8(10):e78105.
62. Hartmann RK, Gossringer M, Spath B, Fischer S, Marchfelder A. The making of tRNAs and more - RNase P and tRNase Z. *Prog Mol Biol Transl Sci*. 2009;85:319–68.
63. Wiesenberger G, Fox TD. Pet127p, a membrane-associated protein involved

- in stability and processing of Saccharomyces cerevisiae mitochondrial RNAs. Mol Cell Biol. 1997 May 1;17(5):2816.*
64. Kuzmenko A, Atkinson GC, Levitskii S, Zenkin N, Tenson T, Hauryliuk V, et al. Mitochondrial translation initiation machinery: Conservation and diversification. *Biochimie. 2014;100:132–40.*
 65. Herrmann JM, Woellhaf MW, Bonnefoy N. Control of protein synthesis in yeast mitochondria: The concept of translational activators. *Biochimica et Biophysica Acta (BBA) - Molecular Cell Research. 2013 Feb;1833(2):286–94.*
 66. Hussain T, Ll acer JL, Wimberly BT, Kieft JS, Ramakrishnan V. Large-Scale Movements of IF3 and tRNA during Bacterial Translation Initiation. *Cell. Cell Press; 2016 Sep 22;167(1):133–144.e13.*
 67. Atkinson GC, Kuzmenko A, Kamenski P, Vysokikh MY, Lakunina V, Tankov S, et al. Evolutionary and genetic analyses of mitochondrial translation initiation factors identify the missing mitochondrial IF3 in *S. cerevisiae*. *Nucleic Acids Research. 2012 Mar 28;40(13):6122–34.*
 68. Kuzmenko A, Derbikova K, Salvatori R, Tankov S, Atkinson GC, Tenson T, et al. Aim-less translation: loss of *Saccharomyces cerevisiae* mitochondrial translation initiation factor mIF3/Aim23 leads to unbalanced protein synthesis. *Sci Rep. 2016 Jan;6:18749.*
 69. Koripella RK, Sharma MR, Haque ME, Risteff P, Spremulli LL, Agrawal RK. Structure of Human Mitochondrial Translation Initiation Factor 3 Bound to the Small Ribosomal Subunit. *iScience. 2019 Feb;12:76–86.*
 70. Haque ME, Grasso D, Spremulli LL. The interaction of mammalian mitochondrial translational initiation factor 3 with ribosomes: evolution of terminal extensions in IF3 mt. *Nucleic Acids Research. 2007 Dec 1;36(2):589–97.*
 71. Kummer E, Leibundgut M, Rackham O, Lee RG, Boehringer D, Filipovska A, et al. Unique features of mammalian mitochondrial translation initiation revealed by cryo-EM. *Nature. 2018 Aug 8;560(7717):263–7.*
 72. Yassin AS, Haque ME, Datta PP, Elmore K, Banavali NK, Spremulli LL, et al. Insertion domain within mammalian mitochondrial translation initiation factor 2 serves the role of eubacterial initiation factor 1. *Proc Natl Acad Sci USA. 2011 Mar 8;108(10):3918.*
 73. Bonnefoy N, Fox TD. In vivo analysis of mutated initiation codons in the mitochondrial COX2 gene of *Saccharomyces cerevisiae* fused to the reporter gene ARG8m reveals lack of downstream reinitiation. *Mol Gen Genet. 2000 Jan;262(6):1036–46.*
 74. Weraarpachai W, Antonicka H, Sasarman F, Seeger J, Schrank B, Kolesar JE,

- et al. Mutation in TACO1, encoding a translational activator of COX I, results in cytochrome c oxidase deficiency and late-onset Leigh syndrome. Nat Genet. 2009 Jul;41(7):833–7.*
75. *Manthey GM, McEwen JE. The product of the nuclear gene PET309 is required for translation of mature mRNA and stability or production of intron-containing RNAs derived from the mitochondrial COX1 locus of Saccharomyces cerevisiae. EMBO J. John Wiley & Sons, Ltd; 1995 Aug 1;14(16):4031–43.*
 76. *Decoster E, Simon M, Hatat D, Faye G. The MSS51 gene product is required for the translation of the COX1 mRNA in yeast mitochondria. Mol Gen Genet. 1990 Oct;224(1):111–8.*
 77. *Costanzo MC, Fox TD. Specific translational activation by nuclear gene products occurs in the 5' untranslated leader of a yeast mitochondrial mRNA. Proceedings of the National Academy of Sciences. National Academy of Sciences; 1988 Apr 1;85(8):2677–81.*
 78. *Salinas-Giegé T, Giegé R, Giegé P. tRNA Biology in Mitochondria. IJMS. MDPI; 2015 Mar;16(3):4518–59.*
 79. *Crick FH. Codon--anticodon pairing: the wobble hypothesis. J Mol Biol. 1966 Aug;19(2):548–55.*
 80. *Alkatib S, Scharff LB, Rogalski M, Fleischmann TT, Matthes A, Seeger S, et al. The contributions of wobbling and superwobbling to the reading of the genetic code. PLoS Genet. Public Library of Science; 2012 Nov 15;8(11):e1003076–6.*
 81. *Mai N, Chrzanowska-Lightowlers ZMA, Lightowlers RN. The process of mammalian mitochondrial protein synthesis. Cell and tissue research. Springer Berlin Heidelberg; 2017;367(1):5–20.*
 82. *Soleimanpour-Lichaei HR, Kühl I, Gaisne M, Passos JF, Wydro M, Rorbach J, et al. mtRF1a is a human mitochondrial translation release factor decoding the major termination codons UAA and UAG. Mol Cell. Cell Press; 2007 Sep 7;27(5):745–57.*
 83. *Askarian-Amiri ME, Pel HJ, Guevremont D, McCaughan KK, Poole ES, Sumpter VG, et al. Functional characterization of yeast mitochondrial release factor 1. Journal of Biological Chemistry. 2000 Jun;275(23):17241–8.*
 84. *Temperley R, Richter R, Dennerlein S, Lightowlers RN, Chrzanowska-Lightowlers ZM. Hungry codons promote frameshifting in human mitochondrial ribosomes. Science. 2010 Jan;327(5963):301.*
 85. *Brown A, Shao S, Murray J, Hegde RS, Ramakrishnan V. Structural basis for stop codon recognition in eukaryotes. Nature. Nature Publishing Group, a*

division of Macmillan Publishers Limited. All Rights Reserved; 2015 Aug 5;524(7566):493–6.

86. *Rorbach J, Richter R, Wessels HJ, Wydro M, Pekalski M, Farhoud M, et al. The human mitochondrial ribosome recycling factor is essential for cell viability. Nucleic Acids Research. Oxford University Press; 2008 Oct 1;36(18):5787–99.*
87. *Tsuboi M, Morita H, Nozaki Y, Akama K, Ueda T, Ito K, et al. EF-G2mt is an exclusive recycling factor in mammalian mitochondrial protein synthesis. Mol Cell. 2009 Aug;35(4):502–10.*
88. *Zavialov AV, Hauryliuk VV, Ehrenberg M. Splitting of the posttermination ribosome into subunits by the concerted action of RRF and EF-G. Mol Cell. 2005 Jun;18(6):675–86.*
89. *Taylor RW, Turnbull DM. Mitochondrial DNA mutations in human disease. Nat Rev Genet. 2005 May 1;6(5):389–402.*
90. *De Silva D, Tu Y-T, Amunts A, Fontanesi F, Barrientos A. Mitochondrial ribosome assembly in health and disease. Cell Cycle. Taylor & Francis; 2015;14(14):2226–50.*
91. *Sasarman F, Antonicka H, Shoubridge EA. The A3243G tRNA^{Leu}(UUR) MELAS mutation causes amino acid misincorporation and a combined respiratory chain assembly defect partially suppressed by overexpression of EFTu and EFG2. Hum Mol Genet. 2008 Dec;17(23):3697–707.*
92. *Prezant TR, Agapian JV, Bohlman MC, Bu X, Oztas S, Qiu WQ, et al. Mitochondrial ribosomal RNA mutation associated with both antibiotic-induced and non-syndromic deafness. Nat Genet. 1993 Jul;4(3):289–94.*
93. *Bykhovskaya Y, Casas K, Mengesha E, Inbal A, Fischel-Ghodsian N. Missense mutation in pseudouridine synthase 1 (PUS1) causes mitochondrial myopathy and sideroblastic anemia (MLSA). Am J Hum Genet. The American Society of Human Genetics; 2004 May 31;74(6):1303–8.*
94. *Rötig A. Human diseases with impaired mitochondrial protein synthesis. Biochim Biophys Acta. 2011 Sep;1807(9):1198–205.*
95. *Neuzil J, Dong L-F, Rohlena J, Truksa J, Ralph SJ. Classification of mitocans, anti-cancer drugs acting on mitochondria. Mitochondrion. 2013 May;13(3):199–208.*
96. *Cairns RA, Harris IS, Mak TW. Regulation of cancer cell metabolism. Nat Rev Cancer. 2011 Feb;11(2):85–95.*
97. *Skrtic M, Sriskanthadevan S, Jhas B, Gebbia M, Wang X, Wang Z, et al. Inhibition of mitochondrial translation as a therapeutic strategy for human acute myeloid leukemia. Cancer Cell. 2011 Nov;20(5):674–88.*

98. Reed GA, Schiller GJ, Kambhampati S, Tallman MS, Douer D, Minden MD, et al. A Phase 1 study of intravenous infusions of tigecycline in patients with acute myeloid leukemia. *Cancer Med.* 2016 Nov;5(11):3031–40.
99. Pfeffer S, Woellhaf MW, Herrmann JM, Förster F. Organization of the mitochondrial translation machinery studied in situ by cryoelectron tomography. *Nat Commun. Nature Publishing Group;* 2015;6:6019.
100. Englmeier R, Pfeffer S, Förster F. Structure of the Human Mitochondrial Ribosome Studied In Situ by Cryoelectron Tomography. *Structure.* 2017 Oct;25(10):1574–1581.e2.
101. Voorhees RM, Hegde RS. Toward a structural understanding of co-translational protein translocation. *Curr Opin Cell Biol.* 2016 May 5;41:91–9.
102. Voorhees RM, Fernández IS, Scheres SHW, Hegde RS. Structure of the mammalian ribosome-Sec61 complex to 3.4 Å resolution. *Cell. Elsevier;* 2014 Jun 19;157(7):1632–43.
103. Szyrach G, Ott M, Bonnefoy N, Neupert W, Herrmann JM. Ribosome binding to the Oxa1 complex facilitates co-translational protein insertion in mitochondria. *EMBO J.* 2003 Dec 15;22(24):6448–57.
104. Jia L, Dienhart M, Schramp M, McCauley M, Hell K, Stuart RA. Yeast Oxa1 interacts with mitochondrial ribosomes: the importance of the C-terminal region of Oxa1. *EMBO J.* 2003 Dec 15;22(24):6438–47.
105. Haque ME, Elmore KB, Tripathy A, Koc H, Koc EC, Spremulli LL. Properties of the C-terminal tail of human mitochondrial inner membrane protein Oxa1L and its interactions with mammalian mitochondrial ribosomes. *J Biol Chem. American Society for Biochemistry and Molecular Biology;* 2010 Sep 3;285(36):28353–62.
106. Neupert W, Herrmann JM. Translocation of Proteins into Mitochondria. *Annu Rev Biochem. Annual Reviews;* 2007 Jun 7;76(1):723–49.
107. Stuart RA. Insertion of proteins into the inner membrane of mitochondria: the role of the Oxa1 complex. *BBA - Molecular Cell Research.* 2002;1592(1):79–87.
108. Herrmann JM, Neupert W, Stuart RA. Insertion into the mitochondrial inner membrane of a polytopic protein, the nuclear-encoded Oxa1p. *EMBO Journal.* 1997;16(9):2217–26.
109. Anghel SA, McGilvray PT, Hegde RS, Keenan RJ. Identification of Oxa1 Homologs Operating in the Eukaryotic Endoplasmic Reticulum. *Cell Rep.* 2017 Dec 26;21(13):3708–16.
110. Harbauer AB, Zahedi RP, Sickmann A, Pfanner N, Meisinger C. The Protein

- Import Machinery of Mitochondria-A Regulatory Hub in Metabolism, Stress, and Disease. Cell Metabolism. Elsevier Inc; 2014 Mar 4;19(3):357–72.*
111. Williams CC, Jan CH, Weissman JS. Targeting and plasticity of mitochondrial proteins revealed by proximity-specific ribosome profiling. *Science. NIH Public Access; 2014 Nov 7;346(6210):748–51.*
 112. Gold VA, Chroscicki P, Bragoszewski P, Chacinska A. Visualization of cytosolic ribosomes on the surface of mitochondria by electron cryotomography. *EMBO Rep. 2017 Aug 21;:e201744261.*
 113. Gold VAM, Ieva R, Walter A, Pfanner N, van der Laan M, Kühlbrandt W. Visualizing active membrane protein complexes by electron cryotomography. *Nat Commun. The Author(s) SN ; 5:4129EP–.*
 114. Couvillion MT, Soto IC, Shipkovenska G, Churchman LS. Synchronized mitochondrial and cytosolic translation programs. *Nature. 2016 May 11;533(7604):499–503.*
 115. Richter-Dennerlein R, Oeljeklaus S, Lorenzi I, Ronsor C, Bareth B, Schendzielorz AB, et al. Mitochondrial Protein Synthesis Adapts to Influx of Nuclear-Encoded Protein. *Cell. 2016 Oct;167(2):471–483.e10.*
 116. Taylor KA, Glaeser RM. Electron microscopy of frozen hydrated biological specimens. *J Ultrastruct Res. 1976 Jun;55(3):448–56.*
 117. Henderson R. The potential and limitations of neutrons, electrons and X-rays for atomic resolution microscopy of unstained biological molecules. *Q Rev Biophys. 1995 May;28(2):171–93.*
 118. Baker LA, Rubinstein JL. Radiation damage in electron cryomicroscopy. *Methods Enzymol. 2010;481:371–88.*
 119. Dubochet J, Lepault J, Freeman R, Berriman JA, Homo JC. Electron microscopy of frozen water and aqueous solutions. *Journal of Microscopy. John Wiley & Sons, Ltd (10.1111); 2011 Aug 2;128(3):219–37.*
 120. Zivanov J, Nakane T, Scheres SHW. A Bayesian Approach to Beam-Induced Motion Correction in Cryo-EM Single-Particle Analysis. *bioRxiv. 2018 Jan 1;:384537.*
 121. Scheres SHW. RELION: implementation of a Bayesian approach to cryo-EM structure determination. *J Struct Biol. 2012 Dec;180(3):519–30.*
 122. Nogales E, Scheres SHW. Cryo-EM: A Unique Tool for the Visualization of Macromolecular Complexity. *Mol Cell. Elsevier; 2015 May;58(4):677–89.*
 123. Nogales E. The development of cryo-EM into a mainstream structural biology technique. *Nature Methods 2015 13:1. Nature Publishing Group; 2015 Dec 30;13(1):24–7.*

124. Brown A, Long F, Nicholls RA, Toots J, Emsley P, Murshudov G. Tools for macromolecular model building and refinement into electron cryo-microscopy reconstructions. *Acta Crystallogr D Biol Crystallogr. International Union of Crystallography*; 2015 Jan 1;71(Pt 1):136–53.
125. Emsley P, Lohkamp B, Scott WG, Cowtan K. Features and development of Coot. *Acta Crystallogr D Biol Crystallogr*. 2010 Apr;66(Pt 4):486–501.
126. Kühlbrandt W. The Resolution Revolution. *Science*. 2014 Mar 27;343(6178):1443.
127. Liao M, Cao E, Julius D, Cheng Y. Structure of the TRPV1 ion channel determined by electron cryo-microscopy. *Nature*. 2013 Dec 4;504(7478):107–12.
128. Wang Z, Hryc CF, Bammes B, Afonine PV, Jakana J, Chen D-H, et al. An atomic model of brome mosaic virus using direct electron detection and real-space optimization. *Nat Commun. Nature Pub. Group*; 2014 Sep 3;5:4808–8.
129. Nogales E. The development of cryo-EM into a mainstream structural biology technique. *Nature Methods* 2015 13:1. Nature Publishing Group, a division of Macmillan Publishers Limited. All Rights Reserved. SN; 13:24EP–.
130. Kaushal PS, Sharma MR, Booth TM, Haque EM, Tung C-S, Sanbonmatsu KY, et al. Cryo-EM structure of the small subunit of the mammalian mitochondrial ribosome. *Proc Natl Acad Sci USA*. 2014 May 20;111(20):7284–9.
131. Saveanu C, Fromont-Racine M, Harington A, Ricard F, Namane A, Jacquier A. Identification of 12 new yeast mitochondrial ribosomal proteins including 6 that have no prokaryotic homologues. *Journal of Biological Chemistry*. 2001 May;276(19):15861–7.
132. Kitakawa M, Graack H-R, Grohmann L, Goldschmidt-Reisin S, Herfurth E, Wittmann-Liebold B, et al. Identification and Characterization of the Genes for Mitochondrial Ribosomal Proteins of *Saccharomyces Cerevisiae*. *Eur J Biochem. John Wiley & Sons, Ltd (10.1111)*; 1997 Apr 15;245(2):449–56.
133. Gardner JM, Jaspersen SL. Manipulating the yeast genome: deletion, mutation, and tagging by PCR. *Methods Mol Biol*. 2014;1205:45–78.
134. Lasserre J-P, Dautant A, Aiyar RS, Kucharczyk R, Glatigny A, Tribouillard-Tanvier D, et al. Yeast as a system for modeling mitochondrial disease mechanisms and discovering therapies. *Dis Model Mech. The Company of Biologists Ltd*; 2015 Jun;8(6):509–26.
135. Desai N, Brown A, Amunts A, Ramakrishnan V. The structure of the yeast mitochondrial ribosome. *Science*. 2017 Feb 2;355(6324):528–31.

136. Tang G, Peng L, Baldwin PR, Mann DS, Jiang W, Rees I, et al. EMAN2: an extensible image processing suite for electron microscopy. *J Struct Biol.* 2007 Jan;157(1):38–46.
137. Brown A, Fernández IS, Gordiyenko Y, Ramakrishnan V. Ribosome-dependent activation of stringent control. *Nature.* 2016 Jun;534(7606):277–80.
138. Ban N, Beckmann R, Cate JH, Dinman JD, Dragon F, Ellis SR, et al. A new system for naming ribosomal proteins. *Folding and binding / Nucleic acids and their protein complexes.* 2014;24:165–9.
139. Petrossian TC, Clarke SG. Multiple Motif Scanning to identify methyltransferases from the yeast proteome. *Mol Cell Proteomics.* 2009 Jul;8(7):1516–26.
140. Park Y, Bader JS. How networks change with time. *Bioinformatics.* 2012 Jun;28(12):i40–8.
141. Barros MH, Myers AM, Van Driesche S, Tzagoloff A. COX24 codes for a mitochondrial protein required for processing of the COX1 transcript. *Journal of Biological Chemistry.* 2006 Feb;281(6):3743–51.
142. Liu Q, Fredrick K. Intersubunit Bridges of the Bacterial Ribosome. *J Mol Biol.* 2016 May;428(10 Pt B):2146–64.
143. Denslow ND, Anders JC, O'Brien TW. Bovine mitochondrial ribosomes possess a high affinity binding site for guanine nucleotides. *Journal of Biological Chemistry.* 1991 May;266(15):9586–90.
144. Hiltunen JK, Mursula AM, Rottensteiner H, Wierenga RK, Kastaniotis AJ, Gurvitz A. The biochemistry of peroxisomal beta-oxidation in the yeast *Saccharomyces cerevisiae*. *FEMS Microbiol Rev.* 2003 Apr;27(1):35–64.
145. Brown GK, Hunt SM, Scholem R, Fowler K, Grimes A, Mercer JF, et al. beta-hydroxyisobutyryl coenzyme A deacylase deficiency: a defect in valine metabolism associated with physical malformations. *Pediatrics.* 1982 Oct;70(4):532–8.
146. Wong BJ, Gerlt JA. Divergent function in the crotonase superfamily: an anhydride intermediate in the reaction catalyzed by 3-hydroxyisobutyryl-CoA hydrolase. *J Am Chem Soc. American Chemical Society;* 2003 Oct 8;125(40):12076–7.
147. Groot GS, Mason TL, Van Harten-Loosbroek N. Var1 is associated with the small ribosomal subunit of mitochondrial ribosomes in yeast. *Mol Gen Genet.* 1979 Jul;174(3):339–42.
148. Bullerwell CE, Burger G, Lang BF. A novel motif for identifying rps3 homologs in fungal mitochondrial genomes. *Trends Biochem Sci.* 2000

Aug;25(8):363–5.

149. Yusupova GZ, Yusupov MM, Cate JH, Noller HF. The path of messenger RNA through the ribosome. *Cell*. 2001 Jul;106(2):233–41.
150. Selmer M, Dunham CM, Murphy FV4, Weixlbaumer A, Petry S, Kelley AC, et al. Structure of the 70S ribosome complexed with mRNA and tRNA. *Science*. 2006 Sep;313(5795):1935–42.
151. Takyar S, Hickerson RP, Noller HF. mRNA helicase activity of the ribosome. *Cell*. 2005 Jan 14;120(1):49–58.
152. Kirthi N, Roy-Chaudhuri B, Kelley T, Culver GM. A novel single amino acid change in small subunit ribosomal protein S5 has profound effects on translational fidelity. *RNA. Cold Spring Harbor Lab*; 2006 Dec;12(12):2080–91.
153. Green-Willms NS, Fox TD, Costanzo MC. Functional interactions between yeast mitochondrial ribosomes and mRNA 5' untranslated leaders. *Mol Cell Biol*. 1998 Apr;18(4):1826–34.
154. Hajnsdorf E, Boni IV. Multiple activities of RNA-binding proteins S1 and Hfq. *Biochimie. France*; 2012 Jul 1;94(7):1544–53.
155. Haffter P, Fox TD. Suppression of carboxy-terminal truncations of the yeast mitochondrial mRNA-specific translational activator PET122 by mutations in two new genes, MRP17 and PET127. *Mol Gen Genet*. 1992 Oct;235(1):64–73.
156. McMullin TW, Haffter P, Fox TD. A novel small-subunit ribosomal protein of yeast mitochondria that interacts functionally with an mRNA-specific translational activator. *Mol Cell Biol*. 1990 Sep;10(9):4590–5.
157. Haffter P, McMullin TW, Fox TD. Functional interactions among two yeast mitochondrial ribosomal proteins and an mRNA-specific translational activator. *Genetics. Genetics Society of America*; 1991 Feb;127(2):319–26.
158. Ramrath DJF, Niemann M, Leibundgut M, Bieri P, Prange C, Horn EK, et al. Evolutionary shift toward protein-based architecture in trypanosomal mitochondrial ribosomes. *Science. American Association for the Advancement of Science*; 2018 Oct 26;362(6413):eaau7735.
159. Sharma MR, Wilson DN, Datta PP, Barat C, Schlutzenzen F, Fucini P, et al. Cryo-EM study of the spinach chloroplast ribosome reveals the structural and functional roles of plastid-specific ribosomal proteins. *Proc Natl Acad Sci USA*. 2007 Dec 3;104(49):19315.
160. Bieri P, Leibundgut M, Saurer M, Boehringer D, Ban N. The complete structure of the chloroplast 70S ribosome in complex with translation factor pY. *EMBO J. John Wiley and Sons Inc*; 2017 Feb 14;36(4):475–86.

161. Perez Boerema A, Aibara S, Paul B, Tobiasson V, Kimanius D, Forsberg BO, et al. Structure of the chloroplast ribosome with chl-RRF and hibernation-promoting factor. *Nature Plants*. 2018;4(4):212–7.
162. Neiman M, Taylor DR. The causes of mutation accumulation in mitochondrial genomes. *Proc Biol Sci*. 2009 Apr;276(1660):1201–9.
163. Lynch M, Koskella B, Schaack S. Mutation Pressure and the Evolution of Organelle Genomic Architecture. *Science*. 2006 Mar 24;311(5768):1727.
164. Li X, Mooney P, Zheng S, Booth CR, Braunfeld MB, Gubbens S, et al. Electron counting and beam-induced motion correction enable near-atomic-resolution single-particle cryo-EM. *Nature Methods* 2015 13:1. 2013 Jun;10(6):584–90.
165. Mindell JA, Grigorieff N. Accurate determination of local defocus and specimen tilt in electron microscopy. *J Struct Biol*. 2003;142(3):334–47.
166. Rosenthal PB, Henderson R. Optimal Determination of Particle Orientation, Absolute Hand, and Contrast Loss in Single-particle Electron Cryomicroscopy. *J Mol Biol*. 2003;333(4):721–45.
167. Pettersen EF, Goddard TD, Huang CC, Couch GS, Greenblatt DM, Meng EC, et al. UCSF Chimera?A visualization system for exploratory research and analysis. *J Comput Chem*. John Wiley & Sons, Ltd; 2004;25(13):1605–12.
168. Sievers F, Wilm A, Dineen D, Gibson TJ, Karplus K, Li W, et al. Fast, scalable generation of high-quality protein multiple sequence alignments using Clustal Omega. *Mol Syst Biol*. John Wiley & Sons, Ltd; 2011 Dec 6;7(1):539.
169. Krissinel E, Henrick K. Inference of Macromolecular Assemblies from Crystalline State. *J Mol Biol*. 2007;372(3):774–97.
170. Holm L, Rosenström PL. Dali server: conservation mapping in 3D. *Nucleic Acids Research*. 2010;38(suppl_2):W545–9.
171. Kelley LA, Mezulis S, Yates CM, Wass MN, Sternberg MJE. The Phyre2 web portal for protein modeling, prediction and analysis. *Nat Protoc*. 2015 Jun;10(6):845–58.
172. Altschul SF, Madden TL, Schäffer AA, Zhang J, Zhang Z, Miller W, et al. Gapped BLAST and PSI-BLAST: a new generation of protein database search programs. *Nucleic Acids Research*. 1997;25(17):3389–402.
173. Cannone JJ, Subramanian S, Schnare MN, Collett JR, D'Souza LM, Du Y, et al. The Comparative RNA Web (CRW) Site: an online database of comparative sequence and structure information for ribosomal, intron, and other RNAs. *BMC Bioinformatics*. 2002;3(1):2.
174. Nicholls RA, Long F, Murshudov GN. Low-resolution refinement tools in REFMAC5. *Acta Crystallogr D Biol Crystallogr*. 2012 Apr;68(Pt 4):404–17.

175. Murshudov GN, Skubak P, Lebedev AA, Pannu NS, Steiner RA, Nicholls RA, et al. *REFMAC5 for the refinement of macromolecular crystal structures. Acta Crystallogr D Biol Crystallogr.* 2011 Apr;67(Pt 4):355–67.
176. Chen VB, Arendall WB3, Headd JJ, Keedy DA, Immormino RM, Kapral GJ, et al. *MolProbity: all-atom structure validation for macromolecular crystallography. Acta Crystallogr D Biol Crystallogr.* 2010 Jan;66(Pt 1):12–21.
177. Kucukelbir A, Sigworth FJ, Tagare HD. *Quantifying the local resolution of cryo-EM density maps. Nature Methods* 2015 13:1. 2014 Jan;11(1):63–5.
178. Lu X-J, Bussemaker HJ, Olson WK. *DSSR: an integrated software tool for dissecting the spatial structure of RNA. Nucleic Acids Research.* 2015 Dec;43(21):e142.
179. Shannon P, Markiel A, Ozier O, Baliga NS, Wang JT, Ramage D, et al. *Cytoscape: a software environment for integrated models of biomolecular interaction networks. Genome Res.* 2003 Nov;13(11):2498–504.
180. Consortium TU. *UniProt: a hub for protein information. Nucleic Acids Research.* 2014;43(D1):D204–12.
181. Stiller SB, Hopker J, Oeljeklaus S, Schutze C, Schrempp SG, Vent-Schmidt J, et al. *Mitochondrial OXA Translocase Plays a Major Role in Biogenesis of Inner-Membrane Proteins. Cell Metabolism.* 2016 May;23(5):901–8.
182. Samuelson JC, Chen M, Jiang F, Möller I, Wiedmann M, Kuhn A, et al. *YidC mediates membrane protein insertion in bacteria. Nature.* 2000;406(6796):637–41.
183. Luijckx J, Samuelsson T, de Gier J-W. *YidC/Oxa1p/Alb3: evolutionarily conserved mediators of membrane protein assembly. FEBS Lett.* 2001;501(1):1–5.
184. Kohler R, Boehringer D, Greber B, Bingel-Erlenmeyer R, Collinson I, Schaffitzel C, et al. *YidC and Oxa1 Form Dimeric Insertion Pores on the Translating Ribosome. Mol Cell.* 2009;34(3):344–53.
185. Bonnefoy N, Kermorgant M, Groudinsky O, Minet M, Slonimski PP, Dujardin G. *Cloning of a human gene involved in cytochrome oxidase assembly by functional complementation of an oxa1- mutation in Saccharomyces cerevisiae. Proc Natl Acad Sci USA.* 1994 Dec 6;91(25):11978.
186. Ott M, Herrmann JM. *Co-translational membrane insertion of mitochondrially encoded proteins. Biochim Biophys Acta.* 2010 Jun;1803(6):767–75.
187. Funes S, Kauff F, van der Sluis EO, Ott M, Herrmann JM. *Evolution of YidC/Oxa1/Alb3 insertases: three independent gene duplications followed*

by functional specialization in bacteria, mitochondria and chloroplasts. Biol Chem. 2011 Jan;392(1-2):13–9.

188. Altamura N, Capitanio N, Bonnefoy N, Papa S, Dujardin G. The *Saccharomyces cerevisiae* OXA1 gene is required for the correct assembly of cytochrome c oxidase and oligomycin-sensitive ATP synthase. *FEBS Lett.* 1996 Mar;382(1-2):111–5.
189. Hell K, Herrmann J, Pratje E, Neupert W, Stuart RA. Oxa1p mediates the export of the N- and C-termini of pCoxII from the mitochondrial matrix to the intermembrane space. *FEBS Lett.* 1997 Dec;418(3):367–70.
190. Hell K, Herrmann JM, Pratje E, Neupert W, Stuart RA. Oxa1p, an essential component of the N-tail protein export machinery in mitochondria. *Proceedings of the National Academy of Sciences.* 1998 Mar;95(5):2250–5.
191. Hell K, Neupert W, Stuart RA. Oxa1p acts as a general membrane insertion machinery for proteins encoded by mitochondrial DNA. *EMBO J.* 2001 Mar;20(6):1281–8.
192. Keil M, Bareth B, Woellhaf MW, Peleh V, Prestele M, Rehling P, et al. Oxa1-ribosome complexes coordinate the assembly of cytochrome C oxidase in mitochondria. *Journal of Biological Chemistry.* 2012 Oct;287(41):34484–93.
193. Jia L, Dienhart MK, Stuart RA. Oxa1 directly interacts with Atp9 and mediates its assembly into the mitochondrial F1Fo-ATP synthase complex. *Mol Biol Cell.* 2007 May;18(5):1897–908.
194. Thompson K, Mai N, Oláhová M, Scialó F, Formosa LE, Stroud DA, et al. OXA1L mutations cause mitochondrial encephalopathy and a combined oxidative phosphorylation defect. *EMBO Mol Med.* John Wiley and Sons Inc; 2018 Nov 1;10(11):e9060.
195. Bieri P, Greber BJ, Ban N. High-resolution structures of mitochondrial ribosomes and their functional implications. *Current Opinion in Structural Biology.* 2018 Apr;49:44–53.
196. Zhang L, Ging NC, Komoda T, Hanada T, Suzuki T, Watanabe K. Antibiotic susceptibility of mammalian mitochondrial translation. *FEBS Lett.* 2005;579(28):6423–7.
197. Wilson DN, Schlutzenzen F, Harms JM, Starosta AL, Connell SR, Fucini P. The oxazolidinone antibiotics perturb the ribosomal peptidyl-transferase center and effect tRNA positioning. *Proceedings of the National Academy of Sciences. National Academy of Sciences;* 2008 Sep 9;105(36):13339–44.
198. Wang X, Ryu D, Houtkooper RH, Auwerx J. Antibiotic use and abuse: A threat to mitochondria and chloroplasts with impact on research, health, and environment. *BioEssays.* John Wiley & Sons, Ltd; 2015 Sep

8;37(10):1045–53.

199. Demirci H, Murphy F4, Murphy E, Gregory ST, Dahlberg AE, Jogle G. A structural basis for streptomycin-induced misreading of the genetic code. *Nat Commun.* 2013;4:1355.
200. Brodersen DE, Clemons WMJ, Carter AP, Morgan-Warren RJ, Wimberly BT, Ramakrishnan V. The structural basis for the action of the antibiotics tetracycline, pactamycin, and hygromycin B on the 30S ribosomal subunit. *Cell.* 2000 Dec;103(7):1143–54.
201. Jenner L, Starosta AL, Terry DS, Mikolajka A, Filonava L, Yusupov M, et al. Structural basis for potent inhibitory activity of the antibiotic tigecycline during protein synthesis. *Proceedings of the National Academy of Sciences.* 2013 Mar;110(10):3812–6.
202. D'Andrea A, Gritti I, Nicoli P, Giorgio M, Doni M, Conti A, et al. The mitochondrial translation machinery as a therapeutic target in Myc-driven lymphomas. *Oncotarget. Impact Journals LLC;* 2016 Aug 31;7(45):72415–30.
203. Holm M, Borg A, Ehrenberg M, Sanyal S. Molecular mechanism of viomycin inhibition of peptide elongation in bacteria. *Proceedings of the National Academy of Sciences. National Academy of Sciences;* 2016 Jan 26;113(4):978–83.
204. Brummett RE. *Drug-induced Ototoxicity. Vol. 19. 1980. 17 p.*
205. Stanley RE, Blaha G, Grodzicki RL, Strickler MD, Steitz TA. The structures of the anti-tuberculosis antibiotics viomycin and capreomycin bound to the 70S ribosome. *Nat Struct Mol Biol.* 2010 Mar 1;17(3):289–93.
206. Pulk A, Cate JHD. Control of ribosomal subunit rotation by elongation factor G. *Science.* 2013 Jun 28;340(6140):1235970–0.
207. Brilot AF, Korostelev AA, Ermolenko DN, Grigorieff N. Structure of the ribosome with elongation factor G trapped in the pretranslocation state. *Proceedings of the National Academy of Sciences. National Academy of Sciences;* 2013 Dec 24;110(52):20994–9.
208. Arnold T, Linke D. *The Use of Detergents to Purify Membrane Proteins. Vol. 43. Hoboken, NJ, USA: John Wiley & Sons, Inc; 2001. 4350 p.*
209. Seddon AM, Curnow P, Booth PJ. Membrane proteins, lipids and detergents: not just a soap opera. *Lipid-Protein Interactions.* 2004;1666(1):105–17.
210. Comte J, Maisterrena B, Gautheron DC. Lipid composition and protein profiles of outer and inner membranes from pig heart mitochondria. Comparison with microsomes. *Biochim Biophys Acta.* 1976 Jan;419(2):271–84.

211. Horvath SE, Daum G. Lipids of mitochondria. *Prog Lipid Res.* 2013 Oct;52(4):590–614.
212. Basu Ball W, Neff JK, Gohil VM. The role of nonbilayer phospholipids in mitochondrial structure and function. *FEBS Lett.* 2018 Apr 1;592(8):1273–90.
213. Juszkievicz S, Chandrasekaran V, Lin Z, Kraatz S, Ramakrishnan V, Hegde RS. ZNF598 Is a Quality Control Sensor of Collided Ribosomes. *Mol Cell.* 2018 Nov;72(3):469–481.e7.
214. Brown A, Rathore S, Kimanius D, Aibara S, Bai X-C, Rorbach J, et al. Structures of the human mitochondrial ribosome in native states of assembly. *Nat Struct Mol Biol.* Nature Publishing Group, a division of Macmillan Publishers Limited. All Rights Reserved; 2017 Sep 11;22(10):914–869.
215. Adilakshmi T, Bellur DL, Woodson SA. Concurrent nucleation of 16S folding and induced fit in 30S ribosome assembly. *Nature.* 2008 Oct;455(7217):1268–72.
216. Li N, Chen Y, Guo Q, Zhang Y, Yuan Y, Ma C, et al. Cryo-EM structures of the late-stage assembly intermediates of the bacterial 50S ribosomal subunit. *Nucleic Acids Research.* Oxford University Press; 2013 Aug 1;41(14):7073–83.
217. Jomaa A, Jain N, Davis JH, Williamson JR, Britton RA, Ortega J. Functional domains of the 50S subunit mature late in the assembly process. *Nucleic Acids Research.* Oxford University Press; 2014 Mar 1;42(5):3419–35.
218. Pearce SF, Rorbach J, Haute LV, D'Souza AR, Rebelo-Guiomar P, Powell CA, et al. Maturation of selected human mitochondrial tRNAs requires deadenylation. Nilsen TW, editor. *Elife.* eLife Sciences Publications, Ltd; 2017;6:e27596.
219. Koripella RK, Sharma MR, Risteff P, Keshavan P, Agrawal RK. Structural insights into unique features of the human mitochondrial ribosome recycling. *Proc Natl Acad Sci USA.* 2019 Apr 23;116(17):8283.
220. Saurer M, Ramrath DJF, Niemann M, Calderaro S, Prange C, Mattei S, et al. Mitoribosomal small subunit biogenesis in trypanosomes involves an extensive assembly machinery. *Science.* 2019 Sep;365(6458):1144–9.
221. Coppinger RJ, Diamond AM. Selenium deficiency and human disease. In: Hatfield DL, editor. *Selenium: Its Molecular Biology and Role in Human Health.* Boston, MA: Springer US; 2001. pp. 219–33. (*Selenium: Its Molecular Biology and Role in Human Health*).
222. Schmidt RL, Simonović M. Synthesis and decoding of selenocysteine and human health. *Croat Med J.* 2012 Dec;53(6):535–50.

223. Benstoem C, Goetzenich A, Kraemer S, Borosch S, Manzanares W, Hardy G, et al. Selenium and its supplementation in cardiovascular disease--what do we know? *Nutrients*. MDPI; 2015 Apr 27;7(5):3094–118.
224. Bosl MR, Takaku K, Oshima M, Nishimura S, Taketo MM. Early embryonic lethality caused by targeted disruption of the mouse selenocysteine tRNA gene (*Trsp*). *Proceedings of the National Academy of Sciences*. 1997 May;94(11):5531–4.
225. Kumaraswamy E, Carlson BA, Morgan F, Miyoshi K, Robinson GW, Su D, et al. Selective removal of the selenocysteine tRNA [*Ser*]Sec gene (*Trsp*) in mouse mammary epithelium. *Mol Cell Biol*. 2003 Mar;23(5):1477–88.
226. Seeher S, Atassi T, Mahdi Y, Carlson BA, Braun D, Wirth EK, et al. *Secisbp2* is essential for embryonic development and enhances selenoprotein expression. *Antioxid Redox Signal*. 2014 Aug;21(6):835–49.
227. Frolova LY, Tsivkovskii RY, Sivolobova GF, Oparina NY, Serpinsky OI, Blinov VM, et al. Mutations in the highly conserved GGQ motif of class 1 polypeptide release factors abolish ability of human eRF1 to trigger peptidyl-tRNA hydrolysis. *RNA*. 1999 Aug;5(8):1014–20.
228. Berry MJ, Banu L, Chen YY, Mandel SJ, Kieffer JD, Harney JW, et al. Recognition of UGA as a selenocysteine codon in type I deiodinase requires sequences in the 3' untranslated region. *Nature*. 1991 Sep;353(6341):273–6.
229. Berry MJ, Banu L, Harney JW, Larsen PR. Functional characterization of the eukaryotic SECIS elements which direct selenocysteine insertion at UGA codons. *EMBO J*. 1993 Aug;12(8):3315–22.
230. Shen Q, Chu FF, Newburger PE. Sequences in the 3'-untranslated region of the human cellular glutathione peroxidase gene are necessary and sufficient for selenocysteine incorporation at the UGA codon. *Journal of Biological Chemistry*. 1993 May;268(15):11463–9.
231. Copeland PR, Fletcher JE, Carlson BA, Hatfield DL, Driscoll DM. A novel RNA binding protein, SBP2, is required for the translation of mammalian selenoprotein mRNAs. *EMBO J*. 2000 Jan;19(2):306–14.
232. Fagegaltier D. Characterization of mSelB, a novel mammalian elongation factor for selenoprotein translation. *EMBO J*. John Wiley & Sons, Ltd; 2000 Sep 1;19(17):4796–805.
233. Tujebajeva RM, Copeland PR, Xu XM, Carlson BA, Harney JW, Driscoll DM, et al. Decoding apparatus for eukaryotic selenocysteine insertion. *EMBO Rep*. 2000 Aug;1(2):158–63.
234. Kossinova O, Malygin A, Krol A, Karpova G. The SBP2 protein central to selenoprotein synthesis contacts the human ribosome at expansion

- segment 7L of the 28S rRNA. RNA. Cold Spring Harbor Laboratory Press; 2014 Jun 16;20(7):1046–56.*
235. *Chavatte L, Brown BA, Driscoll DM. Ribosomal protein L30 is a component of the UGA-selenocysteine recoding machinery in eukaryotes. Nat Struct Mol Biol. 2005 May;12(5):408–16.*
 236. *Wu R, Shen Q, Newburger PE. Recognition and binding of the human selenocysteine insertion sequence by nucleolin. J Cell Biochem. 2000 Apr;77(3):507–16.*
 237. *Budiman ME, Bubenik JL, Miniard AC, Middleton LM, Gerber CA, Cash A, et al. Eukaryotic initiation factor 4a3 is a selenium-regulated RNA-binding protein that selectively inhibits selenocysteine incorporation. Mol Cell. 2009 Aug;35(4):479–89.*
 238. *Shetty SP, Shah R, Copeland PR. Regulation of selenocysteine incorporation into the selenium transport protein, selenoprotein P. Journal of Biological Chemistry. American Society for Biochemistry and Molecular Biology; 2014 Sep 5;289(36):25317–26.*
 239. *Schoenmakers E, Carlson B, Agostini M, Moran C, Rajanayagam O, Bochukova E, et al. Mutation in human selenocysteine transfer RNA selectively disrupts selenoprotein synthesis. J Clin Invest. 2016 Mar 1;126(3):992–6.*
 240. *Turanov AA, Xu X-M, Carlson BA, Yoo M-H, Gladyshev VN, Hatfield DL. Biosynthesis of Selenocysteine, the 21st Amino Acid in the Genetic Code, and a Novel Pathway for Cysteine Biosynthesis. advances. 2011 Mar 3;2(2):122–8.*
 241. *Agamy O, Ben Zeev B, Lev D, Marcus B, Fine D, Su D, et al. Mutations disrupting selenocysteine formation cause progressive cerebello-cerebral atrophy. Am J Hum Genet. Elsevier; 2010 Oct 8;87(4):538–44.*
 242. *Schoenmakers E, Agostini M, Mitchell C, Schoenmakers N, Papp L, Rajanayagam O, et al. Mutations in the selenocysteine insertion sequence-binding protein 2 gene lead to a multisystem selenoprotein deficiency disorder in humans. J Clin Invest. 2010 Dec 1;120(12):4220–35.*
 243. *Fradejas-Villar N. Consequences of mutations and inborn errors of selenoprotein biosynthesis and functions. Selenium Research in Redox Biology, Health and Disease - 200 Years Anniversary Issue. 2018;127:206–14.*
 244. *Maiti B, Arbogast S, Allamand V, Moyle MW, Anderson CB, Richard P, et al. A mutation in the SEPNI selenocysteine redefinition element (SRE) reduces selenocysteine incorporation and leads to SEPNI-related myopathy. Hum Mutat. 2009 Mar 1;30(3):411–6.*

245. Fischer N, Neumann P, Bock LV, Maracci C, Wang Z, Paleskava A, et al. The pathway to GTPase activation of elongation factor SelB on the ribosome. *Nature*. 2016 Dec;540(7631):80–5.
246. Itoh Y, Chiba S, Sekine S-I, Yokoyama S. Crystal structure of human selenocysteine tRNA. *Nucleic Acids Research*. 2009 Aug 19;37(18):6259–68.
247. Dobosz-Bartoszek M, Pinkerton MH, Otwinowski Z, Chakravarthy S, Söll D, Copeland PR, et al. Crystal structures of the human elongation factor eEFSec suggest a non-canonical mechanism for selenocysteine incorporation. *Nat Commun. The Author(s) SN* ; 2016 Oct 6;7:12941.
248. Shao S, Malsburg von der K, Hegde RS. Listerin-dependent nascent protein ubiquitination relies on ribosome subunit dissociation. *Mol Cell. Cell Press*; 2013 Jun 6;50(5):637–48.
249. Gibson DG. Enzymatic assembly of overlapping DNA fragments. *Methods Enzymol*. 2011;498:349–61.
250. Peacock JR, Walvoord RR, Chang AY, Kozlowski MC, Gamper H, Hou Y-M. Amino acid-dependent stability of the acyl linkage in aminoacyl-tRNA. *RNA*. 2014 Jun;20(6):758–64.
251. Pinkerton MH, Copeland PR. In Vitro Translation Assays for Selenocysteine Insertion. *Methods Mol Biol*. 2018;1661:93–101.
252. Gupta N, DeMong LW, Banda S, Copeland PR. Reconstitution of selenocysteine incorporation reveals intrinsic regulation by SECIS elements. *J Mol Biol*. 2013 Jul;425(14):2415–22.
253. Rinehart KLJ, Gloer JB, Hughes RGJ, Renis HE, McGovren JP, Swynenberg EB, et al. Didemnins: antiviral and antitumor depsipeptides from a caribbean tunicate. *Science*. 1981 May;212(4497):933–5.
254. Shao S, Murray J, Brown A, Taunton J, Ramakrishnan V, Hegde RS. Decoding Mammalian Ribosome-mRNA States by Translational GTPase Complexes. *Cell*. 2016 Nov;167(5):1229–1240.e15.
255. Dever TE, Ivanov IP. Roles of polyamines in translation. *Journal of Biological Chemistry*. 2018 Nov;293(48):18719–29.
256. Shetty SP, Sturts R, Vetick M, Copeland PR. Processive incorporation of multiple selenocysteine residues is driven by a novel feature of the selenocysteine insertion sequence. *Journal of Biological Chemistry*. 2018 Dec;293(50):19377–86.
257. Lanman J, Lam TT, Barnes S, Sakalian M, Emmett MR, Marshall AG, et al. Identification of novel interactions in HIV-1 capsid protein assembly by high-resolution mass spectrometry. *J Mol Biol*. 2003 Jan;325(4):759–72.
258. Moore SD, Prevelige PEJ. A P22 scaffold protein mutation increases the

robustness of head assembly in the presence of excess portal protein. J Virol.
2002 Oct;76(20):10245-55.